UNIVERSITY OF CALIFORNIA
SANTA CRUZ

SEARCH FOR SUPERSYMMETRY WITH COMPRESSED MASS SPECTRA USING A VECTOR BOSON FUSION TOPOLOGY WITH THE ATLAS DETECTOR

A dissertation submitted in partial satisfaction
of the requirements for the degree of

DOCTOR OF PHILOSOPHY

in

PHYSICS

by

Nathan J. Kang

September 2024

The Dissertation of Nathan J. Kang
is approved:

_____
Professor Michael Hance, Chair

_____
Professor Jason Nielsen

_____
Professor Bruce Schumm

_____
Peter Biehl
Vice Provost and Dean of Graduate Studies

Contents

Figures and Tables

List of Figures

List of Tables

Abstract

Search for supersymmetry with compressed mass spectra using a vector boson fusion topology with the ATLAS detector

by

Nathan J. Kang

Supersymmetric extensions of the Standard Model of particle physics are theoretically motivated by their ability to potentially address some of the biggest unresolved questions in physics. However thus far there has been no conclusive evidence to support the idea that supersymmetry exists at the energy scales currently being probed by the experiments at the Large Hadron Collider. If supersymmetry does exist in nature, one reason that it may be evading experimental detection is that the production of supersymmetric particles is rare and difficult to distinguish from background processes. To overcome this challenge, thoughtful design of the analysis strategy is required.

This dissertation presents a search for the production of electroweak supersymmetric particles with compressed mass spectra utilizing a vector boson fusion topology. The search was conducted using 140 fb^{-1} of data recorded with the ATLAS detector from proton-proton collisions at $\sqrt{s}$ = 13 TeV. The general search strategy involves selecting events characterized by significant missing transverse momentum, the presence of two forward jets that are consistent with a vector boson fusion signature, and a lepton veto to target models with compressed mass spectra. Additionally, a boosted decision tree algorithm is used to further improve the signal to background separation.

The results of the search show no evidence for supersymmetry, and no significant deviations are found between the prediction based on the Standard Model and the observed data. This search probes models that have yet to be excluded by previous searches and is able to extend existing limits for these compressed supersymmetric scenarios.

For my parents and brothers

Acknowledgements

I would like to first thank Mike Hance for being my advisor and mentor during my time at UCSC. It has been a long journey for me as a graduate student, and you have always been there to support me through all the various ups and downs. You played an invaluable role in getting through key stages of the work presented here when the circumstances seemed uncertain and hopeless. I am deeply grateful for the significant role you have had in my life.

I would like to extend my utmost appreciation to the Compressed VBF SUSY analysis team: Giordon Stark, Da Xu, Lei Guo, Mingjie Zhai, Xuai Zhuang, Tina Potter, Dominic Jones, Jeff Shahinian, and Michael Holzbock. This work would not have been possible without your help and collaboration over the past several years. I am very thankful to have worked with such nice and knowledgeable team members.

I thank Jason Nielsen and Bruce Schumm for being members of my dissertation reading committee and taking the time to review my dissertation. I am also thankful for your mentorship and teaching during my time as a graduate student.

The SCIPP ATLAS group provided a welcoming environment for me to learn and grow as a researcher. A special thanks to Matthew Gignac and Giordon Stark for their guidance and support, especially when I was starting out with my research in ATLAS. I also want to sincerely thank the SCIPP ATLAS ITk Strips group, led by Tony Affolder and Vitaliy Fadeyev. I will never forget my time working on the Strips upgrade, and I am grateful for the skills and knowledge I acquired from those experiences.

I thank my fellow physics grads, both current and former, who have provided me with companionship throughout my graduate school years. I would like to specifically thank Cole Helling, Carolyn Gee, Yuzhan Zhao, Hava Schwartz, Jacob Johnson,

Joseph Connell, and Rene Padilla. I want to especially thank Carolyn and Hava again for all the great memories during my time at CERN.

Finally, I give the greatest thanks to my family. Thank you, Dad, Mom, Ryan, and Darren, for loving and supporting me so that I am able to reach this point in my life.

Chapter 1

Introduction

The Standard Model of particle physics, which describes the fundamental particles and their interactions, is one of the most well-tested theories in science. Developed over several decades during the second half of the 20th century, it has been subjected to rigorous experimental scrutiny and has consistently demonstrated remarkable accuracy and predictive power. With the discovery of the Higgs boson in 2012 at the Large Hadron Collider (LHC) at CERN [16, 51], the experimental confirmation of all the fundamental particles predicted by the Standard Model had been completed. Despite these successes, the Standard Model has limitations and cannot account for certain phenomena. For example, it is unable to provide a viable particle candidate for the dark matter. Other open issues include the hierarchy problem with respect to the mass of the Higgs boson and the unification of the gauge couplings in the context of a Grand Unified Theory.

Supersymmetry is a theoretical framework that if discovered could help answer these questions. Supersymmetry extends the Standard Model of particle physics by introducing a symmetry between bosons and fermions that would manifest as additional fundamental particles called superpartners that pair with the Standard Model particles [75, 91, 112, 113]. For the fermions, there are scalar superpartners

called sfermions, while the fermionic superpartners of the gauge bosons are called gauginos. Additionally, the Higgs field has associated fermionic superpartners known as higgsinos. Supersymmetric particles can result from combinations of these superpartners, as in the case of the electroweakinos, which arise from the mixing of the electroweak gauginos (winos and bino) and higgsinos. The electrically neutral electroweakinos are called neutralinos and the electrically charged electroweakinos are called charginos. The lightest and second lightest neutralinos are denoted as $\tilde{\chi}_1^0$ and $\tilde{\chi}_2^0$ respectively while the lightest chargino is denoted as $\tilde{\chi}_1^{\pm}$.

Significant efforts searching for supersymmetry have been and continue to be undertaken at major particle colliders such as the LHC. However thus far experimental evidence for supersymmetry remains elusive and correspondingly large portions of the parameter space for various supersymmetric models have been excluded. Experimental detection may be hindered due to the rarity of supersymmetric particle production and the difficulty in distinguishing against background processes. This is the case in searches for the electroweak production of supersymmetric particles where analysis strategies need to be carefully devised.

This dissertation reports on the design and results of a search for the production of electroweakinos, with compressed mass spectra utilizing a vector boson fusion topology. This search was conducted using 140 fb^{-1} of data recorded between 2015 and 2018 with the ATLAS Detector from proton-proton collisions at $\sqrt{s}$ = 13 TeV. The models targeted in this search feature compressed mass spectra of the electroweakinos around $\Delta m(\tilde{\chi}_2^0,\tilde{\chi}_1^0)$ of 1 GeV that result in extremely soft decay products and make the models challenging to probe experimentally. These mass splittings are too large to produce a disappearing track signature [36, 41] yet too small to produce reconstructable leptons from the electroweakino decays that could be targeted in multi-lepton searches [30, 109]. The search strategy employed to

target such models involves selecting events with significant missing transverse momentum $E_{\mathrm{T}}^{\mathrm{miss}}$ and the presence of at least two high-p_{T} jets with a large separation in pseudorapidity and large dijet invariant mass that characterize a vector boson fusion process. As the electroweakino decay products are expected to be too soft to be reconstructed, a lepton veto is imposed in the signal regions. This allows the results of the search to be framed in a manner that does not depend on assumptions of the branching ratios of the electroweakinos to leptons as in previous searches targeting similar models [30]. A boosted decision tree classifier is utilized to further improve the signal to background separation, and the output scores from the classifier are used to perform a shape fit and obtain the final results.

It should be noted that a search published by the CMS experiment [52] similarly utilized a vector boson fusion topology in a zero-lepton channel to probe the very compressed mass splittings targeted here. The CMS result showed strong sensitivity reach in this regime with only a portion of the full Run 2 dataset. This result was used as inspiration for the design of this search with the expectation that utilizing the full Run 2 dataset would provide sensitivity reach beyond what was achieved by CMS. However the analysis team for this search was unable to reproduce results with similar sensitivity to that reported in the CMS result. Extensive studies were performed to try and resolve this discrepancy and the cause was ultimately traced to a difference in the generation of the signal samples in regards to the inclusion of interference effects. After several correspondences and discussions between the analysis team and the CMS authors, it was concluded that interference effects between pure QED and mixed QCD and QED signal processes were not properly taken into account during the CMS signal event generation. This leads to a larger expected SUSY signal compared to a setup that takes into account the interference, with the differential cross-section reaching up to a factor of two larger at very large

dijet invariant mass as seen in Figure 1.1. Therefore the sensitivity reach of the CMS result is thought to be overestimated compared to that which is expected based on a "realistic" setup that properly incorporates the interference effects. This search utilizes signal samples that take into account these interference effects, and thus the expected sensitivity of this search is limited compared to the expectations based on the CMS result. For this reason higgsino-like models have not been considered in this search due to their smaller cross sections compared to wino/bino-like scenarios in these vector boson fusion topologies. Despite these challenges, extensive efforts have been made to optimize the analysis strategy to reach a point of being sensitive to unexcluded portions of the parameter space for these signal models.

The following chapters describe various aspects of the search. First the theoretical background and motivation for the search are presented in Chapter 2. The experimental details regarding the LHC and the ATLAS detector are described in Chapter 3. Descriptions of the data and simulated samples are provided in Chapter 4 while Chapter 5 defines the physics objects utilized in the search. Chapters 6–7 describe the strategies for targeting the SUSY signals and estimating the backgrounds. Details on the various systematic uncertainties are discussed in Chapter 8 and finally the results of the search are presented in Chapter 9.

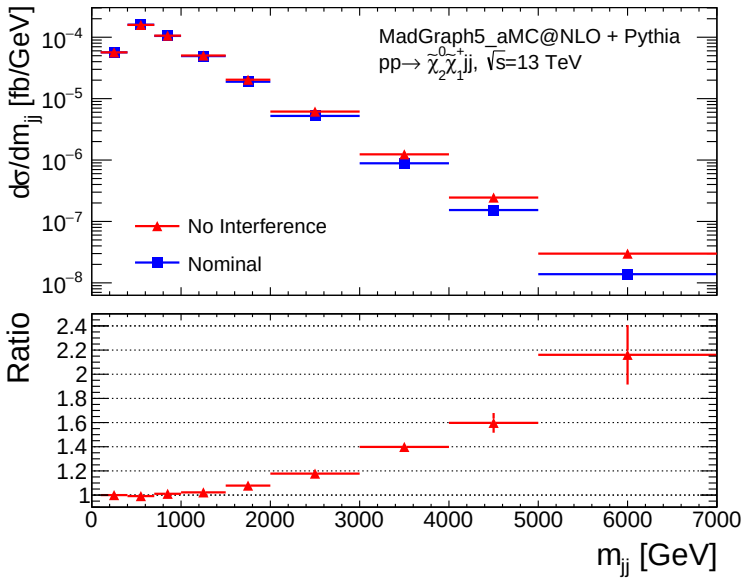

Figure 1.1: Comparison of different process definitions for $\tilde{\chi}_2^0\tilde{\chi}_1^+$ production in association with two jets, made at particle level as a function of the dijet invariant mass. The "Nominal" sample is labeled as such since it properly accounts for all interference effects in the signal processes and is generated according to the details described in Section 4.2. The "No Interference" sample generates pure-QED processes separately from processes with both QCD and QED couplings. Events are selected by requiring two jets with $p_{\mathrm{T}} > 30$ GeV and $|\eta| < 5.0$, and oppositely-signed pseudorapidities.

Chapter 2

The Theoretical Background

2.1. The Standard Model of Particle Physics

The present understanding of how our physical reality works at the smallest length scales is based upon the Standard Model of particle physics. The Standard Model is a relativistic quantum field theory that describes all the known elementary particles and their interactions through the electromagnetic, weak, and strong forces [73, 77, 101, 105, 107, 108, 111]. The Lagrangian density $\mathcal{L}$ of the theory is the mathematical object that encodes this information as a function composed of the underlying quantum fields and is invariant under local gauge transformations of the symmetry group $SU(3)_C \times SU(2)_L \times U(1)_Y$. Here $SU(3)_C$ denotes the symmetry based on the special unitary group of degree 3 that acts on the quantum property of color C and describes the strong interaction in quantum chromodynamics (QCD). The symmetry $SU(2)_L \times U(1)_Y$ corresponds to the product of the special unitary group of degree 2 acting on the weak isospin carried by left-handed particles and the unitary group of degree 1 acting on the weak hypercharge Y. This symmetry defines the electroweak interaction that unifies the theories of the electromagnetic and weak forces. The

electric charge Q is related to the weak isospin T_3 and hypercharge Y by

$$Q = T_3 + Y \,. \tag{2.1.1}$$

The particles of the Standard Model manifest as excitations of their corresponding quantum fields. Their behavior and possible interactions are dictated by the terms in the Lagrangian involving these fields along with the properties of the particles.

Particles can be broadly categorized based on the their spin, with fermions being those that have half-integer values and bosons that have integer values. In the Standard Model, all the elementary fermions have spin $\frac{1}{2}$ and are classified as either quarks or leptons depending on their quantum properties. Quarks carry the color charge with the three possibilities of red, green, and blue that allow them to interact via the strong force. There are six flavors of quarks that are differentiated by their electric charge and mass. Those with an electric charge of $+\frac{2}{3}e$ are known as up-type quarks and include the up, charm, and top quarks. Those with an electric charge of $-\frac{1}{3}e$ are known as down-type quarks and include the down, strange, and bottom quarks. Under the symmetry $SU(2)_L$, the quarks can additionally be arranged according to their mass in three generations composed of doublets of left-handed up-type and down-type quarks while the right-handed quarks are singlets. Leptons do not interact through the strong force in contrast to quarks; however they share the similarity of consisting of six different flavors. Leptons with a charge of -1e, simply referred to as charged leptons, include the electron, muon, and tau. Those that are electrically neutral are known as neutrinos and there is a corresponding neutrino for each charged lepton flavor. The leptons can also be arranged into three generations of $SU(2)_L$ doublets made up of a left-handed charged lepton and its associated neutrino. For each fermion there exists a corresponding antiparticle with the opposite electric charge. Other quantum properties aside from the electric charge may also be different

between particles and antiparticles such as the baryon number or lepton number. While quarks carry color charge, antiquarks carry anticolor charge instead. In the case of the electrically neutral neutrinos, there are antineutrinos that also have no electric charge but are able to be distinguished based on other properties such as chirality and weak isospin.

The elementary bosons in the Standard Model consist of the spin 0 Higgs boson and the spin 1 gauge bosons. The Higgs boson and its associated field are relevant for understanding the origin of the masses of the elementary particles and will be discussed in more detail when describing electroweak symmetry breaking. The spin 1 gauge bosons play the role of mediators for their respective interactions. Gluons are the force carriers for the strong interaction. There are eight types of gluons, corresponding to the eight generators of the $SU(3)_C$ color symmetry group. Although the gluons are massless, the range of the strong force is limited due to the presence of gluon–gluon interactions as described in the theory of color confinement. The $W^{\pm}$ and Z bosons mediate the weak interaction which is also a short-range force. However in this case the range of the force is due to the large masses of these bosons which lie around 80 GeV and 91 GeV for the W and Z bosons respectively [113]. The fact that the weak bosons are massive also allows these particles to decay. For the electromagnetic interaction, the corresponding gauge boson is the photon which interacts with particles carrying electric charge Q. The photon is massless which corresponds to the electromagnetic force being long-ranged.

Gauge invariance determines the types of interaction terms present in the Lagrangian between the fermions and gauge bosons. The kinetic term for a free Dirac fermion is given by

$$\mathcal{L}_{\text{Dirac}} = \bar{\psi}\left(i\gamma^{\mu}\partial_{\mu}\right)\psi \tag{2.1.2}$$

where ψ is a Dirac field and γ^μ are the gamma matrices. This term is not invariant upon performing a gauge transformation for the Standard Model gauge groups. To resolve this, the ordinary derivative ∂_μ in the kinetic term is replaced with the gauge covariant derivative D_μ that ensures that the resulting term is gauge invariant. For example, the $SU(3)_C$ gauge symmetry of QCD requires the gauge covariant derivative that acts on the quark fields to be

$$D_\mu = \partial_\mu - ig_s T^a G_\mu^a \tag{2.1.3}$$

with g_s being the strong coupling constant, T^a are the generators of $SU(3)$, G_μ^a are the gluon fields, and the index a ranges from 1 to 8 corresponding to the gluons being part of a color octet. It can be seen that by imposing gauge invariance, an interaction term between the gluons and the quarks q arises

$$\mathcal{L}_{\text{int}} = \bar{q}\left(-g_s \gamma^\mu T^a G_\mu^a\right) q\,. \tag{2.1.4}$$

The fact that the W and Z bosons are massive was an issue when the electroweak theory was being developed because mass terms for these gauge bosons in the Lagrangian would violate the gauge symmetry. A similar problem is encountered for the fermions where mass terms would also break the gauge invariance. The introduction of electroweak symmetry breaking was able to resolve these issues by explaining how these particles could be massive without breaking the gauge invariance of the theory [105, 111]. The key to electroweak symmetry breaking is the existence of the Higgs field, which is a scalar field defined as a complex $SU(2)_L$ doublet carrying weak isospin of $T_3 = \pm\frac{1}{2}$ and hypercharge $Y = \frac{1}{2}$. The Higgs field has a "sombrero" potential of the form:

$$V(\Phi) = -\mu^2(\Phi^\dagger\Phi) + \lambda(\Phi^\dagger\Phi)^2\,. \tag{2.1.5}$$

In the very early universe when the temperature cooled below a certain threshold (estimated to be approximately 159 GeV [60]) the field acquired a non-zero vacuum expectation value (VEV) when it settled on a particular minimum in the potential. This minimum can be described mathematically as

$$\Phi_0 = \frac{1}{\sqrt{2}}\begin{pmatrix} 0 \\ v \end{pmatrix} \tag{2.1.6}$$

where $v = \sqrt{\frac{-\mu^2}{\lambda}}$. When this VEV is realized, massive weak bosons are generated along with the massless photon via the Higgs mechanism [65, 78, 81]. Before electroweak symmetry breaking, the electroweak theory describes the presence of the three weak isospin fields $W^{1,2,3}$ and the weak hypercharge field B. These electroweak fields interact with the Higgs field Φ through the following terms in the Lagrangian:

$$\mathcal{L} = (D^\mu \Phi)^\dagger (D_\mu \Phi)\,, \tag{2.1.7}$$

$$D_\mu = \partial_\mu - ig\frac{\tau^i}{2}W_\mu^i - ig'\frac{Y}{2}B_\mu\,. \tag{2.1.8}$$

Here g and g' refer to the gauge coupling constants for weak isospin and weak hypercharge respectively, τ^i denotes the generators of $SU(2)$, and Y denotes the weak hypercharge. Once the Higgs field acquires a non-zero vacuum expectation value, these weak fields mix together to produce the fields corresponding to the physical bosons we observe as follows:

$$W_\mu^\pm = \frac{1}{\sqrt{2}}(W_\mu^1 \mp iW_\mu^2)\,, \tag{2.1.9}$$

$$Z_\mu = \frac{1}{\sqrt{g^2 + g'^2}}(gW_\mu^3 - g'B_\mu)\,, \tag{2.1.10}$$

$$A_\mu = \frac{1}{\sqrt{g^2 + g'^2}}(g'W_\mu^3 + gB_\mu)\,. \tag{2.1.11}$$

Substituting the Higgs vacuum expectation value into the Lagrangian and rewriting

it in terms of these physical fields produces the following mass terms for the W and Z bosons

$$\mathcal{L}_{\text{mass}} = \left(\frac{1}{2}gv\right)^2 W_\mu^+ W^{-\mu} + \frac{1}{2}\left(\frac{1}{2}\sqrt{g^2+g'^2}\,v\right)^2 Z_\mu Z^\mu \tag{2.1.12}$$

such that the masses are given by $m_W = \frac{1}{2}gv$ and $m_Z = \frac{1}{2}\sqrt{g^2+g'^2}v$. These mass terms do not exist for A_μ and thus the corresponding gauge boson, the photon, is massless. Thus after electroweak symmetry breaking, three out of the four degrees of freedom of the Higgs field give rise to the mass of the weak bosons. The remaining degree of freedom is what manifests as the physical Higgs boson. The fluctuation around the vacuum expectation value of the Higgs field can be written as:

$$\Phi = \frac{1}{\sqrt{2}}\begin{pmatrix} 0 \\ v + h(x) \end{pmatrix} \tag{2.1.13}$$

where $h(x)$ is a scalar field corresponding to the Higgs boson. Expanding the Higgs potential in terms of the field definition above and then collecting the terms quadratic in $h(x)$ gives

$$V(\Phi) = \lambda v^2 h(x)^2 \,. \tag{2.1.14}$$

Thus the mass of the Higgs boson is given by $m_h = \sqrt{2\lambda}v$.

Masses for the fermions also arise from interactions with the Higgs field following electroweak symmetry breaking. The fermions interact with the Higgs field via Yukawa couplings of the form:

$$\mathcal{L}_{\text{Yukawa}} = -\lambda_e \bar{L} H e_R - \lambda_u \bar{Q}\tilde{H} u_R - \lambda_d \bar{Q} H d_R \,. \tag{2.1.15}$$

Here the λ_i terms correspond to the Yukawa coupling constants. $\bar{L}$ and $\bar{Q}$ are the left-handed lepton and quark doublets while e_R, u_R, and d_R are the right-handed

singlets for the electron, up quark, and down quark respectively. H denotes the Higgs doublet with $\tilde{H}$ being its conjugate. Similar terms are found for antifermions by taking the Hermitian conjugate. Once the Higgs field acquires a vacuum expectation value, the Yukawa interaction terms between the fermions and the Higgs effectively become mass terms:

$$m_e = \frac{\lambda_e v}{\sqrt{2}}\,, \tag{2.1.16}$$

$$m_u = \frac{\lambda_u v}{\sqrt{2}}\,, \tag{2.1.17}$$

$$m_d = \frac{\lambda_d v}{\sqrt{2}}\,, \tag{2.1.18}$$

$$\mathcal{L}_{\text{mass}} = -m_e \bar{e}_L e_R - m_u \bar{u}_L u_R - m_d \bar{d}_L d_R\,. \tag{2.1.19}$$

It can be seen that the masses are proportional to the Higgs vacuum expectation value v and the Yukawa coupling term λ for the corresponding fermion.

Figure 2.1 provides a depiction of the content and structure of the Standard Model.

2.2. Supersymmetry

Supersymmetry (SUSY) [75, 91, 112, 113] posits the existence of an additional symmetry in nature between fermions and bosons. This symmetry can be described through an operator Q that transforms fermionic fields to bosonic ones or vice-versa

$$Q\psi = \phi\,, \tag{2.2.1}$$

$$Q\phi = \psi\,. \tag{2.2.2}$$

The existence of such a symmetry would lead to each particle in the Standard Model having a corresponding partner particle referred to as a superpartner. A particle and its superpartner are both part of a supermultiplet which is a representation of the

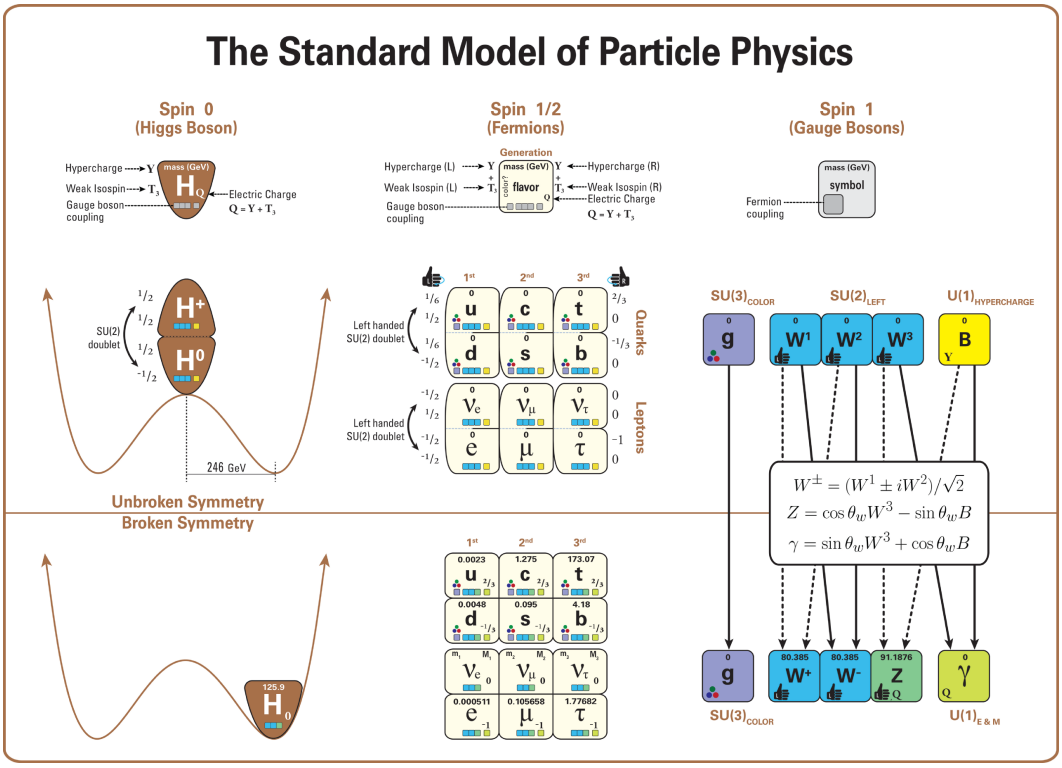

Figure 2.1: This diagram visually depicts all the particles of the Standard Model and their properties. It also demonstrates how the particles change following electroweak symmetry breaking when the Higgs field acquires a nonzero vacuum expectation value. [43]

supersymmetry algebra. The supersymmetry generators Q and $Q^\dagger$ commute with the generators for the Standard Model gauge symmetries. Thus the superpartners would differ from their partner particles by a spin of $\frac{1}{2}$ but would otherwise share the same quantum numbers. The simplest model that extends the Standard Model to incorporate supersymmetry is the Minimal Supersymmetric Standard Model (MSSM). The following details in this section are framed in the context of the MSSM since the search presented in this dissertation is also based on it.

The superpartners for the fermions would be spin 0 scalar particles called sfermions. For quarks and leptons specifically the superpartners are referred to as squarks and sleptons respectively. Since the left-handed and right-handed fermions transform differently under the Standard Model gauge symmetries, they belong in separate chiral supermultiplets which consist of a Weyl fermion and a complex scalar. Thus for each of the quarks and charged leptons in the Standard Model there are two corresponding sfermions: a scalar superpartner of the left-handed fermion $\tilde{f}_L$ and a scalar superpartner of the right-handed fermion $\tilde{f}_R$. In the Standard Model the neutrinos are always left-handed so the sneutrinos do not need a subscript to indicate the handedness of the corresponding neutrino.

For the spin 1 gauge bosons, their superpartners would be spin $\frac{1}{2}$ fermions called gauginos. The superpartner for the gluon g is the gluino $\tilde{g}$. In the case of the electroweak bosons, there are three winos $\tilde{W}^\mu$ and the bino $\tilde{B}$ which are the superpartners corresponding to the fields prior to electroweak symmetry breaking.

To incorporate the Higgs in a supersymmetric extension of the Standard Model, two Higgs chiral supermultiplets are introduced. By having two Higgs supermultiplets the theory avoids a gauge anomaly that would otherwise be present in a theory with just one Higgs supermultiplet [91]. The two Higgs supermultiplets differ in the weak hypercharge Y with the corresponding $SU(2)_L$ doublet having $Y = +\frac{1}{2}$ denoted as H_u

and the one with $Y = -\frac{1}{2}$ denoted as H_d. The subscript labels here for H are based on how the fermion masses arise, with H_u generating masses for the up-type quarks and H_d doing the same for down-type quarks and the charged leptons. Both doublets consist of components having an electric charge of 0 and 1 with $H_u = (H_u^+, H_u^0)$ and $H_d = (H_d^0, H_d^-)$. From the introduction of these two Higgs doublets it follows that there would also be spin $\frac{1}{2}$ superpartners associated with them which are called higgsinos. The higgsinos are denoted as $\tilde{H}_u = (\tilde{H}_u^+, \tilde{H}_u^0)$ and $\tilde{H}_d = (\tilde{H}_d^0, \tilde{H}_d^-)$.

The superpotential that encodes the supersymmetric interactions in the Lagrangian can generically include terms that violate baryon number B and lepton number L. The existence of such processes that violate B or L are strongly constrained by experiments such as searches for proton decay, which has yet to be observed with lower bounds of 10^{34} years [57]. To account for this, the MSSM introduces a symmetry based on R-parity [67]

$$P_R = (-1)^{3(B-L)+2s} \tag{2.2.3}$$

that depends on the spin s of the particle in addition to B and L. R-parity conservation requires that the product of P_R for all fields in an interaction should be equal to +1. The Standard Model particles all have P_R = +1 while all supersymmetric particles have P_R = -1. This implies that there must be an even number of supersymmetric particles in an interaction that conserves R-parity. It follows that the lightest supersymmetric particle (LSP) would be unable to decay and should therefore be stable. The LSP plays an important role in particle phenomenology as a candidate for particle dark matter. Dark matter is hypothesized to be an undiscovered form of matter that does not interact electromagnetically. The existence of dark matter is suggested by a variety of astronomical observations such as those of galaxy rotation curves [104], gravitational lensing of galaxy clusters [49], and the cosmic microwave

background [56]. One prevalent model for what composes the dark matter are particles that interact gravitationally and possibly through other forces but with very weak interaction strengths and are termed weakly interacting massive particles (WIMPs). If the LSP is electrically neutral it can play the role of a WIMP and thus could explain the source of dark matter.

One of the motivations for introducing supersymmetry as an extension of the Standard Model is to address the so called "hierarchy problem." The Higgs boson mass should include quantum corrections from fermions f with Yukawa couplings λ_f of the form

$$\Delta m_H^2 = -\frac{|\lambda_f|^2}{8\pi^2}\Lambda_{UV}^2 + \dots \tag{2.2.4}$$

that result in the physical mass of around 125 GeV that is observed. The Λ_{UV} term represents the energy scale at which new physics enters, and if this is taken to be the Planck scale (around 2.4×10^{18} GeV) then one might question why these corrections to the mass are many orders of magnitude larger than the mass itself. Similar correction terms would be present for any potentially undiscovered heavy particle that couples to the Higgs field. In the case of a heavy complex scalar particle denoted as S, the correction terms would be

$$\Delta m_H^2 = \frac{\lambda_S}{16\pi^2}\Lambda_{UV}^2 + \dots \tag{2.2.5}$$

where λ_S is the coupling between the Higgs and scalar fields. The diagrams corresponding to these mass corrections are shown in Figure 2.2.

It can be seen that the equations 2.2.4 and 2.2.5 appear similar but are different by a relative minus sign. These mass correction terms would exactly cancel if for each fermion there are two complex scalars along with requiring $\lambda_S = |\lambda_f|^2$. This is exactly the situation in unbroken supersymmetry and thus addresses how the

Higgs mass can be protected against the large corrections through these cancellations. However unbroken supersymmetry would imply that the superpartners would be degenerate in mass with their partner particles. This follows from the fact that the supersymmetry generators Q and $Q^\dagger$ commute with the squared-mass operator $-P^2$ so that the particles in a supermultiplet should have the same mass. Clearly this cannot correspond to the universe in the present as then these superpartners would have been expected to be discovered already. Thus supersymmetry, if it exists, must be a broken symmetry. Although broken supersymmetry no longer features the exact cancellation of the correction terms to the Higgs mass, it can still address the hierarchy problem as long as the superpartner masses are not too much larger than the partner masses. Some estimates suggest they should not exceed the TeV scale [91]. Soft supersymmetry breaking [72] is introduced such that the Lagrangian can be separated in two terms: $\mathcal{L}_{SUSY}$ that contains the terms that respect supersymmetry and $\mathcal{L}_{soft}$ that violates it. $\mathcal{L}_{soft}$ contains mass terms for the supersymmetric particles that give rise to the mass splittings between them and their partners. In addition to these masses there are various mixing angles and CP-violating phases that can be included from $\mathcal{L}_{soft}$ that result in over 100 new parameters. However many of the new parameters can be constrained based on experimental observations since they would be associated with flavor-changing or CP-violating processes. It is possible to greatly reduce the number of free parameters that are introduced by including additional

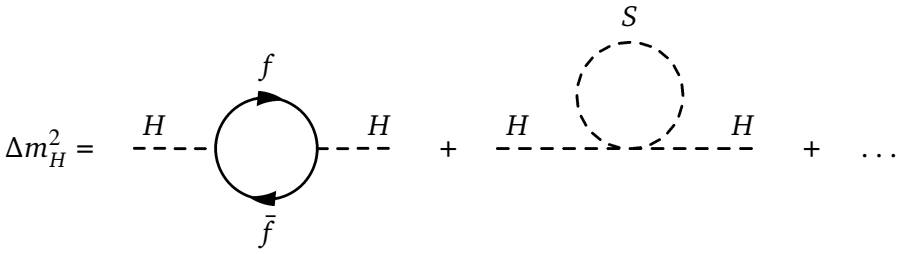

Figure 2.2: Diagrams for the leading corrections to the Higgs boson mass arising from the coupling to fermions f and scalars S.

assumptions as is the case in the phenomenological MSSM (pMSSM) [62].

Another consequence of extending the Standard Model to include supersymmetry is that it can help lead to the unification of the gauge couplings [61]. The gauge couplings g are running values that have a dependence on the energy scale of the interaction μ due to higher order quantum effects which are described by renormalization group equations. The running of the gauge couplings is shown in Figure 2.3. It can be seen that in the Standard Model the three couplings fail to unify when extrapolated to high energies. On the other hand in the MSSM they appear to unify at an energy scale around 10^{16} GeV. In the context of a Grand Unified Theory (GUT), this energy scale would be associated with the unification of the electroweak and strong interactions as part of a larger symmetry group. The unification of the gauge couplings thus motivates incorporating supersymmetry within a GUT. This along with the previous discussions regarding the hierarchy problem and dark matter make supersymmetry an appealing framework for extending physics beyond the Standard Model.

Just as in the Standard Model, electroweak symmetry breaking plays an important role in determining the particle spectrum of the MSSM. The neutral components of the two Higgs doublets H_u^0 and H_d^0 would each acquire non-zero vacuum expectation values v_u and v_d. These VEVs are related to the the VEV of the Higgs in the Standard Model by

$$v = \sqrt{v_u^2 + v_d^2} \tag{2.2.6}$$

and their ratio is written as the parameter

$$\tan\beta = \frac{v_u}{v_d}\,. \tag{2.2.7}$$

There would be five Higgs scalar particles after electroweak symmetry breaking,

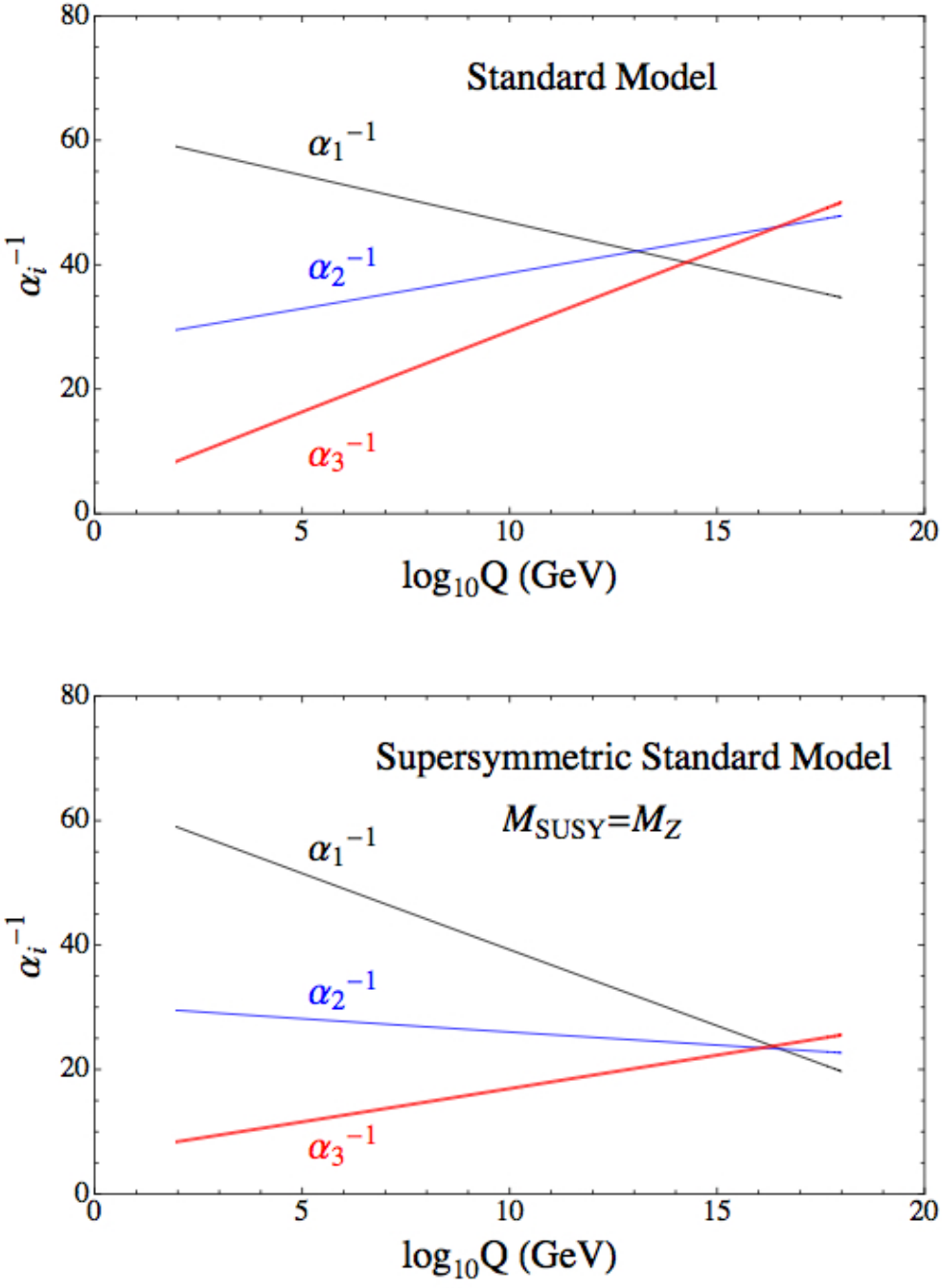

Figure 2.3: The running of the gauge couplings within the Standard Model and the MSSM. [86]

corresponding to the fact that there are eight initial degrees of freedom associated with the two complex Higgs doublets, but three degrees of freedom are "eaten" to make the W and Z bosons massive. The remaining five Higgs particles would consist of the CP-even neutral h^0 and H^0, the CP-odd neutral A^0, and the $H^\pm$ with charge ± 1. Following electroweak symmetry breaking, the higgsinos and electroweak gauginos mix to form the physical mass eigenstates known as the electroweakinos. They consist of four neutralinos $\tilde{\chi}^0_{1,2,3,4}$, which as the name suggests are electrically neutral, and two charginos $\tilde{\chi}^\pm_{1,2}$ with charge ± 1. The electroweakinos may also be alternatively denoted as $\tilde{N}_{1,2,3,4}$ for the neutralinos and $\tilde{C}^\pm_{1,2}$ for the charginos. The mass for the neutralinos is determined by the neutralino mass matrix

$$\mathbf{M}_{\tilde{\chi}^0} = \begin{pmatrix} M_1 & 0 & -\frac{g' v_d}{\sqrt{2}} & \frac{g' v_u}{\sqrt{2}} \\ 0 & M_2 & \frac{g v_d}{\sqrt{2}} & -\frac{g v_u}{\sqrt{2}} \\ -\frac{g' v_d}{\sqrt{2}} & \frac{g v_d}{\sqrt{2}} & 0 & -\mu \\ \frac{g' v_u}{\sqrt{2}} & -\frac{g v_u}{\sqrt{2}} & -\mu & 0 \end{pmatrix} \tag{2.2.8}$$

where M_1 and M_2 are the bino and wino mass terms from $\mathcal{L}_{soft}$ and μ is the Higgsino mass parameter. The mass matrix can be diagonalized by a matrix N referred to as the neutralino mixing matrix that defines how the gauge eigenstates mix. There is a corresponding mass matrix for the charginos as well, defined as

$$\mathbf{M}_{\tilde{\chi}^\pm} = \begin{pmatrix} 0 & X^T \\ X & 0 \end{pmatrix}, \tag{2.2.9}$$

$$X = \begin{pmatrix} M_2 & g v_u \\ g v_d & \mu \end{pmatrix}. \tag{2.2.10}$$

This mass matrix can be similarly diagonalized by the two matrices U and V defined

as

$$\begin{pmatrix} \tilde{\chi}_1^+ \\ \tilde{\chi}_2^+ \end{pmatrix} = V \begin{pmatrix} \tilde{W}^+ \\ \tilde{H}_u^+ \end{pmatrix}, \tag{2.2.11}$$

$$\begin{pmatrix} \tilde{\chi}_1^- \\ \tilde{\chi}_2^- \end{pmatrix} = U \begin{pmatrix} \tilde{W}^- \\ \tilde{H}_d^- \end{pmatrix}, \tag{2.2.12}$$

$$U^* X V^{-1} = \begin{pmatrix} m_{\tilde{\chi}_1} & 0 \\ 0 & m_{\tilde{\chi}_2} \end{pmatrix}. \tag{2.2.13}$$

The third generation squarks and sleptons can also have substantial mixing due to their large Yukawa couplings that lead to the mass eigenstates being a mixture of the left-handed and right-handed superpartners. In comparison, the first and second generation sfermions have small Yukawa couplings, so their mixing is expected to be negligible.

2.3. Signal Model

The search presented in this dissertation was done based on a simplified model of supersymmetry [5, 7, 8] that focuses on the electroweakinos $\tilde{\chi}_1^0$, $\tilde{\chi}_1^\pm$, and $\tilde{\chi}_2^0$ with masses around the weak scale. The model assumes R-parity is conserved such that the lightest neutralino $\tilde{\chi}_1^0$ is stable and can serve as a candidate for the dark matter. The mass of the $\tilde{\chi}_1^0$ in this model is assumed to be close to the masses of the lightest chargino $\tilde{\chi}_1^\pm$ and the second lightest neutralino $\tilde{\chi}_2^0$. Thus the model is described as having a "compressed" mass spectrum. The mixing and masses of the electroweakinos depend on the parameters M_1, M_2, and μ. The model considered in this search assumes $|M_1| < |M_2| \ll |\mu|$ such that the the higgsino mass parameter is effectively decoupled. This results in the electroweakinos being wino/bino-like and

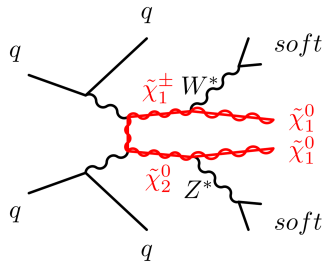

Figure 2.4: Diagram showing the pair production of $\tilde{\chi}_2^0\tilde{\chi}_1^{\pm}$. The $\tilde{\chi}_1^{\pm}$ and $\tilde{\chi}_2^0$ subsequently decay via off-shell W^* and Z^* bosons to a $\tilde{\chi}_1^0$.

such scenarios have been used to explain the observed dark matter relic density via coannihilation processes during the early universe [64, 76].

In particular, the simplified signal model considered in this search assumes a pure bino $\tilde{\chi}_1^0$ and pure wino $\tilde{\chi}_1^{\pm}$ and $\tilde{\chi}_2^0$. The $\tilde{\chi}_1^{\pm}$ and $\tilde{\chi}_2^0$ are assumed to be degenerate in mass and each respectively decays via off-shell W^* and Z^* bosons to a $\tilde{\chi}_1^0$ with a 100% branching fraction. The product of the signed neutralino mass eigenvalues $m(\tilde{\chi}_2^0) \times m(\tilde{\chi}_1^0)$ is chosen to be positive. An example of a signal process is shown in Figure 2.4 for the pair production of $\tilde{\chi}_2^0\tilde{\chi}_1^{\pm}$ along with their subsequent decays. The masses of the other SUSY particles are assumed to be much larger than $m(\tilde{\chi}_2^0)$ so as to effectively suppress the processes associated with them. Therefore the simplified model consists of just two free parameters: the mass of the $\tilde{\chi}_1^0$ and the mass of $\tilde{\chi}_1^{\pm}/\tilde{\chi}_2^0$.

Chapter 3

The Experiment

3.1. The Large Hadron Collider

The Large Hadron Collider (LHC) is a particle accelerator built by the European Organization for Nuclear Research (CERN) near Geneva, Switzerland. The LHC lies in a circular tunnel with a circumference of 27 km located underground at depths of up to 175 m. Situated around the accelerator ring are four interaction points that host the detectors for the four main LHC experiments: ALICE [2], ATLAS [13], CMS [50], and LHCb [88]. ATLAS and CMS are general purpose detectors while the other detectors are more specialized, with ALICE focusing on studying heavy ion collisions and LHCb's focus being on physics related to the b quark.

The LHC is part of a broader accelerator complex at CERN as shown in Figure 3.1. The protons enter the LHC with an energy of 450 GeV after having been accelerated by a chain of particle accelerators that progressively ramp up their energy. Two parallel beamlines circulate the beams of protons around the ring in opposite directions. The protons are accelerated to 6.5 TeV corresponding to a center-of-mass energy of $\sqrt{s} = 13$ TeV for pp collisions. Superconducting magnets are used to steer and focus the proton beams. The magnets are made from niobium–titanium alloy and

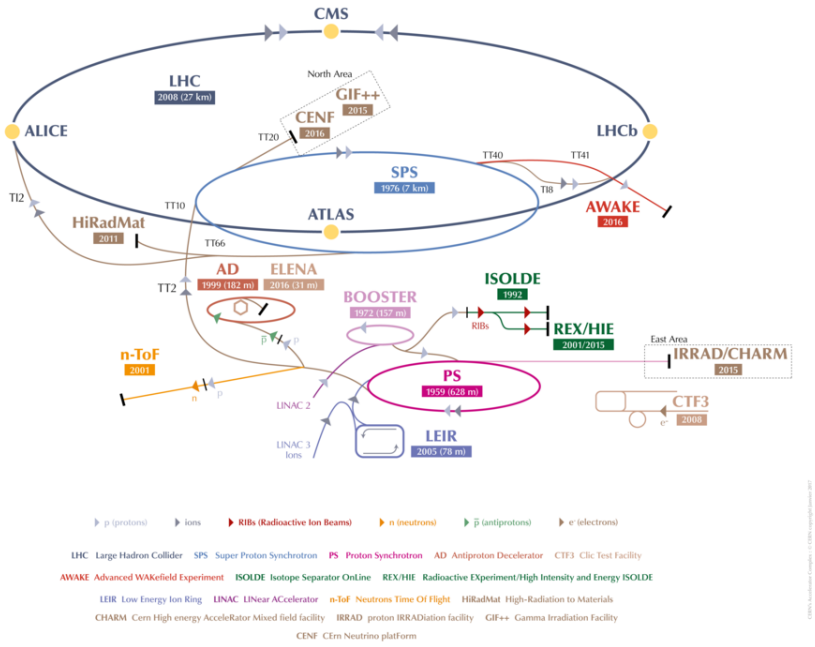

Figure 3.1: The various accelerators making up the CERN accelerator complex are shown along with the experiments. [92]

need to be cooled with liquid helium to 1.9 K in order for them to operate in the superconducting state. The proton beams are comprised of bunches that contain over 10^{11} protons, and the bunches of the two beams interact in 25 ns intervals that corresponds to a collision rate of 40 MHz [66].

The total number of pp collisions that occur over a period of time t is reflected by the integrated luminosity $\mathcal{L}$

$$\mathcal{L} = \int L(t)\, dt \tag{3.1.1}$$

where $L(t)$ is the instantaneous luminosity that depends on the beam parameters. The expected number of an events for a specific process can be obtained by multiplying the integrated luminosity $\mathcal{L}$ by the corresponding cross-section σ. However this

number does not take into account factors such as the detector acceptance and event selection that may significantly reduce the number of events that can be expected in a realistic search.

3.2. The ATLAS Detector

The ATLAS (A Toroidal LHC ApparatuS) detector [13] is a general purpose detector located at Interaction Point (IP1) of the LHC. The detector is composed of sub-detector systems: the Inner Detector, the Electromagnetic Calorimeter, the Hadronic Calorimeter, and the Muon Spectrometer. These systems are arranged concentrically around the beam axis in layers. Two superconducting magnet systems are used for bending the trajectories of charged particles such that their charge and momenta can be measured. For the Inner Detector a solenoid magnet provides a magnetic field of 2 T while for the Muon Spectrometer the magnetic field is provided by toroid magnets. Figure 3.2 shows a graphical overview of the components of the ATLAS detector.

ATLAS uses a right-handed coordinate system in which the x-axis points towards the center of the LHC ring, the y-axis points vertically upwards, and the z-axis points along the beam axis. The azimuthal angle ϕ is defined as the angle from the x-axis in the x-y plane. The polar angle θ from the z-axis is used to define the pseudorapidity η

$$\eta = -\ln\left(\tan\frac{\theta}{2}\right) . \tag{3.2.1}$$

3.2.1. Inner Detector

The Inner Detector is used for tracking of charged particles in order to identify and measure the momenta of the particles. This is done based on the bending of the

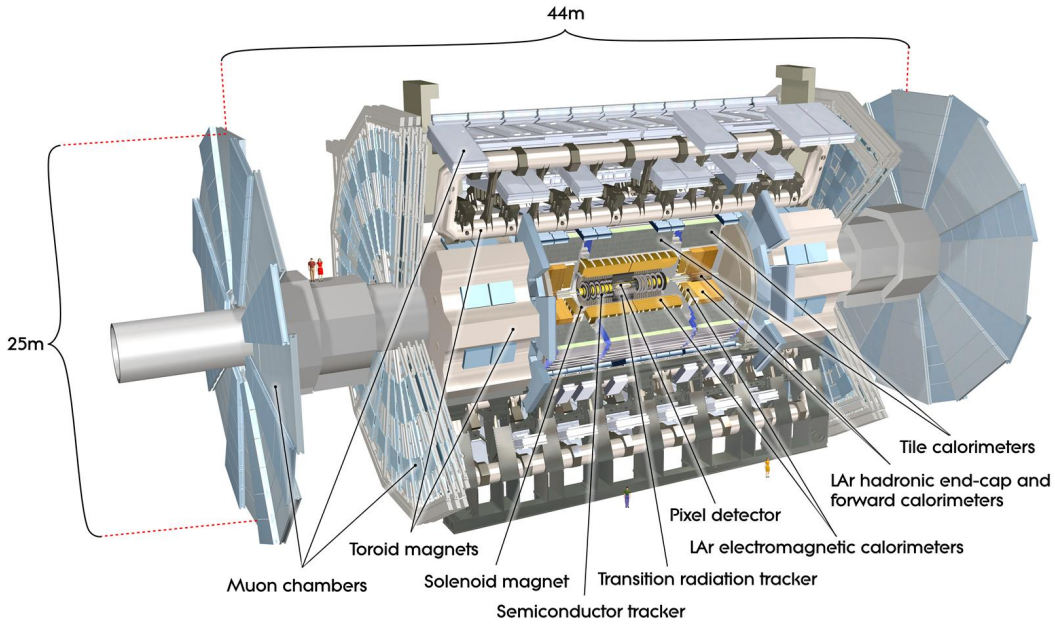

Figure 3.2: General overview of the ATLAS detector and its sub-systems. [99]

trajectories of the charged particles in the presence of the 2 T magnetic field produced by the solenoid magnet. The Inner Detector is composed of three parts: the Pixel Detector, the Semiconductor Tracker (SCT), and the Transition Radiation Tracker (TRT). The layout of the Inner Detector is shown in Figure 3.3, and a cross-sectional view of the barrel region is shown in Figure 3.4.

The Pixel Detector [53] is the innermost part and consists of silicon pixel sensors that are arranged in four concentric layers in the barrel region and three disk-shaped layers in the end-cap regions. These sensors operate on the basis of recording electric currents that are produced when charged particles pass through the silicon. These currents are converted into digital signals as "hits" that indicate points where the charged particle passed through the detector. These hits can then be input into track reconstruction algorithms that are used to determine the particle's trajectory. The innermost layer at approximately 3.3 cm from the beam axis is the Insertable B-Layer

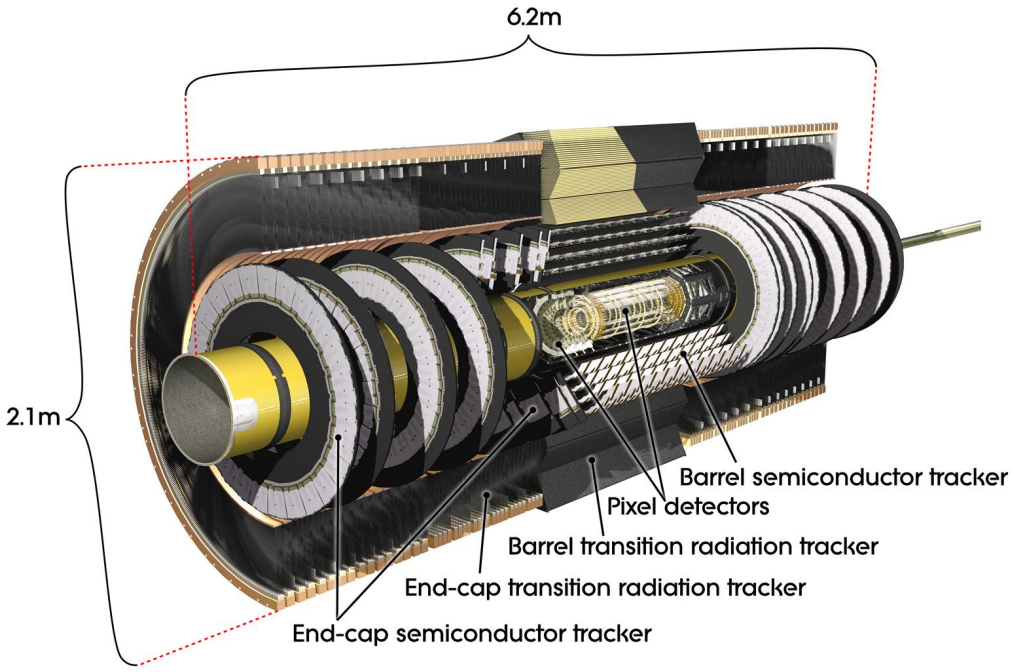

Figure 3.3: Layout of the Inner Detector. [97]

(IBL) [14] which is made up of pixels 50 µm × 250 µm in size in the the transverse and longitudinal directions. Pixels in the other layers are larger with dimensions of 50 µm × 400 µm. The resolution of the pixel sensors in the $r - \phi$ direction is 10 µm. In the z direction the resolution is 60 µm and 115 µm for the IBL and other layers respectively. In total the Pixel Detector has more than 92 million readout channels and covers $|\eta| < 2.5$.

The Semiconductor Tracker [35] is a silicon strip detector located in the middle of the Inner Detector that also has a coverage of $|\eta| < 2.5$. There are four layers of silicon strip sensors in the barrel region and nine disk-shaped layers in the end-cap regions. The detector modules consist of two sensors on each side that form 12 cm long strips with the silicon strips having a pitch of 80 µm. The modules have a second layer of sensors that is at a stereo angle of 40 mrad with the first layer such that a two-dimensional measurement can be made. The resolution of the SCT is 17

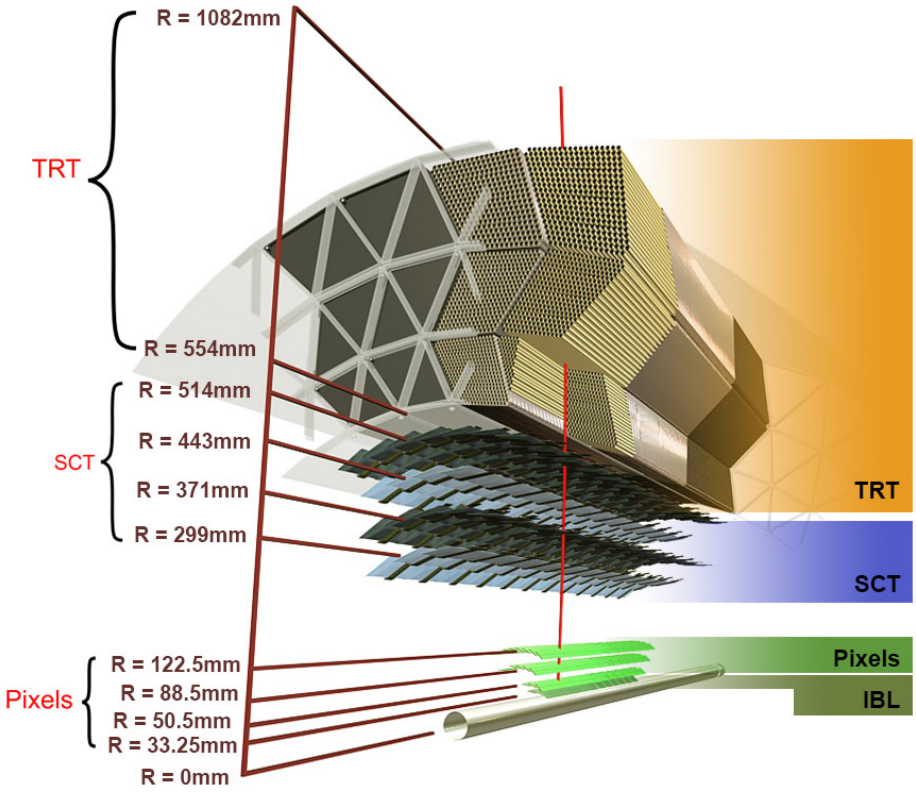

Figure 3.4: Cross-sectional view of the barrel region of the Inner Detector. [54]

μm in the $r - \phi$ direction and 580 μm in the z direction. The SCT consists of more than 6 million readout channels in total.

The Transition Radiation Tracker [15] is the outermost part of the Inner Detector with a coverage of $|\eta| < 2$. It consists of approximately 300,000 drift tubes that are 4 mm in diameter. The drift tubes are filled with a Xe-CO_2-O_2 gas mixture and contain an anode wire in the center. The straws are held at a potential around -1.5 kV such that an electric signal is generated in the wire when a charged particle passes through the tube and ionizes the gas. The spatial resolution of the drift tubes in the $r - \phi$ direction is approximately 130 μm. Between the straw tubes there are polypropylene fibers or polyethylene foils that are used as radiator materials. Light charged particles that pass through the TRT will produce transition radiation due to the differing dielectric constants of these materials. The energy loss through transition radiation of a particle of mass m and energy E in the relativistic limit is proportional to the Lorentz factor $\gamma = \frac{E}{m}$ [63]. Thus for a fixed energy E particles that are lighter will produce more transition radiation. This fact can be utilized to distinguish between particles of different masses such as between electrons and charged pions. The transition radiation produced by charged particles in the TRT are X-rays in the keV range and lead to large signals in the drift tubes. Thus the TRT has two readout thresholds: a low threshold at approximately 300 eV used for tracking and a high threshold at approximately 6 keV for detecting transition radiation.

3.2.2. Electromagnetic Calorimeter

The Electromagnetic (EM) Calorimeter is used to measure the energy of particles that interact through the electromagnetic forces. It consists of components of the Liquid Argon (LAr) Calorimeter [10] including the electromagnetic barrel covering

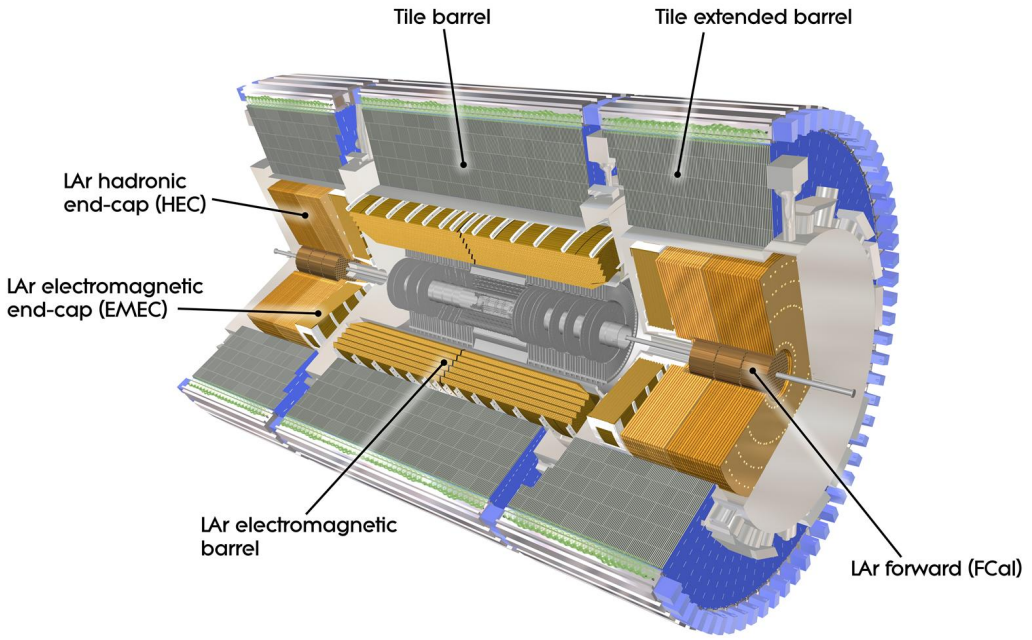

Figure 3.5: The components of the ATLAS calorimeter system. [96]

$|\eta| < 1.475$ and the two electromagnetic end-caps covering $1.375 < |\eta| < 3.2$. These sub-detector components consist of three layers with varying sizes of the calorimetric cells. The first layer is finely segmented with cell sizes of approximately $\Delta\eta \times \Delta\phi = \frac{0.025}{8} \times 0.1$ and is used for distinguishing prompt photons from photons coming from the decay $\pi^0 \rightarrow \gamma\gamma$. The second layer has cell sizes of approximately $\Delta\eta \times \Delta\phi = 0.025 \times 0.025$ and is where most of the energy from electromagnetic showers is deposited as it is also the thickest layer at 16 radiation lengths (X_0). The third layer has cell sizes of approximately $\Delta\eta \times \Delta\phi = 0.05 \times 0.025$ and measures the electromagnetic showers that were not contained within the previous layers. An additional pre-sampling layer is included for $|\eta| < 1.8$ that corrects for energy losses due to the upstream portion of the detector. These layers consist of lead absorber plates and liquid argon that are sandwiched together into an accordion-like structure as seen in Figure 3.6. Particles produce electromagnetic showers when they interact

with the absorbing material and this in turn ionizes the liquid argon to produce a measurable current. The energy of the particle can then be determined based on detecting these currents and the calibration of the calorimeter response. The relative energy resolution of the EM Calorimeter depends on the energy E of the incident particle as

$$\frac{\sigma_E}{E} = \frac{10\%}{\sqrt{E}} \oplus \frac{0.3}{E} \oplus 0.4\% \tag{3.2.2}$$

where E is in units of GeV. The first term proportional to $\frac{1}{\sqrt{E}}$ is due to statistical fluctuations in the number of photoelectrons produced in the electromagnetic showers, the second term proportional to $\frac{1}{E}$ comes from electronic noise, and the last term comes from energy-independent factors such as the nonuniformities of the detector geometry. It can be seen that the energy resolution improves with increasing energy of the incident particle.

3.2.3. Hadronic Calorimeter

The Hadronic Calorimeter is used for measuring the energy of hadrons and consists of the Tile Calorimeter, the hadronic end-caps, and the Forward Calorimeter (FCal). The Tile Calorimeter [11] covers $|\eta| < 1.7$ and is composed of layers of steel absorber plates and plastic scintillating tiles. Particle showers that are produced when particles interact with the absorbers cause the scintillating tiles to emit photons. These photons are collected by wavelength-shifting fibers that then lead to photomultiplier tubes (PMTs) which produce the electronic signals that can be used for determining the incident particle's energy. The Tile Calorimeter is made up of three layers with the inner two layers having cell sizes of $\Delta\eta \times \Delta\phi = 0.1 \times 0.1$ while the outer layer has $\Delta\eta \times \Delta\phi = 0.2 \times 0.1$ cells. The layers consist of modules with a layout as that shown

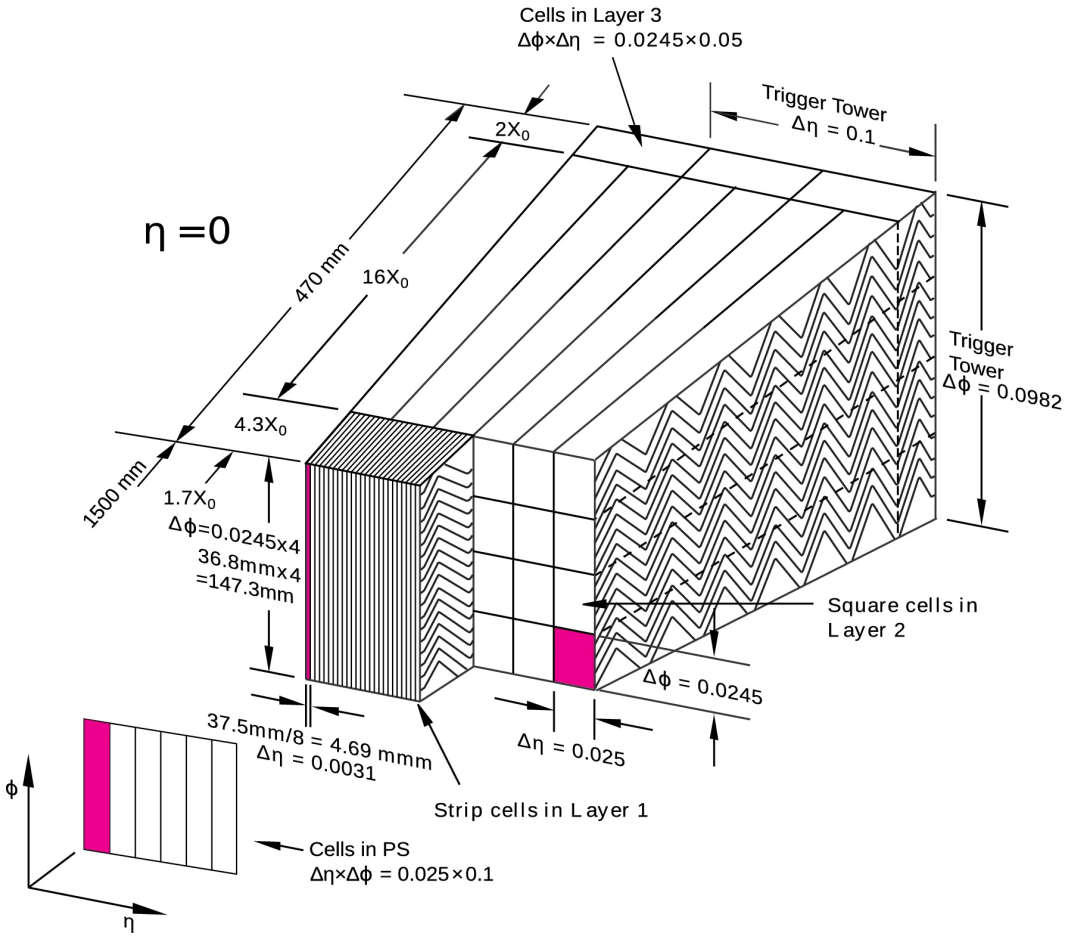

Figure 3.6: Barrel module of the LAr Calorimeter. [19]

in Figure 3.7. The design energy resolution of the Tile Calorimeter is $\frac{\sigma_E}{E} = \frac{50\%}{\sqrt{E}} \oplus 3\%$ with E in GeV.

The hadronic end-caps use a combination of copper as the absorber and liquid argon as the active material, and they cover the range of $1.5 < |\eta| < 3.2$. The Forward Calorimeter further extends the coverage in the forward regions with a range of $3.1 < |\eta| < 4.9$ and measures both electromagnetic and hadronic showers. It is composed of three layers with the first layer utilizing a copper absorber for measuring electromagnetic showers while the other two layers use a tungsten absorber for measuring the hadronic showers. Liquid argon is also the active material for the Forward Calorimeter. The design energy resolution of the Forward Calorimeter is $\frac{\sigma_E}{E} = \frac{100\%}{\sqrt{E}} \oplus 10\%$ with E in GeV.

3.2.4. Muon Spectrometer

The Muon Spectrometer [12] is used to identify and measure the momenta of muons which are able to pass through all the detector components. Measurements of the muons are performed based on the bending of their trajectories in the presence of the magnetic field created by the three superconducting toroid magnets. The magnetic field integral of the toroid magnets ranges between 2 T·m in the barrel and 6 T·m in the end-caps. There are four gaseous detectors that make up the Muon Spectrometer: Monitored Drift Tubes (MDTs), Cathode Strip Chambers (CSCs), Resistive Plate Chambers (RPCs), and Thin Gap Chambers (TGCs). The MDTs and CSCs are designed for tracking and cover $|\eta| < 2.7$ while the RPCs and TGCs are utilized for triggering and cover $|\eta| < 2.4$. RPCs and TGCs further provide measurements in the ϕ direction. The layout of the Muon Spectrometer is depicted in Figure 3.8.

The Monitored Drift Tubes comprise of three layers of drift tube detectors. The

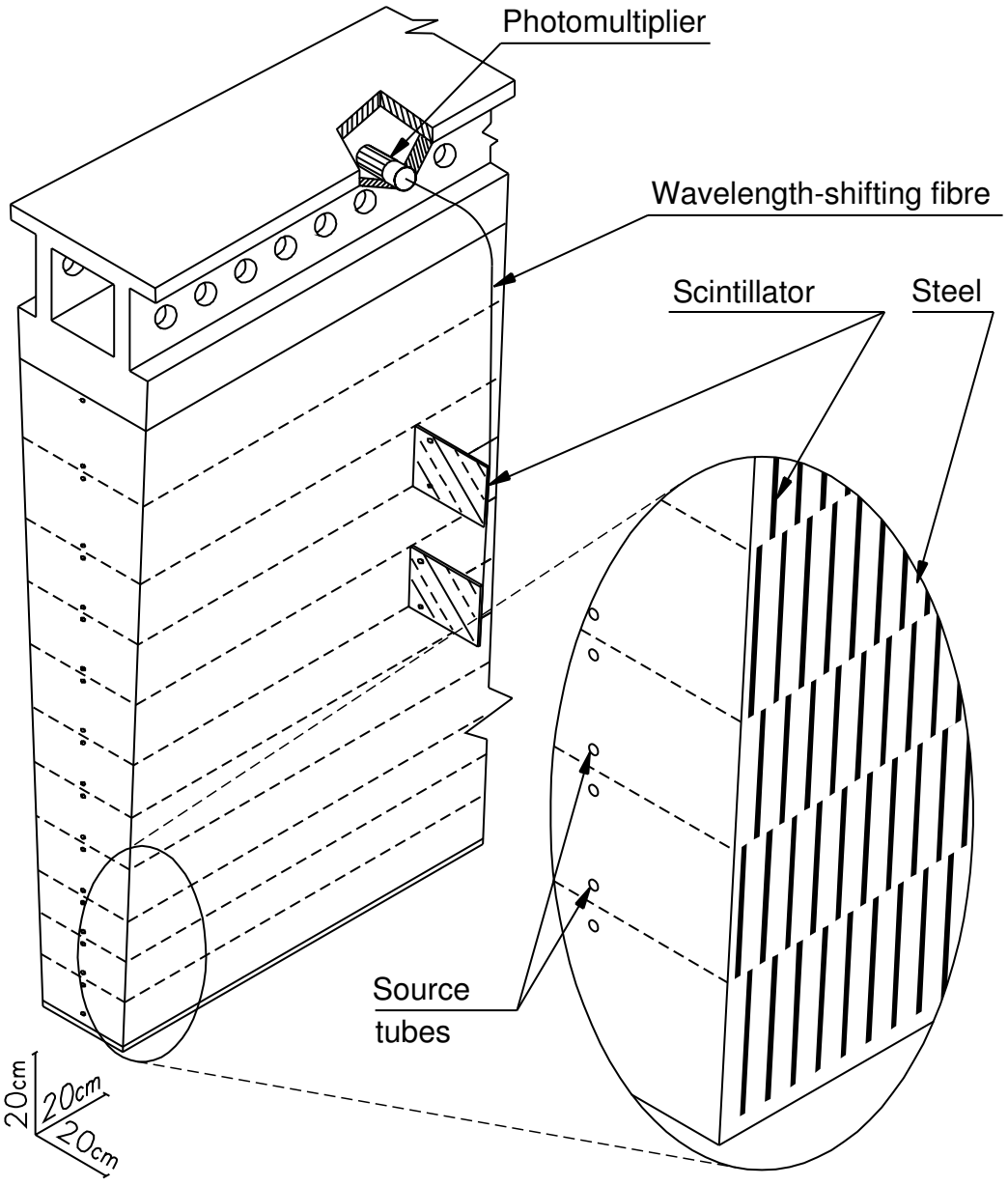

Figure 3.7: Layout of a Tile Calorimeter module. [13]

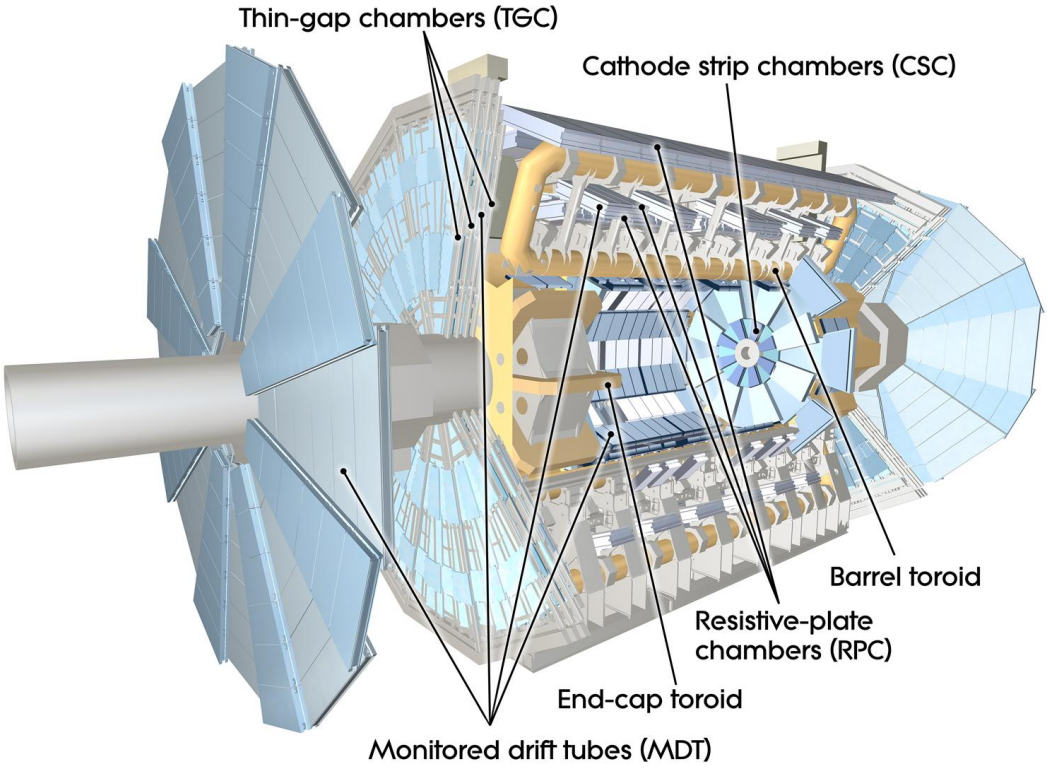

Figure 3.8: Layout of the Muon Spectrometer. [98]

drift tubes are made of aluminum with a diameter around 30 mm and have a central anode wire that is held at a potential of around 3 kV. They are filled with a gas mixture of argon and CO_2. When a muon traverses the drift tube, the gas becomes ionized and causes electrons to drift towards the anode wire. The drift time is used for determining the muon's trajectory with a single tube having a spatial resolution of approximately 80 μm. Collections of monitored drift tubes are contained within MDT chambers that make up the three layers. The MDTs have a coverage of $|\eta| < 2.7$ except for in the innermost layer of the end-cap at $2.0 < |\eta| < 2.7$ where tracking coverage is provided by the CSCs as they are more suitable for the higher particle rates there.

The Cathode Strip Chambers are multi-wire proportional chambers consisting of a series of cathode strips and anode wires. A gas mixture of argon and CO_2 is also used in this case. There are four layers of gas chambers making up the CSCs. The CSCs have a spatial resolution in the muon bending plane of approximately 60 μm and around 5 mm in the non-bending plane.

Resistive Plate Chambers provide triggering for the barrel region of $|\eta| < 1.05$ and consist of gaseous detectors made up of two parallel resistive plates separated by a 2 mm gap that is filled with gas. The gas is a mixture of tetrafluoroethane, isobutane, and sulfur hexafluoride. High voltage is applied across the resistive plates such that a strong electric field is produced within the gas gap. Metallic strips are placed on the outer surfaces of the resistive plates and are used for readout of the electrical signal when the gas is ionized by a muon. The RPCs are arranged in three concentric double layers and have a timing resolution of roughly 1 to 2 ns.

The Thin Gap Chambers extend the triggering capability to the end-cap regions of $1.0 < |\eta| < 2.4$. They are multi-wire proportional chambers containing a gas mixture of n-pentane and carbon dioxide. The chambers have thin gaps of 1.4 mm

between the anode wires and the cathode as compared to the 1.8 mm separation between each anode wire, hence their name. The TGCs are arranged as one triplet layer followed by two doublet layers in the middle end-cap and a single doublet layer in the inner end-cap. The timing resolution of the TGCs is approximately 4 ns.

3.2.5. Trigger System

Each raw data event recorded by the ATLAS detector is approximately 1.6 MB in size and since the proton-proton collisions occur at a rate of 40 MHz the total data rate would be larger than 60 TB/s. It is unfeasible to store the data to disk at this rate and by only saving the interesting events the data rate can be lowered to a manageable level. The ATLAS trigger system [24] is responsible for determining whether events should be saved to disk or discarded. It consists of two levels: a low-level hardware-based trigger and a high-level software-based trigger.

The first level is the hardware-based trigger called the Level 1 trigger (L1). The L1 trigger uses coarse detector information from the Calorimeters and Muon Spectrometer to make a decision to save or reject the event within 2.5 μs. This reduces the event rate from 40 MHz to below 100 kHz. The High Level Trigger (HLT) is the software-based trigger that follows the L1 trigger. It utilizes algorithms that make use of the full detector readout for particular Regions of Interest in order to decide which events to save within 200 ms. The HLT further reduces the event rate to 1 kHz.

Chapter 4

Data and Simulation

4.1. Data

This search makes use of the full Run 2 pp collision data at $\sqrt{s}$ = 13 TeV collected by the ATLAS detector during the years 2015 to 2018. This dataset corresponds to a total integrated luminosity of 140 fb^{-1} that has passed various data quality requirements such that it is deemed suitable for use in physics analysis. Figure 4.1 shows the evolution of the integrated luminosity as a function of the time. The distribution of the mean number of interactions per bunch-crossing for each of the data-taking years is shown in Figure 4.2 as well as the mean value over all the data-taking years which is found to be $\langle \mu \rangle = 33.7$.

The data-taking runs that have passed these data quality requirements are compiled into Good Runs Lists (GRLs). The GRLs used in this search include:

- data15_13TeV.periodAllYear_DetStatus-v89-pro21-02_Unknown_PHYS _StandardGRL_All_Good_25ns.xml
- data16_13TeV.periodAllYear_DetStatus-v89-pro21-01_DQDefects -00-02-04_PHYS_StandardGRL_All_Good_25ns.xml

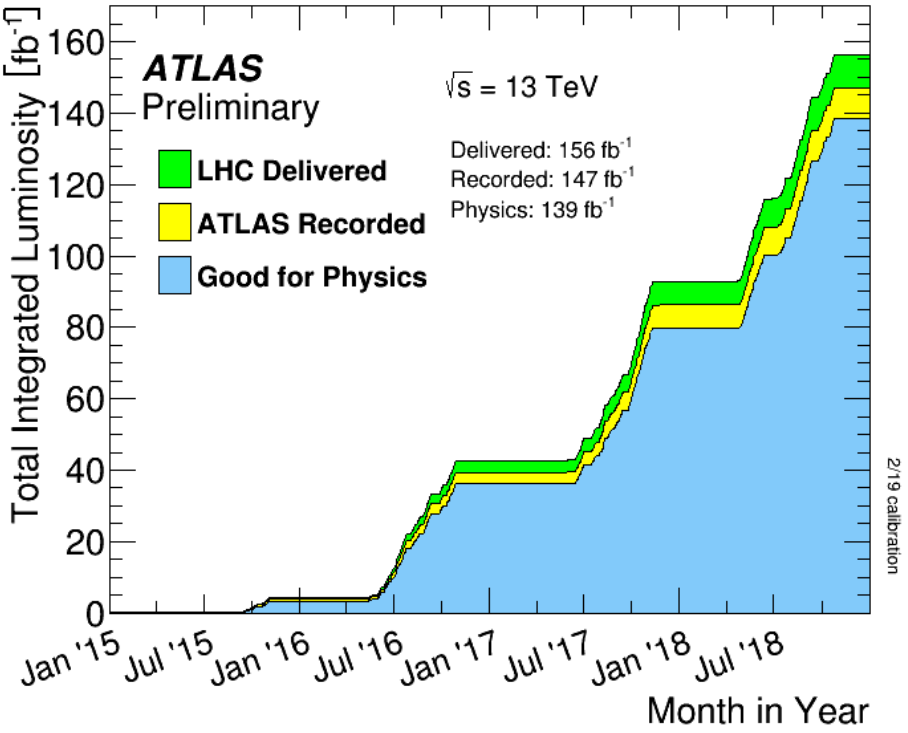

Figure 4.1: The cumulative luminosity as a function of time that was delivered to ATLAS (green), recorded by ATLAS (yellow), and passed data quality checks (blue) from 2015 to 2018. [39]

- data17_13TeV.periodAllYear_DetStatus-v99-pro22-01_Unknown_PHYS _StandardGRL_All_Good_25ns_Triggerno17e33prim.xml

- data18_13TeV.periodAllYear_DetStatus-v102-pro22-04_Unknown_PHYS _StandardGRL_All_Good_25ns_Triggerno17e33prim.xml

The triggers used in this search include $E_{\mathrm{T}}^{\mathrm{miss}}$ triggers and single-lepton triggers. The $E_{\mathrm{T}}^{\mathrm{miss}}$ trigger is used in order to target events compatible with the production of the SUSY signal, as these events are characterized by the presence of large $E_{\mathrm{T}}^{\mathrm{miss}}$ due to the LSP neutralinos escaping the detector. The $E_{\mathrm{T}}^{\mathrm{miss}}$ triggers are chosen with the lowest $E_{\mathrm{T}}^{\mathrm{miss}}$ thresholds as well as to be unprescaled and inclusive. For $E_{\mathrm{T}}^{\mathrm{miss}} > 200$ GeV, the $E_{\mathrm{T}}^{\mathrm{miss}}$ triggers are found to be fully efficient such that the associated trigger

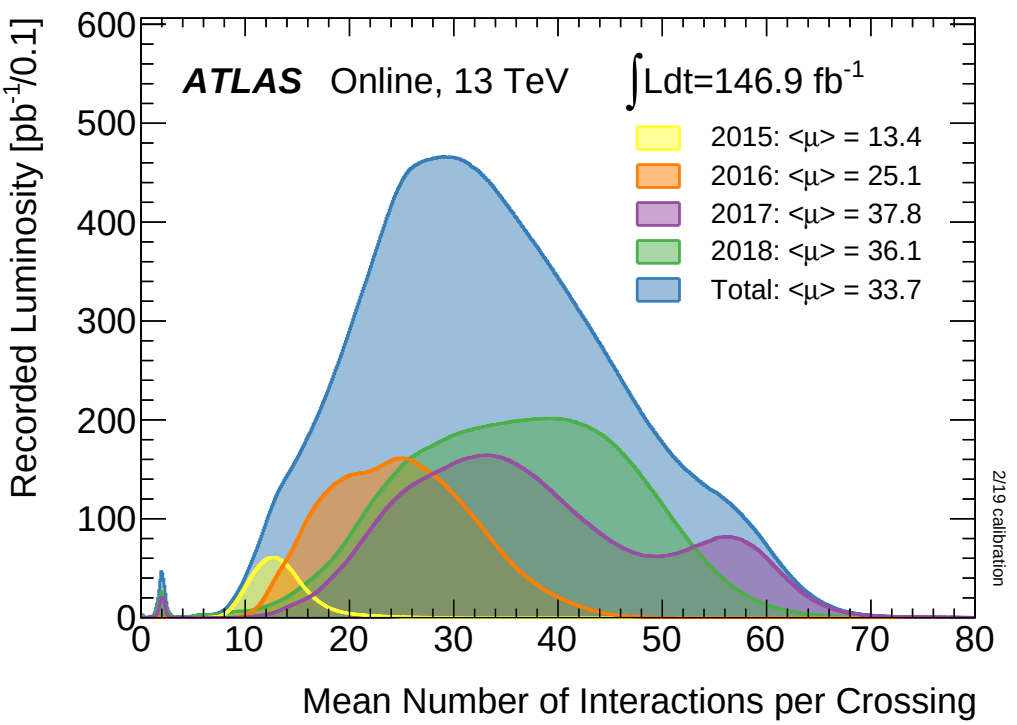

Figure 4.2: The distribution of the mean number of interactions per bunch-crossing during the data-taking years from 2015 to 2018. [39]

scale factors should be compatible with unity as seen in Figure 4.3. Furthermore a requirement of $E_{\mathrm{T}}^{\mathrm{miss}} > 250$ GeV used in the event selection for the analysis regions is well within the trigger efficiency plateau and thus there was no need to apply $E_{\mathrm{T}}^{\mathrm{miss}}$ trigger scale factors to the simulated samples in order to match the data.

Single-lepton triggers are used for selecting events in the analysis regions designed to estimate the dominant backgrounds in the search. These triggers are also chosen with the lowest thresholds and to be unprescaled. A summary of the triggers used is shown in Tables 4.1 and 4.2 for the $E_{\mathrm{T}}^{\mathrm{miss}}$ and single-lepton triggers respectively.

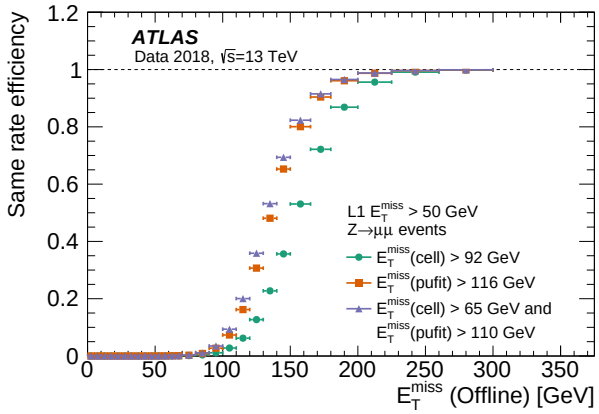

Figure 4.3: $E_{\mathrm{T}}^{\mathrm{miss}}$ trigger efficiency in Run 2 [29]. The efficiency changes with the period, but above 200 GeV, the efficiency is kept above 95% at a stable level.

Period		Chain
2015		HLT_xe70_mht
2016	A - D3	HLT_xe90_mht_L1XE50
	D4 - F1	HLT_xe100_mht_L1XE50
	F2 -	HLT_xe110_mht_L1XE50
2017		HLT_xe110_pufit_L1XE55
2018	B - C5	HLT_xe110_pufit_xe70_L1XE50
	C6 -	HLT_xe110_pufit_xe65_L1XE50

Table 4.1.: Summary of $E_{\mathrm{T}}^{\mathrm{miss}}$ trigger chains.

Period	Muon Triggers	Electron Triggers
2015	HLT_mu20_iloose_L1MU15 HLT_mu50	HLT_e24_lhmedium_L1EM20VH HLT_e60_lhmedium HLT_e120_lhloose
2016–2018	HLT_mu26_ivarmedium HLT_mu50	HLT_e24_lhtight_nod0_ivarloose HLT_e60_lhmedium_nod0 HLT_e140_lhloose_nod0

Table 4.2.: Summary of single-lepton trigger chains.

4.2. Signal Simulation

The simulation of the signal model described in Section 2.3 begins with event generation using MG5_aMC@NLO (MadGraph v2.7.3.atlas6) [6]. The MSSM_SLHA2 [4] model is used for incorporating the SUSY sector in the event generation. Events are generated for $\tilde{\chi}_2^0\tilde{\chi}_1^+$, $\tilde{\chi}_2^0\tilde{\chi}_1^-$, $\tilde{\chi}_1^+\tilde{\chi}_1^-$, $\tilde{\chi}_1^-\tilde{\chi}_1^-$, $\tilde{\chi}_1^+\tilde{\chi}_1^+$, and $\tilde{\chi}_2^0\tilde{\chi}_2^0$ pair production along with two jets using the following process strings:

```
generate p p > n2 x1+ j j QED=99 QCD=99 @1
add process p p > n2 x1- j j QED=99 QCD=99 @2
add process p p > x1+ x1- j j QED=99 QCD=99 @3
add process p p > x1- x1- j j QED=99 QCD=99 @4
add process p p > x1+ x1+ j j QED=99 QCD=99 @5
add process p p > n2 n2 j j QED=99 QCD=99 @6
```

Specifying "QED=99 QCD=99" in the process strings allows for diagrams at all orders in the QED and QCD couplings such that interference effects between diagrams will be fully captured. Examples of the possible diagrams for the signal processes are shown in Figure 4.4.

While $\tilde{\chi}_2^0\tilde{\chi}_1^\pm$ and $\tilde{\chi}_1^\pm\tilde{\chi}_1^\mp$ production includes all the possible diagrams shown in Figure 4.4, only the VBF diagrams with QED=4 contribute to the production for $\tilde{\chi}_2^0\tilde{\chi}_2^0$, $\tilde{\chi}_1^+\tilde{\chi}_1^+$, and $\tilde{\chi}_1^-\tilde{\chi}_1^-$. In the simplified model of the SUSY signal that this search is targeting, the electroweakinos are assumed to be purely wino or bino. This poses an issue when the MSSM_SLHA2 model is used, as it has been found that the branching ratio of $\tilde{\chi}_2^0$ to leptons becomes much larger than that of the W/Z bosons for masses near the $\tilde{\chi}_2^0$-$\tilde{\chi}_1^0$ mass splitting. Since one of the main strategies employed in this

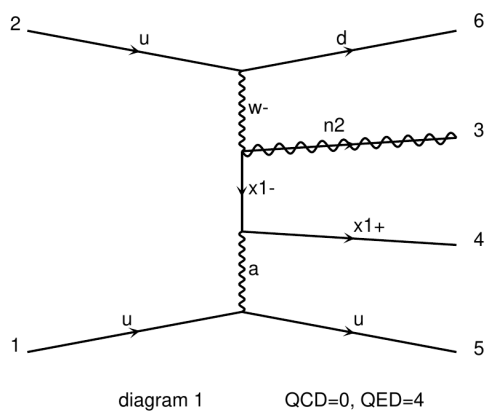

(a) QED=4, VBF

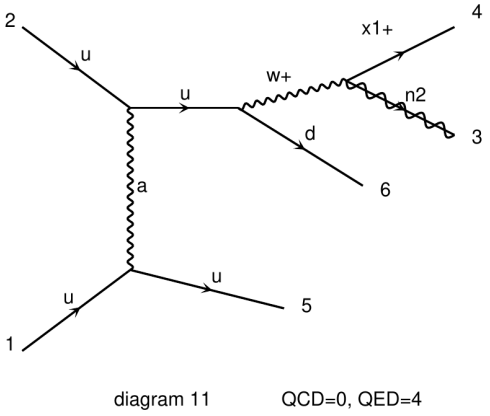

(b) QED=4, DY

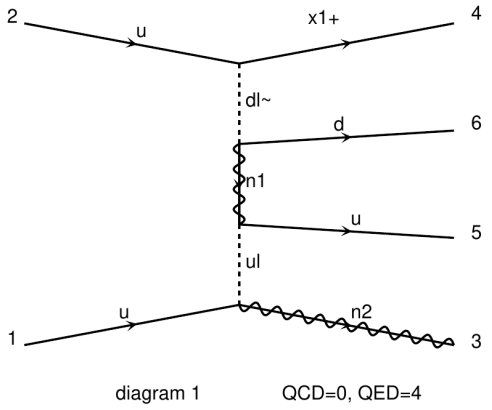

(c) QED=4, VBF with strong SUSY

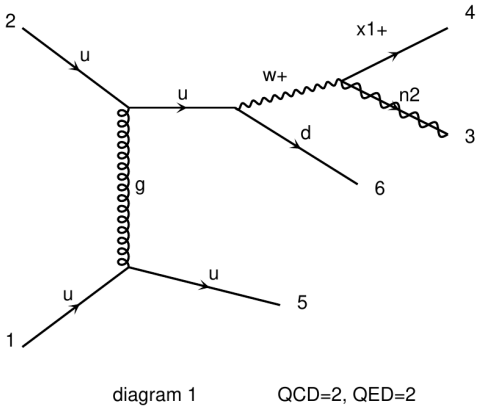

(d) QED=2, QCD=2

Figure 4.4: Example of the possible diagrams contributing to the signal processes. Diagrams (a) and (c) illustrate VBF-like diagrams, while diagrams (b) and (d) show Drell-Yan diagrams where the SUSY particles are produced through an *s*-channel process. Diagram (c) shows a diagram that includes (virtual) strong SUSY particles.

search includes a lepton veto, the larger branching ratio to leptons will negatively impact the signal acceptance. To resolve this issue, slightly off-diagonal components are introduced to the electroweakino mixing matrices such that the $\tilde{\chi}_2^0$ and $\tilde{\chi}_1^\pm$ contain small higgsino and bino components while still being mostly wino-like. In doing so, SM-like branching ratios for the electroweakinos are preserved. Although the signal events are generated with this slightly off-diagonal mixing, the cross sections used to

normalize the samples are still computed separately for the pure wino/bino scenario and they are slightly larger than the cross sections for the signal processes produced with off-diagonal components. Due to the absence of a reliable next-to-leading order (NLO) cross-section calculator for VBF production, this analysis makes use of the leading order (LO) cross-sections that are directly reported by the event generation with MG5_aMC@NLO.

The generator level cuts include the following cuts on the jet transverse momentum and the pseudorapidity difference between the two leading jets:

- $p_{\mathrm{T}}(j) > 30$ GeV
- $\Delta\eta(jj) > 2.5$.

MadSpin [9] is used for modeling the decays of electroweakinos with a 100% branching ratio to the LSP $\tilde{\chi}_1^0$ and a pair of SM fermions. Following this the events are then interfaced with PYTHIA 8.244 [110] for modeling the parton shower and hadronization. The generator tune is configured as A14 [17] NNPDF2.3LO [94]. The signal events are processed with Atlfast-II [89] for fast simulation of the detector response. The simulated events are reconstructed using Release 21 of the Athena software framework. The samples were produced for the official mc16 production campaigns that match the data conditions, trigger menu, and pileup for the data-taking years from 2015 to 2018.

Signal samples were generated for different settings of mass and mass splittings for the SUSY particles as depicted in Figure 4.5. The lightest neutralino, second lightest neutralino, and lightest chargino are denoted as $\tilde{\chi}_1^0$, $\tilde{\chi}_2^0$, and $\tilde{\chi}_1^{\pm}$ respectively. This signal grid consists of five choices of mass splittings between the $\tilde{\chi}_2^0$ and $\tilde{\chi}_1^0$ (0.2 GeV, 0.5 GeV, 1 GeV, 2 GeV, 5 GeV), and a range of $\tilde{\chi}_2^0$ masses from 75 GeV to 175 GeV.

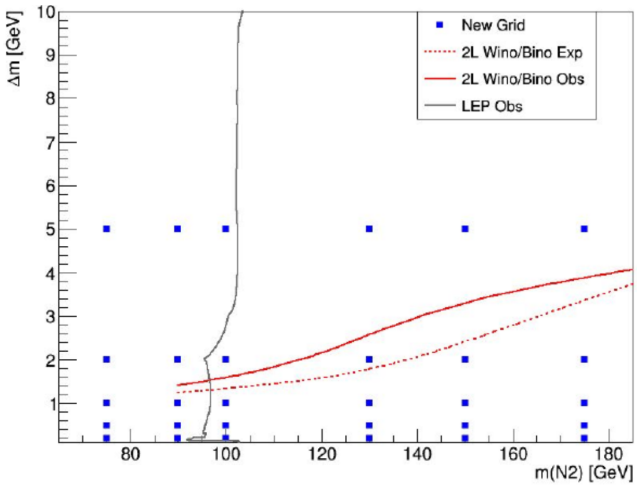

Figure 4.5: Signal grid used in the search as a function of the $\tilde{\chi}_2^0$ mass and the $\tilde{\chi}_2^0$-$\tilde{\chi}_1^0$ mass splitting. The gray and red lines indicate constraints from LEP experiment and the ATLAS soft 2L search, respectively.

Figures 4.6 and 4.7 show the cross-sections and uncertainties evaluated for each signal process. The total signal cross section including all production mode ranges from approximately 1.6 pb to 0.06 pb for $\tilde{\chi}_1^{\pm}/\tilde{\chi}_2^0$ masses between 75 GeV and 175 GeV. The signal cross-section uncertainties have been evaluated by considering the factorization and renormalization scale variations and PDF variations.

Truth-level distributions for relevant kinematic quantities are shown in Figures 4.8 and 4.9. The distributions are produced after applying similar criteria to that used in the analysis:

- $E_{\mathrm{T}}^{\mathrm{miss}} > 200$ GeV
- Two VBF-tagged jets satisfying $m_{\mathrm{jj}} > 500$ GeV
- $\mathrm{j}_1^{\mathrm{VBF}}$ $p_{\mathrm{T}} > 80$ GeV
- $\mathrm{j}_2^{\mathrm{VBF}}$ $p_{\mathrm{T}} > 40$ GeV .

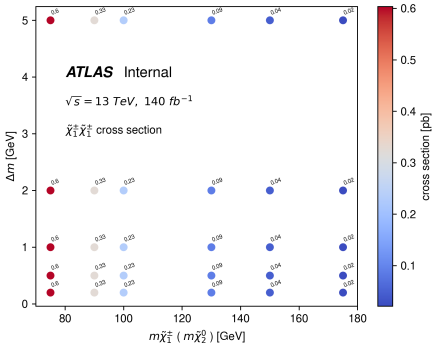

(a) $\tilde{\chi}_1^{\pm}\tilde{\chi}_1^{\mp}$ cross-section

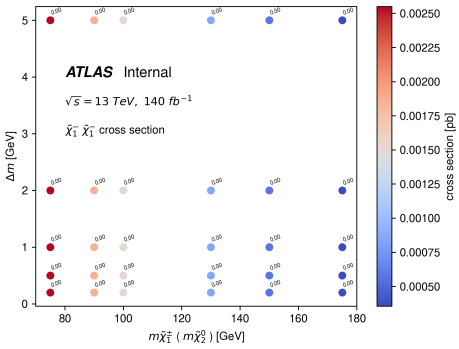

(b) $\tilde{\chi}_1^{-}\tilde{\chi}_1^{-}$ cross-section

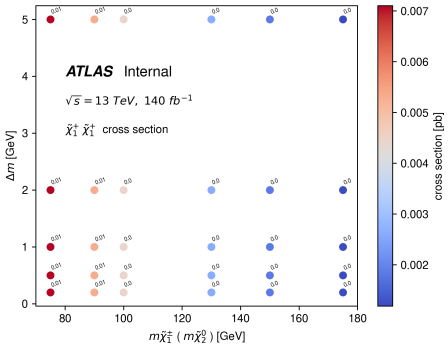

(c) $\tilde{\chi}_1^{+}\tilde{\chi}_1^{+}$ cross-section

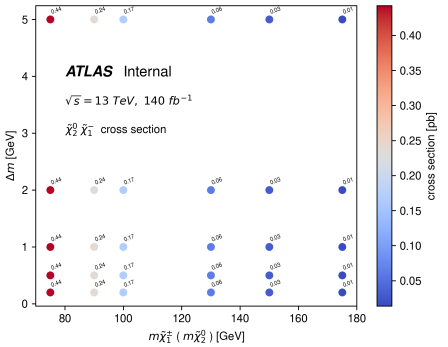

(d) $\tilde{\chi}_2^0\tilde{\chi}_1^{-}$ cross-section

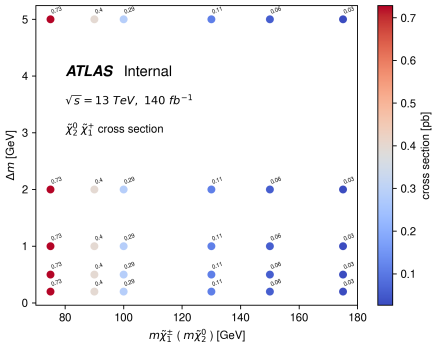

(e) $\tilde{\chi}_2^0\tilde{\chi}_1^{+}$ cross-section

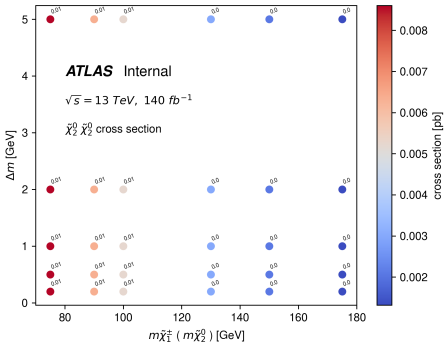

(f) $\tilde{\chi}_2^0\tilde{\chi}_2^0$ cross-section

Figure 4.6: Signal cross-section for each signal process.

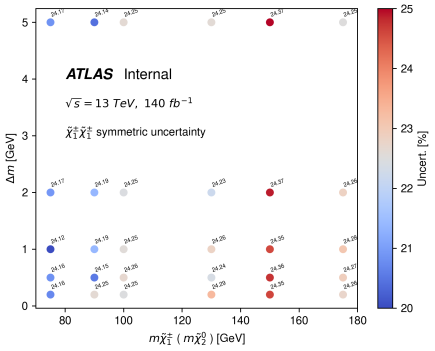

(a) $\tilde{\chi}_1^{\pm}\tilde{\chi}_1^{\mp}$ cross-section uncertainty

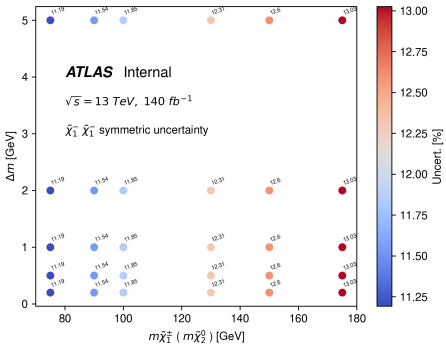

(b) $\tilde{\chi}_1^{-}\tilde{\chi}_1^{-}$ cross-section uncertainty

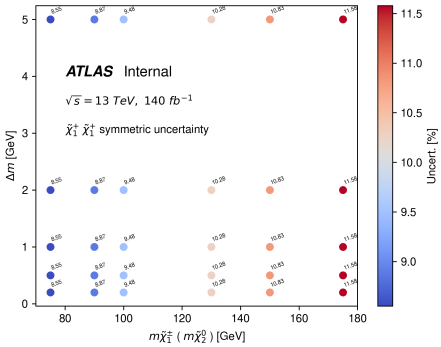

(c) $\tilde{\chi}_1^{+}\tilde{\chi}_1^{+}$ cross-section uncertainty

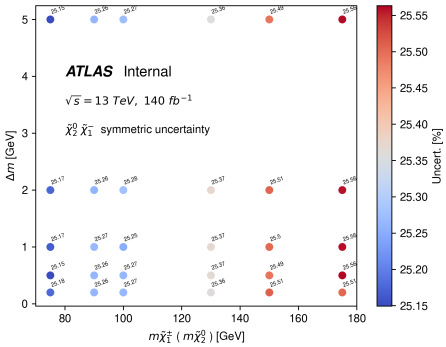

(d) $\tilde{\chi}_2^0\tilde{\chi}_1^{-}$ cross-section uncertainty

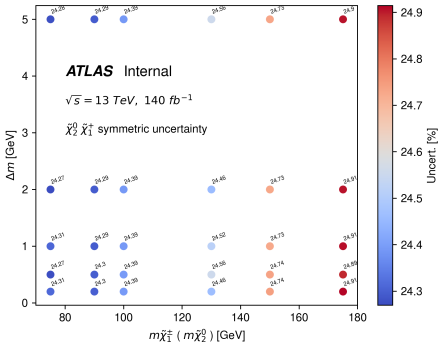

(e) $\tilde{\chi}_2^0\tilde{\chi}_1^{+}$ cross-section uncertainty

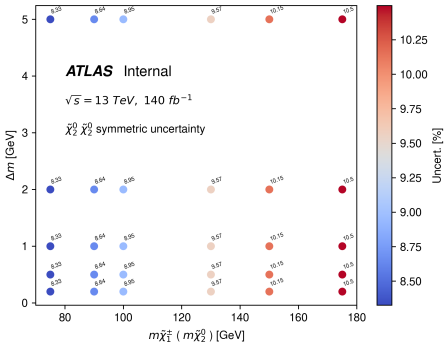

(f) $\tilde{\chi}_2^0\tilde{\chi}_2^0$ cross-section uncertainty

Figure 4.7: Signal cross-section uncertainties for each signal process.

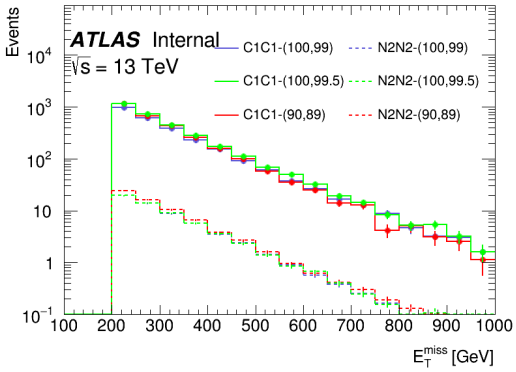

(a) $E_{\mathrm{T}}^{\mathrm{miss}}$

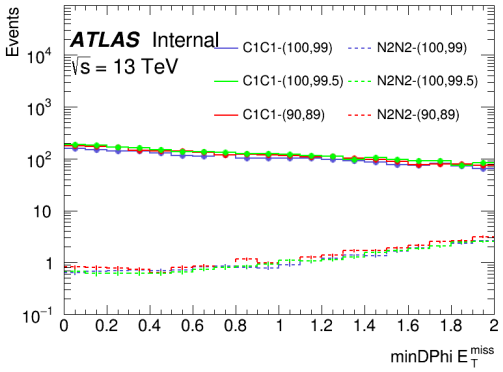

(b) $\min(\Delta\phi(j, E_{\mathrm{T}}^{\mathrm{miss}}))$

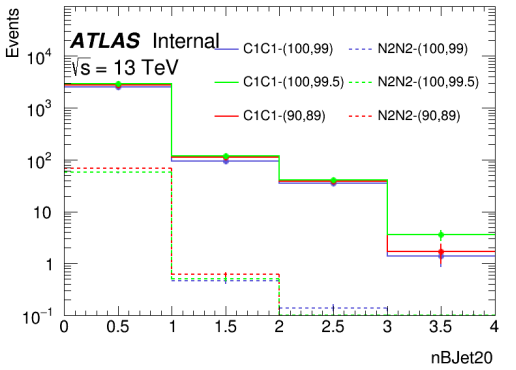

(c) b-jet multiplicity

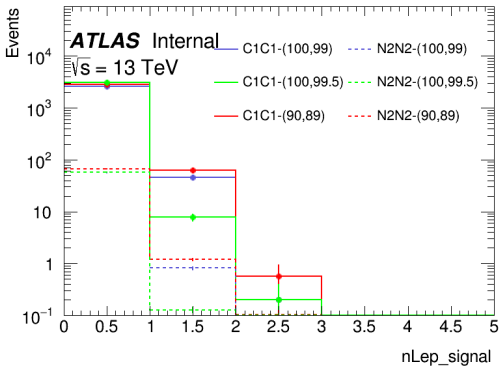

(d) lepton multiplicity

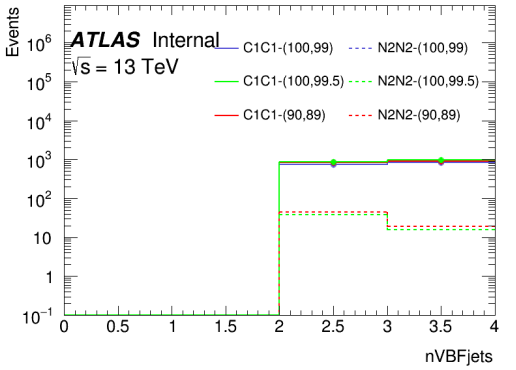

(e) jet multiplicity

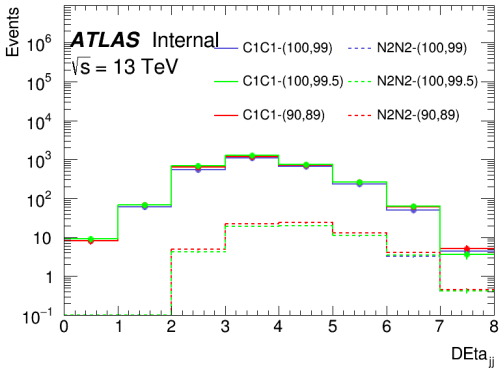

(f) $\Delta\eta_{\mathrm{jj}}$

Figure 4.8: (Part 1) Signal kinematic distributions at truth-level for the $\tilde{\chi}_1^{\pm}\tilde{\chi}_1^{\mp}$ and $\tilde{\chi}_2^0\tilde{\chi}_2^0$ processes.

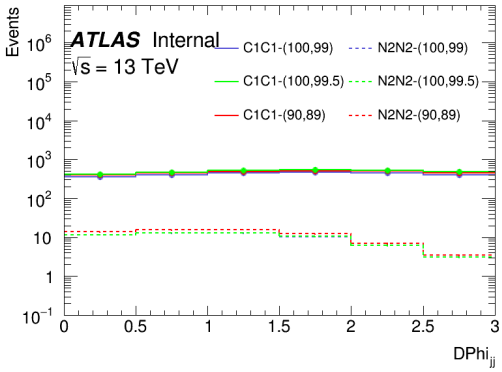

(a) $\Delta\phi(j_1,j_2)$

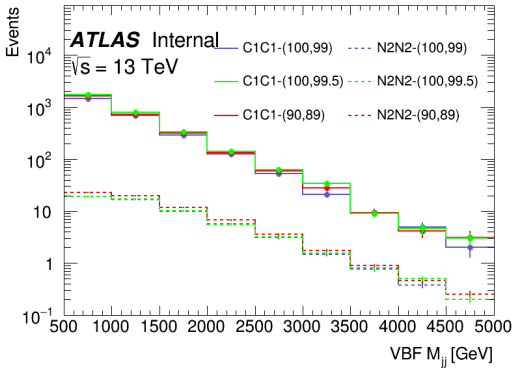

(b) m_{jj}

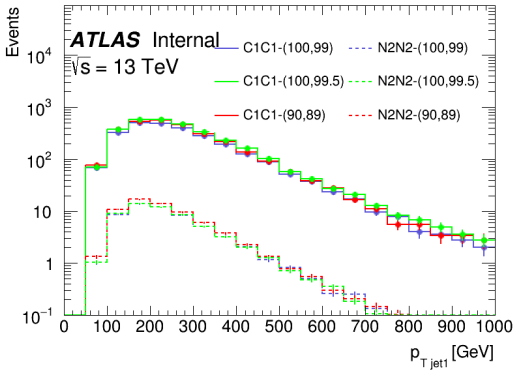

(c) $p_{\mathrm{T}}(\mathrm{j}_1)$

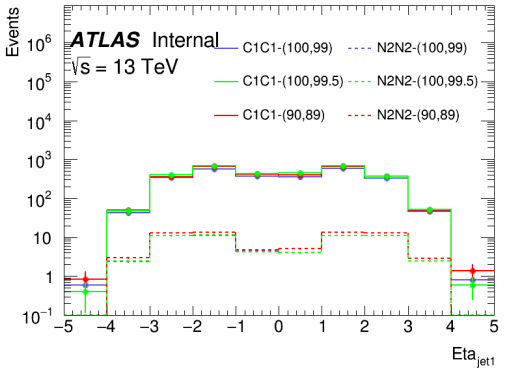

(d) $\eta(\mathrm{j}_1)$

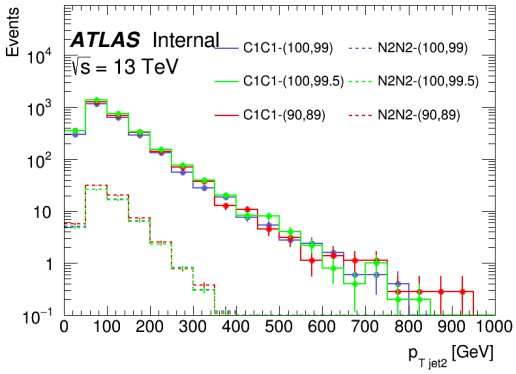

(e) $p_{\mathrm{T}}(\mathrm{j}_2)$

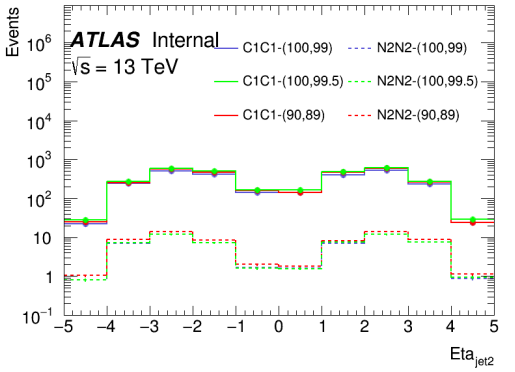

(f) $\eta(\mathrm{j}_2)$

Figure 4.9: (Part 2) Signal kinematic distributions at truth-level for the $\tilde{\chi}_1^{\pm}\tilde{\chi}_1^{\mp}$ and $\tilde{\chi}_2^0\tilde{\chi}_2^0$ processes.

4.3. Background Simulation

The simulated background samples used in the search will be described here. An overview of the various background samples is included in the appendix in Table 1.

The dominant background for this search comes from V + jets where the weak boson decays to a lepton-antilepton pair. The V + jets backgrounds can be separated into two production modes: strong and electroweak. Figure 4.10 shows example diagrams for the strong and electroweak production of Z + jets. The strong production of W and Z bosons in association with multiple jets is generated with SHERPA 2.2.11 [42]. Events are generated with up to 2 additional partons at NLO and up to 5 additional partons at LO using the NNPDF3.0NNLO [95] PDF set. The samples are enhanced in $\max(H_T, p_T^V)$ and sliced based on the quark flavor content. For the electroweak production of V + jets, samples are also generated using SHERPA 2.2.11 with 2 to 3 additional partons at LO using the NNPDF3.0NNLO PDF set.

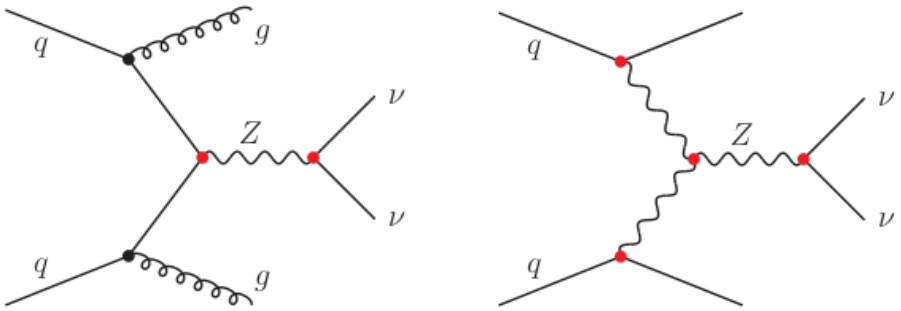

(a) Strong Z + jets (b) Electroweak Z + jets

Figure 4.10: Diagrams showing examples of the strong and electroweak production of Z + jets.

The diboson (VV) background was simulated using SHERPA 2.2.1 or 2.2.2 depending on the specific type of process. Both the fully leptonic final states and semileptonic final states, in which one boson decays leptonically and the other hadronically,

were generated at NLO in QCD for up to one additional parton and at LO for up to three additional partons. Triboson (VVV) events were simulated using SHERPA 2.2.2 at NLO for the inclusive process and to LO for up to two additional parton emissions. For both of these multiboson samples, the matrix element calculations were matched and merged with the SHERPA parton shower based on Catani–Seymour dipole factorization [74, 106] using the MEPS@NLO prescription [48, 82, 83, 84].

For $t\bar{t}$ production, samples were generated using POWHEG BOX v2 [3, 69, 70, 93] at NLO with the NNPDF3.0NLO [95] PDF set and the h_{damp} parameter set to $1.5\,m_{\text{top}}$ [21]. The events were interfaced to PYTHIA 8.230 [110] for modeling the parton shower, hadronization, and underlying event. The generator parameters were set according to the A14 tune [17] and using the NNPDF2.3LO PDF set [94]. The decays of bottom and charm hadrons were performed by EVTGEN 1.6.0 [87]. The associated production of top quarks with W bosons (tW) was modeled using the POWHEG BOX v2 [3, 69, 93, 102] generator at NLO in QCD using the five-flavor scheme and the NNPDF3.0NLO PDF set [95]. The diagram removal scheme [71] was used to remove interference and overlap with the $t\bar{t}$ production. These events were interfaced to PYTHIA 8.230 [110] using the A14 tune [17] and the NNPDF2.3LO set of PDFs [94]. For single-top production via t-channel and s-channel, POWHEG BOX v2 [3, 68, 69, 93] generator was used at NLO in QCD using the four-flavor and five-flavor schemes for each channel respectively and with the corresponding NNPDF3.0NLO set of PDFs [95]. The events were interfaced with PYTHIA 8.230 [110] using the A14 tune [17] and the NNPDF2.3LO set of PDFs [94].

For the multijet background, events were generated using PYTHIA 8.230 [110] with leading-order matrix elements for dijet production which were matched to the parton shower. The renormalization and factorization scales were set to the geometric mean of the squared transverse masses of the two outgoing particles in the matrix element,

$p_{\mathrm{T}}^{\mathrm{hat}} = \sqrt{(p_{\mathrm{T},1}^2 + m_1^2)(p_{\mathrm{T},2}^2 + m_2^2)}$. The NNPDF2.3LO PDF set [94] was used in the ME generation, the parton shower, and the simulation of the multi-parton interactions with the A14 [17] set of tuned parameters.

4.4. Derivation

The analysis makes use of the EXOT5 DAOD (Derived Analysis Object Data) data format for both data and Monte Carlo samples. To minimize the size of the datasets to be used for physics analysis, the EXOT5 derivation applies a filter to select only those events that satisfy either a single-lepton trigger or an $E_{\mathrm{T}}^{\mathrm{miss}}$ trigger along with at least one jet with $p_{\mathrm{T}} > 100$ GeV or if the following requirements are satisfied:

- At least two jets
- The leading and sub-leading calibrated jets must have $p_T > 40$ GeV
- The leading two calibrated jets must have a dijet mass greater than 150 GeV and a separation in pseudorapidity $|\Delta\eta_{jj}|$ greater than 2.5

EXOT5 DAODs were processed for all of the samples of the analysis through the SusySkimHiggsino package to produce the ntuples used for doing studies and obtaining results. The SusySkimHiggsino package applies many of the aspects of the analysis that will be discussed in later sections during the ntuple production such as the physics object definitions and calibrations, preselection cuts through the selector, and more. The build of SusySkimHiggsino used is based on release 21.2.222 of AnalysisBase.

Chapter 5

Physics Objects

Dedicated algorithms are used to identify and reconstruct the physics objects in an event recorded by the ATLAS detector. These reconstruction algorithms utilize the unique signatures left by different particle types in the detector in order to identify and classify physics objects. Figure 5.1 provides a visualization of how the different particles interact with the detector.

Additional quality criteria can be imposed on reconstructed physics objects in order to maximize the signal efficiency and decrease misidentification rates. For this search the reconstructed electrons, muons, and jets are classified into two categories based on the object quality requirements that are imposed: baseline and signal. The requirements for baseline objects are looser than those of the signal objects such that they can be used for making more aggressive selections, such as the lepton veto used in this search. The signal objects are used to minimize the likelihood that the reconstructed physics object has been misidentified. A summary of the physics object definitions is shown in Table 5.1.

Property	Signal	Baseline
Electrons		
Kinematic	$p_{\mathrm{T}} > 4.5$ GeV, $\lvert\eta\rvert < 2.47$ (include crack)	$p_{\mathrm{T}} > 4.5$ GeV
Identification	TightLLH	LooseAndBLayerLLH
Isolation	Loose_VarRad	–
Impact parameter	$\lvert d_0/\sigma(d_0)\rvert < 5$, $\lvert z_0 \sin\theta\rvert < 0.5$ mm	$\lvert z_0 \sin\theta\rvert < 0.5$ mm
Muons		
Kinematic	$p_{\mathrm{T}} > 3$ GeV, $\lvert\eta\rvert < 2.5$	$p_{\mathrm{T}} > 3$ GeV, $\lvert\eta\rvert < 2.7$
Identification	Medium	Loose
Isolation	Loose_VarRad	–
Impact parameter	$\lvert d_0/\sigma(d_0)\rvert < 3$ & $\lvert z_0 \sin\theta\rvert < 0.5$ mm	$\lvert z_0 \sin\theta\rvert < 0.5$ mm
Jets (Anti-k_t $R = 0.4$ PFlow)		
Kinematic	$p_{\mathrm{T}} > 30$ GeV, $\lvert\eta\rvert < 4.5$	$p_{\mathrm{T}} > 20$ GeV, $\lvert\eta\rvert < 4.5$
Pileup mitigation	JVT Medium for $p_{\mathrm{T}} < 60$ GeV, $\lvert\eta\rvert < 2.4$ fJVT Loose for $p_{\mathrm{T}} < 120$ GeV, $\lvert\eta\rvert > 2.5$	–
b-Jets (Anti-k_t $R = 0.4$ PFlow)		
Kinematic	$p_{\mathrm{T}} > 20$ GeV, $\lvert\eta\rvert < 2.5$	
Pileup mitigation	JVT Medium for $p_{\mathrm{T}} < 60$ GeV, $\lvert\eta\rvert < 2.4$	
b-tagging	DL1r FixedCutBeff 85%	
VBF jets (Anti-k_t $R = 0.4$ PFlow)		
Kinematic	$p_{\mathrm{T}} > 30$ GeV, $\lvert\eta\rvert < 4.5$	
Pileup mitigation	JVT Medium for $p_{\mathrm{T}} < 60$ GeV, $\lvert\eta\rvert < 2.4$ fJVT Loose for $p_{\mathrm{T}} < 120$ GeV, $\lvert\eta\rvert > 2.5$	
Flavor tagging	non b-tagged	

Table 5.1.: Summary of object definitions.

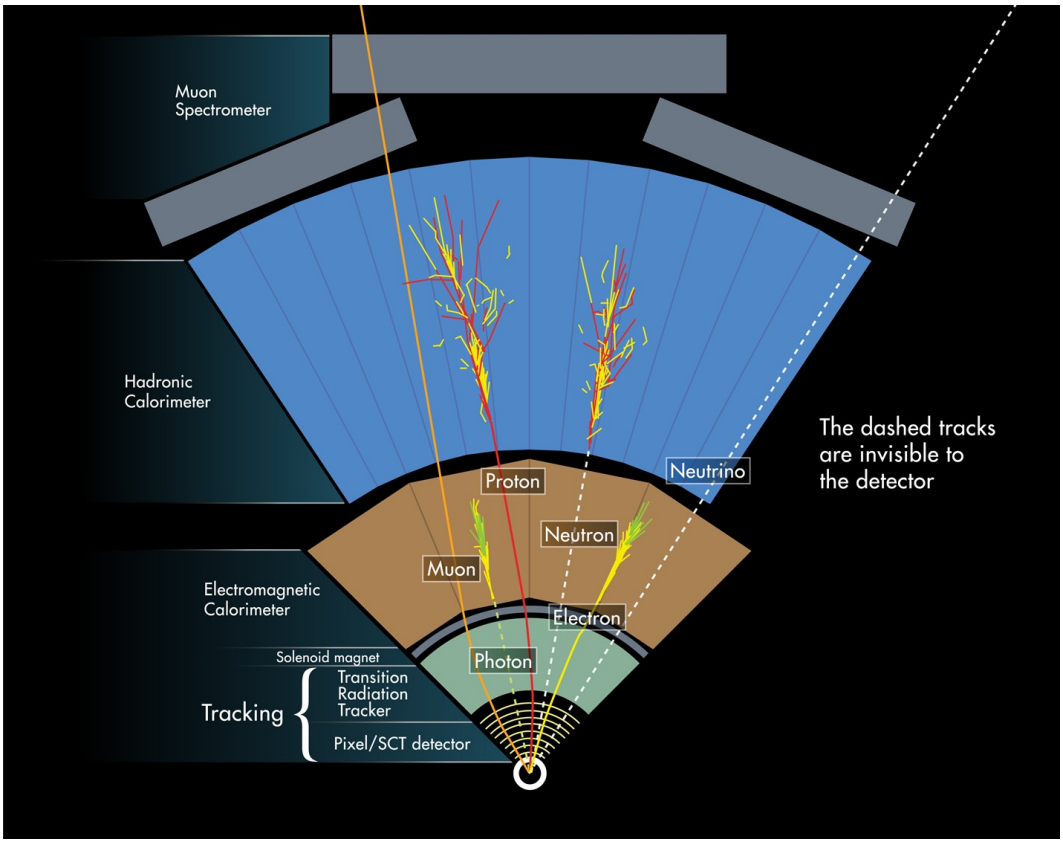

Figure 5.1: Cross-sectional view of the ATLAS detector showing the types of signatures produced by different types of particles. [100]

5.1. Electrons

Electrons produce a signature of tracks in the Inner Detector and a particle shower in the EM Calorimeter. The reconstruction of electrons starts with the identification of clusters of energy deposits in the EM calorimeter [27]. A sliding-window algorithm is used to search for these clusters with a window size of $\Delta\eta \times \Delta\phi = 3 \times 5$ "towers" with each tower having a size of $\Delta\eta \times \Delta\phi = 0.025 \times 0.025$. The energy in the towers is summed for each layer of the calorimeter, and the algorithm detects when the total transverse energy exceeds 2.5 GeV. These calorimeter clusters are matched with track candidates in the Inner Detector that match most closely in η and ϕ to produce the electron candidates. The baseline electrons used in this search must

satisfy $p_{\mathrm{T}} > 4.5$ GeV and $|\eta| < 2.47$ with a *LooseAndBLayerLLH* identification. The longitudinal impact parameter of baseline electron tracks is required to satisfy $|z_0 \sin\theta| < 0.5$ mm. Signal electrons must in addition pass *Loose_VarRad* isolation, likelihood-based *TightLLH* identification criteria, together with impact parameter satisfying the transverse $|d_0/\sigma(d_0)| < 5$ requirement.

5.2. Muons

Muon reconstruction is based on utilizing information from both the Inner Detector and the Muon Spectrometer [32]. Track candidates in the Muon Spectrometer are formed by fitting the track segments from different layers together. The track segments in the middle layers are used as seeds, and the track segments in the other layers are chosen based on hit multiplicity and fit quality criteria. A global χ^2 fit is applied to the track candidates to determine the muon's predicted trajectory. After this initial χ^2 fit outlier hits can be removed and missing hits can be added to refine the track candidate. Combined muons are one of the types of reconstructed muons and are used in this search. They use a combined fit based on hits from both the Inner Detector and Muon Spectrometer which have been reconstructed independently. An "outside-in" method is used for combined muons where the muon track candidates are reconstructed first and then extrapolated inwards to match tracks in the Inner Detector. There is also a complementary "inside-out" method that goes in reverse starting from Inner Detector tracks and extrapolated outwards to match the tracks in the Muon Spectrometer. Baseline muons are required to have $p_{\mathrm{T}} > 3$ GeV and $|\eta| < 2.7$, with tracks satisfying the $|z_0 \sin\theta| < 0.5$ mm requirement on the longitudinal impact parameter. They are also required to pass *Loose* identification criteria. Signal muons must in addition pass the *Loose_VarRad* isolation and *Medium*

identification requirements, have $|\eta| < 2.5$, and satisfy a $|d_0/\sigma(d_0)| < 3$ requirement on the transverse impact parameter.

5.3. Jets

Free quarks and gluons are not directly observed by the detector as they are color-charged particles and the phenomenon of color confinement only allows for color-neutral composite particles to be observed. They are instead detected indirectly as jets of hadrons produced from the hadronization process. These jets are reconstructed based on clustering algorithms that make use of the energy deposits left in the calorimeters by the hadrons. These algorithms use topological clusters (topo-clusters) consisting of adjacent calorimeter cells that have energies exceeding four times the background noise thresholds. Jets are reconstructed based on Particle Flow (PFlow) [23] algorithms that make use of both tracks from the Inner Detector and the calorimeter energy deposits. Tracks in the Inner Detector are matched with topo-clusters in the calorimeters and are identified as charged Particle Flow objects. Topo-clusters that are not matched with tracks are associated with neutral particles and are identified as neutral Particle Flow objects. The anti-k_t algorithm [46] with radius parameter $R = 0.4$ is used to reconstruct jets from these Particle Flow objects. Baseline jets are required to have $p_{\mathrm{T}} > 20$ GeV and $|\eta| < 4.5$. Signal jets rely on pileup mitigation using the Jet Vertex Tagger (JVT) [20] employing the *Medium* working point which is applied for jets satisfying $p_{\mathrm{T}} < 60$ GeV and $|\eta| < 2.4$. Pileup mitigation in the forward region is achieved using the forward Jet Vertex Tagger (fJVT) [22] with the *Loose* working point for jets satisfying $p_{\mathrm{T}} < 120$ GeV and $|\eta| > 2.5$. Signal jets satisfy $p_{\mathrm{T}} > 30$ GeV while jets used in the construction of the VBF system, referred to as VBF jets, need to be in addition not identified as a

jet originating from bottom quarks (not $b-$tagged). The $b-$tagged jets are baseline jets within $|\eta| < 2.5$ that are identified with the *DL1r* [37] algorithm, using the 85% working point.

5.4. Missing Transverse Energy

The partons that collide during the pp collisions should not carry momentum in the transverse plane and thus to conserve momentum the sum of the transverse momenta of the final-state particles coming from a parton-parton interaction should be zero. This fact is exploited to indirectly detect the presence of particles that pass through the detector without leaving any visible signatures such as neutrinos and hypothetical Beyond Standard Model (BSM) particles. An event in which these particles are produced would feature a non-zero total transverse momentum based on the detected particles. Thus the presence of these non-detected particles can be determined based on the missing transverse momentum $\mathbf{p}_{\mathrm{T}}^{\mathrm{miss}}$ defined as the negative vector sum of the transverse momenta of all identified physics objects with an additional soft term:

$$\mathbf{p}_{\mathrm{T}}^{\mathrm{miss}} = -\left(\sum_{\text{leptons}} \mathbf{p}_{\mathrm{T},l} + \sum_{\text{jets}} \mathbf{p}_{\mathrm{T},j} + \sum_{\text{photons}} \mathbf{p}_{\mathrm{T},\gamma} + \sum_{\text{soft}} \mathbf{p}_{\mathrm{T},s} \right). \tag{5.4.1}$$

The magnitude of the $\mathbf{p}_{\mathrm{T}}^{\mathrm{miss}}$ vector is denoted as $E_{\mathrm{T}}^{\mathrm{miss}}$. The soft term is constructed from all tracks that are not associated with any physics object, and that are associated to the primary vertex. In this way, the missing transverse momentum is adjusted for the best calibration of the jets and the other identified physics objects above, while maintaining pileup independence in the soft term. An additional version of $E_{\mathrm{T}}^{\mathrm{miss}}$ is also considered in this search in which leptons are considered as invisible in the calculation.

5.5. Overlap Removal

An overlap removal (OR) procedure is done to prevent double counting of reconstructed objects that would otherwise lead to redundant or misidentified objects. This procedure uses collections of electrons, muons, and jets, and it removes overlapping objects based on ΔR matching or shared Inner Detector tracks. The "boosted leptons" functionality of the overlap removal is used in which a sliding cone ΔR shrinking with the jet p_{T} is used in the lepton-jet overlap removal step (see below). The order of overlaps removed between collections is outlined as follows:

Muon-electron OR reject muon if Inner Detector track is shared with electron

Jet-electron OR reject jet if $\Delta R < 0.2$

Electron-jet OR reject electron if $\Delta R < 0.4 < \min(0.4, 0.04 + 10\ \mathrm{GeV}/p_{\mathrm{T}}(e))$

Jet-muon OR reject jet if fewer than three associated tracks and has a muon track ghost-associated [47] to it or $\Delta R < 0.2$

Muon-jet OR reject muon if $\Delta R < 0.4 < \min(0.4, 0.04 + 10\ \mathrm{GeV}/p_{\mathrm{T}}(\mu))$

5.6. Reconstruction of the VBF System

To select the two jets that will make up the VBF system, the following procedure is used. An iteration is performed over all jets in the event to consider all possible jet pairs in which the two jets are pointing into opposite hemispheres, i.e. $\eta(j_1)\cdot\eta(j_2) < 0$. For all eligible jet pairs, the invariant mass m_{jj} is calculated and the pair with the highest m_{jj} is chosen as the prospective VBF system. The jet with the higher (lower) p_{T} in this pair is referred to as $\mathrm{j}_1^{\mathrm{VBF}}$ ($\mathrm{j}_2^{\mathrm{VBF}}$).

Chapter 6

Analysis Strategy

6.1. Basic Event Selection and Event Cleaning

The recorded data events selected for this analysis are required to pass a set of cleaning requirements that are recommended centrally within ATLAS. This includes requiring events to pass the Good Runs Lists (GRLs) as described in Section 4.1. Bad, corrupted, and incomplete events are also rejected. These rejected events include those due to LAr noise bursts, data corruption, single event upsets in the SCT, and missing detector information. Events are required to have at least one reconstructed pp interaction vertex with a minimum of two associated tracks, each with $p_{\mathrm{T}} > 500$ MeV. In events with multiple vertices, the hard-scatter vertex is defined as the primary vertex with the highest $\sum p_{\mathrm{T}}^2$ of associated tracks. Jet cleaning is applied for the leading p_{T} jet by requiring it to pass the requirements of the tight-jet working point [18]. The tight working point is applied for only the leading p_{T} jet since it is found to be sufficient to reduce the non-collision beam background while also avoiding a reduction in the signal selection efficiency that would occur if it was also imposed for the sub-leading p_{T} jet. Events with jets that could be affected by a dead Tile Calorimeter module are also vetoed as listed in Table 6.1.

Year	RunNumber	Module name	η region	ϕ region
2015	266904–284484	LBA10	$0 < \eta < 0.9$	$0.8 < \phi < 1.0$
		EBC21	$-1.6 < \eta < -0.9$	$1.9 < \phi < 2.1$
2016	302053–311481	LBA52	$0 < \eta < 0.9$	$-1.33 < \phi < -1.13$
	306988–311481	LBC5	$-0.9 < \eta < 0$	$0.34 < \phi < 0.54$
2017	325713–340453	LBC63	$-0.9 < \eta < 0$	$-0.25 < \phi < -0.05$
		EBA3	$0.8 < \eta < 1.7$	$0.14 < \phi < 0.34$
2018	350310–352514	LBA29, 30	$0 < \eta < 0.9$	$2.7 < \phi < 3.0$
	355261–364292	LBA32	$0 < \eta < 0.9$	$\lvert\phi\rvert > 3.0$

Table 6.1.: Dead tile modules over the course of Run 2.

6.2. Preselection

In addition to the basic cleaning selections described above, a preselection is defined to loosely select the phase space of interest for this analysis. The selections are summarized below:

- Pass $E_{\mathrm{T}}^{\mathrm{miss}}$ trigger
- $E_{\mathrm{T}}^{\mathrm{miss}} > 250$ GeV (trigger plateau cut)
- Presence of a VBF jet pair (see Section 5.6)
- $m_{\mathrm{jj}} > 600$ GeV
- $|\Delta\eta_{\mathrm{jj}}| > 3.0$
- $p_{\mathrm{T}}(\mathrm{j}_1^{\mathrm{VBF}}) > 80$ GeV
- $p_{\mathrm{T}}(\mathrm{j}_2^{\mathrm{VBF}}) > 40$ GeV
- Baseline lepton veto
- Veto of events with any $b-$tagged jet

- $\min(\Delta\phi(j, E_{\mathrm{T}}^{\mathrm{miss}})) > 0.4$

The cut values used in the selections were determined based on an optimization procedure to provide the best discrimination between the signal and background, in conjunction with the cuts placed on the output scores of the boosted decision tree classifier that will be discussed later in this chapter. When constructing analysis regions, the selections in the preselection are applied collectively rather than individually in a specific order.

The search targets signal processes with a vector boson fusion plus missing transverse momentum signature. Vector boson fusion is characterized by the presence of two high-p_{T} jets with large separation in pseudorapidity. The VBF jets are expected to be more forward and have a larger dijet invariant mass than jets coming from background processes. In order to be consistent with the VBF topology we select events with at least two jets that satisfy these characteristics. A significant amount of missing transverse momentum is also expected due to the LSP $\tilde{\chi}_1^0$ that is able to escape without being detected. Thus the $E_{\mathrm{T}}^{\mathrm{miss}}$ trigger is used in conjunction with a requirement of large $E_{\mathrm{T}}^{\mathrm{miss}}$ to target signal events.

The signal models being targeted here consist of those with compressed mass spectra. Due to these small mass splittings, leptons that arise as decay products from the signal processes are expected to have low p_{T} and not be reconstructed. Therefore we reject events that include one or more baseline leptons in the signal region. This veto on leptons also helps to suppress backgrounds such as $W+$ jets and $Z+$ jets in which the W and Z bosons decay leptonically.

Additional selections are also imposed to reduce various background processes. Events from the QCD multijet background may be able to pass the large $E_{\mathrm{T}}^{\mathrm{miss}}$ requirement due to mismeasurements of jets. By requiring the minimum azimuthal

difference between any jet with $p_T > 30$ GeV and the E_T^{miss} to be greater than 0.4 this possibility can be mitigated. A veto on b-tagged jets is included to reduce the contribution of the $t\bar{t}$ background.

The distributions of important kinematic variables at preselection level are shown in Figure 6.1. These include the E_T^{miss}, the invariant mass of the VBF-tagged jets, the p_T of the leading and sub-leading VBF-tagged jets, the $\Delta\eta$ between the VBF-tagged jets, and the minimum $\Delta\phi$ between all jets and the E_T^{miss}. The dominant backgrounds are $Z+$jets and $W+$jets production. The modeling is in general at a reasonable level but some slopes, for example in m_{jj}, will be addressed by the background estimation strategy.

Preselection requirements are also imposed when training the boosted decision tree model that will be discussed in the proceeding section. To ensure that all input features to the BDT are well-behaved, a check of the agreement between the data and background prediction was performed for each input feature with preselection cuts. As the training was based on an earlier ntuple version where the skimming was different than in the ntuples used for the final results, the selection for training happens to be slightly relaxed with respect to the preselection requirements listed above. The following cuts are modified compared to the preselection requirements:

- $m_{jj} > 500$ GeV
- $|\Delta\eta_{jj}| > 2.5$

Furthermore this check was done separately for events with only two jets and for three or more jets since the analysis strategy that will be described later involves the splitting of regions based on the jet multiplicity. For the QCD multijet background, a Monte Carlo sample is used in this check although in the final analysis a data-driven approach will be used to estimate the background.

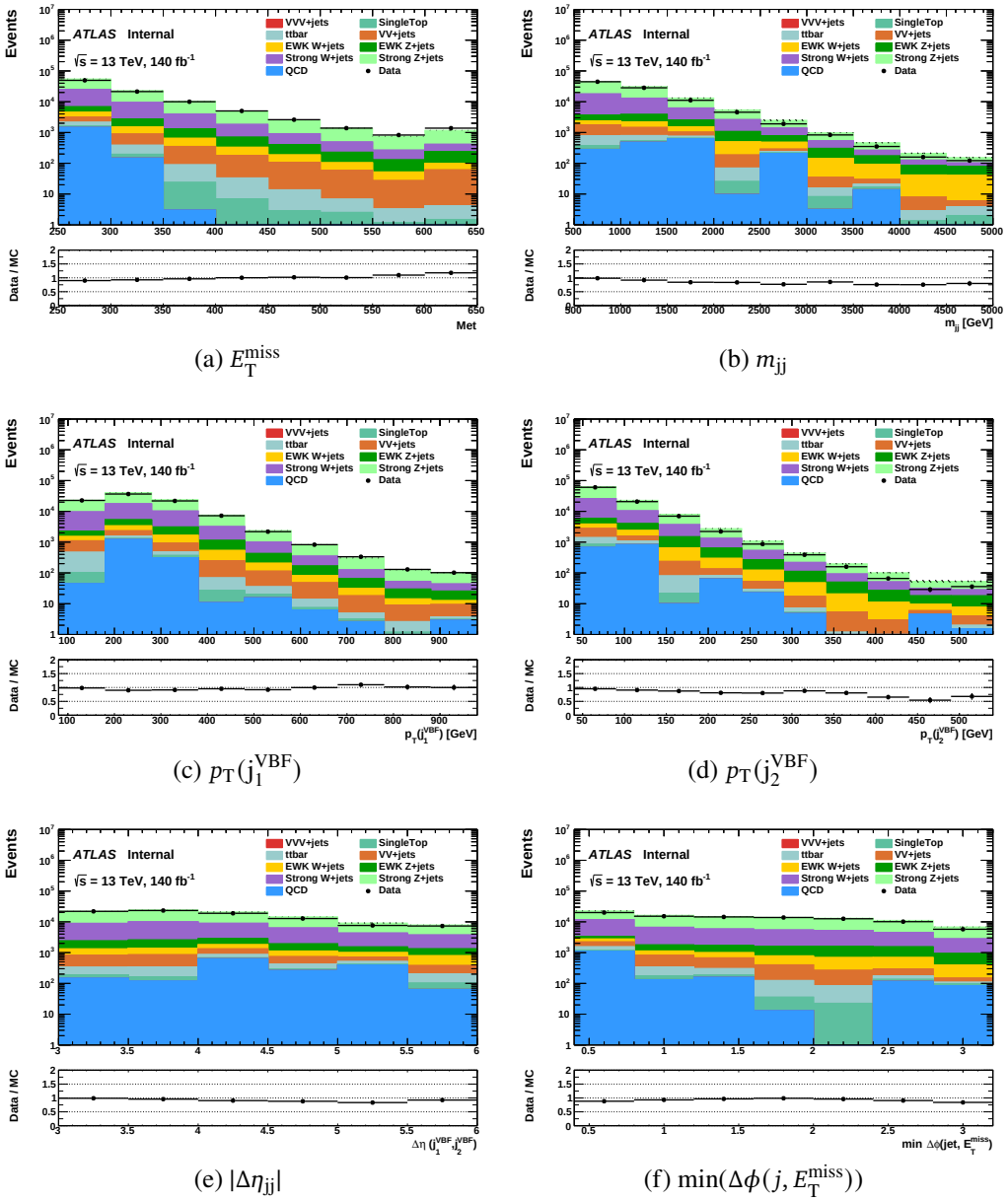

(a) $E_{\mathrm{T}}^{\mathrm{miss}}$ (b) m_{jj}

(c) $p_{\mathrm{T}}(\mathrm{j}_1^{\mathrm{VBF}})$ (d) $p_{\mathrm{T}}(\mathrm{j}_2^{\mathrm{VBF}})$

(e) $|\Delta\eta_{\mathrm{jj}}|$ (f) $\min(\Delta\phi(j, E_{\mathrm{T}}^{\mathrm{miss}}))$

Figure 6.1: Kinematic distributions at preselection level. For the QCD multijet background, the Monte Carlo sample is used.

The input features include variables that involve "jet Y" and "jet Z". "jet Y" corresponds to the jet in the event that has the minimum $\Delta\phi(j, E_{\mathrm{T}}^{\mathrm{miss}})$ while "jet Z" corresponds to the jet having the minimum $m_T(j, E_{\mathrm{T}}^{\mathrm{miss}})$ - 80 GeV. The transverse

mass m_T of two objects X and Y is defined the usual way as

$$m_T = \sqrt{m_X^2 + m_Y^2 + 2\left(E_{X,T}E_{Y,T} - \mathbf{p}_{X,T}\mathbf{p}_{Y,T}\right)} \tag{6.2.1}$$

where $E_T = \sqrt{m^2 + \mathbf{p}_T^2}$. When calculating m_T with $E_{\mathrm{T}}^{\mathrm{miss}}$, the associated mass m is set to 0. The reason for the inclusion of such "jet Y" and "jet Z" variables is to reduce the $W \rightarrow \tau\nu$ background in which the jet in these variables could be identified as coming from the hadronic decay of the τ. For these variables the jets considered include those down to 20 GeV in p_{T} (note that the cut on $\min(\Delta\phi(j, E_{\mathrm{T}}^{\mathrm{miss}}))$ only considers jets with $p_{\mathrm{T}} > 30$ GeV).

The preselection plots of the input features for events with two jets are shown in Figures 6.2–6.9 for $\mathcal{L} = 140$ fb^{-1} at $\sqrt{s} = 13$ TeV. Those for events with three or more jets are shown in Figures 6.10–6.17. For events with two jets, it can be seen that in general the ratio of the data to predicted background is visibly less than 1, but this should be accounted for by the normalization factors for the V + jets backgrounds in the simultaneous fit including the W and Z control regions, which will be described later in the chapter on background estimation. As part of the background estimation strategy, there are separate normalization factors based on the jet multiplicity. The fitted values for the two jet normalization factors are around 0.8 which is compatible with the data-to-Monte Carlo ratio seen in these figures. For the events with three or more jets the agreement between the data and predicted background seems satisfactory with the ratio being for the most part close to 1. To address some of the discrepancies that appear in these figures, the following points are useful to keep in context:

- The additional cuts that will be applied in the signal region compared to the preselection

- The Monte Carlo sample being used for the QCD multijet background in this comparison instead of the planned data-driven estimation
- Some of the discrepancies appear where the signal contribution is negligible

Taking into consideration these points along with the earlier comments on the background normalization, the input features seem to be reasonably modeled at this stage.

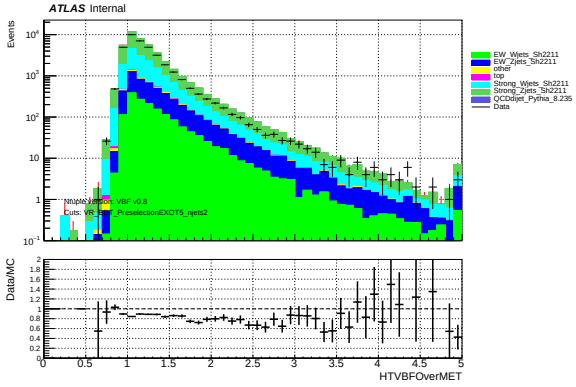

(a) $H_T^{(VBF)}$ / $E_{\mathrm{T}}^{\mathrm{miss}}$

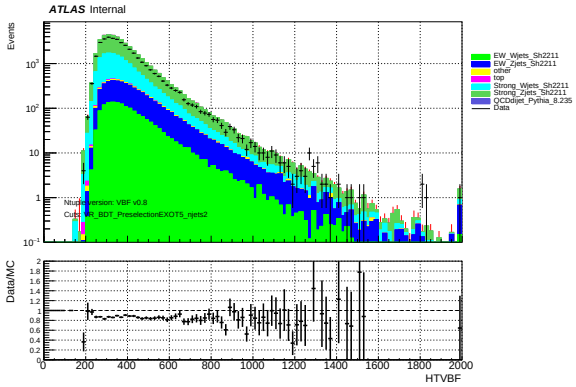

(b) $H_T^{(VBF)}$ [GeV]

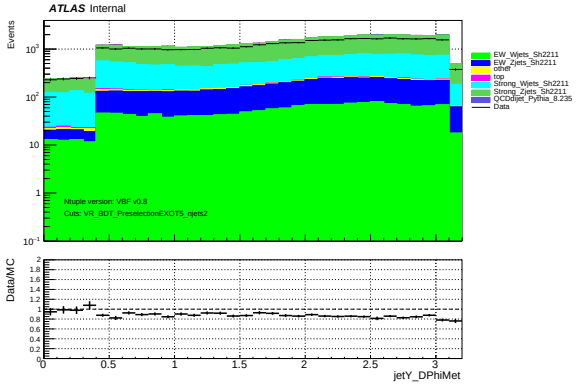

(c) $\Delta\phi$(jetY,$E_{\mathrm{T}}^{\mathrm{miss}}$)

Figure 6.2: Preselection plots showing data and the predicted background of the input features to BDT for events with two jets for $\mathcal{L}$ = 140 fb^{-1} at $\sqrt{s}$ = 13 TeV. Shown here specifically are the distributions for $H_T^{(VBF)}$ / $E_{\mathrm{T}}^{\mathrm{miss}}$, $H_T^{(VBF)}$, and $\Delta\phi$(jetY,$E_{\mathrm{T}}^{\mathrm{miss}}$).

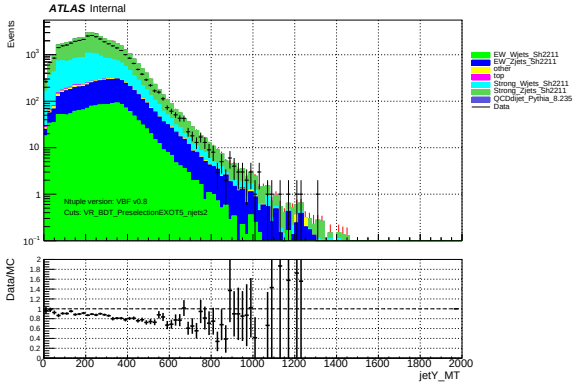

(a) M_T(jetY,$E_{\mathrm{T}}^{\mathrm{miss}}$) [GeV]

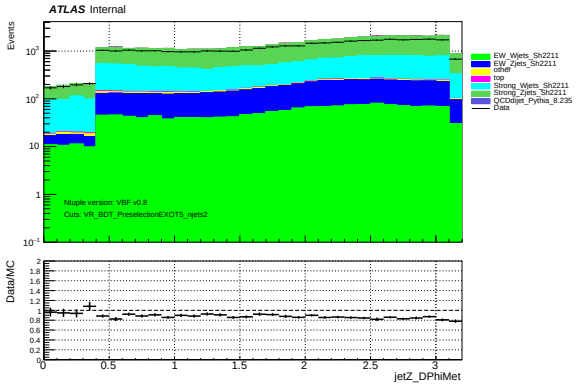

(b) $\Delta\phi$(jetZ,$E_{\mathrm{T}}^{\mathrm{miss}}$)

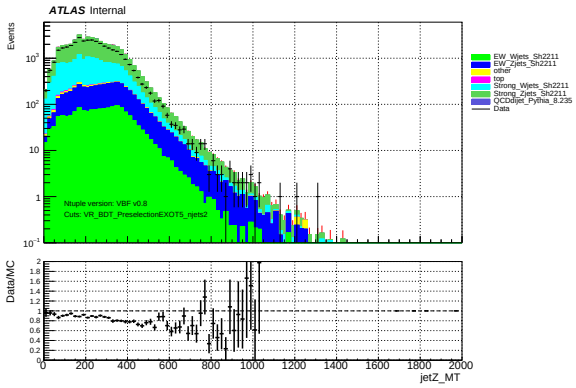

(c) M_T(jetZ,$E_{\mathrm{T}}^{\mathrm{miss}}$) [GeV]

Figure 6.3: Preselection plots showing data and the predicted background of the input features to BDT for events with two jets for $\mathcal{L}$ = 140 fb^{-1} at $\sqrt{s}$ = 13 TeV. Shown here specifically are the distributions for M_T(jetY,$E_{\mathrm{T}}^{\mathrm{miss}}$), $\Delta\phi$(jetZ,$E_{\mathrm{T}}^{\mathrm{miss}}$), and M_T(jetZ,$E_{\mathrm{T}}^{\mathrm{miss}}$).

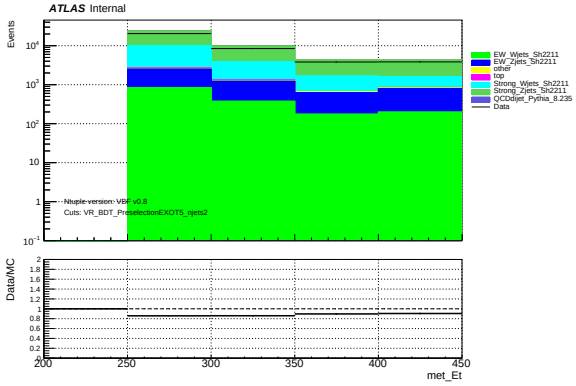

(a) $E_{\mathrm{T}}^{\mathrm{miss}}$ [GeV]

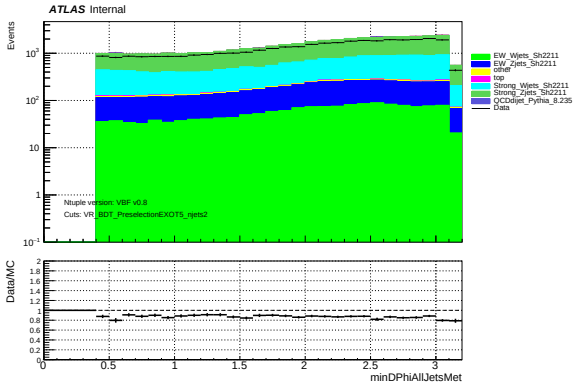

(b) $\min(\Delta\phi(j, E_{\mathrm{T}}^{\mathrm{miss}}))$

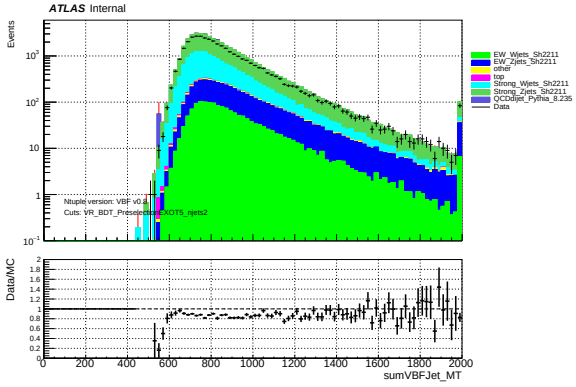

(c) $M_T(j_1,E_{\mathrm{T}}^{\mathrm{miss}})$+$M_T(j_2,E_{\mathrm{T}}^{\mathrm{miss}})$ [GeV]

Figure 6.4: Preselection plots showing data and the predicted background of the input features to BDT for events with two jets for $\mathcal{L} = 140$ fb^{-1} at $\sqrt{s} = 13$ TeV. Shown here specifically are the distributions for $E_{\mathrm{T}}^{\mathrm{miss}}$, $\min(\Delta\phi(j, E_{\mathrm{T}}^{\mathrm{miss}}))$, and $M_T(j_1,E_{\mathrm{T}}^{\mathrm{miss}})$+$M_T(j_2,E_{\mathrm{T}}^{\mathrm{miss}})$.

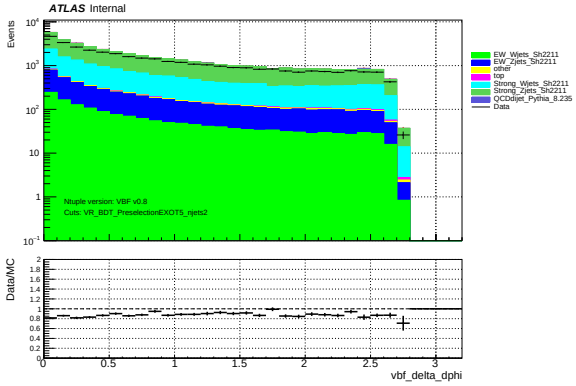

(a) $|\Delta\phi(j_1,E_{\mathrm{T}}^{\mathrm{miss}})$ - $\Delta\phi(j_2,E_{\mathrm{T}}^{\mathrm{miss}})|$

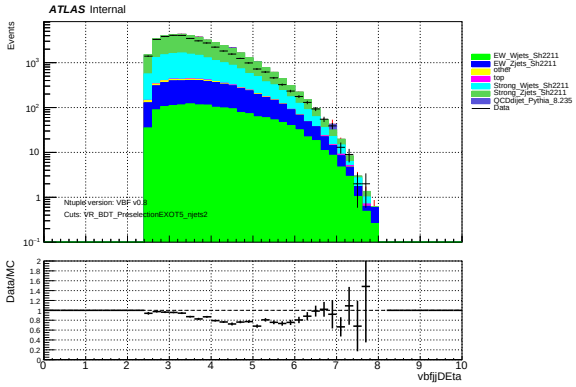

(b) $|\Delta\eta_{\mathrm{jj}}|$

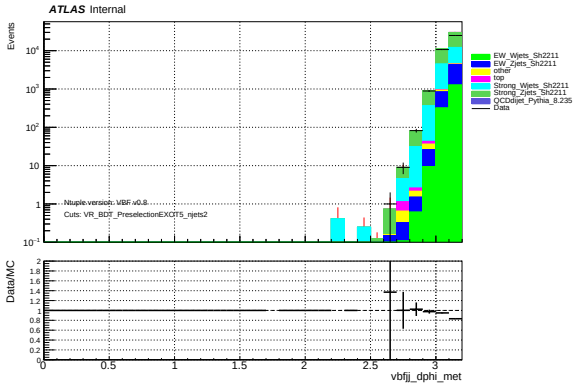

(c) $\Delta\phi(jj,E_{\mathrm{T}}^{\mathrm{miss}})$

Figure 6.5: Preselection plots showing data and the predicted background of the input features to BDT for events with two jets for $\mathcal{L}$ = 140 fb^{-1} at $\sqrt{s}$ = 13 TeV. Shown here specifically are the distributions for $|\Delta\phi(j_1,E_{\mathrm{T}}^{\mathrm{miss}})$ - $\Delta\phi(j_2,E_{\mathrm{T}}^{\mathrm{miss}})|$, $|\Delta\eta_{\mathrm{jj}}|$, and $\Delta\phi(jj,E_{\mathrm{T}}^{\mathrm{miss}})$.

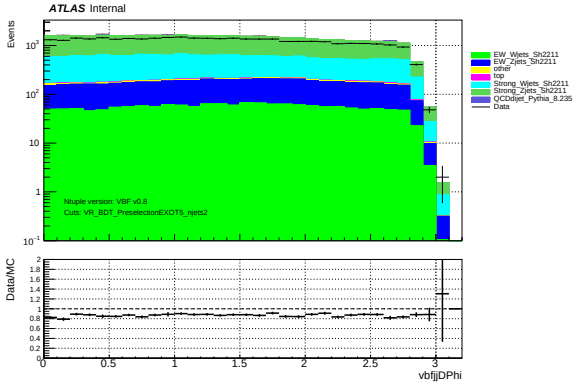

(a) $\Delta\phi(j_1, j_2)$

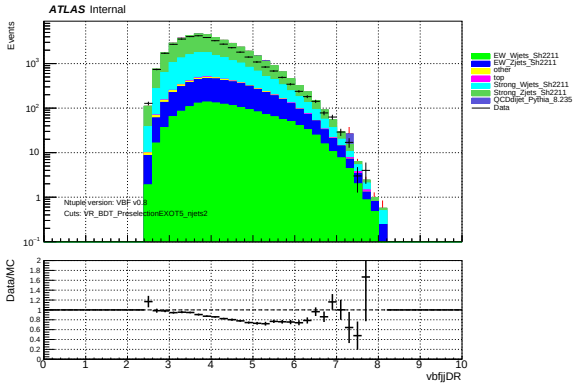

(b) ΔR_{jj}

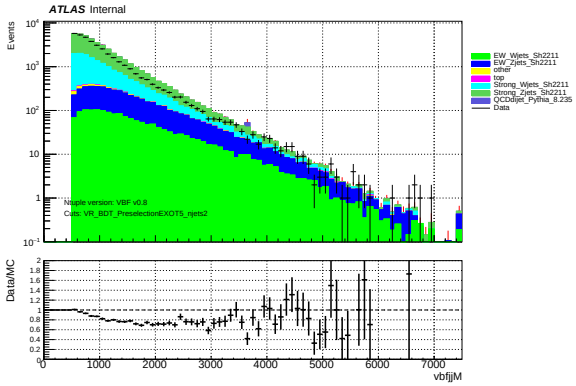

(c) m_{jj} [GeV]

Figure 6.6: Preselection plots showing data and the predicted background of the input features to BDT for events with two jets for $\mathcal{L} = 140$ fb^{-1} at $\sqrt{s} =$ 13 TeV. Shown here specifically are the distributions for $\Delta\phi(j_1, j_2)$, ΔR_{jj}, and m_{jj}.

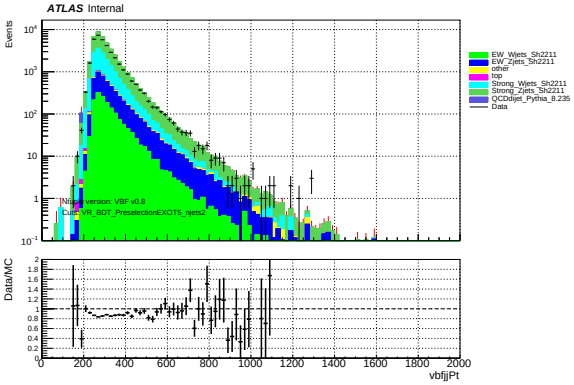

(a) p_{T} (j,j) [GeV]

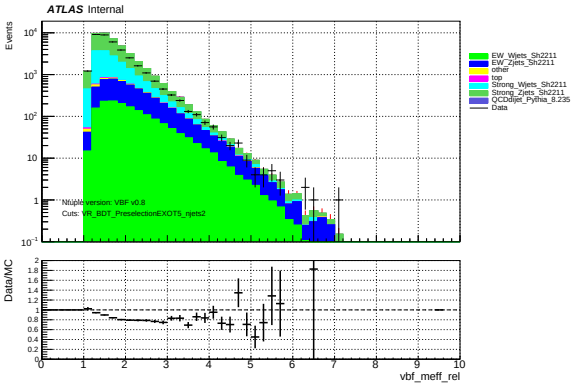

(b) m_{eff}(jj,$E_{\mathrm{T}}^{\mathrm{miss}}$)

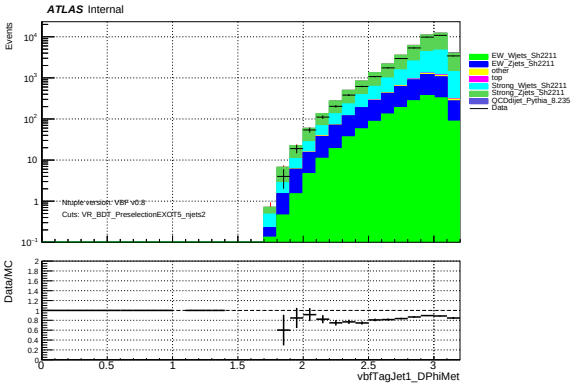

(c) $\Delta\phi(j_1,E_{\mathrm{T}}^{\mathrm{miss}})$

Figure 6.7: Preselection plots showing data and the predicted background of the input features to BDT for events with two jets for $\mathcal{L}$ = 140 fb^{-1} at $\sqrt{s}$ = 13 TeV. Shown here specifically are the distributions for p_{T} (j,j), m_{eff}(jj,$E_{\mathrm{T}}^{\mathrm{miss}}$), and $\Delta\phi(j_1,E_{\mathrm{T}}^{\mathrm{miss}})$.

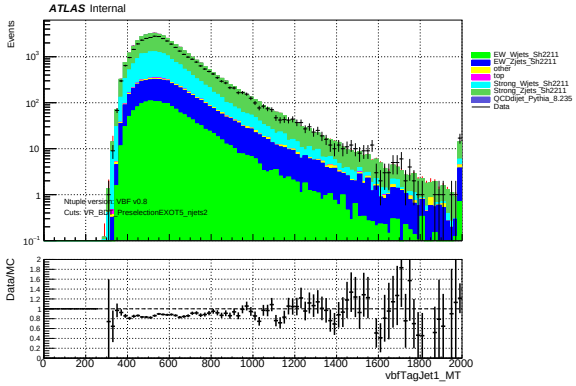

(a) $M_T(j_1,E_{\mathrm{T}}^{\mathrm{miss}})$ [GeV]

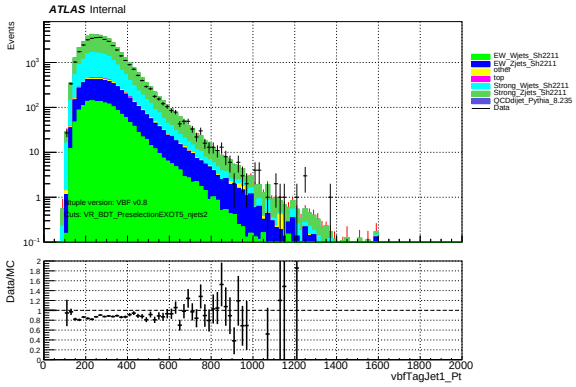

(b) $p_{\mathrm{T}}(\mathrm{j}_1)$ [GeV]

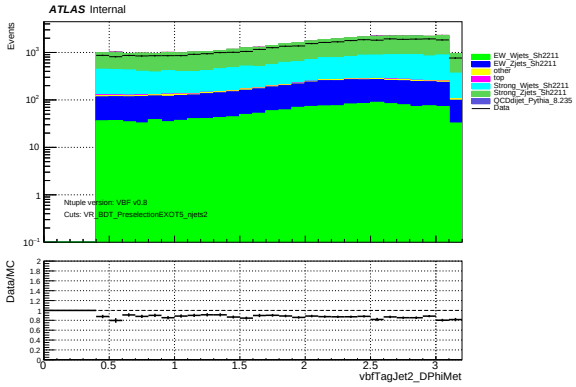

(c) $\Delta\phi(j_2,E_{\mathrm{T}}^{\mathrm{miss}})$

Figure 6.8: Preselection plots showing data and the predicted background of the input features to BDT for events with two jets for $\mathcal{L}$ = 140 fb^{-1} at $\sqrt{s}$ = 13 TeV. Shown here specifically are the distributions for $M_T(j_1,E_{\mathrm{T}}^{\mathrm{miss}})$, $p_{\mathrm{T}}(\mathrm{j}_1)$, and $\Delta\phi(j_2,E_{\mathrm{T}}^{\mathrm{miss}})$.

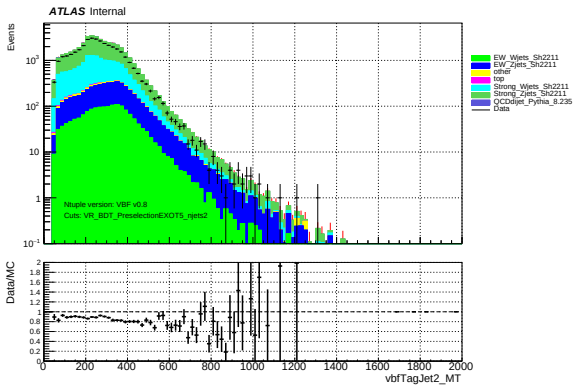

(a) $M_T(j_2,E_{\mathrm{T}}^{\mathrm{miss}})$ [GeV]

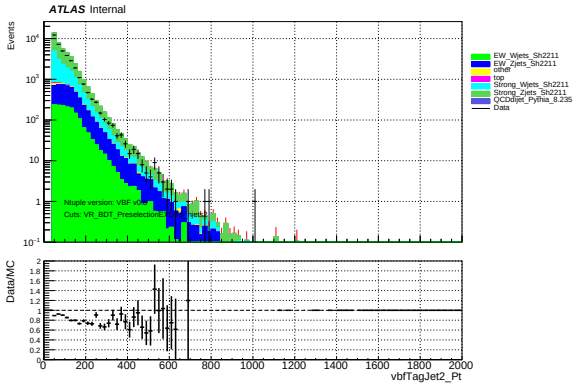

(b) $p_{\mathrm{T}}(\mathrm{j}_2)$ [GeV]

Figure 6.9: Preselection plots showing data and the predicted background of the input features to BDT for events with two jets for $\mathcal{L} = 140$ fb^{-1} at $\sqrt{s} =$ 13 TeV. Shown here specifically are the distributions for $M_T(j_2,E_{\mathrm{T}}^{\mathrm{miss}})$ and $p_{\mathrm{T}}(\mathrm{j}_2)$.

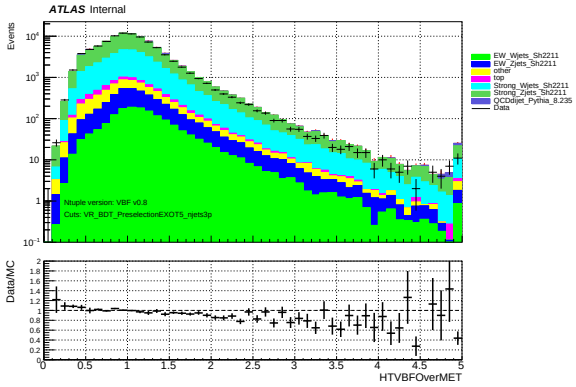

(a) $H_T^{(VBF)}$ / $E_{\mathrm{T}}^{\mathrm{miss}}$

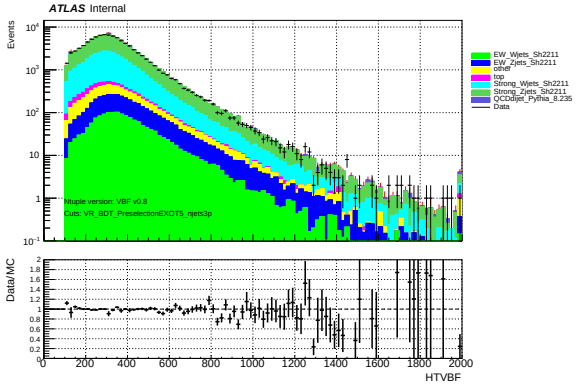

(b) $H_T^{(VBF)}$ [GeV]

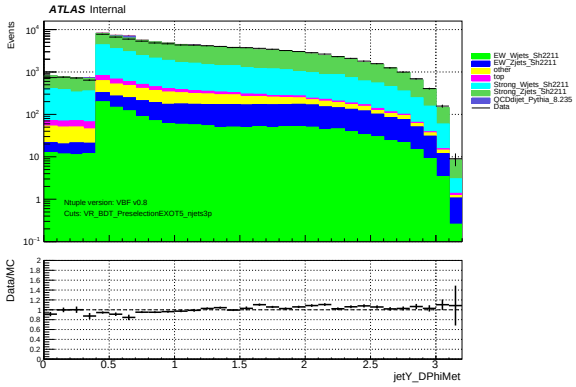

(c) $\Delta\phi$(jetY,$E_{\mathrm{T}}^{\mathrm{miss}}$)

Figure 6.10: Preselection plots showing data and the predicted background of the input features to BDT for events with three or more jets for $\mathcal{L} = 140\ \mathrm{fb}^{-1}$ at $\sqrt{s} = 13$ TeV. Shown here specifically are the distributions for $H_T^{(VBF)}$ / $E_{\mathrm{T}}^{\mathrm{miss}}$, $H_T^{(VBF)}$, and $\Delta\phi$(jetY,$E_{\mathrm{T}}^{\mathrm{miss}}$).

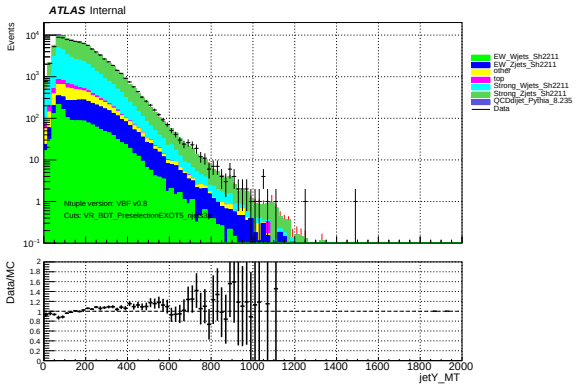

(a) M_T(jetY,$E_{\mathrm{T}}^{\mathrm{miss}}$) [GeV]

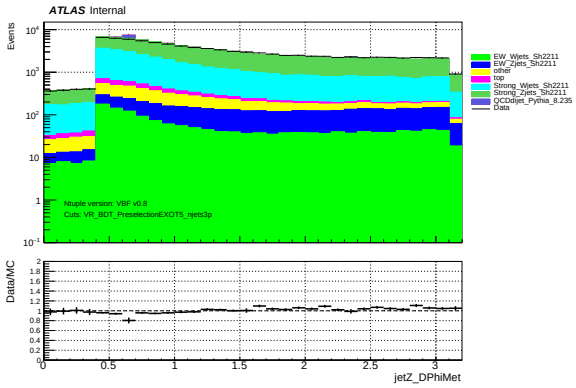

(b) $\Delta\phi$(jetZ,$E_{\mathrm{T}}^{\mathrm{miss}}$)

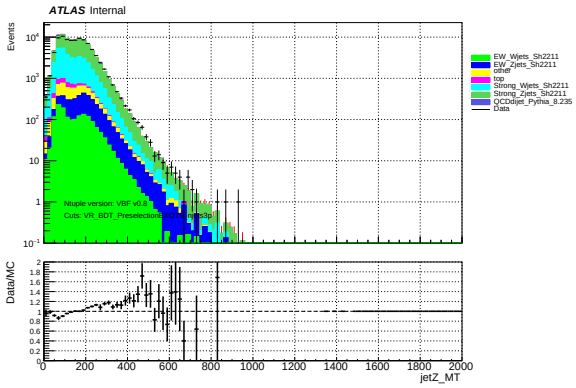

(c) M_T(jetZ,$E_{\mathrm{T}}^{\mathrm{miss}}$) [GeV]

Figure 6.11: Preselection plots showing data and the predicted background of the input features to BDT for events with three or more jets for $\mathcal{L}$ = 140 fb^{-1} at $\sqrt{s}$ = 13 TeV. Shown here specifically are the distributions for M_T(jetY,$E_{\mathrm{T}}^{\mathrm{miss}}$), $\Delta\phi$(jetZ,$E_{\mathrm{T}}^{\mathrm{miss}}$), and M_T(jetZ,$E_{\mathrm{T}}^{\mathrm{miss}}$).

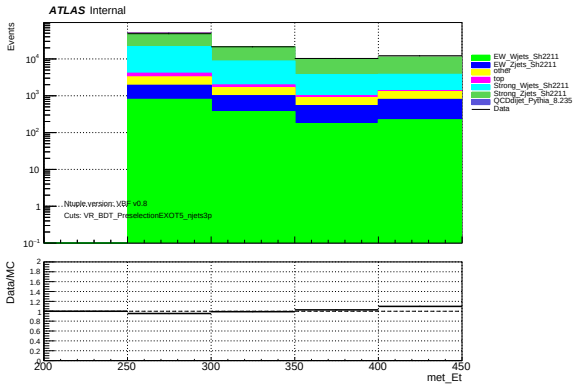

(a) $E_{\mathrm{T}}^{\mathrm{miss}}$ [GeV]

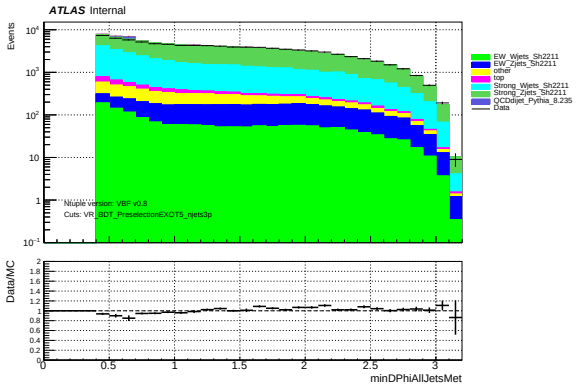

(b) $\min(\Delta\phi(j, E_{\mathrm{T}}^{\mathrm{miss}}))$

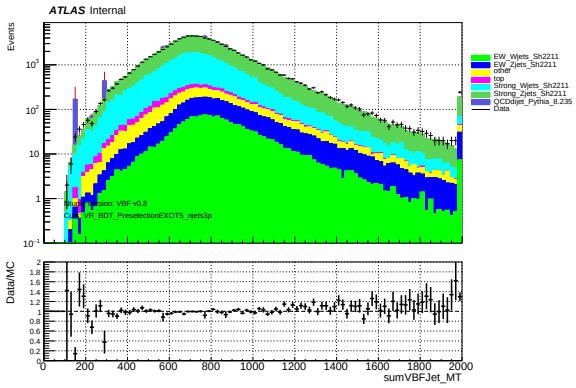

(c) $M_T(j_1,E_{\mathrm{T}}^{\mathrm{miss}})$+$M_T(j_2,E_{\mathrm{T}}^{\mathrm{miss}})$ [GeV]

Figure 6.12: Preselection plots showing data and the predicted background of the input features to BDT for events with three or more jets for $\mathcal{L} = 140\,\mathrm{fb}^{-1}$ at $\sqrt{s} = 13$ TeV. Shown here specifically are the distributions for $E_{\mathrm{T}}^{\mathrm{miss}}$, $\min(\Delta\phi(j, E_{\mathrm{T}}^{\mathrm{miss}}))$, and $M_T(j_1,E_{\mathrm{T}}^{\mathrm{miss}})$+$M_T(j_2,E_{\mathrm{T}}^{\mathrm{miss}})$.

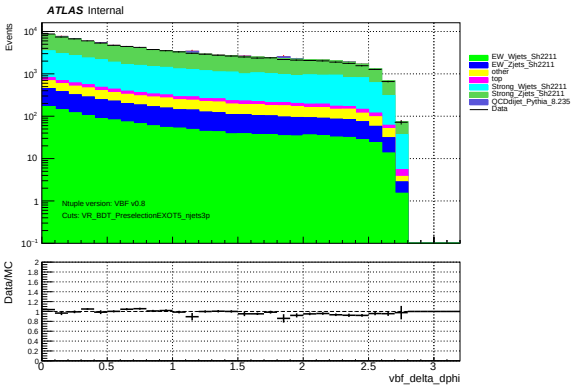

(a) $|\Delta\phi(j_1,E_{\mathrm{T}}^{\mathrm{miss}})$ - $\Delta\phi(j_2,E_{\mathrm{T}}^{\mathrm{miss}})|$

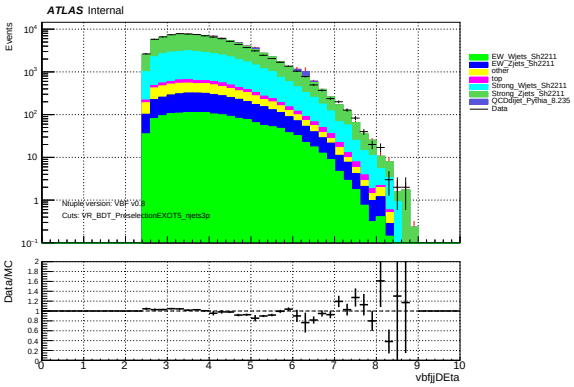

(b) $|\Delta\eta_{\mathrm{jj}}|$

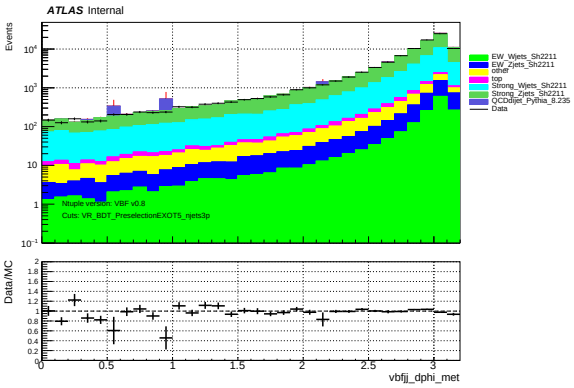

(c) $\Delta\phi(jj,E_{\mathrm{T}}^{\mathrm{miss}})$

Figure 6.13: Preselection plots showing data and the predicted background of the input features to BDT for events with three or more jets for $\mathcal{L}$ = 140 fb^{-1} at $\sqrt{s}$ = 13 TeV. Shown here specifically are the distributions for $|\Delta\phi(j_1,E_{\mathrm{T}}^{\mathrm{miss}})$ - $\Delta\phi(j_2,E_{\mathrm{T}}^{\mathrm{miss}})|$, $|\Delta\eta_{\mathrm{jj}}|$, and $\Delta\phi(jj,E_{\mathrm{T}}^{\mathrm{miss}})$.

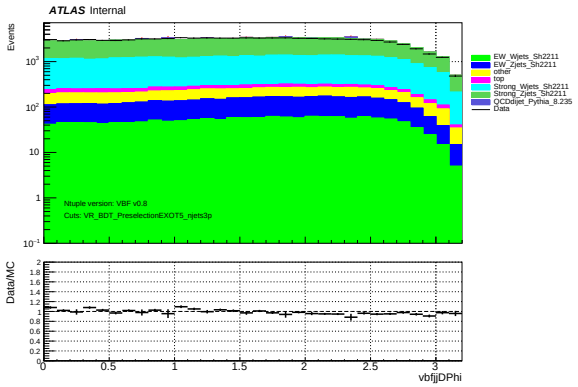

(a) $\Delta\phi(j_1, j_2)$

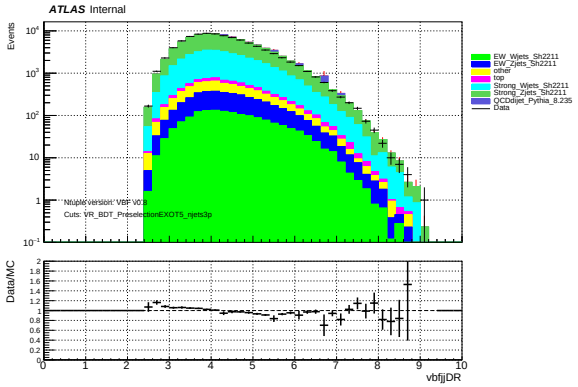

(b) ΔR_{jj}

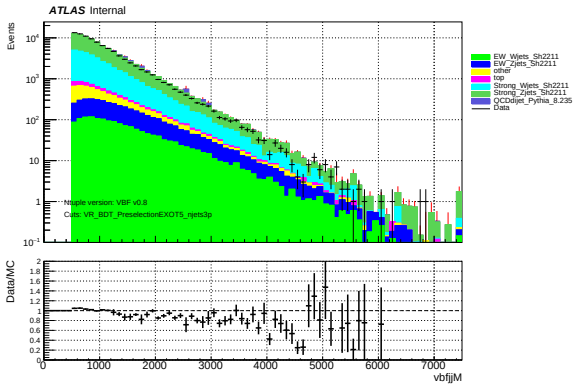

(c) m_{jj} [GeV]

Figure 6.14: Preselection plots showing data and the predicted background of the input features to BDT for events with three or more jets for $\mathcal{L} = 140\,\mathrm{fb}^{-1}$ at $\sqrt{s} = 13$ TeV. Shown here specifically are the distributions for $\Delta\phi(j_1, j_2)$, ΔR_{jj}, and m_{jj}.

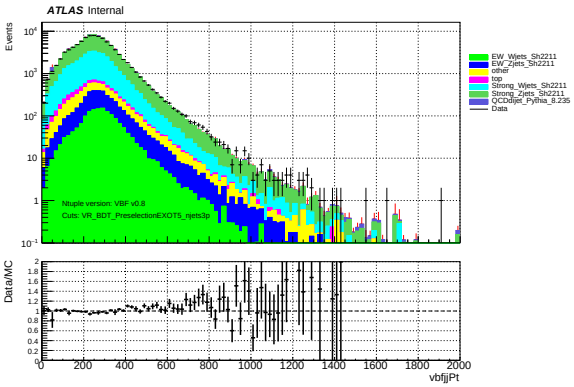

(a) p_{T} (j,j) [GeV]

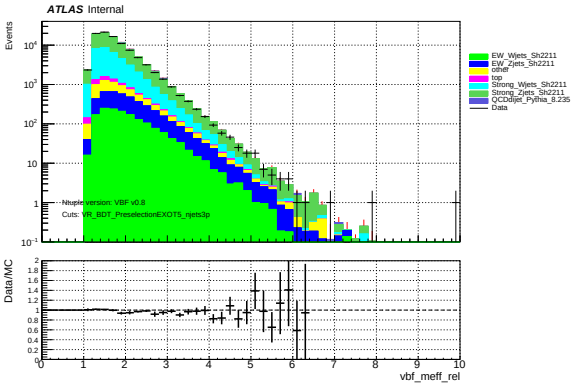

(b) m_{eff}(jj,$E_{\mathrm{T}}^{\mathrm{miss}}$)

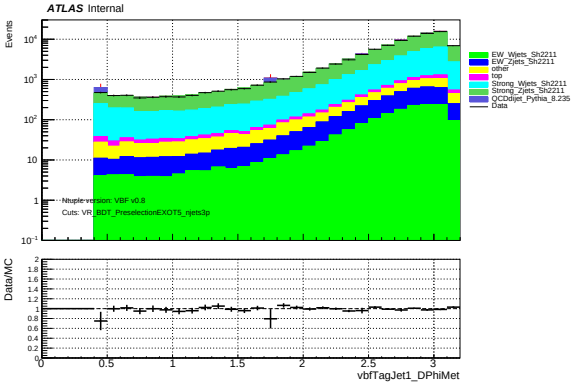

(c) $\Delta\phi(j_1,E_{\mathrm{T}}^{\mathrm{miss}})$

Figure 6.15: Preselection plots showing data and the predicted background of the input features to BDT for events with three or more jets for $\mathcal{L} = 140\,\mathrm{fb}^{-1}$ at $\sqrt{s} = 13$ TeV. Shown here specifically are the distributions for p_{T} (j,j), m_{eff}(jj,$E_{\mathrm{T}}^{\mathrm{miss}}$), and $\Delta\phi(j_1,E_{\mathrm{T}}^{\mathrm{miss}})$.

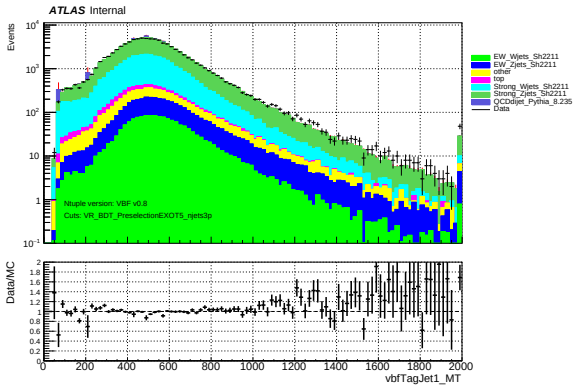

(a) $M_T(j_1,E_{\mathrm{T}}^{\mathrm{miss}})$ [GeV]

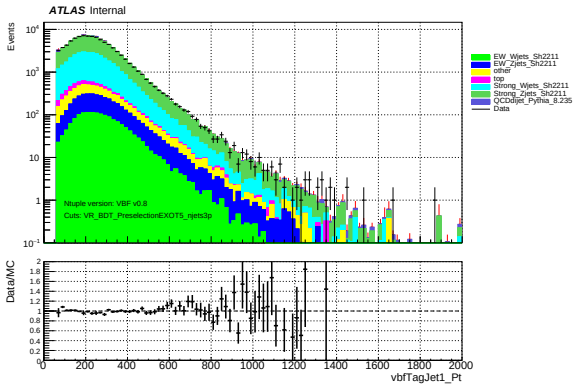

(b) $p_{\mathrm{T}}(\mathrm{j}_1)$ [GeV]

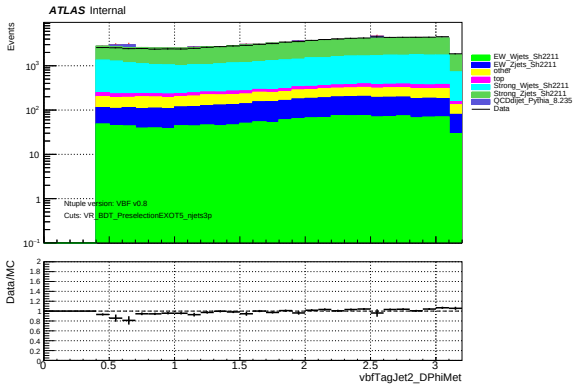

(c) $\Delta\phi(j_2,E_{\mathrm{T}}^{\mathrm{miss}})$

Figure 6.16: Preselection plots showing data and the predicted background of the input features to BDT for events with three or more jets for $\mathcal{L}$ = 140 fb^{-1} at $\sqrt{s}$ = 13 TeV. Shown here specifically are the distributions for $M_T(j_1,E_{\mathrm{T}}^{\mathrm{miss}})$, $p_{\mathrm{T}}(\mathrm{j}_1)$, and $\Delta\phi(j_2,E_{\mathrm{T}}^{\mathrm{miss}})$.

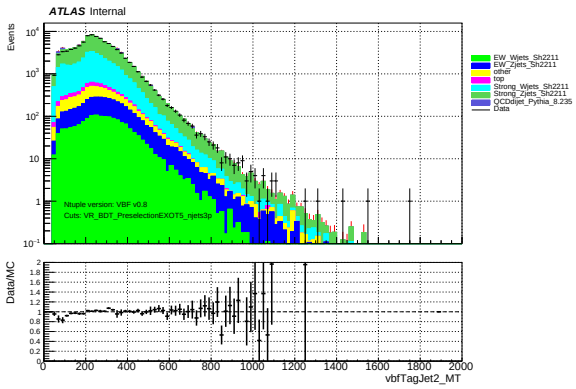

(a) $M_T(j_2,E_{\mathrm{T}}^{\mathrm{miss}})$ [GeV]

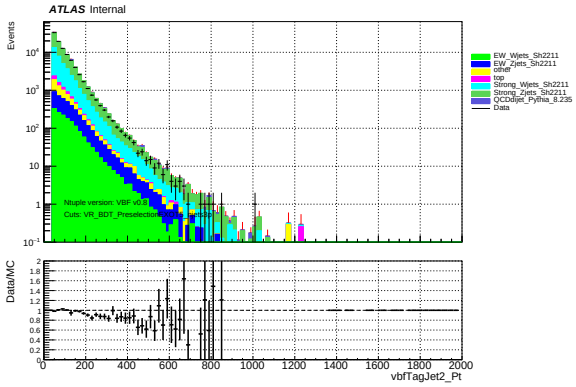

(b) $p_{\mathrm{T}}(\mathrm{j}_2)$ [GeV]

Figure 6.17: Preselection plots showing data and the predicted background of the input features to BDT for events with three or more jets for $\mathcal{L}$ = 140 fb^{-1} at $\sqrt{s}$ = 13 TeV. Shown here specifically are the distributions for $M_T(j_2,E_{\mathrm{T}}^{\mathrm{miss}})$ and $p_{\mathrm{T}}(\mathrm{j}_2)$.

6.3. Boosted Decision Tree

A boosted decision tree (BDT) algorithm is used to optimize the separation of the signal and background events. The LightGBM [85] framework is used for setting up the BDT model. The model is trained for binary classification that outputs a score for each event ranging from 0 (background-like) to 1 (signal-like). The k-fold cross-validation technique is used with k=5 folds such that five separate BDT models are constructed. For each BDT, k-2=3 folds are used for the training. One fold is used as a validation set for the purposes of early stopping and model selection during the optimization of the BDT weights. The last fold is then used as the test set for evaluating the performance of the model. Each BDT is trained, validated, and tested with a distinct combination of the folds as shown in Figure 6.18. The splitting of the input data into the 5 folds is done on the basis of the event number such that the BDT model to be used for the evaluation is determined as (Event number mod 5) + 1. Thus the final BDT scores are evaluated based on the BDT model for which that event was not used in the training or the validation. A hyperparameter optimization was done, testing around 100 different configurations of the BDT setup. In this optimization also the k-fold approach was used and the performance in the test folds was averaged to compare the various configurations. Information on the training of the latest version of the BDT model, referred to as "Mjj600_NoNeg_FixedQCD_Best_retrain1", is described in the following:

- The input signal sample used in the training consists of a combination of the grid points with $m(\tilde{\chi}_2^0, \tilde{\chi}_1^\pm) = 100$ GeV. To account for this inclusion of multiple signal points in the training, the signal sample weights are scaled during the training such that the total weight of all signals will equal the total weight of all background samples.

- For the input background samples, all backgrounds are included with the exception of the QCD Monte Carlo due to the very limited statistics of the sample. Additionally, QCD multijet is expected to be a minor background and it was determined that excluding it would not significantly change the performance of the BDT.
- Hyperparameters:
  - minimal number of data in one leaf 'min_child_samples' : 50,
  - minimal sum hessian in one leaf 'min_child_weight' : 100,
  - number of boosting iterations 'n_estimators' : 1500,
  - limit of the max depth for tree model 'max_depth' : 5,
  - learning rate for each tree 'learning_rate' : 0.1,
  - max number of leaves in a tree 'num_leaves' : 8,
  - max number of bins that feature values will be bucketed in 'max_bin' : 255,
  - percentage of features randomly selected at each tree node 'feature_fraction_bynode' : 0.7,
  - minimal number of data inside one bin 'min_data_in_bin' : 100,
  - L1 regularization parameter 'reg_alpha' : 0,
  - L2 regularization parameter 'reg_lambda' : 1,
- Input variables (the associated variable names used in figures are given in square brackets):
  - Transverse momentum p_{T} of the two VBF-tagged jets $p_{\mathrm{T}}(\mathrm{j}_1)$ [vbfTagJet1_Pt] and $p_{\mathrm{T}}(\mathrm{j}_2)$ [vbfTagJet2_Pt], and the p_{T} of the dijet system p_{T} (j,j) [vbfjjPt]

– Missing transverse energy $E_{\mathrm{T}}^{\mathrm{miss}}$ [effMET]

– Dijet invariant mass of the VBF-tagged jets m_{jj} [vbfjjM]

– Individual and sum of transverse mass of VBF-tagged jets with $E_{\mathrm{T}}^{\mathrm{miss}}$: $M_T(j_1,E_{\mathrm{T}}^{\mathrm{miss}})$ [vbfTagJet1_MT_effMET], $M_T(j_2,E_{\mathrm{T}}^{\mathrm{miss}})$ [vbfTagJet2_MT_effMET], $M_T(j_1,E_{\mathrm{T}}^{\mathrm{miss}})$+$M_T(j_2,E_{\mathrm{T}}^{\mathrm{miss}})$ [sumVBFJet_MT_effMET]

– Azimuthal angle difference $\Delta\phi$ between the VBF-tagged jets and between the VBF-tagged jets and $E_{\mathrm{T}}^{\mathrm{miss}}$: $\Delta\phi(j_1,j_2)$ [vbfjjDPhi], $\Delta\phi(j_1,E_{\mathrm{T}}^{\mathrm{miss}})$ [vbfTagJet1_DPhi_effMET], $\Delta\phi(j_2,E_{\mathrm{T}}^{\mathrm{miss}})$ [vbfTagJet2_DPhi_effMET], $\Delta\phi(jj,E_{\mathrm{T}}^{\mathrm{miss}})$ [vbfjj_dphi_effMET]; additionally the absolute difference $|\Delta\phi(j_1,E_{\mathrm{T}}^{\mathrm{miss}})$ - $\Delta\phi(j_2,E_{\mathrm{T}}^{\mathrm{miss}})|$ [vbf_delta_dphi_effMET]

– Angular separation between the VBF-tagged jets ΔR_{jj} [vbfjjDR]

– Scalar sum of p_{T} of VBF-tagged jets $H_T^{(VBF)}$ [HTVBF] along with its ratio compared to $E_{\mathrm{T}}^{\mathrm{miss}}$ ($H_T^{(VBF)}$ / $E_{\mathrm{T}}^{\mathrm{miss}}$) [HTVBFOver_effMET]

– Separation in pseudorapidity of the VBF-tagged jets $|\Delta\eta_{\mathrm{jj}}|$ [vbfjjDEta]

– min($\Delta\phi(j, E_{\mathrm{T}}^{\mathrm{miss}})$) [minDPhiAllJets_effMET], the minimum azimuthal difference between any jet with p_{T} > 30 GeV and the $E_{\mathrm{T}}^{\mathrm{miss}}$

– Relative effective mass m_{eff}(jj,$E_{\mathrm{T}}^{\mathrm{miss}}$) [vbf_meff_rel_effMET] of VBF-tagged jets with $E_{\mathrm{T}}^{\mathrm{miss}}$ (defined as m_{jj}/1430 + $E_{\mathrm{T}}^{\mathrm{miss}}$/320) *

– Transverse mass M_T(jetY,$E_{\mathrm{T}}^{\mathrm{miss}}$) [jetY_MT_effMET] and $\Delta\phi$(jetY,$E_{\mathrm{T}}^{\mathrm{miss}}$) [jetY_DPhi_effMET] for $E_{\mathrm{T}}^{\mathrm{miss}}$ with the jet that

*These "normalizing" values were derived based on the average value of those variables in the backgrounds (without multijet) at preselection level

has the minimum $\Delta\phi(j, E_{\mathrm{T}}^{\mathrm{miss}})$ (referred to as "jet Y")

– Transverse mass M_T(jetZ,$E_{\mathrm{T}}^{\mathrm{miss}}$) [jetZ_MT_effMET] and $\Delta\phi$(jetZ,$E_{\mathrm{T}}^{\mathrm{miss}}$) [jetZ_DPhi_effMET] for $E_{\mathrm{T}}^{\mathrm{miss}}$ with the jet that has the minimum $M_T(j, E_{\mathrm{T}}^{\mathrm{miss}})$ - 80 GeV (referred to as "jet Z")

- Preselection cuts: $E_{\mathrm{T}}^{\mathrm{miss}}$ > 250 GeV and passing the $E_{\mathrm{T}}^{\mathrm{miss}}$ trigger, zero leptons, min($\Delta\phi(j, E_{\mathrm{T}}^{\mathrm{miss}})$) > 0.4, b-tagged jet veto

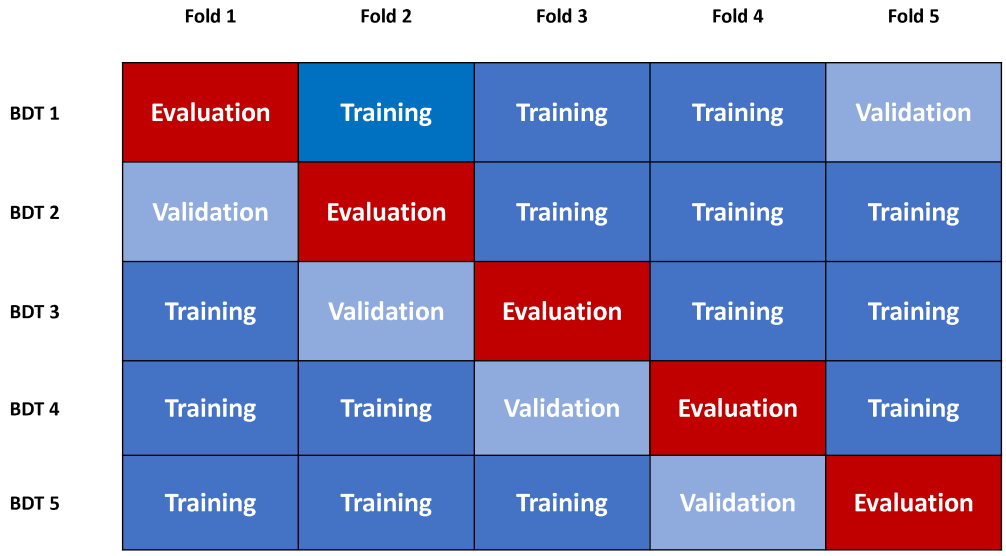

Figure 6.18: Visualization of the splitting of the input data into train, validation, and test sets for each of the five BDT models in the k-fold cross validation.

Comparisons of the BDT score distribution between the train and test data sets are shown in Figure 6.19 for each BDT model and in general good agreement is found. There is no clear part of the BDT score spectrum in which the signal distribution can be clearly distinguished from the background distribution, and is indicative of the challenges in separating the signal from the background. Receiver operating characteristic (ROC) curves are shown in Figure 6.20 for each model, and it can be seen that the performance on both train and test sets are similar with the area

under curve (AUC) being between 0.73 to 0.74 in all instances. A ranking of the input features based on importance is shown in Figure 6.21 for each model. The two highest ranking features for all models are found to be vbfjjDEta ($|\Delta\eta_{jj}|$) and vbfTagJet2_Pt (sub-leading VBF-tagged jet p_T). The SHAP (SHapley Additive exPlanations) [90] values in Figure 6.22 show a visualization for the impact of the input features on the output for each BDT model. Each point in the beeswarm plots represents a distinct event and the distribution of points along the y-axis indicates the density of events. The color of the points reflects the value of the feature and the position of the point on the x-axis shows how the particular feature value is correlated to the model's output. Thus we can see that high values for $|\Delta\eta_{jj}|$ and $p_T(j_2)$ tend to have a positive impact on the BDT output while high values for $H_T^{(VBF)}$ / E_T^{miss} and $p_T(j_1)$ have the opposite effect.

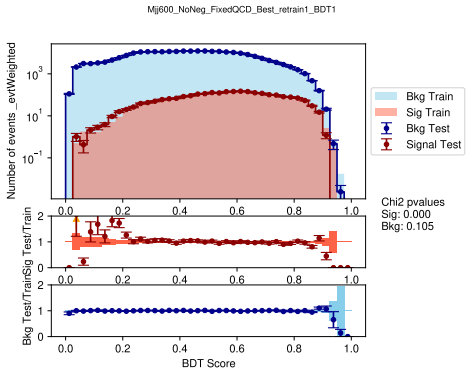

(a) BDT 1

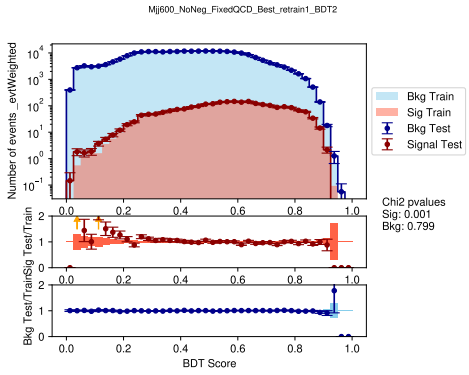

(b) BDT 2

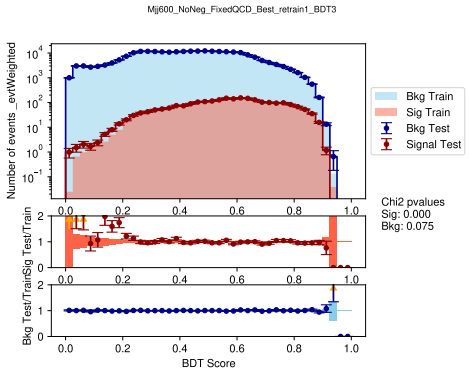

(c) BDT 3

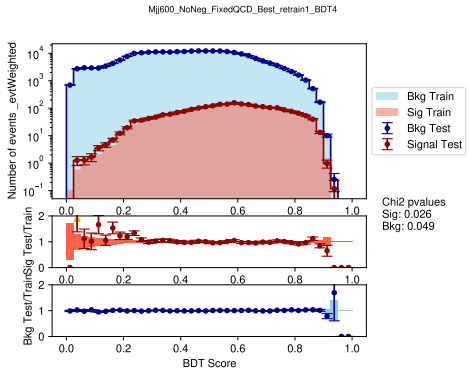

(d) BDT 4

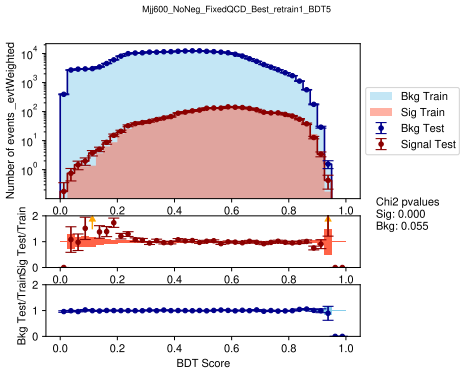

(e) BDT 5

Figure 6.19: BDT score distributions of the train and test data sets for each BDT model.

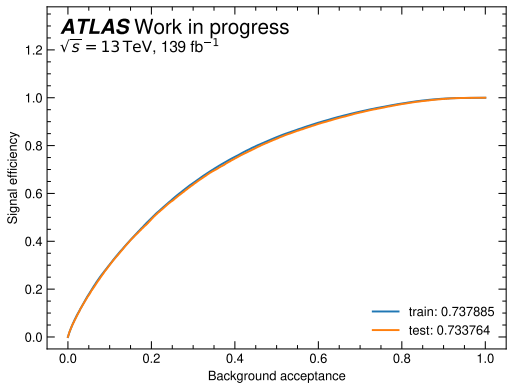

(a) BDT 1

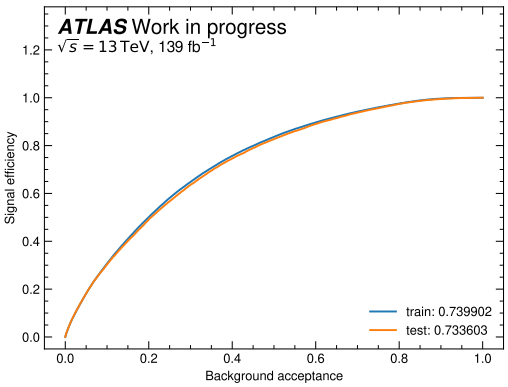

(b) BDT 2

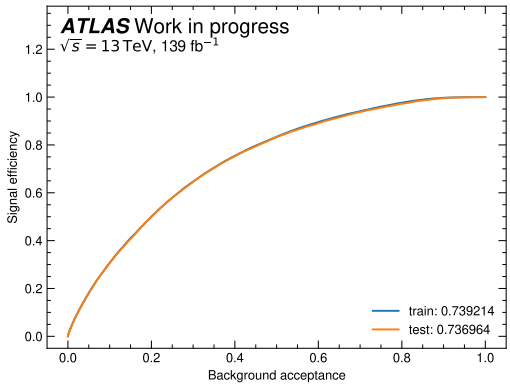

(c) BDT 3

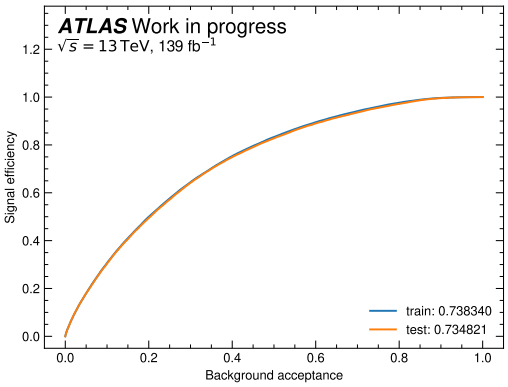

(d) BDT 4

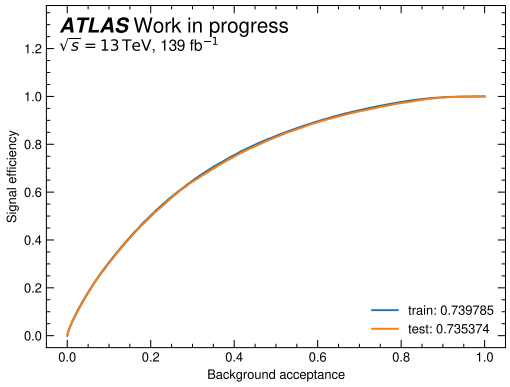

(e) BDT 5

Figure 6.20: ROC curves of train and test data sets for each BDT model with AUC provided in the legend.

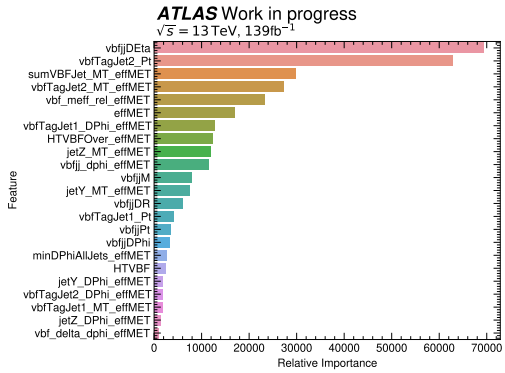

(a) BDT 1

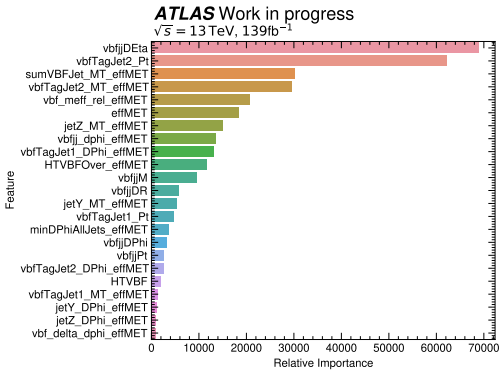

(b) BDT 2

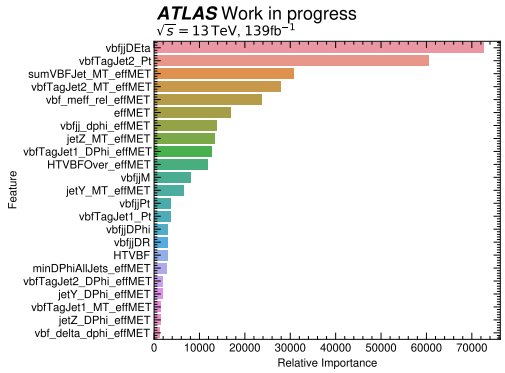

(c) BDT 3

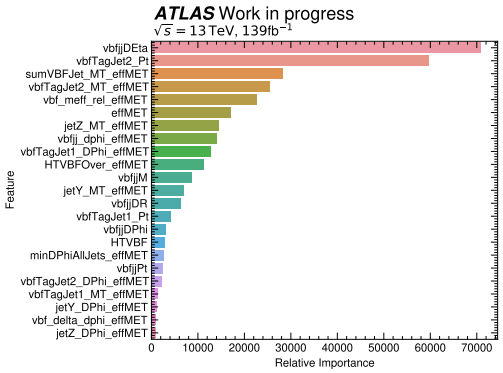

(d) BDT 4

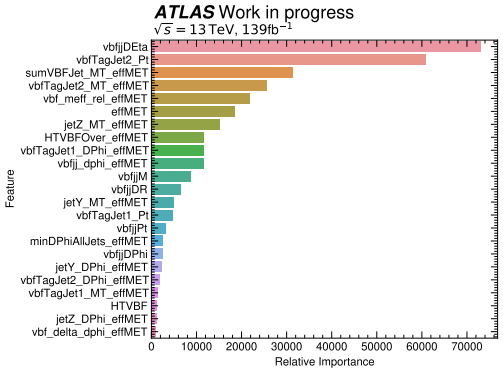

(e) BDT 5

Figure 6.21: Ranking of feature importance for each BDT model.

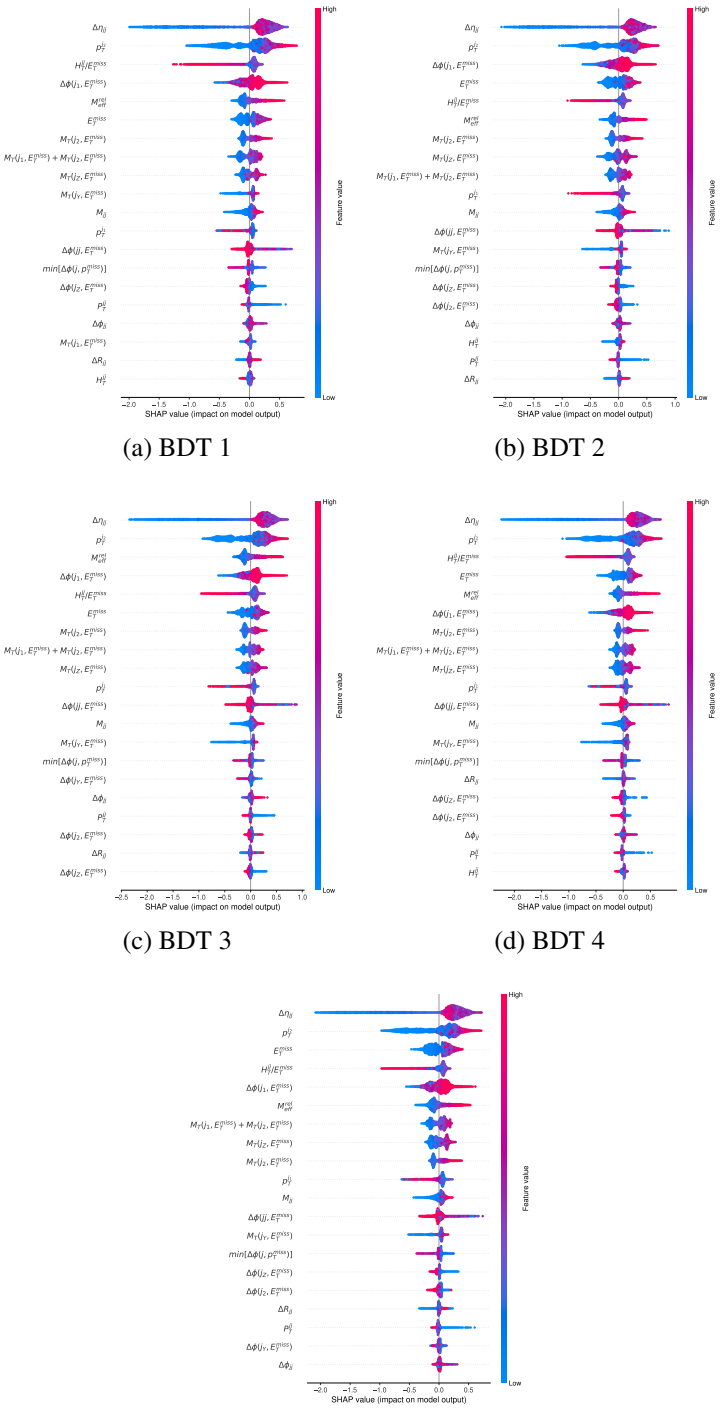

(a) BDT 1

(b) BDT 2

(c) BDT 3

(d) BDT 4

(e) BDT 5

Figure 6.22: Beeswarm plots showing SHAP values of input features for each BDT model.

6.4. Signal Regions

After imposing these requirements of the preselection, the signal region (SR) is constructed by binning the region based on the BDT scores evaluated from the model described in the previous section. In particular, 8 bins are used that range between 0.6 and 0.92 in the BDT score. All bins have the same width of 0.04 except the last BDT score bin that acts as an overflow bin. This specific binning of the BDT score distribution was selected to optimize the expected sensitivity while avoiding significant constraints on nuisance parameters that would arise from using a finer binning. Uniform bin widths were chosen to simplify the implementation of these regions when constructing the statistical model in addition to the fact that no significant improvement in the expected sensitivity was found when adopting non-uniform widths.

Furthermore, the signal region definition is split into two separate regions based on the jet multiplicity. There is one region for events with exactly two jets (corresponding to the two required VBF-tagged jets) and another region requiring three or more jets. These are referred to as SR_VBF_njets2 and SR_VBF_njets3p respectively. There are several reasons for splitting the regions based on the number of jets in the event. The primary reason is in regards to the background modeling in which there is a clear difference between the V + jets background normalizations derived from events with two jets compared to those with three or more. This will be described in further detail when discussing the background estimation. Secondly, the scale variations for the V + jets backgrounds also differ visibly in magnitude between the 2 and 3+ jet events. Because of this difference, when the region is defined inclusively in the number of jets the scale variations have a very large impact on the overall sensitivity. There is also an additional benefit of a small boost in sensitivity to the signal for

the setup with regions split based on the number jets compared to the single region setup. A plot comparing the signal and background based on the jet multiplicity after including the signal region cuts is shown in Figure 6.23. It can be seen that the signal-to-background ratio is relatively flat as a function of the number of jets, so there should not be a significant improvement in the sensitivity from attempting to split the regions further based on the jet multiplicity. Another reason to avoid splitting the regions further based on the number of jets is that the signal process is generated with only two jets at the matrix element level. Thus to minimize potential issues related to the modeling of the jet multiplicity, the splitting of the regions is restricted to just the 2 and 3+ jet cases for the reasons already described above.

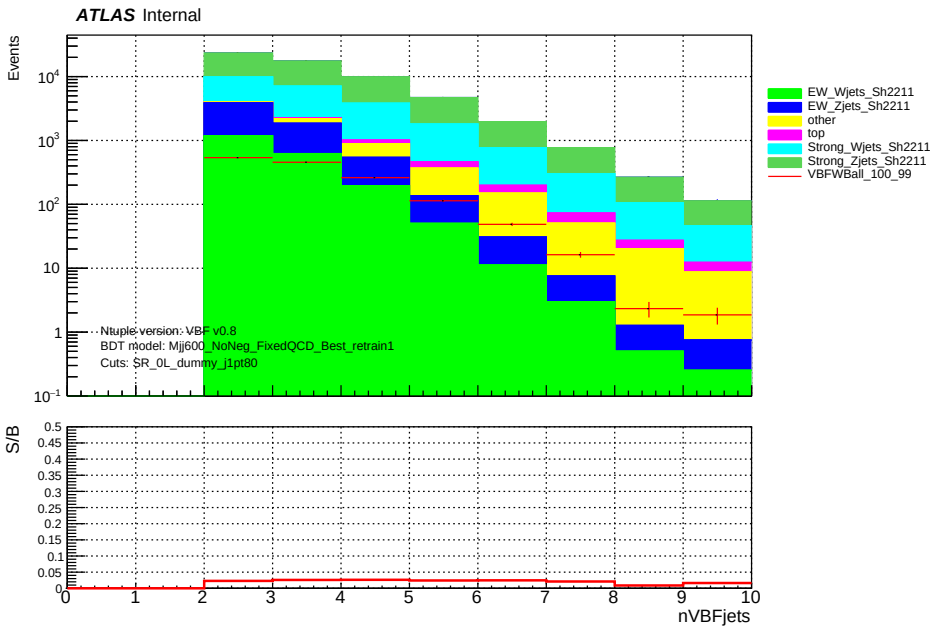

Figure 6.23: Comparison of the jet multiplicity for the signal and background after applying the signal region selection for $\mathcal{L} = 140$ fb^{-1} at $\sqrt{s} = 13$ TeV.

The pre-fit BDT score distributions in Figures 6.24 and 6.25 show both a finely binned version with the signal region selection and then the distribution with the actual binning used in the signal regions SR_VBF_njets2 and SR_VBF_njets3p. It

can be seen that the signal-to-background ratio approaches at most 15% for very high BDT scores but that for the majority of the distribution it is around a few percent. More pre-fit signal region distributions for other key observables that were used as inputs for the BDT are shown in Figures 6.26–6.33 for SR_VBF_njets2. Those for SR_VBF_njets3p are shown in Figures 6.34–6.41. From an inspection of these various figures, there are no obvious cuts that could be additionally imposed on the input features that would lead to a significant improvement in the separation of the signal and background. The BDT score appears to provide the best sensitivity in terms of the signal-to-background ratio across its distribution and this reinforces using it to define the binning of the analysis regions.

The dominant backgrounds in the signal regions come from the $W+$jets and $Z+$jets backgrounds which are constrained by dedicated control regions. These will be described in further detail when discussing the strategy for the background estimation. Validation regions are also defined to assess the reliability of the background estimations based on the control regions and will also be described. The signal regions and all control regions are included in a simultaneous binned likelihood fit in order to set exclusion limits on the signal model.

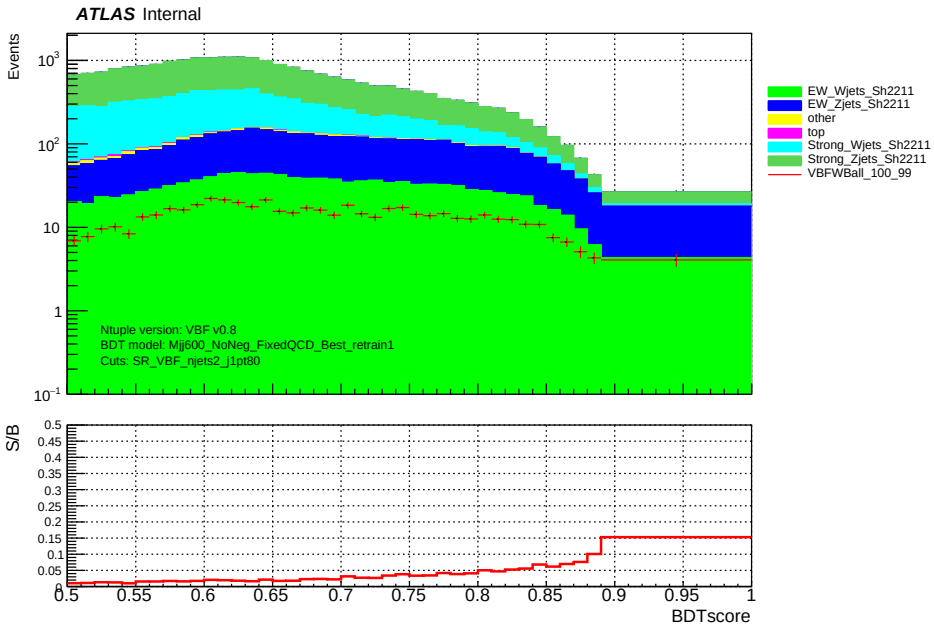

(a) SR_VBF_njets2 (fine binning)

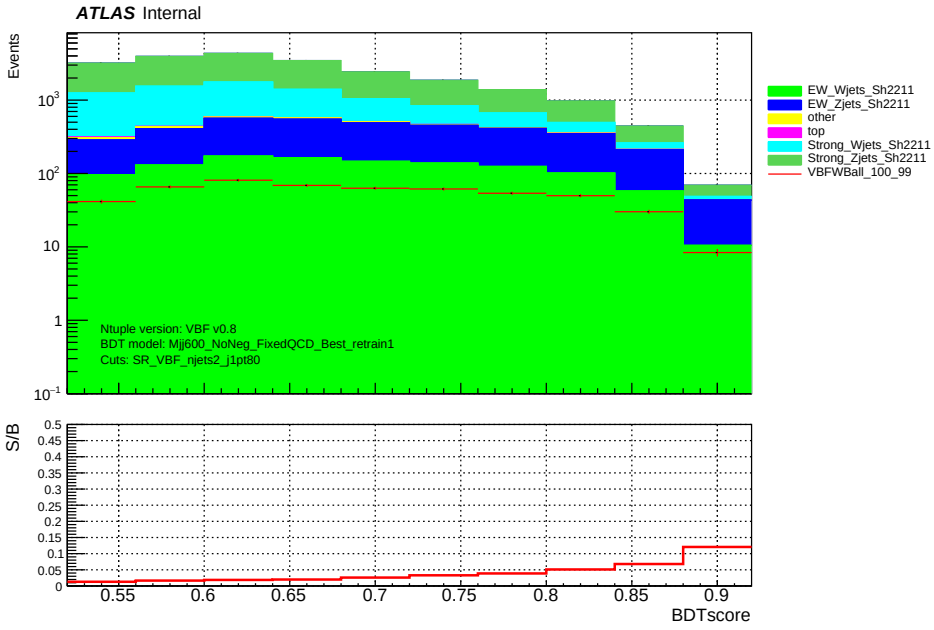

(b) SR_VBF_njets2 (actual binning)

Figure 6.24: Pre-fit distributions of the BDT score in SR_VBF_njets2 for $\mathcal{L}$ = 140 fb^{-1} at $\sqrt{s}$ = 13 TeV.

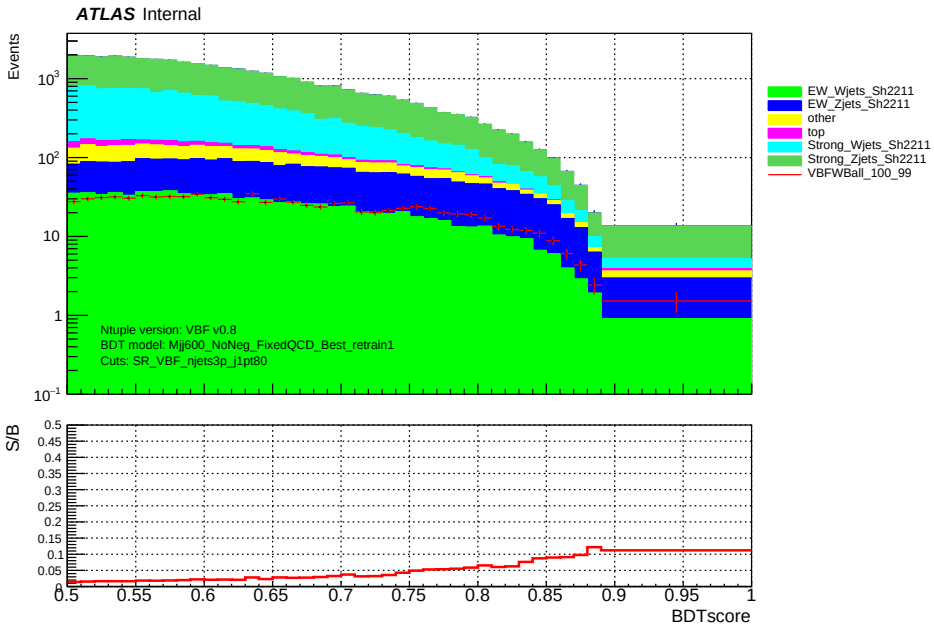

(a) SR_VBF_njets3p (fine binning)

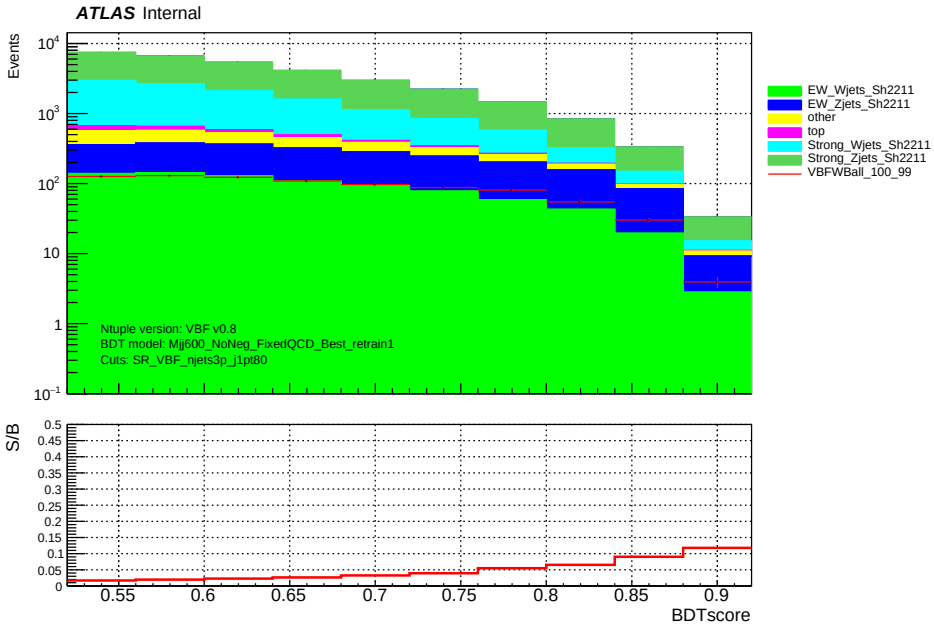

(b) SR_VBF_njets3p (actual binning)

Figure 6.25: Pre-fit distributions of the BDT score in SR_VBF_njets3p for $\mathcal{L}$ = 140 fb^{-1} at $\sqrt{s}$ = 13 TeV.

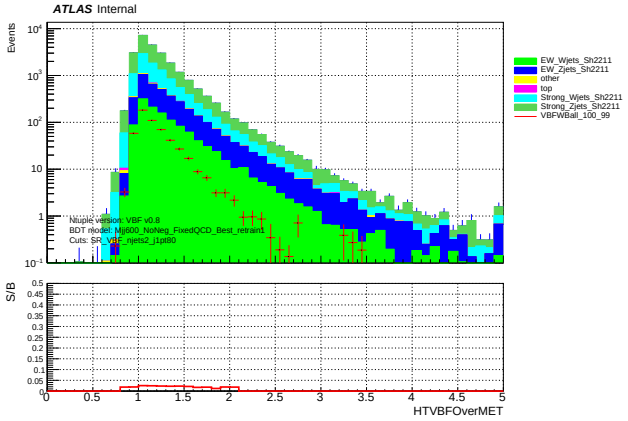

(a) $H_T^{(VBF)}$ / $E_{\mathrm{T}}^{\mathrm{miss}}$

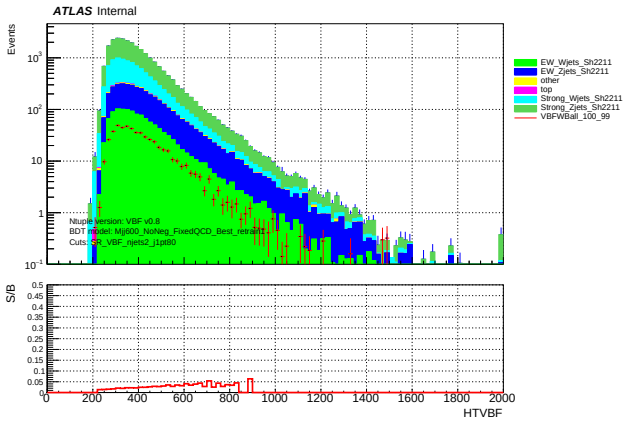

(b) $H_T^{(VBF)}$ [GeV]

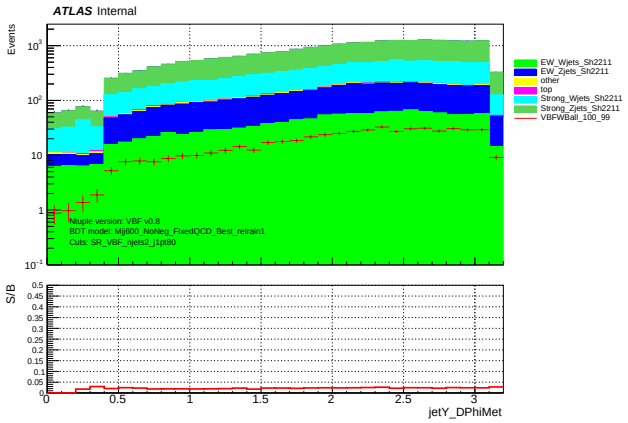

(c) $\Delta\phi$(jetY,$E_{\mathrm{T}}^{\mathrm{miss}}$)

Figure 6.26: Pre-fit distributions in the signal region SR_VBF_njets2 for key observables for $\mathcal{L}$ = 140 fb^{-1} at $\sqrt{s}$ = 13 TeV. Shown here specifically are the distributions for $H_T^{(VBF)}$ / $E_{\mathrm{T}}^{\mathrm{miss}}$, $H_T^{(VBF)}$, and $\Delta\phi$(jetY,$E_{\mathrm{T}}^{\mathrm{miss}}$).

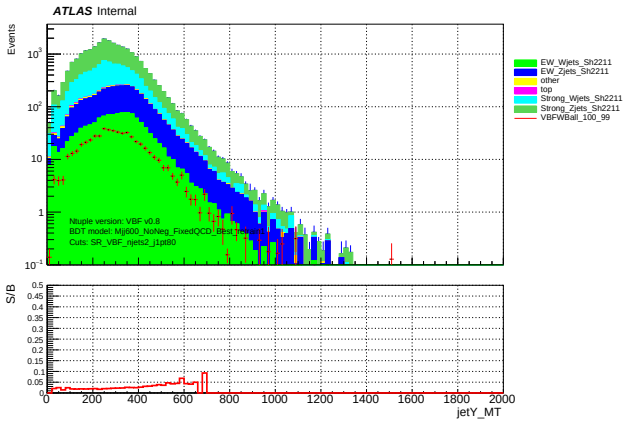

(a) M_T(jetY,$E_{\mathrm{T}}^{\mathrm{miss}}$) [GeV]

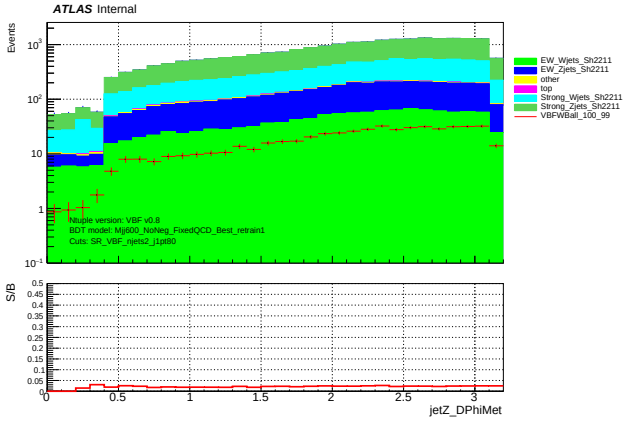

(b) $\Delta\phi$(jetZ,$E_{\mathrm{T}}^{\mathrm{miss}}$)

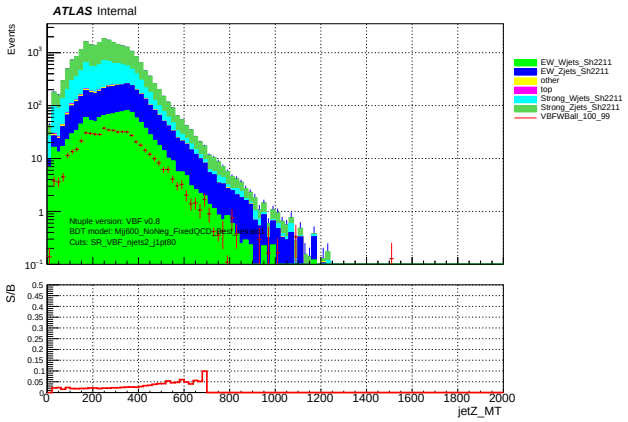

(c) M_T(jetZ,$E_{\mathrm{T}}^{\mathrm{miss}}$) [GeV]

Figure 6.27: Pre-fit distributions in the signal region SR_VBF_njets2 for key observables for $\mathcal{L}$ = 140 fb^{-1} at $\sqrt{s}$ = 13 TeV. Shown here specifically are the distributions for M_T(jetY,$E_{\mathrm{T}}^{\mathrm{miss}}$), $\Delta\phi$(jetZ,$E_{\mathrm{T}}^{\mathrm{miss}}$), and M_T(jetZ,$E_{\mathrm{T}}^{\mathrm{miss}}$).

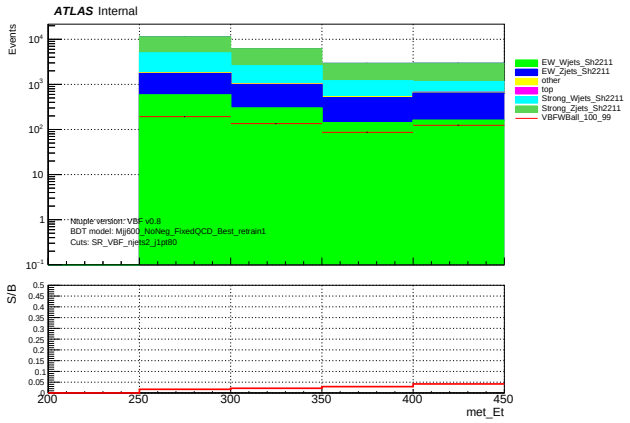

(a) $E_{\mathrm{T}}^{\mathrm{miss}}$ [GeV]

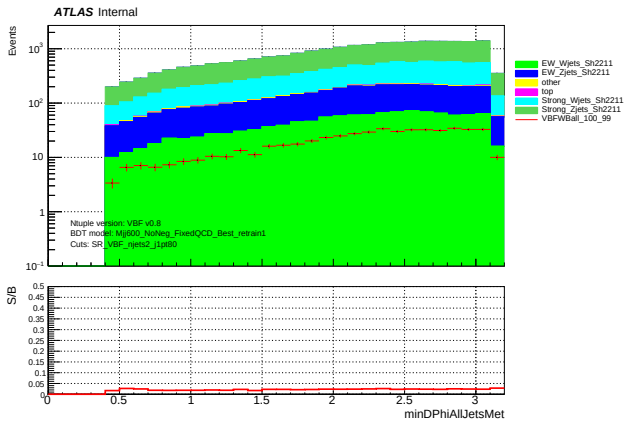

(b) $\min(\Delta\phi(j, E_{\mathrm{T}}^{\mathrm{miss}}))$

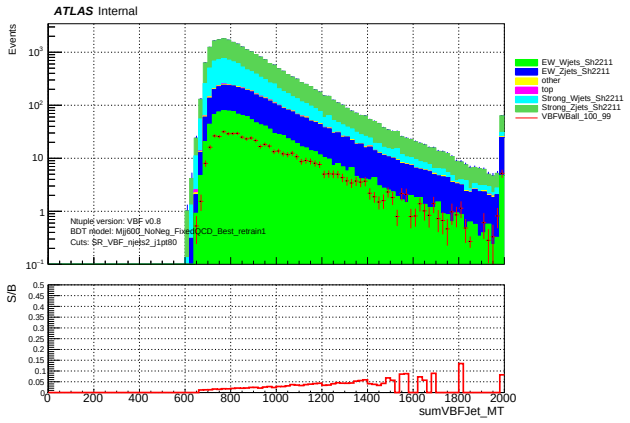

(c) $M_T(j_1,E_{\mathrm{T}}^{\mathrm{miss}})+M_T(j_2,E_{\mathrm{T}}^{\mathrm{miss}})$ [GeV]

Figure 6.28: Pre-fit distributions in the signal region SR_VBF_njets2 for key observables for $\mathcal{L} = 140\,\mathrm{fb}^{-1}$ at $\sqrt{s} = 13$ TeV. Shown here specifically are the distributions for $E_{\mathrm{T}}^{\mathrm{miss}}$, $\min(\Delta\phi(j, E_{\mathrm{T}}^{\mathrm{miss}}))$, and $M_T(j_1,E_{\mathrm{T}}^{\mathrm{miss}})+M_T(j_2,E_{\mathrm{T}}^{\mathrm{miss}})$.

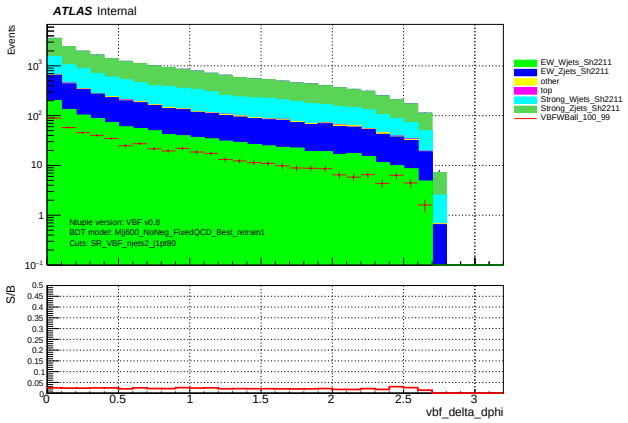

(a) $|\Delta\phi(j_1,E_{\mathrm{T}}^{\mathrm{miss}})$ - $\Delta\phi(j_2,E_{\mathrm{T}}^{\mathrm{miss}})|$

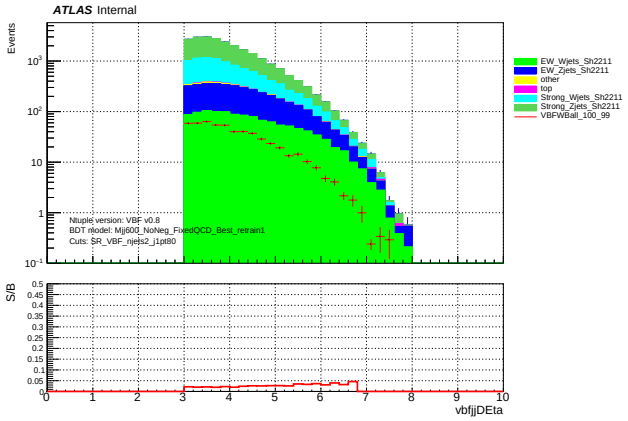

(b) $|\Delta\eta_{\mathrm{jj}}|$

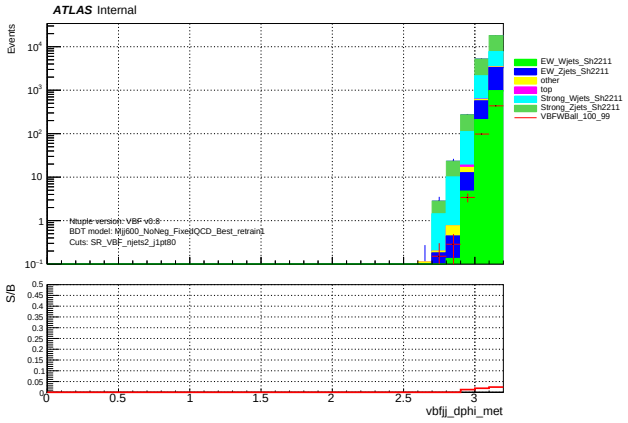

(c) $\Delta\phi(jj,E_{\mathrm{T}}^{\mathrm{miss}})$

Figure 6.29: Pre-fit distributions in the signal region SR_VBF_njets2 for key observables for $\mathcal{L}$ = 140 fb^{-1} at $\sqrt{s}$ = 13 TeV. Shown here specifically are the distributions for $|\Delta\phi(j_1,E_{\mathrm{T}}^{\mathrm{miss}})$ - $\Delta\phi(j_2,E_{\mathrm{T}}^{\mathrm{miss}})|$, $|\Delta\eta_{\mathrm{jj}}|$, and $\Delta\phi(jj,E_{\mathrm{T}}^{\mathrm{miss}})$.

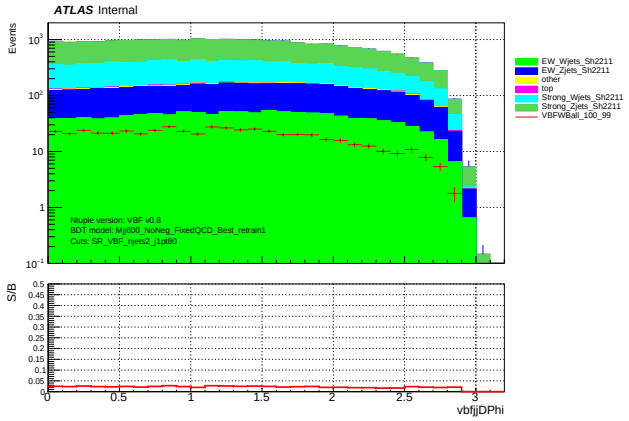

(a) $\Delta\phi(j_1,j_2)$

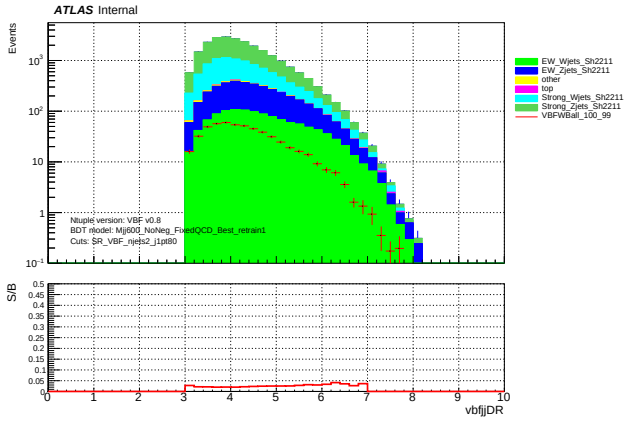

(b) ΔR_{jj}

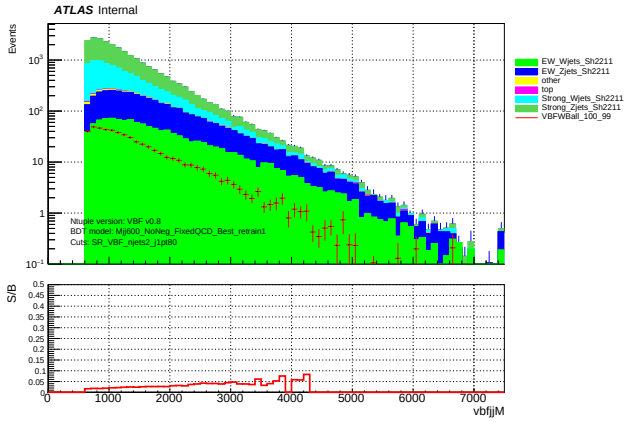

(c) m_{jj} [GeV]

Figure 6.30: Pre-fit distributions in the signal region SR_VBF_njets2 for key observables for $\mathcal{L} = 140$ fb^{-1} at $\sqrt{s} = 13$ TeV. Shown here specifically are the distributions for $\Delta\phi(j_1,j_2)$, ΔR_{jj}, and m_{jj}.

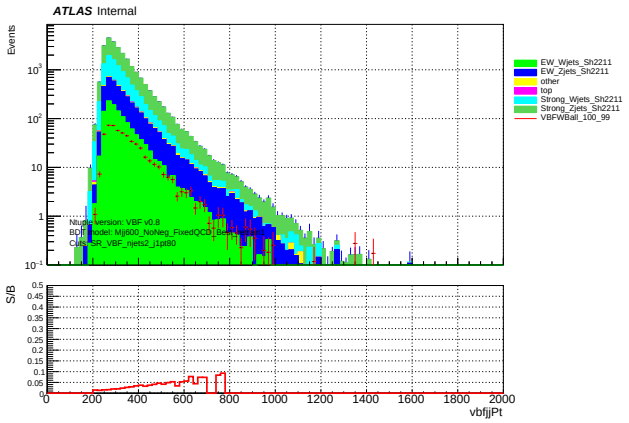

(a) p_{T} (j,j) [GeV]

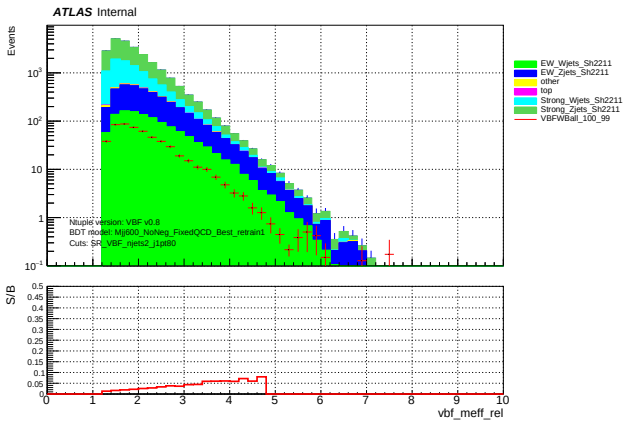

(b) m_{eff}(jj,$E_{\mathrm{T}}^{\mathrm{miss}}$)

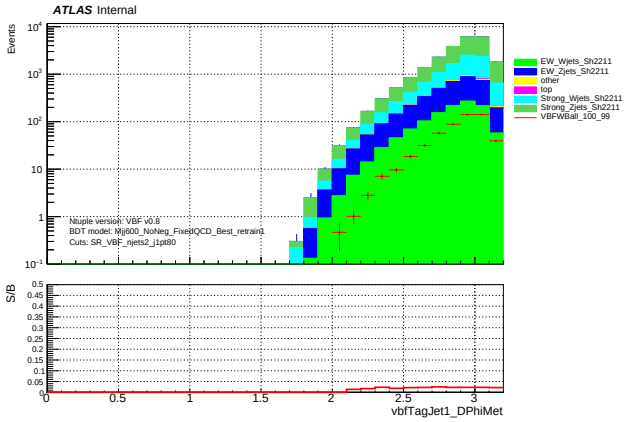

(c) $\Delta\phi(j_1,E_{\mathrm{T}}^{\mathrm{miss}})$

Figure 6.31: Pre-fit distributions in the signal region SR_VBF_njets2 for key observables for $\mathcal{L}$ = 140 fb^{-1} at $\sqrt{s}$ = 13 TeV. Shown here specifically are the distributions for p_{T} (j,j), m_{eff}(jj,$E_{\mathrm{T}}^{\mathrm{miss}}$), and $\Delta\phi(j_1,E_{\mathrm{T}}^{\mathrm{miss}})$.

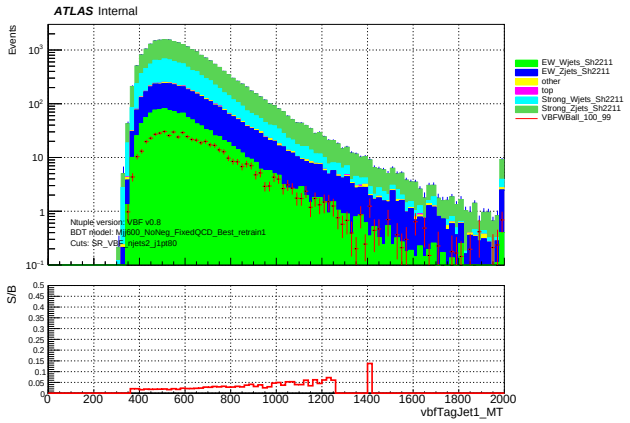

(a) $M_T(j_1,E_{\mathrm{T}}^{\mathrm{miss}})$ [GeV]

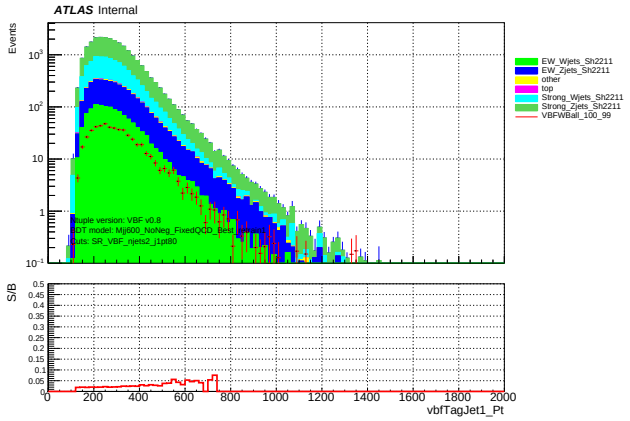

(b) $p_{\mathrm{T}}(\mathrm{j}_1)$ [GeV]

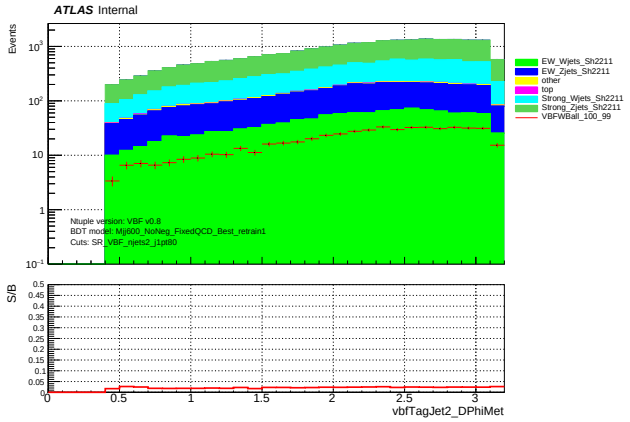

(c) $\Delta\phi(j_2,E_{\mathrm{T}}^{\mathrm{miss}})$

Figure 6.32: Pre-fit distributions in the signal region SR_VBF_njets2 for key observables for $\mathcal{L} = 140$ fb^{-1} at $\sqrt{s} = 13$ TeV. Shown here specifically are the distributions for $M_T(j_1,E_{\mathrm{T}}^{\mathrm{miss}})$, $p_{\mathrm{T}}(\mathrm{j}_1)$, and $\Delta\phi(j_2,E_{\mathrm{T}}^{\mathrm{miss}})$.

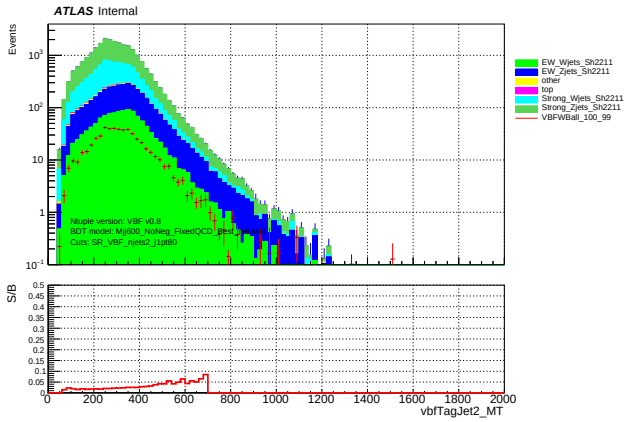

(a) $M_T(j_2,E_{\mathrm{T}}^{\mathrm{miss}})$ [GeV]

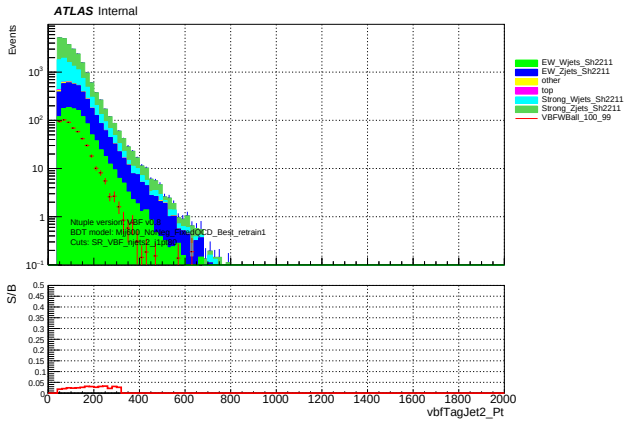

(b) $p_{\mathrm{T}}(\mathrm{j}_2)$ [GeV]

Figure 6.33: Pre-fit distributions in the signal region SR_VBF_njets2 for key observables for $\mathcal{L} = 140$ fb^{-1} at $\sqrt{s} = 13$ TeV. Shown here specifically are the distributions for $M_T(j_2,E_{\mathrm{T}}^{\mathrm{miss}})$ and $p_{\mathrm{T}}(\mathrm{j}_2)$.

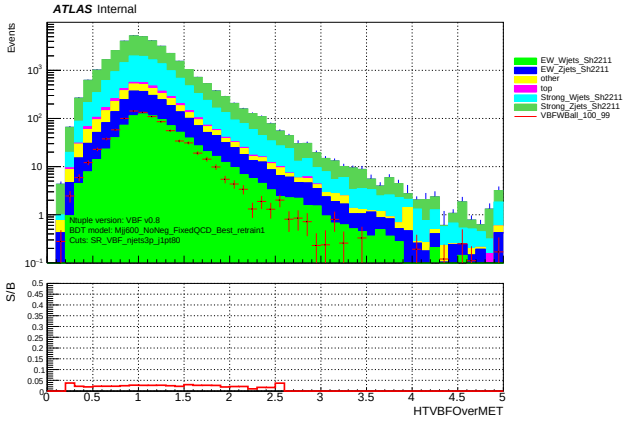

(a) $H_T^{(VBF)}$ / $E_{\mathrm{T}}^{\mathrm{miss}}$

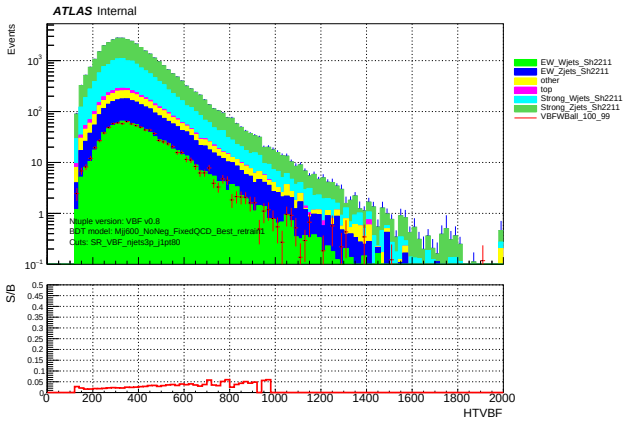

(b) $H_T^{(VBF)}$ [GeV]

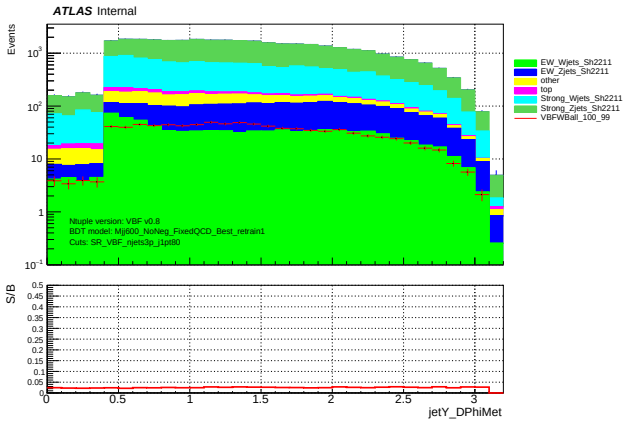

(c) $\Delta\phi$(jetY,$E_{\mathrm{T}}^{\mathrm{miss}}$)

Figure 6.34: Pre-fit distributions in the signal region SR_VBF_njets3p for key observables for $\mathcal{L}$ = 140 fb^{-1} at $\sqrt{s}$ = 13 TeV. Shown here specifically are the distributions for $H_T^{(VBF)}$ / $E_{\mathrm{T}}^{\mathrm{miss}}$, $H_T^{(VBF)}$, and $\Delta\phi$(jetY,$E_{\mathrm{T}}^{\mathrm{miss}}$).

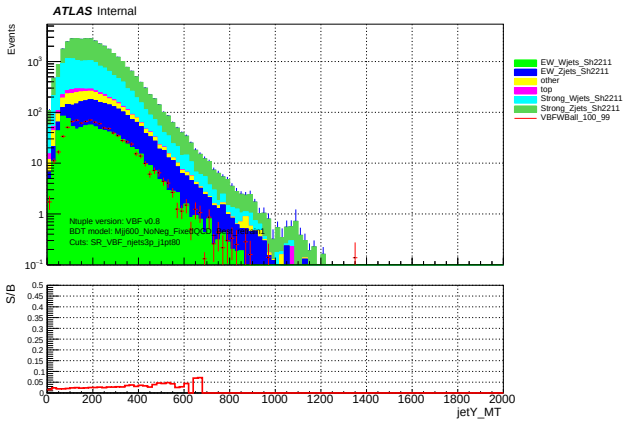

(a) M_T(jetY,$E_{\mathrm{T}}^{\mathrm{miss}}$) [GeV]

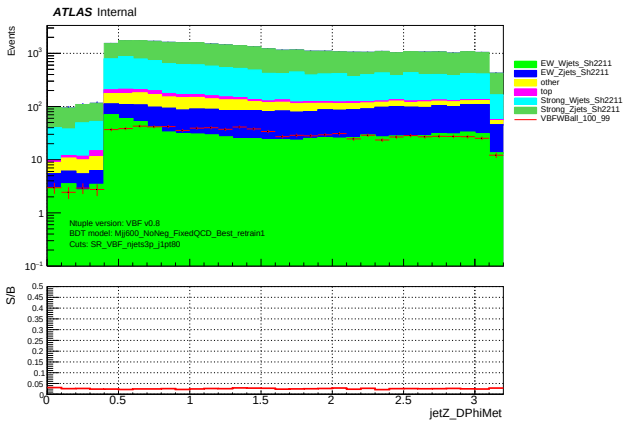

(b) $\Delta\phi$(jetZ,$E_{\mathrm{T}}^{\mathrm{miss}}$)

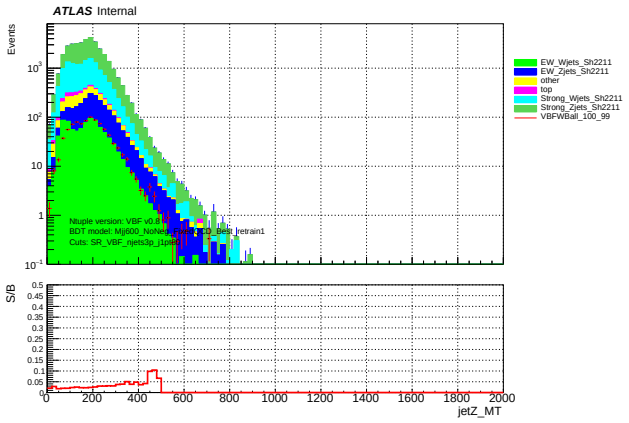

(c) M_T(jetZ,$E_{\mathrm{T}}^{\mathrm{miss}}$) [GeV]

Figure 6.35: Pre-fit distributions in the signal region SR_VBF_njets3p for key observables for $\mathcal{L} = 140\,\mathrm{fb}^{-1}$ at $\sqrt{s} = 13$ TeV. Shown here specifically are the distributions for M_T(jetY,$E_{\mathrm{T}}^{\mathrm{miss}}$), $\Delta\phi$(jetZ,$E_{\mathrm{T}}^{\mathrm{miss}}$), and M_T(jetZ,$E_{\mathrm{T}}^{\mathrm{miss}}$).

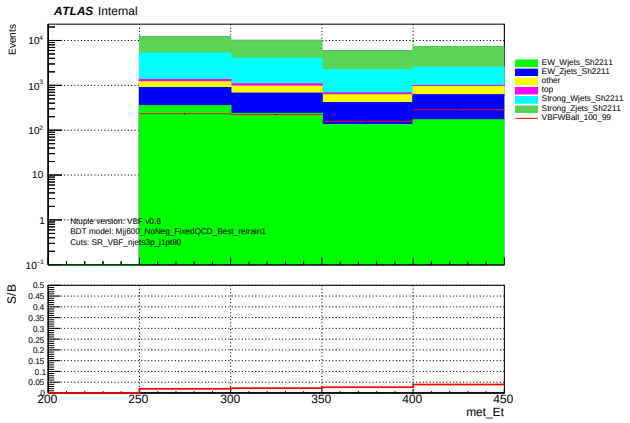

(a) $E_{\mathrm{T}}^{\mathrm{miss}}$ [GeV]

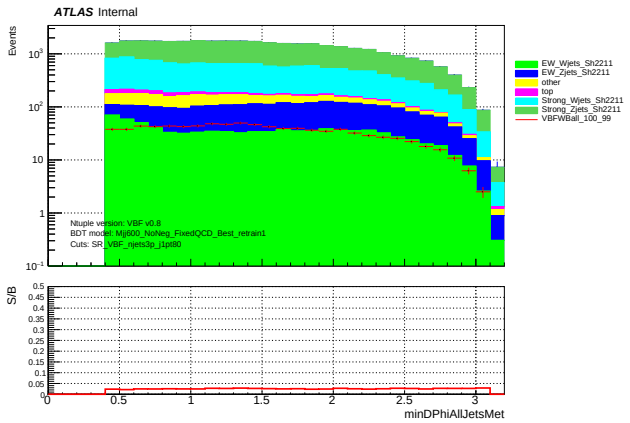

(b) $\min(\Delta\phi(j, E_{\mathrm{T}}^{\mathrm{miss}}))$

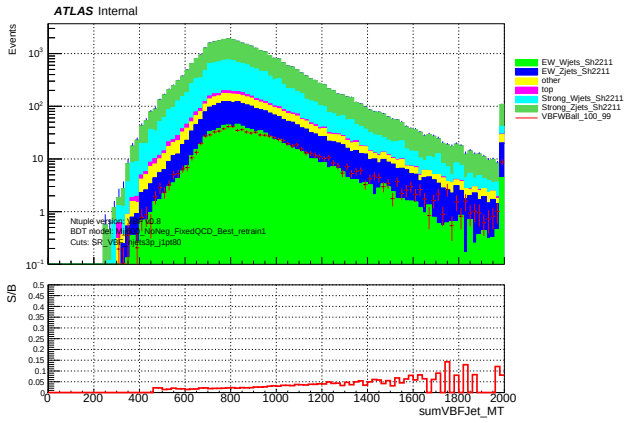

(c) $M_T(j_1,E_{\mathrm{T}}^{\mathrm{miss}})$+$M_T(j_2,E_{\mathrm{T}}^{\mathrm{miss}})$ [GeV]

Figure 6.36: Pre-fit distributions in the signal region SR_VBF_njets3p for key observables for $\mathcal{L} = 140\,\mathrm{fb}^{-1}$ at $\sqrt{s} = 13$ TeV. Shown here specifically are the distributions for $E_{\mathrm{T}}^{\mathrm{miss}}$, $\min(\Delta\phi(j, E_{\mathrm{T}}^{\mathrm{miss}}))$, and $M_T(j_1,E_{\mathrm{T}}^{\mathrm{miss}})$+$M_T(j_2,E_{\mathrm{T}}^{\mathrm{miss}})$.

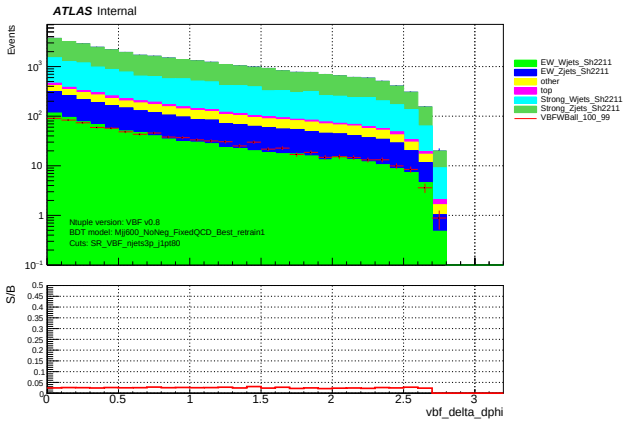

(a) $|\Delta\phi(j_1,E_{\mathrm{T}}^{\mathrm{miss}})$ - $\Delta\phi(j_2,E_{\mathrm{T}}^{\mathrm{miss}})|$

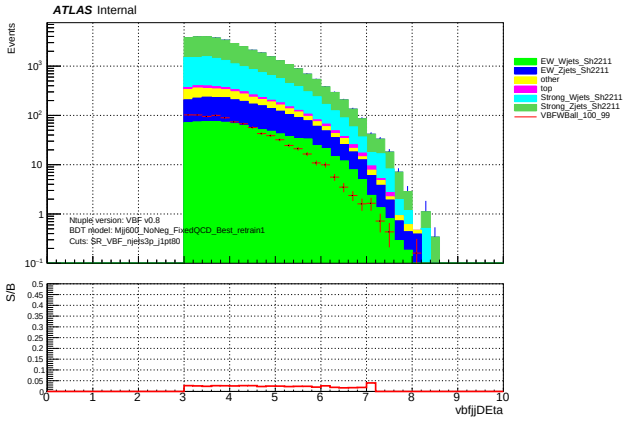

(b) $|\Delta\eta_{\mathrm{jj}}|$

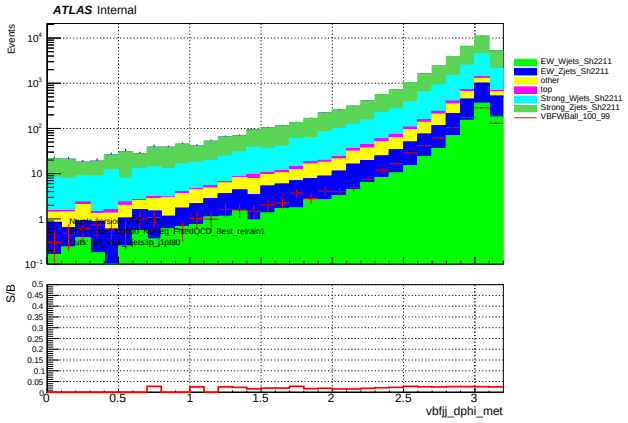

(c) $\Delta\phi(jj,E_{\mathrm{T}}^{\mathrm{miss}})$

Figure 6.37: Pre-fit distributions in the signal region SR_VBF_njets3p for key observables for $\mathcal{L} = 140\,\mathrm{fb}^{-1}$ at $\sqrt{s} = 13$ TeV. Shown here specifically are the distributions for $|\Delta\phi(j_1,E_{\mathrm{T}}^{\mathrm{miss}})$ - $\Delta\phi(j_2,E_{\mathrm{T}}^{\mathrm{miss}})|$, $|\Delta\eta_{\mathrm{jj}}|$, and $\Delta\phi(jj,E_{\mathrm{T}}^{\mathrm{miss}})$.

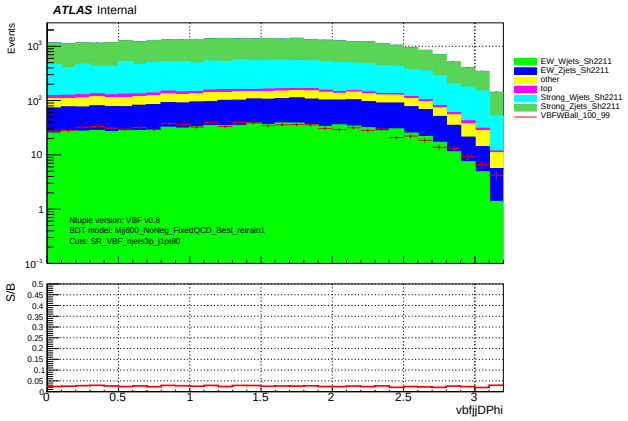

(a) $\Delta\phi(j_1,j_2)$

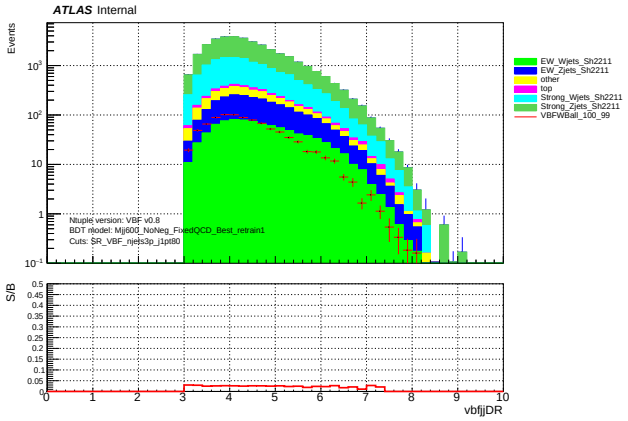

(b) ΔR_{jj}

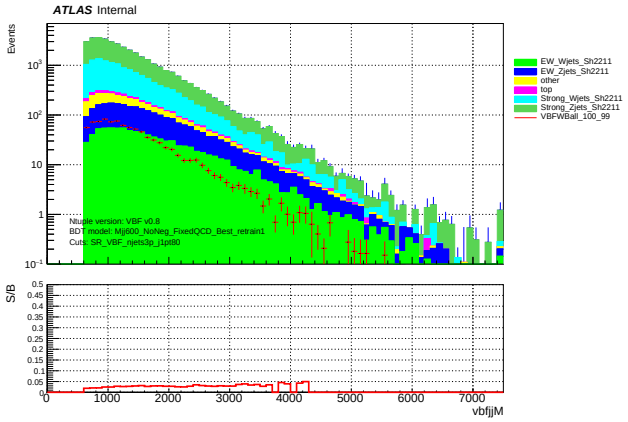

(c) m_{jj} [GeV]

Figure 6.38: Pre-fit distributions in the signal region SR_VBF_njets3p for key observables for $\mathcal{L} = 140$ fb^{-1} at $\sqrt{s} = 13$ TeV. Shown here specifically are the distributions for $\Delta\phi(j_1,j_2)$, ΔR_{jj}, and m_{jj}.

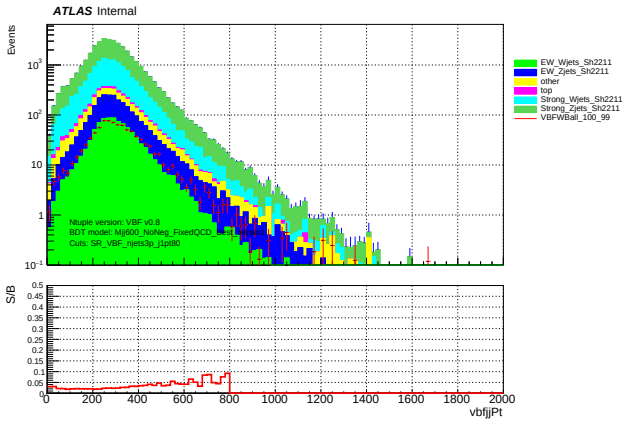

(a) p_{T} (j,j) [GeV]

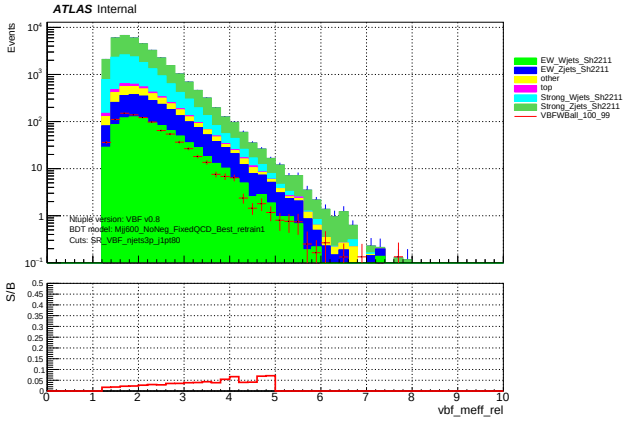

(b) m_{eff}(jj,$E_{\mathrm{T}}^{\mathrm{miss}}$)

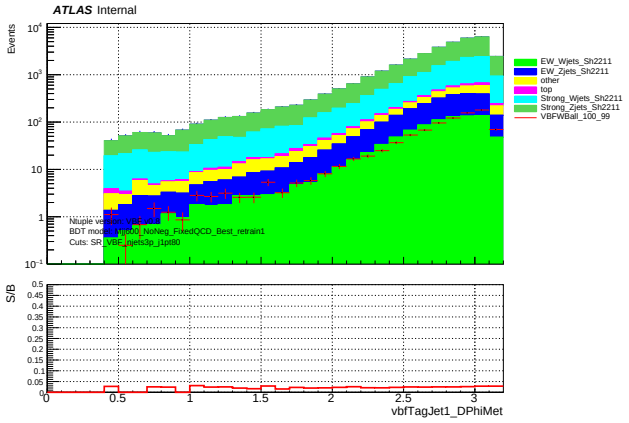

(c) $\Delta\phi(j_1,E_{\mathrm{T}}^{\mathrm{miss}})$

Figure 6.39: Pre-fit distributions in the signal region SR_VBF_njets3p for key observables for $\mathcal{L}$ = 140 fb^{-1} at $\sqrt{s}$ = 13 TeV. Shown here specifically are the distributions for p_{T} (j,j), m_{eff}(jj,$E_{\mathrm{T}}^{\mathrm{miss}}$), and $\Delta\phi(j_1,E_{\mathrm{T}}^{\mathrm{miss}})$.

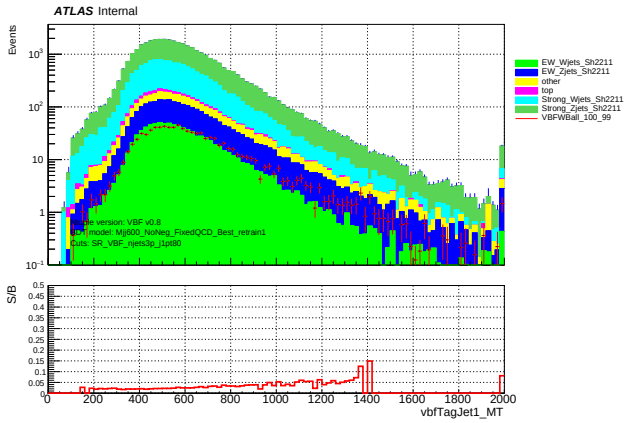

(a) $M_T(j_1,E_{\mathrm{T}}^{\mathrm{miss}})$ [GeV]

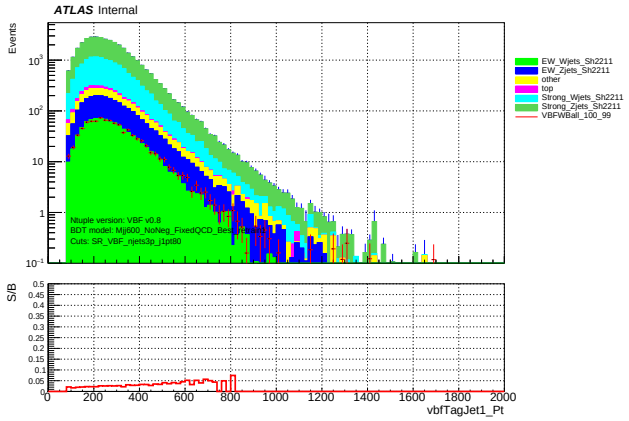

(b) $p_{\mathrm{T}}(\mathrm{j}_1)$ [GeV]

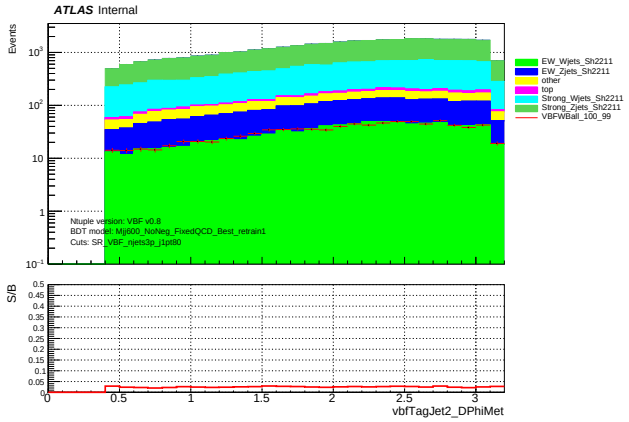

(c) $\Delta\phi(j_2,E_{\mathrm{T}}^{\mathrm{miss}})$

Figure 6.40: Pre-fit distributions in the signal region SR_VBF_njets3p for key observables for $\mathcal{L} = 140$ fb^{-1} at $\sqrt{s} = 13$ TeV. Shown here specifically are the distributions for $M_T(j_1,E_{\mathrm{T}}^{\mathrm{miss}})$, $p_{\mathrm{T}}(\mathrm{j}_1)$, and $\Delta\phi(j_2,E_{\mathrm{T}}^{\mathrm{miss}})$.

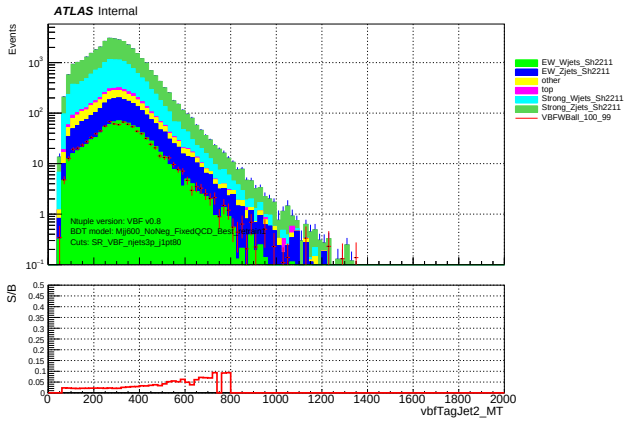

(a) $M_T(j_2, E_{\mathrm{T}}^{\mathrm{miss}})$ [GeV]

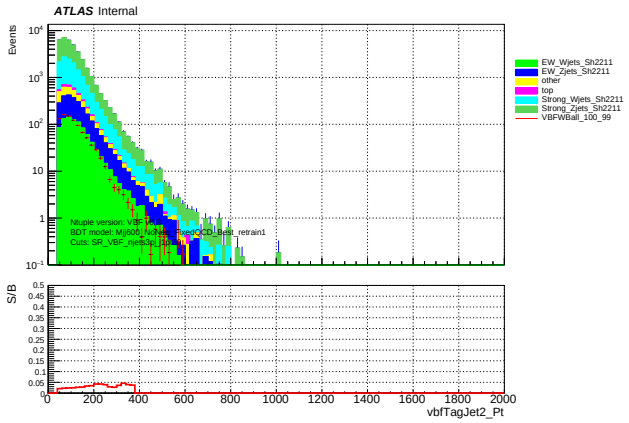

(b) $p_{\mathrm{T}}(\mathrm{j}_2)$ [GeV]

Figure 6.41: Pre-fit distributions in the signal region SR_VBF_njets3p for key observables for $\mathcal{L} = 140$ fb^{-1} at $\sqrt{s} = 13$ TeV. Shown here specifically are the distributions for $M_T(j_2, E_{\mathrm{T}}^{\mathrm{miss}})$ and $p_{\mathrm{T}}(\mathrm{j}_2)$.

Chapter 7

Background Estimation

Dedicated control regions (CR) are used to accurately model the contribution of the major backgrounds in the signal region. The control regions are defined by altering one or more requirements in the event selection so as to create a region enriched in the specific background under consideration. The rest of the event selection criteria are kept to make the control region as close kinematically to the signal region as possible. Normalization factors are applied for these backgrounds as free parameters when performing the simultaneous fit such that the background contribution in all regions are scaled by the fitted background normalizations. For the estimation of the QCD multijet background a semi-data driven method is utilized that provides a more accurate treatment than using Monte Carlo samples that may be statistically limited.

7.1. W+ jets Control Region

The W+ jets background can enter the signal region when the lepton coming from $W \rightarrow \ell\nu$ falls outside of the detector acceptance and fails to be reconstructed thereby passing the lepton veto. To construct the control region for W+ jets the signal region selection is altered to instead require exactly one lepton. The lepton may be of

either flavor (electron or muon) and must have $p_{\mathrm{T}} > 27$ GeV as well as pass the corresponding signal lepton object criteria. Electrons are further required to have $|\eta| < 1.37$ or $|\eta| > 1.52$ to be outside of the calorimeter crack region. To suppress the contribution of fake electrons an additional requirement on electron events is imposed on the missing transverse momentum significance variable [25] $E_{\mathrm{T}}^{\mathrm{miss}}/\sqrt{\Sigma E_T}$ $> 5.0\sqrt{\mathrm{GeV}}$ defined as

$$E_{\mathrm{T}}^{\mathrm{miss}}/\sqrt{\Sigma E_T} = \frac{E_{\mathrm{T}}^{\mathrm{miss}}}{\sqrt{p_{\mathrm{T}}(j_1) + p_{\mathrm{T}}(j_2) + p_{\mathrm{T}}(e)}}$$

where j_1 and j_2 denote the VBF-tagged jets and the electron e. The trigger requirements for events is also altered to require passing one of the following: the $E_{\mathrm{T}}^{\mathrm{miss}}$ trigger, single-electron trigger, or single-muon trigger.

In order to make the $E_{\mathrm{T}}^{\mathrm{miss}}$ distribution in the control region compatible with that of the signal region in which no reconstructed lepton is present, any variable used in the event selection associated with $E_{\mathrm{T}}^{\mathrm{miss}}$ is altered to treat the lepton as invisible. This also includes the BDT score where a separate score is produced based on the BDT evaluation that has utilized these variables with the leptons being treated invisible. An exception to this is in the trigger requirements: the events that pass through the $E_{\mathrm{T}}^{\mathrm{miss}}$ trigger must also pass $E_{\mathrm{T}}^{\mathrm{miss}} > 250$ GeV, where the $E_{\mathrm{T}}^{\mathrm{miss}}$ here is the standard one without this treatment regarding leptons.

7.2. Z + jets Control Region

The $Z(\rightarrow \nu\nu)$+jets background in the signal region is estimated by constructing a $Z(\rightarrow \ell\ell)$ control region with the same kinematics. This is done by selecting events with two same-flavor opposite-sign leptons while still including the other signal region requirements aside from the lepton veto. As with the W+ jets control region,

the variables associated with $E_{\mathrm{T}}^{\mathrm{miss}}$ are altered to treat the leptons as invisible such that the leptons from the Z effectively model the neutrinos from the $Z(\rightarrow \nu\nu)$+jets background. Both leptons must also pass the signal object criteria. The dilepton invariant mass $m_{\ell\ell}$ is required to be within 30 GeV of the Z boson mass in order to target lepton pairs consistent with those coming from the Z. Events in this region must pass one of the single-lepton triggers and the leading lepton is required to have $p_{\mathrm{T}} > 27$ GeV to be in the trigger plateau region. Electrons must be outside of the crack region ($1.37 < |\eta| < 1.52$), and the sub-leading electron (muon) is required to have $p_{\mathrm{T}} > 25$ (9) GeV.

7.3. W/Z+jets estimation for BDT SR

The W and Z control regions described in the previous sections are used to extract normalization factors for the corresponding backgrounds and extrapolated to the signal regions in a simultaneous fit. Since these control regions are used for only deriving the background normalizations, no shape information is needed and they are defined as single-bin regions. The same BDT used for defining the signal region is also used for the control regions. An alternative set of BDT scores has been evaluated for events with one or two signal leptons in which the input variables that include $E_{\mathrm{T}}^{\mathrm{miss}}$ were modified to use the version in which the lepton is treated as invisible. The BDT score is required to be between 0.5 and 0.84 for these control regions. The lower cut on the BDT score of 0.5 is chosen to be close to that in the signal region while benefiting from having increased background statistics by using a slightly lower value. The upper cut on the BDT score of 0.84 is included to allow for higher BDT score regions to be used for validation of the background estimation. Each of these control regions are further divided into two separate regions based on the jet multiplicity

in the same manner as the signal region. The W control regions are denoted as CR_1L_njets2 and CR_1L_njets3p for the 2 jet and 3+ jet regions respectively, where the 1L refers to the one lepton requirement in the regions. Correspondingly the Z control regions are denoted as CR_2L_njets2 and CR_2L_njets3p with 2L referring to the requirement of two leptons. Separate background normalizations are derived for the 2 jet regions as well as for the 3+ jet regions. Furthermore, the background normalizations that are derived from the control regions for the strong and electroweak components of the V + jets backgrounds are set to be the same.

The use of flat background normalization factors for the extrapolation to multi-bin signal regions requires some justification since the assumption is that there is no significant change in the background normalization bin-by-bin. To justify this approach, the agreement between the data and the background expectation in the control regions as a function of the BDT score is checked before and after applying the fitted background normalizations as shown in Figures 7.1 and 7.2. It can be seen that after the flat background normalizations are applied, the agreement to the data improves and the ratio is roughly flat across the BDT score distribution.

The purity of the W and Z control regions in the corresponding backgrounds is found to be high. For the W control regions, W+ jets makes up 95% and 86% of the total expected background in CR_1L_njets2 and CR_1L_njets3p respectively. The purity of Z + jets in the Z control regions are 97% and 93% for CR_2L_njets2 and CR_2L_njets3p respectively.

There are two main points of motivation in regards to the choice of applying the same background normalization for both the electroweak and strong V + jets backgrounds. First, the strong V + jets backgrounds are by far the dominant component of the total background in the control regions with the ratio of strong to EW V + jets ranging from 3.9 to 12.1 depending on the control region. For this reason the idea of

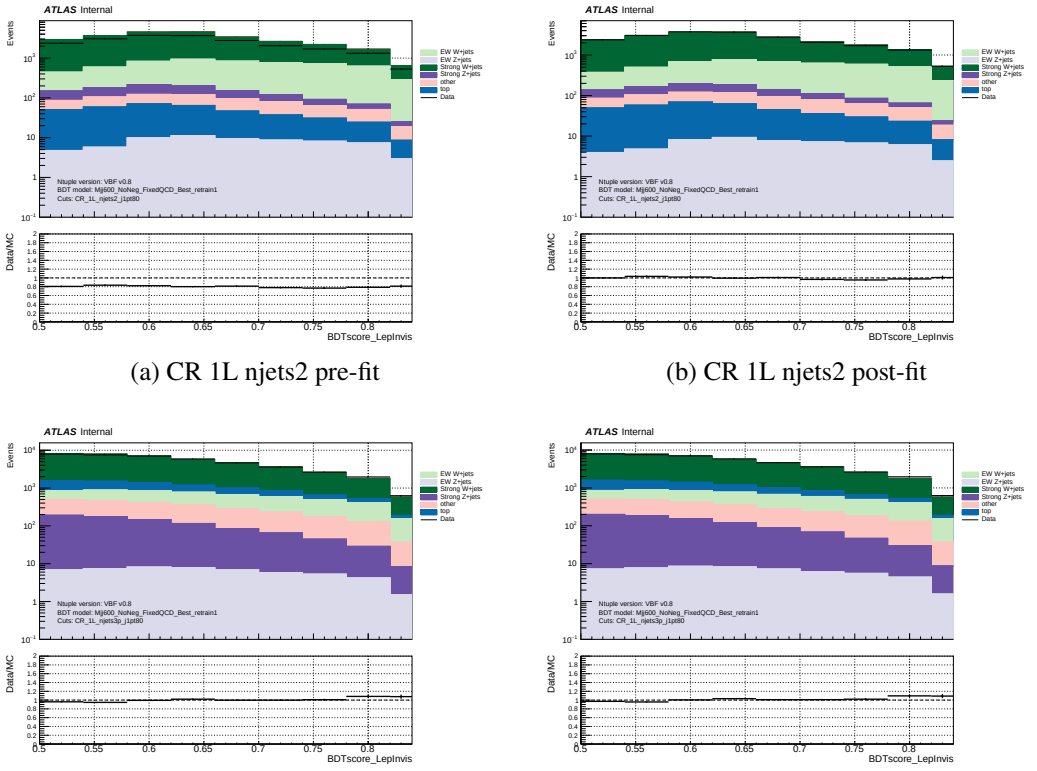

(a) CR 1L njets2 pre-fit

(b) CR 1L njets2 post-fit

(c) CR 1L njets3p pre-fit

(d) CR 1L njets3p post-fit

Figure 7.1: Data and Monte Carlo background comparisons for the BDT score distribution in the W control regions before and after applying fitted background normalizations. Only the statistical error is included in the error bars.

keeping the same control regions but defining normalization factors separately for the EW and strong components does not provide sensible results since the normalization for the EW background in this configuration is driven towards zero during the fit. Second, it would difficult to split the Z + jets control regions further to define separate control regions for normalizing the EW V + jets backgrounds due to the low purity as already mentioned as well as these regions already having limited statistics. Figures 7.3 and 7.4 compare the background yields in the control regions between strong and EW V + jets as a function of the BDT score and dijet invariant mass respectively. The strong V + jets dominates for most parts of the distributions but there

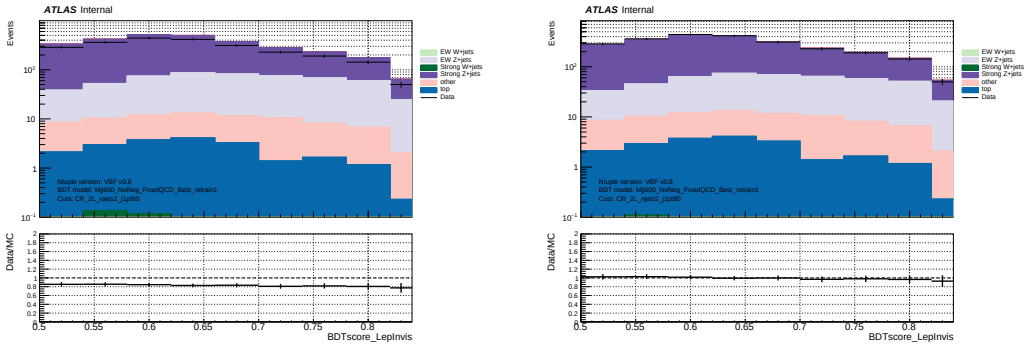

(a) CR 2L njets2 pre-fit

(b) CR 2L njets2 post-fit

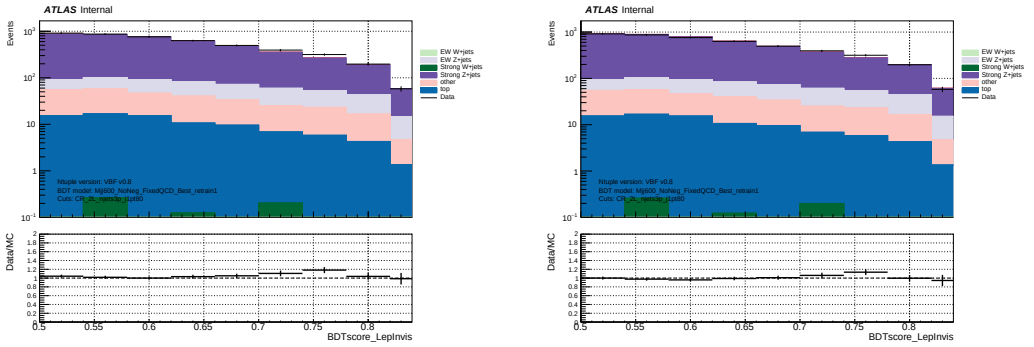

(c) CR 2L njets3p pre-fit

(d) CR 2L njets3p post-fit

Figure 7.2: Data and Monte Carlo background comparisons for the BDT score distribution in the Z control regions before and after applying fitted background normalizations. Only the statistical error is included in the error bars.

are instances at high BDT score and large m_{jj} where the EW background becomes comparable or exceeds the strong background. However, these regions where the EW V + jets background would be high in purity are also where the background yields are quite small. This would result in a large uncertainty on the background normalization if these were defined as separate EW V + jets control regions. This is in addition to the fact that the Z + jets control regions are already statistically limited due to small branching ratio of $\mathrm{Z}(\rightarrow ll)$ along with the requirement of two reconstructed leptons that pass the criteria described earlier.

The pre-fit p_{T}, η and ϕ distributions of the lepton(s) in the W and Z control

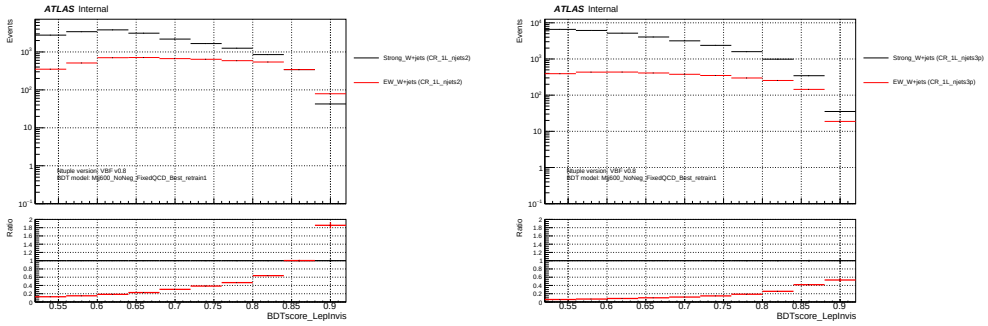

(a) $W+$ jets in CR 1L njets2

(b) $W+$ jets in CR 1L njets3p

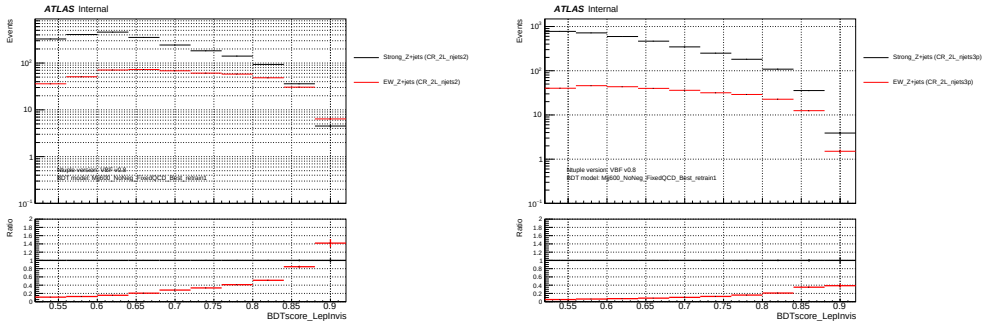

(c) $Z+$ jets in CR 2L njets2

(d) $Z+$ jets in CR 2L njets3p

Figure 7.3: Comparison in the relative background contribution of strong vs electroweak $V+$jets in the control regions as a function of the BDT score.

regions are shown in Figures 7.5 and 7.6 inclusively in the jet multiplicity. While the agreement with the data is roughly flat in ϕ as would be expected, there are some slight trends that may indicate worse modeling with increasing lepton η.

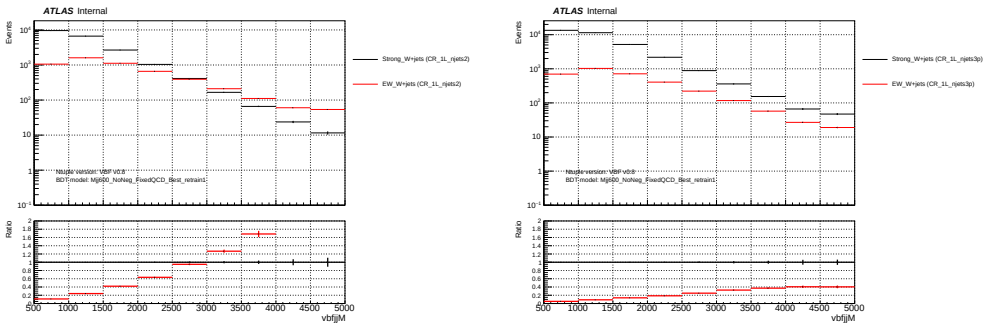

(a) $W+$ jets in CR 1L njets2

(b) $W+$ jets in CR 1L njets3p

(c) $Z+$ jets in CR 2L njets2

(d) $Z+$ jets in CR 2L njets3p

Figure 7.4: Comparison in the relative background contribution of strong vs electroweak $V+$jets in the control regions as a function of dijet invariant mass m_{jj} [GeV].

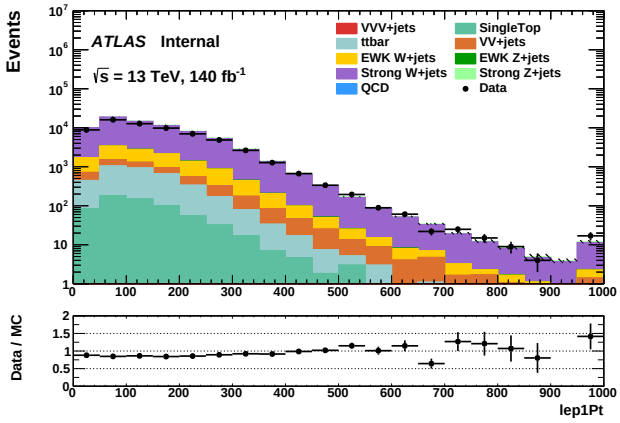

(a) $p_{\mathrm{T}}(\ell_1)$ [GeV]

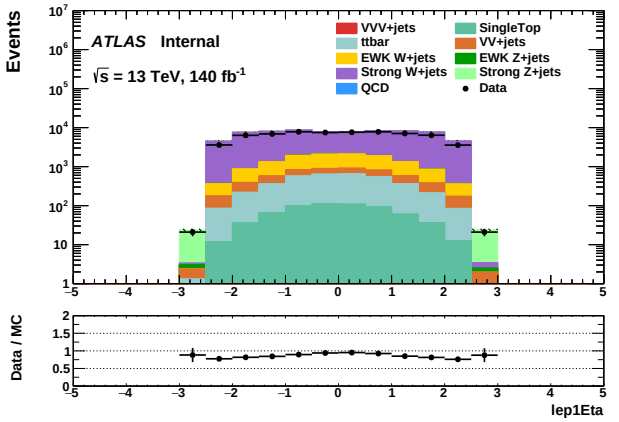

(b) $\eta(\ell_1)$

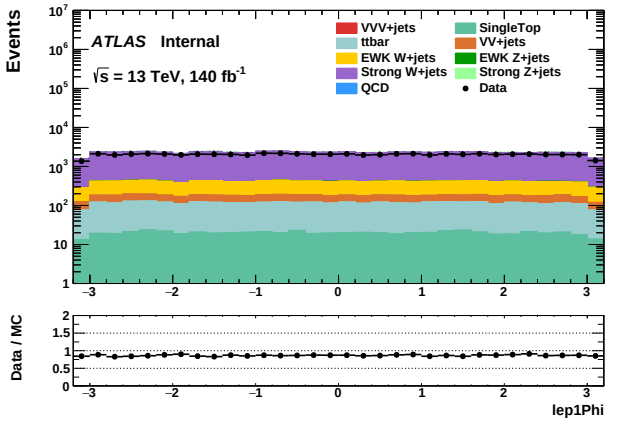

(c) $\phi(\ell_1)$

Figure 7.5: The pre-fit p_{T}, η and ϕ distributions of the leading lepton in the W control region inclusively in the jet multiplicity. Only the statistical error is included in the error bars.

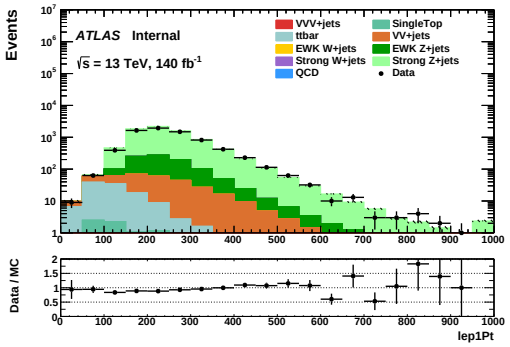

(a) $p_{\mathrm{T}}(\ell_1)$ [GeV]

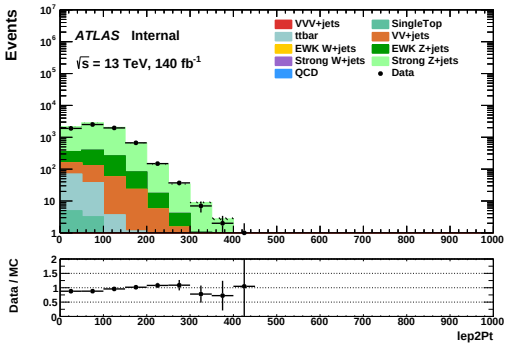

(b) $p_{\mathrm{T}}(\ell_2)$ [GeV]

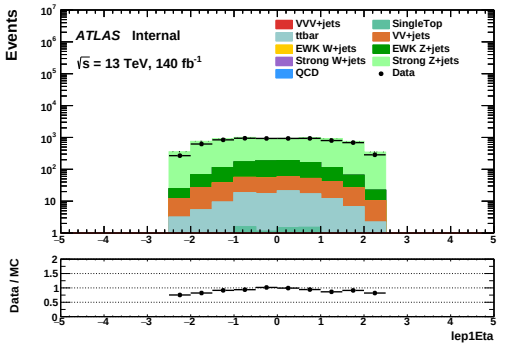

(c) $\eta(\ell_1)$

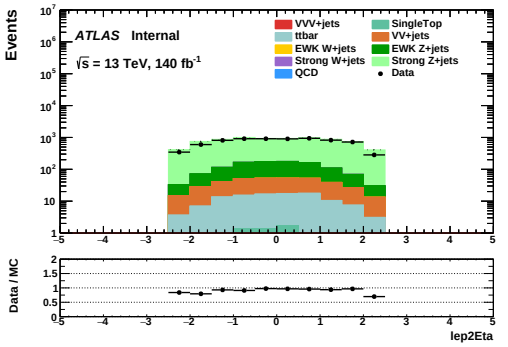

(d) $\eta(\ell_2)$

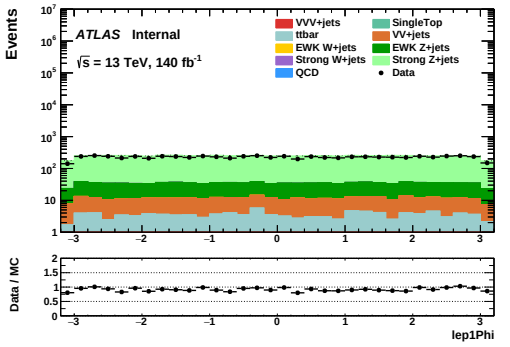

(e) $\phi(\ell_1)$

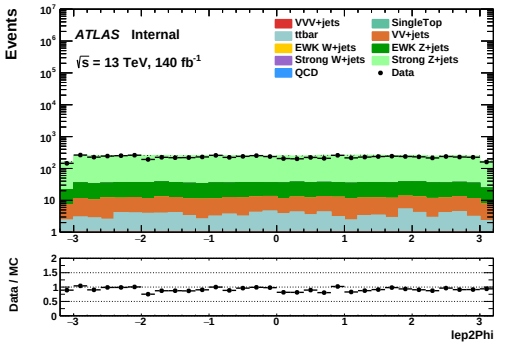

(f) $\phi(\ell_2)$

Figure 7.6: The pre-fit p_{T}, η and ϕ distributions of the leading and sub-leading leptons in the Z control region inclusively in the jet multiplicity. Only the statistical error is included in the error bars.

7.4. Validation Regions

To verify the extrapolation of the normalization factors for Z + jets and W+ jets holds, two types of validation regions (VR) are defined. The first type are 1L and 2L VRs, which share the exact same definition as the 1L and 2L CRs but are located at the very end of the BDT score distribution. The 1L and 2L VRs consist of two bins of width 0.04 from 0.84 to 0.92, where the last bin contains the overflow. Naturally, these VRs are rather pure in W+ jets and Z + jets, respectively. This makes it possible to verify that the W+ jets and Z + jets normalization factors derived at medium BDT score values are also valid in the tail of the BDT score, where the most sensitive SRs bins are located. The second type is a 0L VR (0L here referring to a zero lepton requirement) sharing the exact same selections as the SR but is located at lower BDT score, from 0.4 to 0.6 (5 equidistant VR bins of width 0.04). This allows to verify that the normalization factors derived in 1L and 2L events are also applicable in 0L events as in the SR. These 0L VRs contain a mix of backgrounds, similar to the SRs, and are of high statistics making any signal contamination sufficiently small. All VRs are separated into 2 jet and 3+ jet events as the CRs. The post-fit results of the VRs will be described in Section 9.3.

A summary of the region definitions for this search are shown in Table 7.1.

7.5. QCD Multijet Estimation

The multijet background (also referred to as the QCD/fake background) is estimated using a data-driven ABCD approach which is illustrated in Fig. 7.8. Two sets of kinematic variables with little correlation are chosen to define four regions denoted as A, B, C, and D. Three of these regions are used as control regions that are

Variable	SR	VR-0L	CR-1L	VR-1L	CR-2L	VR-2L
Trigger	$E_{\mathrm{T}}^{\mathrm{miss}}$ trigger		$E_{\mathrm{T}}^{\mathrm{miss}}$ OR single-lepton trigger		single-lepton trigger	
$n_{\mathrm{lep}}^{\mathrm{base}}$	0		–			
$n_{\mathrm{lep}}^{\mathrm{sig}}$	–		1		2	
$E_{\mathrm{T}}^{\mathrm{miss}}$	$E_{\mathrm{T}}^{\mathrm{miss}} > 250$ GeV		$E_{\mathrm{T}}^{\mathrm{miss,\ inv\ }\ell} > 250$ GeV			
Electron Crack Veto	no		yes			
$p_{\mathrm{T}}(\ell_1)$	–		> 27 GeV			
$p_{\mathrm{T}}(\ell_2)$			–		$> 25(9)$ GeV for $e(\mu)$	
$E_{\mathrm{T}}^{\mathrm{miss}}/\sqrt{\Sigma E_T}$	–		$> 5\sqrt{\mathrm{GeV}}$		–	
$m_{\ell\ell}$			–		$\lvert m_{\ell\ell} < m_Z \rvert < 30$ GeV	
BDT Score	≥ 0.6	[0.4, 0.6)	[0.50, 0.84)	≥ 0.84	[0.50, 0.84)	≥ 0.84

Table 7.1.: Summary of the definitions defining the control regions (CRs), validation regions (VRs), and signal regions (SRs). Each region is additionally split into $n_{\mathrm{jet}} == 2$ and $n_{\mathrm{jet}} \geq 3$ categories. The requirements of the preselection are also applied with the exception that the lepton veto is flipped in the single lepton (1L) and dilepton (2L) regions. If an event was triggered by the $E_{\mathrm{T}}^{\mathrm{miss}}$ trigger a $E_{\mathrm{T}}^{\mathrm{miss}} > 250$ GeV requirement is applied, while events selected by single-lepton triggers require a p_{T} of the leading lepton > 27 GeV.

background dominated while the last region is the signal region for which the estimated background is extrapolated to. In this search the control regions are defined as CRA, CRB, CRC and the signal region is denoted as SRD. Two validation regions VRE and VRF are defined to validate this approach. The QCD contribution in the CRs can be derived by subtracting the other predicted backgrounds from the data in the corresponding regions. A fake transfer factor (TF) can be derived from CRB to CRC as $\frac{(data-otherMC)_{CRC}}{(data-otherMC)_{CRB}}$ and later applied to CRA to extrapolate the QCD yields in the SR. The two sets of variables used are $E_{\mathrm{T}}^{\mathrm{miss}}$ and the BDT score, versus $\min(\Delta\phi(j, E_{\mathrm{T}}^{\mathrm{miss}}))$. A looser cut on the BDT score compared to the SR is utilized in order to increase the statistics in the ABCD regions. A check of the correlations among the ABCD variables is shown in Figure 7.7; the variables are found to be roughly uncorrelated. A cut of $\min(\Delta\phi(j, E_{\mathrm{T}}^{\mathrm{miss}})) < 0.4$ is used to enrich the regions

in multijet events that will be used to extrapolate the QCD background from after applying the transfer factor. The measurement region of the TF CRB further requires 200 GeV $< E_{\mathrm{T}}^{\mathrm{miss}} <$ 220 GeV and a BDT score > 0.4. The TFs are validated in VRs that require 220 GeV $< E_{\mathrm{T}}^{\mathrm{miss}} <$ 250 GeV and the same cut on the BDT score. Events in CRA, where the TF is applied to extrapolate into the SR, share the same requirements as the SR: $E_{\mathrm{T}}^{\mathrm{miss}} > 250$ GeV and BDT score > 0.6 .

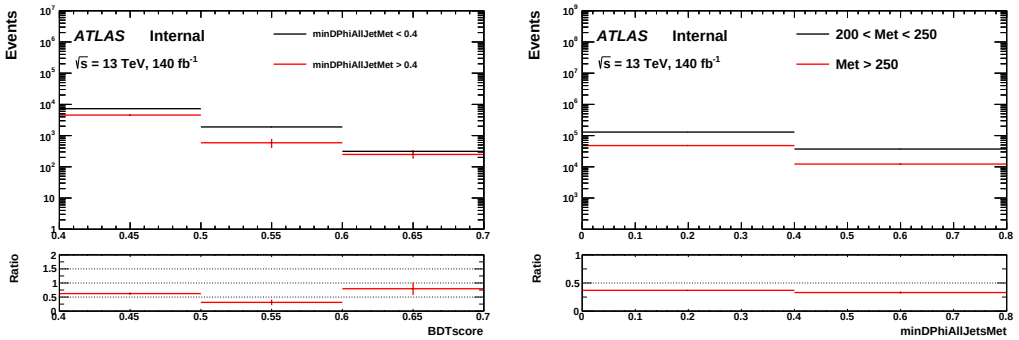

(a) (b)

Figure 7.7: (a): The data-other MC correlation between the BDT score and $\min(\Delta\phi(j, E_{\mathrm{T}}^{\mathrm{miss}}))$. (b) The data-other MC correlation between $E_{\mathrm{T}}^{\mathrm{miss}}$ and $\min(\Delta\phi(j, E_{\mathrm{T}}^{\mathrm{miss}}))$. Only the statistical error is considered.

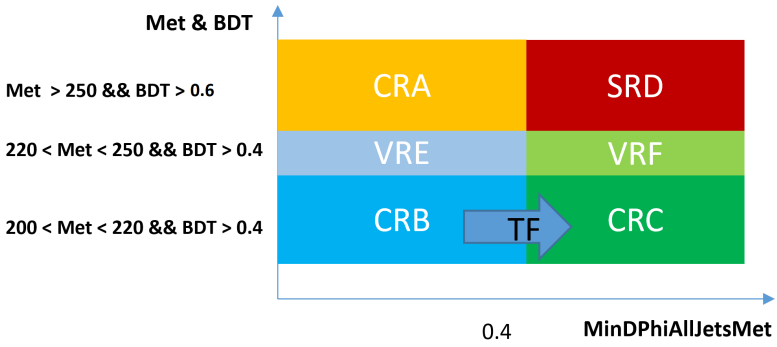

(a)

Figure 7.8: Diagram showing the regions defined in this search for the ABCD method to estimate the multijet background based on $E_{\mathrm{T}}^{\mathrm{miss}}$ and the BDT score versus $\min(\Delta\phi(j, E_{\mathrm{T}}^{\mathrm{miss}}))$.

Separate normalizations for W+ jets and Z + jets are derived for the ABCD regions

to improve the background modeling and make the data-driven estimate more accurate. Corresponding 1L (2L) regions for the ABCD CRs/VRs are used to derive the W/Z normalization factors in those ABCD regions from a background-only fit to the data. The fitted values for the W/Z normalization factors in each region are shown in Table 7.2.

	SRD	CRC/VRF	CRA	CRB/VRE
NF_W	0.897	0.845	0.847	0.781
NF_Z	0.962	0.894	0.818	0.766

Table 7.2.: W and Z normalization factors for each QCD CR/VR and SR obtained from a background-only fit in corresponding regions requiring one lepton or two leptons respectively.

The breakdown of the yields and transfer factor derived from ABCD method are presented in Table 7.3. The transfer factor is found to be 0.665 ± 0.052 and is used for estimating the QCD for VRF from VRE and for SRD from CRA. The last two rows of the table compare the data and SM background modeling in VRF when using the QCD MC sample versus using the estimated QCD, and the agreement is found to be improved when using the estimated QCD from the ABCD method.

	CRB	CRC	VRE	VRF	CRA	SRD
data	8805	40575	9537	43105	10808	–
Total background (Using QCD MC)	13718 ± 701	45106 ± 2934	13701 ± 410	44669 ± 763	13275 ± 206	59796 ± 713
data - Other background	5072 ± 105	3371 ± 253	4319 ± 115	-	2197 ± 117	-
TF	0.665 ± 0.052					
Estimated QCD	-	-	-	2242 ± 185	-	1461 ± 138
Total background (Using Estimated QCD)	-	-	-	43768 ± 237	-	59339 ± 197
Data/MC (Using QCD MC)	-	-	-	0.965 ± 0.014	-	-
Data/MC (Using Estimated QCD)	-	-	-	0.985 ± 0.007	-	-

Table 7.3.: Yields for the data, "data - other MC," estimated QCD, and total background using either the QCD MC or the estimated QCD in the various ABCD regions. Also shown are the transfer factor and the ratio of the data to the total background depending on if the QCD MC or the estimated QCD is used. Only the statistical error is considered here.

The ABCD method outlined above for estimating the multijet background is

extrapolated to the signal regions which are split based on the jet multiplicity. Due to the low statistics in the high BDT score bins, a fit is performed in the CRA regions and used to extrapolate the yields to the SR regions, which can be done separately for the 2 jet and 3+ jet cases. However, it is observed that the fake contribution and statistics are both limited in the 2 jet CRA, which is somewhat expected as the multijet background contribution is small in the 2 jet VBF regions. The strategy employed is to instead perform a fit in the inclusive (2+ jet) region and another fit in the 3+ jet region. The yields obtained from these fits can be subtracted from one another to be then applied as the estimate for the 2 jet region. The fit is performed as a function of the BDT score with identical binning to that of the SR, with each bin including the yields for the other backgrounds subtracted from the data. Several empirical fit functions were tested for use with this method, with the best function being a combined "Gaussian + Linear" function with the following fitted values for the constants:

(7.5.1) Inclusive CRA : $QCD = 2393 * e^{-(BDTscore-0.250)^2/0.151} - 1532 + 1545 * BDTscore$,

(7.5.2) $\text{CRA}_{\geq 3J}$: $QCD = 2251 * e^{-(BDTscore-0.250)^2/0.130} - 1121 + 1151 * BDTscore$.

The results of the fits are shown in Figure 7.9. The yields for the raw "data - other MC" and fitted value (given by the integral of the fit functions) in each bin for CRA is shown in Table 7.4 and Table 7.5. The fitted QCD yields are set to zero for the bins in which the fit function gives a negative fitted value. The estimated QCD yield in each BDT score bin of the SR is then obtained after applying the transfer factor to the fitted CRA yields and are shown in Figure 7.10. In general the estimated QCD contribution in the signal regions is found to be small with QCD representing no more than 5% of the total background in any bin.

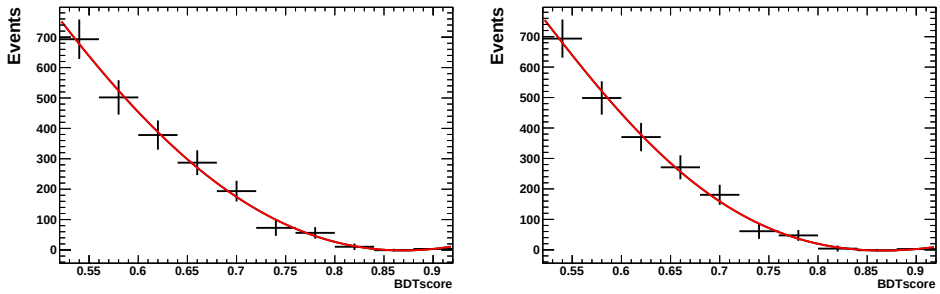

Figure 7.9: BDT score distribution for the data-other MC and corresponding fit function in the inclusive CRA (left) and 3+ jet CRA (right).

	Data - other MC	Fitted QCD
0.52 < BDTscore < 0.56	693 ± 65	672.7
0.56 < BDTscore < 0.6	502 ± 57	527.0
0.6 < BDTscore < 0.64	378 ± 48	392.0
0.64 < BDTscore < 0.68	287 ± 41	273.5
0.68 < BDTscore < 0.72	194 ± 34	175.3
0.72 < BDTscore < 0.76	73 ± 26	99.1
0.76 < BDTscore < 0.8	56 ± 19	45.4
0.8 < BDTscore < 0.84	11 ± 11	13.0
0.84 < BDTscore < 0.88	−1 ± 5	0.06
BDTscore > 0.88	3 ± 2	4.0

Table 7.4.: Data - other MC and fitted QCD in each BDT score bin of the inclusive CRA.

The kinematic distributions for data and the SM background in VRF are shown in Figures 7.11 and 7.12 comparing when the QCD MC and the ABCD-estimated QCD are used. Better agreement is found between the data and predicted background when using the ABCD-estimated QCD.

As described previously, validation regions requiring zero leptons (0L VR) are defined to be the same as the signal regions except with the cut on the BDT score being inverted. These validation regions are used to validate the background extrapolation from the 1L/2L regions to the 0L regions. The QCD background for the 0L VRs are also estimated using the same data-driven ABCD method. The definitions of the CRB, CRC, VRE, and VRF regions are kept the same as the ones for the SR so

	Data - other MC	Fitted QCD
0.52 < BDTscore < 0.56	694 ± 63	679.9
0.56 < BDTscore < 0.6	499 ± 55	521.6
0.6 < BDTscore < 0.64	370 ± 46	379.1
0.64 < BDTscore < 0.68	271 ± 39	257.7
0.68 < BDTscore < 0.72	181 ± 33	160.1
0.72 < BDTscore < 0.76	61 ± 25	87.0
0.76 < BDTscore < 0.8	47 ± 18	37.4
0.8 < BDTscore < 0.84	4 ± 10	8.8
0.84 < BDTscore < 0.88	−1 ± 4	0
BDTscore > 0.88	2.5 ± 1.7	3.0

Table 7.5.: Data - other MC and fitted QCD in each BDT score bin of the 3+ jet CRA.

the same transfer factor is also used as the one derived for the SR. The definition of CRA is the same as the one for the SR except that the BDT score range is 0.4 < BDTscore < 0.6. The data-driven estimate for the QCD background is obtained by the "data-other MC" in CRA multiplied by the transfer factor. In this case the raw "data-other MC" is used instead of relying on a fit function since this range of the BDT score distribution is not subject to low statistics. A comparison of the yields between the data-driven estimated QCD and the QCD MC in the 0L VRs is shown in Table 7.6. The statistical uncertainties of the data-driven estimate of the QCD are found to be generally smaller than those of the QCD MC and the distribution for the data-driven estimate is much smoother than that for the QCD MC in the 3+ jet case. For the 2 jet case, the data-driven QCD suffers from poor statistics in CRA and yields a fluctuating estimate similar to the one from the QCD MC; however this should be less of an issue due to the smaller background contribution that QCD has here compared to the 3+ jet case.

	data-driven QCD (2J)	QCD MC (2J)	data-driven QCD (>=3J)	QCD MC (>=3J)
0.4< BDTscore < 0.44	48 ± 16	7.7 ± 3.3	653 ± 53	333 ± 242
0.44 < BDTscore < 0.48	16 ± 15	12 ± 7	591 ± 50	84 ± 57
0.48 < BDTscore < 0.52	42 ± 13	136 ± 70	489 ± 48	119 ± 42
0.52 < BDTscore < 0.56	0	11 ± 5	461 ± 42	475 ± 318
0.56 < BDTscore < 0.6	2 ± 9	27 ± 19	331 ± 36	77 ± 23

Table 7.6.: Data-driven estimate of QCD and QCD MC in each BDT score bin in the 0L VRs. The data-driven estimate of QCD with 0.52 < BDTscore < 0.56 in the 2 jet case is set to zero, as the "data-other MC" in the corresponding bin of CRA is negative.

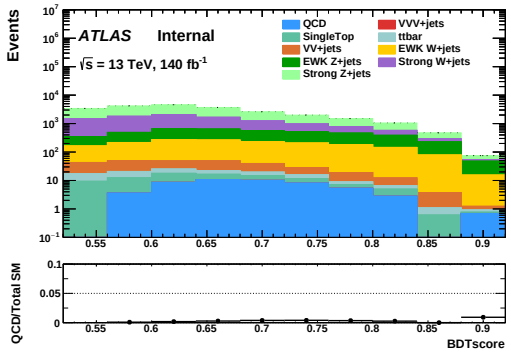

(a)

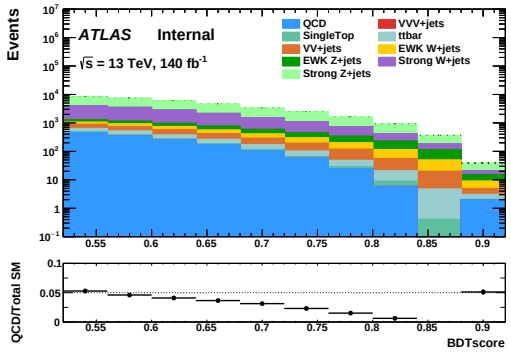

(b)

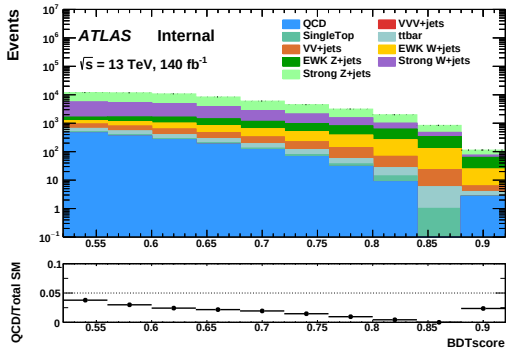

(c)

Figure 7.10: The BDT score distributions after including the estimated multijet background in the 2 jet SR (a), 3+ jet SR (b) and inclusive SR (c). The multijet estimate is obtained using the ABCD method described in the text; the QCD in each bin is extrapolated from the fitted "data - other MC" in CRA multiplied by the derived transfer factor. Only the statistical error is considered in these plots. The bottom panel of each plot indicates the relative fraction of the estimated QCD background with respect to the total background.

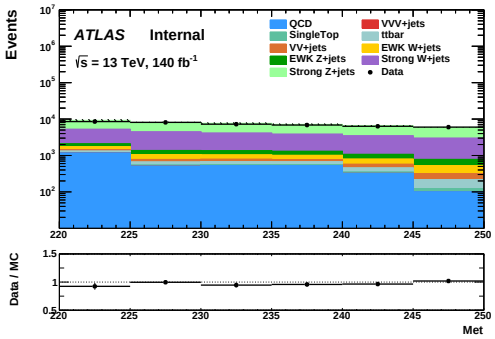

(a) $E_{\mathrm{T}}^{\mathrm{miss}}$ [GeV] (MC)

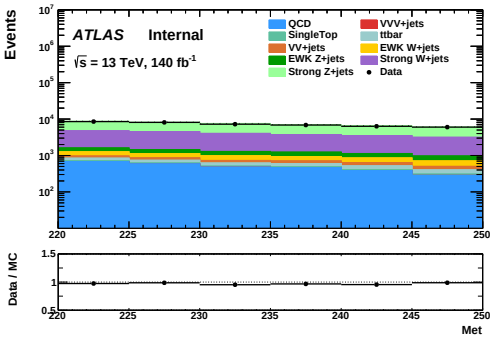

(b) $E_{\mathrm{T}}^{\mathrm{miss}}$ [GeV] (ABCD)

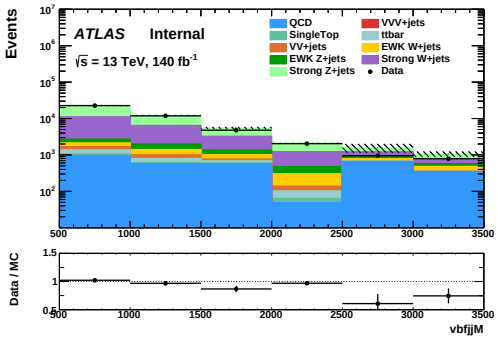

(c) m_{jj} [GeV] (MC)

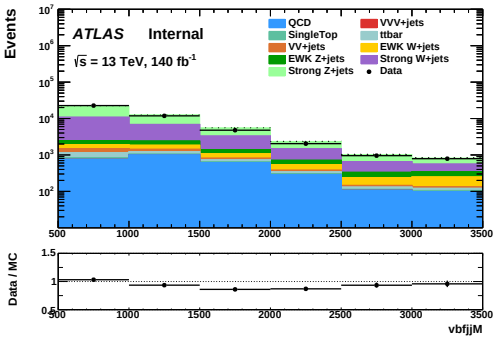

(d) m_{jj} [GeV] (ABCD)

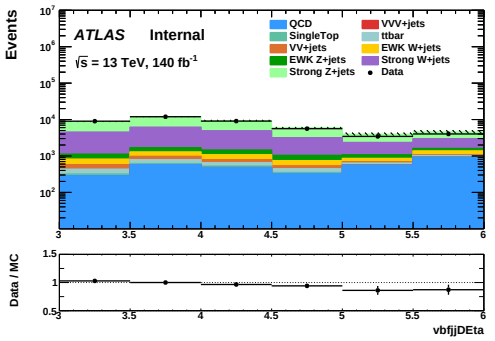

(e) $\Delta\eta_{\mathrm{jj}}$ (MC)

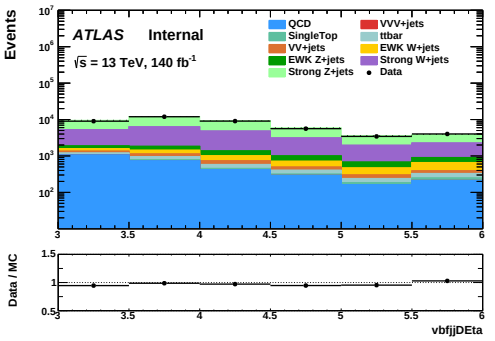

(f) $\Delta\eta_{\mathrm{jj}}$ (ABCD)

Figure 7.11: The distributions of $E_{\mathrm{T}}^{\mathrm{miss}}$, m_{jj}, and $\Delta\eta_{\mathrm{jj}}$ for data and the SM background in VRF. Left: QCD MC is applied. Right: ABCD-estimated QCD is applied. Only the statistical error is considered in these plots.

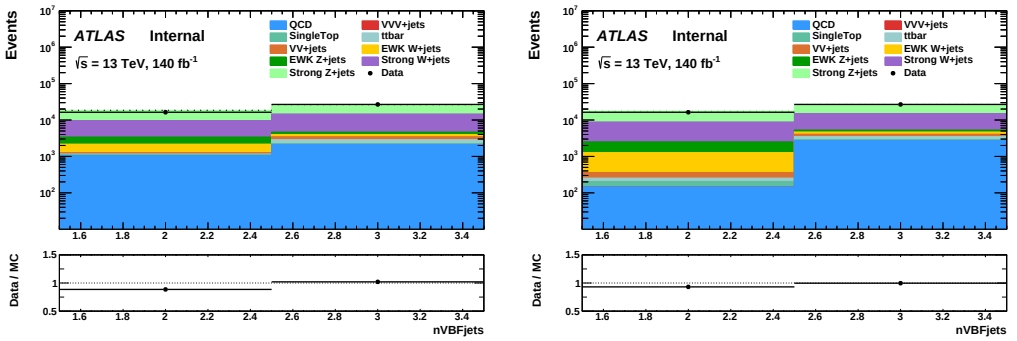

(a) n_{jets} (MC)

(b) n_{jets} (ABCD)

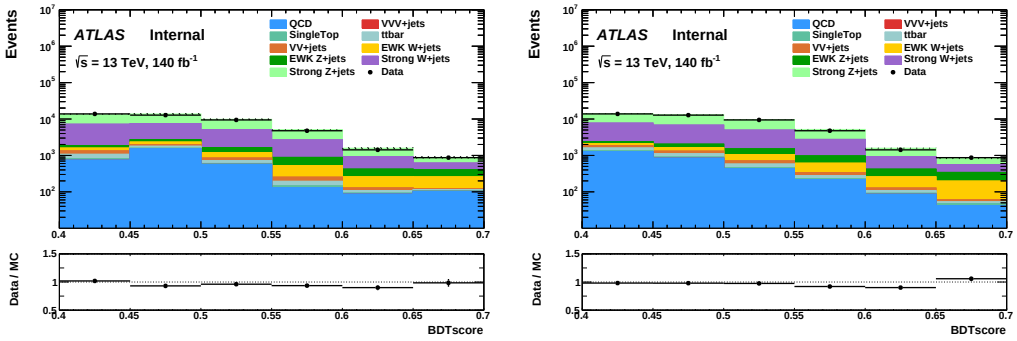

(c) BDT score (MC)

(d) BDT score (ABCD)

Figure 7.12: The distributions of n_{jets} and BDT score for data and the SM background in VRF. Left: QCD MC is applied. Right: ABCD-estimated QCD is applied. Only the statistical error is considered in these plots.

Chapter 8

Systematic Uncertainties

The systematic uncertainties in this search come from two categories of sources: experimental and theoretical sources. The experimental uncertainties encompass those related to the reconstruction and identification of physics objects, the triggers used to collect the data, the integrated luminosity of the dataset, pile-up, and the data-driven estimation of backgrounds. Theoretical uncertainties include those related to the simulation of signal and background processes such as the cross-sections, choice of the PDF sets, and the factorization and renormalization scales.

8.1. Experimental Uncertainties

Experimental uncertainties having to do with the detector performance and data-taking conditions need to be taken into account when performing the statistical analysis in this search. The recommendations and prescriptions for evaluating these experimental uncertainties are provided centrally within ATLAS through dedicated working groups. The relevant set of experimental systematic uncertainties taken into account in this analysis are summarized in Table 8.1.

Systematic uncertainty	Short description
	Event
Luminosity	uncertainty on the total integrated luminosity
PRW_DATASF	uncertainty on data SF used for the computation of pile-up reweighting
	Electrons
EL_EFF_Trigger_TOTAL_1NPCOR_PLUS_UNCOR	trigger efficiency SF uncertainty
EL_EFF_TriggerEff_TOTAL_1NPCOR_PLUS_UNCOR	trigger efficiency uncertainty
EL_EFF_Reco_TOTAL_1NPCOR_PLUS_UNCOR	reconstruction efficiency uncertainty
EL_EFF_ID_TOTAL_1NPCOR_PLUS_UNCOR	ID efficiency uncertainty
EL_EFF_Iso_TOTAL_1NPCOR_PLUS_UNCOR	isolation efficiency uncertainty
EG_SCALE_ALL	energy scale uncertainty
EG_RESOLUTION_ALL	energy resolution uncertainty
	Muons
MUON_EFF_TrigStatUncertainty MUON_EFF_TrigSystUncertainty	trigger efficiency uncertainties
MUON_EFF_RECO_STAT MUON_EFF_RECO_SYS	reconstruction uncertainty for $p_{\mathrm{T}} > 15$ GeV
MUON_EFF_RECO_STAT_LOWPT MUON_EFF_RECO_SYS _LOWPT	reconstruction and ID efficiency uncertainty for $p_{\mathrm{T}} < 15$ GeV
MUON_ISO_STAT MUON_ISO_SYS	isolation efficiency uncertainty
MUON_TTVA_STAT MUON_TTVA_SYS	track-to-vertex association efficiency uncertainty
MUONS_SCALE	energy scale uncertainty
MUONS_SAGITTA_RHO	variations in the scale of the momentum (charge dependent)
MUONS_SAGITTA_RESBIAS	variations in the scale of the momentum (charge dependent)
MUONS_ID	energy resolution uncertainty from inner detector
MUONS_MS	energy resolution uncertainty from muon system
	Small-R Jets
JET_JER_X	jet energy resolution uncertainties (13 variations)
JET_JES_X	jet energy scale uncertainties (30 variations), where JES is e.g. EffectiveNP
JET_JvtEfficiency	JVT efficiency uncertainty
JET_fJvtEfficiency	fJVT efficiency uncertainty
FT_EFF_B_systematics	b-tagging efficiency uncertainties (BTAG_MEDIUM):
FT_EFF_C_systematics	
FT_EFF_Light_systematics	
FT_EFF_extrapolation	b-tagging efficiency uncertainty on the extrapolation on high p_{T}-jets
FT_EFF_extrapolation_from_charm	b-tagging efficiency uncertainty on τ-jets
	$E_{\mathrm{T}}^{\mathrm{miss}}$-Terms
MET_SoftTrk_ResoPerp	track-based soft term related to transversal resolution uncertainty
MET_SoftTrk_ResoPara	track-based soft term related to longitudinal resolution uncertainty
MET_SoftTrk_Scale	track-based soft term related to longitudinal scale uncertainty

Table 8.1.: Qualitative summary of the experimental systematic uncertainties considered in this analysis.

A brief description of the different experimental sources is listed here:

- **Luminosity**: The uncertainty on the integrated luminosity is ±0.83% for the combined 2015 to 2018 dataset. This was determined based on ATLAS van der Meer beam separation scans and measurements from luminosity-sensitive detectors as described in [38].

- **Trigger**: As described earlier in Section 4.1, the offline selection of $E_{\mathrm{T}}^{\mathrm{miss}} >$ 250 GeV should put the analysis well into the trigger efficiency plateau where the inclusive triggers are fully efficient thus no $E_{\mathrm{T}}^{\mathrm{miss}}$ trigger efficiency scale factors are needed. When this is not the case, as for the control regions that rely on electron and muon triggers, the trigger efficiency scale factors and their associated uncertainties are included.

- **Electron reconstruction**: Uncertainties on the electron energy scale and resolution, reconstruction, identification, and isolation efficiency scale factors are considered using their $\pm 1\sigma$ variations as derived by the ATLAS Electron and Photon Performance Group [26].

- **Muon reconstruction**: Uncertainties related to muon reconstruction are provided by the Muon Performance Group [32]. This includes uncertainties on the muon momentum scale and resolution that factor in the effects of the muon sagitta and differences in the measurements from the Inner Detector and Muon Spectrometer. Additionally, the $\pm 1\sigma$ variations on the muon reconstruction, identification, and isolation efficiency scale factors are considered to account for efficiency differences observed between the data and MC. Uncertainties related to the track-to-vertex association (TTVA) are also considered.

- **Jet energy scale and resolution**: The Jet/EtMiss Combined Performance

Group provides prescriptions for evaluating the uncertainties on the jet energy scale and resolution [31]. A reduced set of nuisance parameters are applied using the `CategoryReduction` and `FullJER` schemes that result in 30 and 13 parameters describing the uncertainties for the jet energy scale and resolution respectively. Additional uncertainties are applied to account for efficiency differences between the data and MC in the JVT and fJVT selections. Similarly, uncertainties are applied to account for efficiency differences between the data and MC with respect to the b-tagging identification algorithm.

- $E_{\mathbf{T}}^{\mathbf{miss}}$: Uncertainties on the missing transverse energy arise from propagating the uncertainties on the transverse momentum of the hard physics objects used in its calculation. Additional uncertainties on the scale and resolution of the "soft term" coming from tracks that are associated to the primary vertex but not to any physics objects are also considered.

- **Pile-up**: An assumption is made on the $\langle\mu\rangle$ profile when simulating multiple pile-up interactions in the MC samples used in this analysis. As such the $\langle\mu\rangle$ distribution in MC may not necessarily agree with the one observed in data. To account for this, an improved pile-up description is achieved by re-weighting the MC $\langle\mu\rangle$ distribution to the distribution measured in the data. An uncertainty on this reweighting procedure is considered through $\pm1\sigma$ variations on the applied pile-up weight.

8.2. Theoretical Uncertainties

8.2.1. Scale, PDF, and α_s

The uncertainties associated with the renormalization and factorization scales for both the strong and electroweak production of V + jets are evaluated using on-the-fly event weights. Seven of these weights are each applied separately to produce the 7-point scale variations corresponding to the central value, the renormalization and factorization scales each independently varied up or down by a factor of 2, and finally both scales simultaneously varied up or down by a factor of 2. The envelope of these 7 variations is then used as the systematic template to be treated as the uncertainty associated with the renormalization and factorization scales. This uncertainty is evaluated individually per background process and per analysis region. Within the statistical fit the uncertainty is treated as uncorrelated between different background processes so as to be separated between strong and electroweak as well between W and Z processes. For each individual background process the uncertainty is treated as correlated across both signal and control regions. The variations for electroweak V + jets are found to be around 20-25%. For strong V + jets, the variations for the 2 jet regions are also around 20-25% but for the 3+ jet regions the up variations are mostly around 40-45% while the down variations are at the level of 25-30%. The magnitude of the variations is found to be roughly compatible between signal and control regions. The up and down variations of the envelope are also found to be stable and being consistently made up of variations associated with both scales being simultaneously varied down by a factor of 2 and up by a factor of 2 respectively.

Uncertainties associated with the parton distribution functions (PDF) are also evaluated using on-the-fly event weights. There are one hundred distinct weights that are each separately applied corresponding to a set of 101 PDFs. The standard

deviation of the 101 variations produced after applying these weights is used as the PDF uncertainty. Similarly to the scale uncertainties, the PDF uncertainty is evaluated individually per background process and per analysis region. The PDF uncertainty is treated as correlated across both background processes and analysis regions. The PDF uncertainty is generally found to not exceed 5%.

The uncertainty on the value of the strong coupling constant α_s is taken into account by comparing the nominal PDF set with two other PDF sets that have the value of α_s varied up and down. The PDF sets used are NNPDF30_nnlo_as_0119 and NNPDF30_nnlo_as_0117. The magnitude of the α_s uncertainties is at most 2%.

Plots of these theory uncertainties are shown in Figures 8.1 and 8.2 for electroweak V + jets, and Figures 8.3 and 8.4 for strong V + jets.

8.2.2. Electroweak corrections for strong V + jets backgrounds

The strong V + jets samples generated with Sherpa include on-the-fly weights for applying approximate NLO EW corrections based on the electroweak virtual approximation [34]. Three different weights are used corresponding to the following three approaches for evaluating the electroweak correction: additive, multiplicative, and exponential. The procedure for applying the electroweak correction and evaluating its uncertainty is as follows:

1. The weights corresponding to the three approaches for the electroweak correction are applied to produce three different templates for the strong V + jets prediction in the chosen observable.

2. The approach that gives the smallest difference compared to the QCD-only nominal prediction is used as the new nominal prediction.

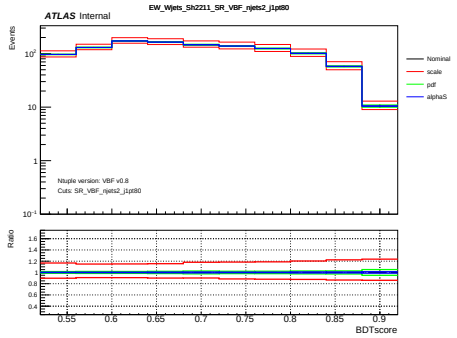

(a) EW W+jets in SR_VBF_njets2

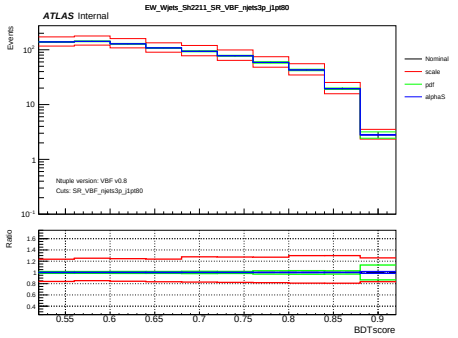

(b) EW W+jets in SR_VBF_njets3p

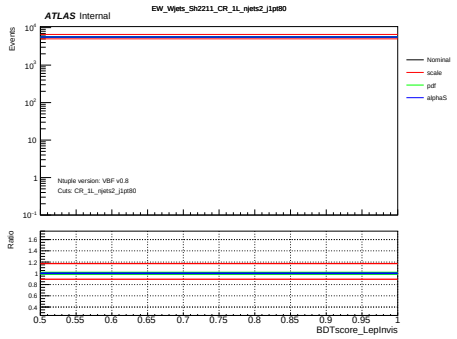

(c) EW W+jets in CR_1L_njets2

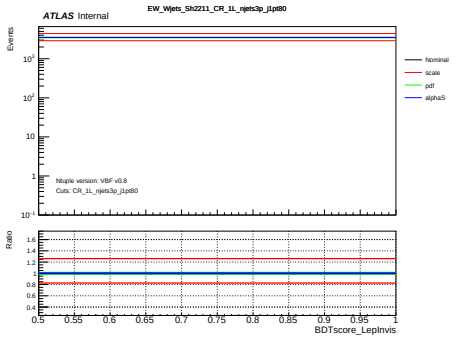

(d) EW W+jets in CR_1L_njets3p

Figure 8.1: Theory uncertainties for EW W+jets in the multi-bin signal regions and single-bin control regions as a function of the BDT score. The BDT score for the control regions denoted as "BDTscore_LepInvis" has been evaluated with input features that treat leptons as invisible.

3. The approach that gives the largest difference compared to the new nominal prediction is used to assign an uncertainty on the correction by symmetrizing the difference to the nominal.

Figure 8.5 shows the prediction for strong V+jets using the three approaches in the various analysis regions. The additive approach is found to be the closest to the QCD-only nominal prediction in all cases and thus the corresponding weight is applied to give the new nominal prediction for the strong V+jets backgrounds. The multiplicative approach produces the largest difference and is used to set the uncertainty on the electroweak correction.

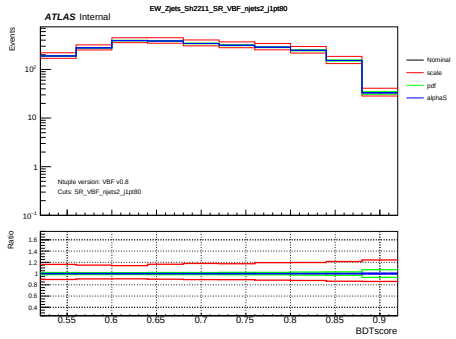

(a) EW Z + jets in SR_VBF_njets2

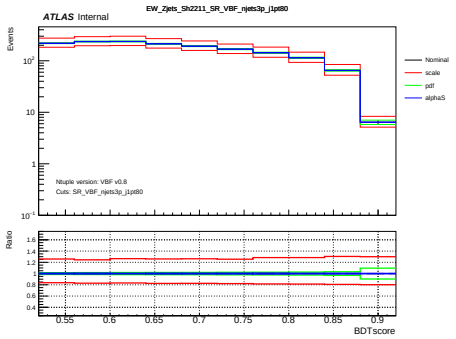

(b) EW Z + jets in SR_VBF_njets3p

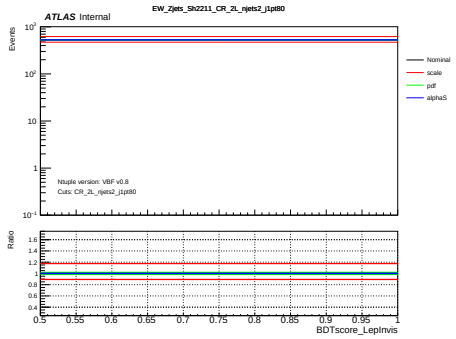

(c) EW Z + jets in CR_2L_njets2

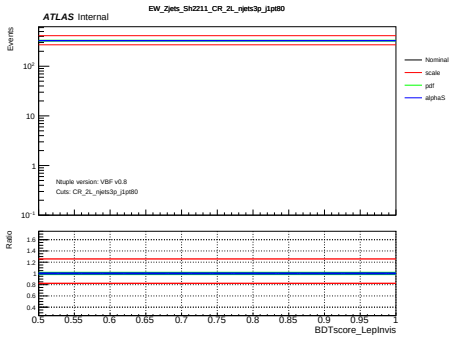

(d) EW Z + jets in CR_2L_njets3p

Figure 8.2: Theory uncertainties for EW Z + jets in the multi-bin signal regions and single-bin control regions as a function of the BDT score. The BDT score for the control regions denoted as "BDTscore_LepInvis" has been evaluated with input features that treat leptons as invisible.

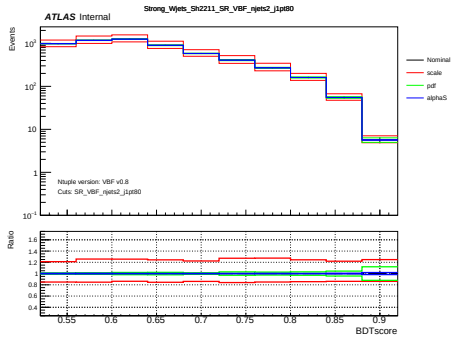

(a) Strong W+ jets in SR_VBF_njets2

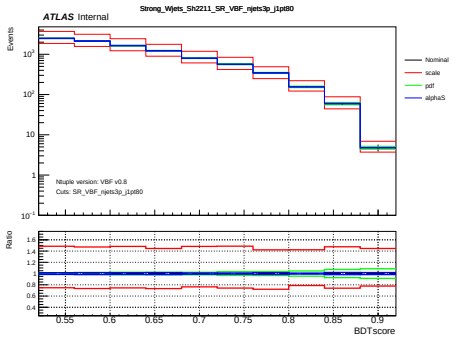

(b) Strong W+ jets in SR_VBF_njets3p

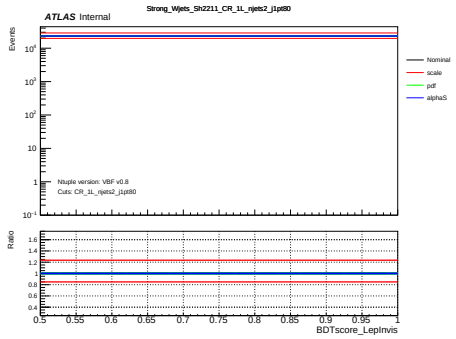

(c) Strong W+ jets in CR_1L_njets2

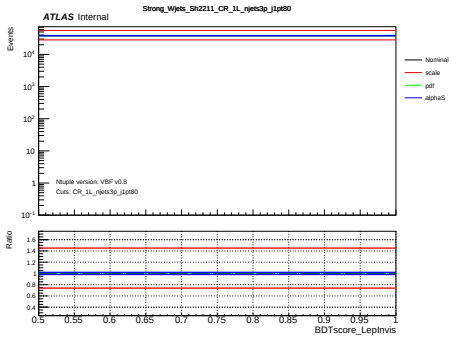

(d) Strong W+ jets in CR_1L_njets3p

Figure 8.3: Theory uncertainties for Strong W+ jets in the multi-bin signal regions and single-bin control regions as a function of the BDT score. The BDT score for the control regions denoted as "BDTscore_LepInvis" has been evaluated with input features that treat leptons as invisible.

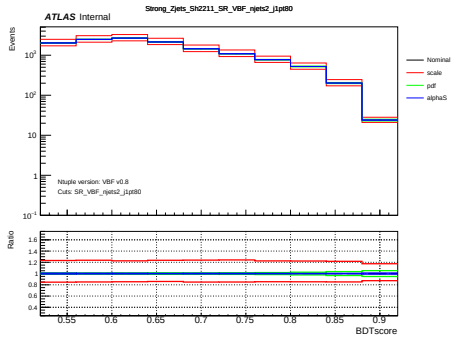

(a) Strong Z + jets in SR_VBF_njets2

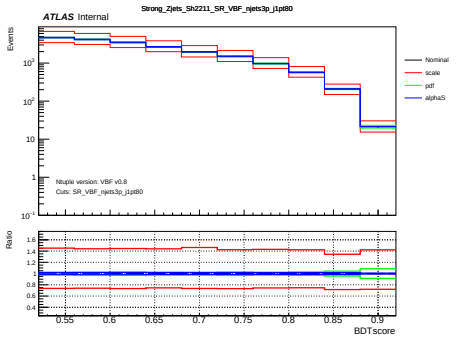

(b) Strong Z + jets in SR_VBF_njets3p

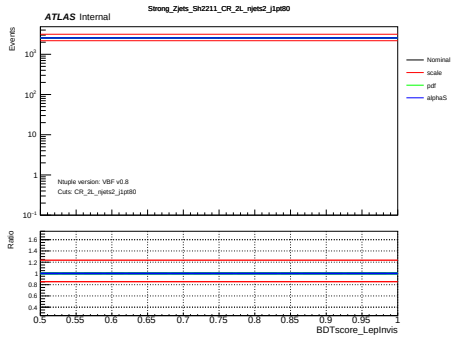

(c) Strong Z + jets in CR_2L_njets2

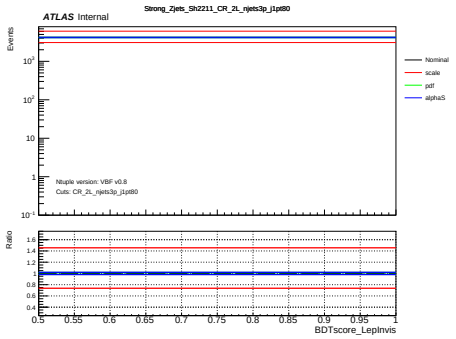

(d) Strong Z + jets in CR_2L_njets3p

Figure 8.4: Theory uncertainties for Strong Z + jets in the multi-bin signal regions and single-bin control regions as a function of the BDT score. The BDT score for the control regions denoted as "BDTscore_LepInvis" has been evaluated with input features that treat leptons as invisible.

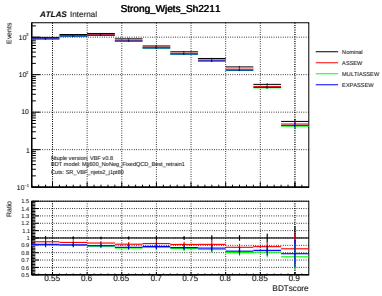

(a) Strong W+ jets in SR_VBF_njets2

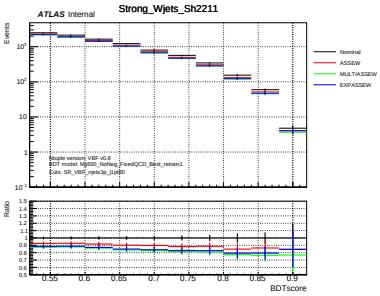

(b) Strong W+ jets in SR_VBF_njets3p

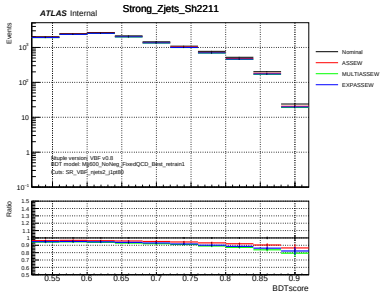

(c) Strong Z + jets in SR_VBF_njets2

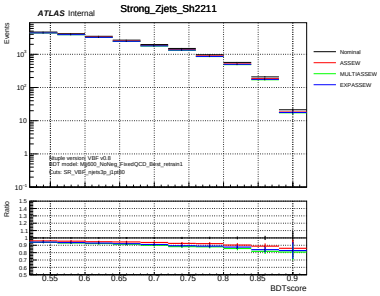

(d) Strong Z + jets in SR_VBF_njets3p

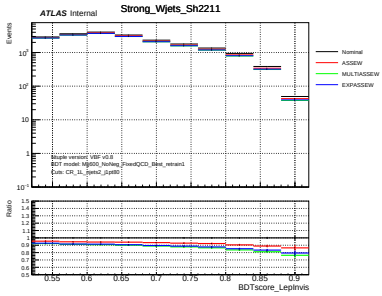

(e) Strong W+ jets in CR_1L_njets2

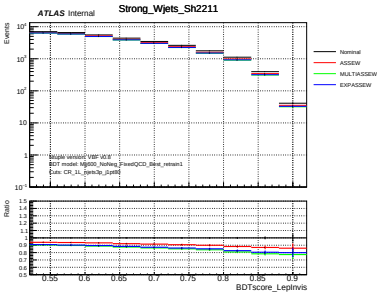

(f) Strong W+ jets in CR_1L_njets3p

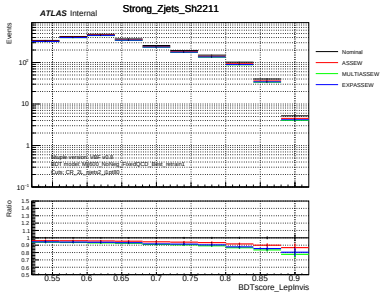

(g) Strong Z + jets in CR_2L_njets2

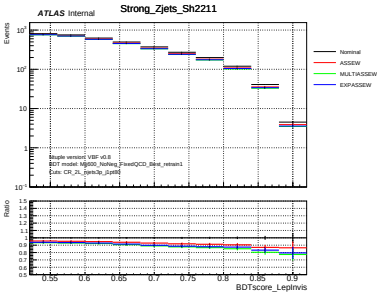

(h) Strong Z + jets in CR_2L_njets3p

Figure 8.5: Prediction for strong V + jets in analysis regions for each of the three different approaches for applying the electroweak correction. The different approaches are labeled as follows: additive (ASSEW), multiplicative (MULTIASSEW), and exponential (EXPASSEW).

8.2.3. Uncertainties on minor backgrounds

For the minor backgrounds such as top and diboson that do not have a dedicated estimation strategy and use Monte Carlo predictions directly, a flat ±30% systematic is applied in the signal regions as a conservative estimate on the impact of theoretical uncertainties.

8.2.4. Theoretical Uncertainties on the expected signal rate

This section describes the general method used for the calculation of the theoretical systematic uncertainties associated with the SUSY signal processes. The uncertainties are calculated in each analysis region for each sample separately.

The following theoretical sources of uncertainty are considered: scale variations, radiation uncertainties, and PDF uncertainties, and the signal cross-section uncertainty. The scale variations have two uncertainties: the factorization and renormalization scale variations (scup and scdw). The radiation uncertainties (up and dw) have five variations: Var1, Var2, Var3a, Var3b, Var3c. They are enveloped by adding in quadrature. Radiation uncertainties are measured by comparing the event yields of the truth-level samples. The scale uncertainty and PDF uncertainty are derived from reconstructed samples.

The final theory uncertainty results for each signal point are calculated. The scale dw/up uncertainties for the 2 jet SR are shown in Table 8.2 and Table 8.4. The scale dw/up uncertainties for the 3+ jet SR are shown in Table 8.3 and Table 8.5. The PDF uncertainties for the 2 jet SR are shown in Table 8.6. The PDF uncertainties for the 3+ jet SR are shown in Table 8.7. The radiation uncertainties for the 2 jet SR are shown in Table 8.8. The radiation uncertainties for the 3+ jet SR are shown in Table 8.9. The dominant theoretical uncertainty comes from the scale uncertainties.

BDT Score	[0.60,0.64]		[0.64,0.68]		[0.68,0.72]		[0.72,0.76]		[0.76,0.80]		[0.80,0.84]		[0.84,0.88]		[0.88,0.92[	
m($\tilde{\chi}_2^0/\tilde{\chi}_1^\pm$,$\tilde{\chi}_1^0$)	dw	up	dw	up	dw	up	dw	up	dw	up	dw	up	dw	up	dw	up
(100,95)	-11.31	14.52	-10.87	13.81	-10.76	13.58	-10.23	12.70	-10.79	13.46	-10.82	13.38	-11.86	14.82	-13.60	17.36
(100,98)	-11.42	14.70	-10.85	13.77	-10.45	13.15	-10.36	12.88	-10.59	13.16	-10.93	13.57	-11.41	14.16	-13.54	17.32
(100,99)	-11.29	14.51	-10.59	13.42	-10.30	12.88	-10.46	13.06	-10.87	13.59	-11.09	13.79	-11.57	14.43	-13.62	17.44
(100,99.5)	-11.52	14.92	-10.79	13.75	-10.88	13.80	-10.51	13.16	-10.76	13.42	-11.13	13.90	-11.52	14.36	-13.41	17.11
(100,99.8)	-11.37	14.66	-10.82	13.75	-10.44	13.13	-10.60	13.28	-10.84	13.57	-11.06	13.80	-11.62	14.50	-13.47	17.19
(130,125)	-10.63	13.43	-10.22	12.79	-10.29	12.82	-10.23	12.61	-10.58	13.06	-11.23	13.96	-11.81	14.78	-13.65	17.44
(130,128)	-10.32	12.97	-9.85	12.17	-10.25	12.76	-10.15	12.50	-10.51	13.00	-10.82	13.34	-11.72	14.60	-13.38	17.02
(130,129)	-10.38	13.08	-10.39	13.05	-10.00	12.39	-10.21	12.62	-10.13	12.37	-11.01	13.63	-11.56	14.38	-13.30	16.92
(130,129.5)	-10.29	12.91	-10.05	12.51	-9.90	12.20	-10.30	12.75	-10.23	12.56	-10.72	13.21	-11.58	14.41	-13.22	16.78
(130,129.8)	-10.35	13.01	-10.02	12.46	-10.10	12.52	-10.17	12.55	-10.44	12.88	-10.91	13.50	-11.53	14.34	-13.27	16.87
(150,145)	-10.45	13.14	-10.55	13.24	-10.45	13.02	-10.48	13.01	-10.59	13.08	-11.09	13.75	-11.64	14.47	-13.48	17.17
(150,148)	-10.59	13.31	-10.41	13.08	-9.96	12.29	-10.46	12.97	-10.44	12.88	-11.00	13.61	-11.54	14.34	-13.27	16.84
(150,149)	-10.44	13.12	-10.06	12.48	-10.27	12.78	-10.25	12.65	-10.55	13.04	-10.84	13.38	-11.63	14.49	-13.41	17.07
(150,149.5)	-10.32	12.95	-10.25	12.79	-10.29	12.78	-10.37	12.84	-10.40	12.81	-10.94	13.52	-11.64	14.49	-13.34	16.95
(150,149.8)	-10.71	13.55	-10.29	12.88	-10.19	12.64	-10.30	12.74	-10.47	12.92	-10.95	13.53	-11.57	14.39	-13.37	17.01

Table 8.2.: (Part 1) Scale dw/up uncertainties for the 2 jet SR. All results are reported as percentages.

BDT Score	[0.60,0.64]		[0.64,0.68]		[0.68,0.72]		[0.72,0.76]		[0.76,0.80]		[0.80,0.84]		[0.84,0.88]		[0.88,0.92[	
m($\tilde{\chi}_2^0/\tilde{\chi}_1^\pm$,$\tilde{\chi}_1^0$)	dw	up	dw	up	dw	up	dw	up	dw	up	dw	up	dw	up	dw	up
(100,95)	-15.39	20.84	-14.98	20.15	-13.93	18.48	-14.96	20.08	-14.44	19.17	-14.77	19.64	-14.97	19.80	-15.41	20.48
(100,98)	-15.14	20.49	-14.70	19.75	-14.50	19.38	-14.51	19.39	-14.32	19.03	-14.24	18.78	-14.95	19.83	-15.89	21.16
(100,99)	-15.36	20.89	-15.18	20.49	-14.97	20.18	-14.57	19.50	-14.32	18.99	-14.79	19.71	-14.78	19.54	-15.37	20.30
(100,99.5)	-15.28	20.71	-14.86	20.00	-14.95	20.14	-15.12	20.37	-14.76	19.71	-14.54	19.28	-14.94	19.81	-15.59	20.61
(100,99.8)	-14.90	20.15	-15.33	20.76	-15.17	20.48	-14.96	20.13	-14.63	19.48	-14.60	19.36	-14.81	19.59	-15.31	20.23
(130,125)	-13.41	17.70	-13.26	17.44	-13.33	17.46	-13.71	18.08	-13.23	17.22	-13.80	18.02	-14.10	18.37	-15.10	19.84
(130,128)	-13.66	18.14	-13.45	17.79	-13.32	17.53	-13.28	17.36	-13.55	17.78	-13.94	18.30	-14.16	18.50	-14.67	19.13
(130,129)	-13.79	18.35	-13.78	18.26	-13.16	17.26	-13.11	17.14	-13.40	17.52	-13.37	17.35	-13.84	17.99	-14.59	19.01
(130,129.5)	-13.32	17.56	-13.60	17.95	-13.67	18.07	-13.39	17.58	-13.38	17.48	-13.63	17.80	-13.54	17.52	-14.57	18.94
(130,129.8)	-13.28	17.57	-13.50	17.89	-13.30	17.49	-13.29	17.40	-13.50	17.68	-13.74	17.96	-13.71	17.83	-14.90	19.50
(150,145)	-13.65	18.13	-13.42	17.72	-13.29	17.46	-13.48	17.70	-13.40	17.48	-13.51	17.55	-13.87	18.02	-14.63	19.09
(150,148)	-13.76	18.30	-13.33	17.58	-13.38	17.60	-13.16	17.20	-13.35	17.38	-13.53	17.60	-13.84	17.99	-15.00	19.73
(150,149)	-13.57	17.99	-13.71	18.15	-13.19	17.30	-13.26	17.33	-13.16	17.08	-13.22	17.11	-13.79	17.93	-14.74	19.23
(150,149.5)	-13.58	17.98	-13.31	17.53	-13.31	17.49	-13.39	17.56	-13.21	17.16	-13.63	17.78	-13.86	18.07	-14.68	19.12
(150,149.8)	-13.65	18.11	-13.75	18.28	-13.06	17.07	-13.06	17.02	-13.58	17.81	-13.52	17.57	-13.63	17.65	-14.81	19.38

Table 8.3.: (Part 1) Scale dw/up uncertainties for the 3+ jet SR. All results are reported as percentages.

BDT Score	[0.60,0.64]		[0.64,0.68]		[0.68,0.72]		[0.72,0.76]		[0.76,0.80]		[0.80,0.84]		[0.84,0.88]		[0.88,0.92[	
m($\tilde{\chi}_2^0/\tilde{\chi}_1^\pm$,$\tilde{\chi}_1^0$)	dw	up	dw	up	dw	up	dw	up	dw	up	dw	up	dw	up	dw	up
(175,170)	-10.98	13.96	-10.67	13.40	-10.35	12.84	-10.63	13.22	-10.94	13.61	-11.18	13.87	-11.91	14.89	-13.51	17.21
(175,173)	-10.86	13.75	-10.39	12.98	-10.60	13.25	-10.66	13.26	-10.63	13.13	-11.31	14.07	-11.89	14.87	-13.47	17.17
(175,174)	-10.99	13.94	-10.97	13.90	-10.34	12.86	-10.45	12.95	-10.78	13.35	-11.12	13.80	-11.81	14.75	-13.48	17.20
(175,174.5)	-10.98	13.94	-10.50	13.17	-10.62	13.31	-10.72	13.36	-10.87	13.49	-11.25	14.00	-11.89	14.85	-13.47	17.16
(175,174.8)	-11.16	14.18	-10.60	13.32	-10.31	12.79	-10.73	13.39	-10.69	13.23	-11.26	14.02	-11.84	14.80	-13.48	17.18
(75,70)	-12.78	16.87	-11.48	14.84	-11.31	14.52	-11.11	14.06	-11.10	13.93	-11.34	14.21	-12.10	15.27	-13.54	17.30
(75,73)	-12.38	16.27	-11.65	15.04	-11.24	14.39	-11.00	13.92	-11.00	13.85	-11.49	14.51	-11.99	15.10	-13.54	17.30
(75,74)	-12.36	16.17	-11.82	15.38	-11.18	14.32	-11.12	14.16	-10.94	13.74	-11.36	14.25	-11.76	14.77	-13.55	17.37
(75,74.5)	-12.68	16.67	-11.87	15.39	-11.73	15.17	-11.26	14.34	-11.00	13.84	-11.69	14.81	-11.80	14.84	-13.59	17.43
(75,74.8)	-12.90	17.05	-12.28	16.09	-11.62	15.00	-11.46	14.66	-11.13	14.03	-11.59	14.63	-11.78	14.79	-13.54	17.36
(90,85)	-11.29	14.50	-10.91	13.93	-10.59	13.35	-10.44	12.98	-10.33	12.73	-11.22	13.99	-12.19	15.38	-13.61	17.41
(90,88)	-11.82	15.36	-11.21	14.39	-10.78	13.66	-10.64	13.32	-10.69	13.34	-11.22	14.03	-11.58	14.45	-13.39	17.08
(90,89)	-11.99	15.63	-11.03	14.10	-10.77	13.67	-10.71	13.46	-10.84	13.55	-11.12	13.86	-11.76	14.72	-13.34	17.01
(90,89.5)	-11.57	14.97	-11.02	14.10	-10.92	13.86	-10.62	13.31	-10.66	13.28	-11.07	13.80	-11.70	14.63	-13.31	16.94
(90,89.8)	-11.57	15.00	-11.29	14.53	-10.85	13.76	-10.57	13.30	-10.55	13.12	-11.03	13.74	-11.70	14.62	-13.38	17.08

Table 8.4.: (Part 2) Scale dw/up uncertainties for the 2 jet SR. All results are reported as percentages.

BDT Score	[0.60,0.64]		[0.64,0.68]		[0.68,0.72]		[0.72,0.76]		[0.76,0.80]		[0.80,0.84]		[0.84,0.88]		[0.88,0.92[	
m($\tilde{\chi}_2^0/\tilde{\chi}_1^\pm$,$\tilde{\chi}_1^0$)	dw	up	dw	up	dw	up	dw	up	dw	up	dw	up	dw	up	dw	up
(175,170)	-13.64	18.07	-13.53	17.84	-13.57	17.86	-13.24	17.28	-13.81	18.14	-13.80	18.02	-14.32	18.71	-15.03	19.72
(175,173)	-13.97	18.60	-13.74	18.20	-13.87	18.34	-13.62	17.89	-13.65	17.87	-14.12	18.56	-14.00	18.26	-14.87	19.48
(175,174)	-14.30	19.15	-13.75	18.21	-14.00	18.57	-13.77	18.14	-13.87	18.26	-14.04	18.41	-13.73	17.79	-14.92	19.53
(175,174.5)	-14.08	18.76	-13.76	18.22	-13.86	18.31	-13.26	17.32	-13.94	18.32	-13.91	18.23	-13.98	18.22	-14.92	19.51
(175,174.8)	-13.93	18.52	-13.94	18.49	-13.81	18.27	-13.55	17.80	-13.74	18.01	-13.72	17.86	-14.07	18.37	-15.11	19.86
(75,70)	-16.48	22.63	-16.12	22.01	-15.91	21.68	-15.84	21.52	-15.51	20.91	-16.13	21.87	-16.34	22.00	-16.70	22.46
(75,73)	-17.00	23.48	-16.09	21.98	-16.12	22.02	-15.71	21.34	-16.02	21.69	-15.59	21.04	-15.57	20.85	-17.06	23.17
(75,74)	-16.81	23.14	-16.71	22.93	-16.21	22.13	-16.00	21.74	-15.78	21.36	-15.61	21.01	-16.04	21.59	-16.24	21.74
(75,74.5)	-16.88	23.19	-16.70	22.97	-16.23	22.16	-16.32	22.26	-16.25	22.11	-15.85	21.41	-16.12	21.76	-16.48	22.14
(75,74.8)	-16.96	23.36	-16.79	23.09	-16.58	22.74	-15.98	21.75	-15.67	21.20	-16.02	21.67	-15.49	20.69	-16.78	22.69
(90,85)	-15.57	21.15	-15.19	20.58	-15.33	20.70	-14.55	19.42	-14.67	19.57	-14.63	19.41	-15.38	20.49	-16.26	21.88
(90,88)	-15.88	21.71	-15.39	20.87	-15.59	21.14	-15.34	20.70	-15.32	20.65	-15.01	20.06	-15.11	20.10	-16.04	21.39
(90,89)	-15.78	21.55	-15.50	21.06	-15.24	20.58	-15.11	20.31	-14.93	20.02	-15.01	20.05	-15.18	20.21	-15.95	21.28
(90,89.5)	-15.64	21.29	-15.87	21.64	-15.56	21.11	-15.20	20.49	-15.14	20.34	-15.18	20.28	-15.09	20.06	-16.18	21.69
(90,89.8)	-15.95	21.73	-15.47	20.96	-15.50	20.99	-15.66	21.21	-14.82	19.84	-15.12	20.20	-14.77	19.51	-15.88	21.17

Table 8.5.: (Part 2) Scale dw/up uncertainties for the 3+ jet SR. All results are reported as percentages.

BDT bin	bin1	bin2	bin3	bin4	bin5	bin6	bin7	bin8
m($\tilde{\chi}_2^0/\tilde{\chi}_1^\pm$,$\tilde{\chi}_1^0$)	Symmetric uncertainty [%]							
(100,95)	7.03	6.35	7.05	6.69	7.55	7.51	8.73	8.85
(100,98)	6.73	7.20	7.68	7.89	6.93	8.37	10.74	11.69
(100,99)	5.66	6.35	6.42	5.30	6.52	9.55	9.44	11.10
(100,99.5)	5.78	6.64	8.30	6.11	8.02	7.67	7.15	10.58
(100,99.8)	5.24	7.04	6.49	7.21	7.52	8.34	8.56	12.62
(130,125)	6.61	6.90	8.27	7.20	7.18	8.56	12.82	17.54
(130,128)	5.77	6.74	7.37	6.86	8.45	8.36	11.04	9.92
(130,129)	5.02	7.93	5.44	8.36	8.49	10.04	9.73	11.24
(130,129.5)	5.04	6.59	6.46	7.52	7.74	8.91	8.74	10.60
(130,129.8)	6.29	6.55	6.28	5.53	10.41	8.73	11.00	10.07
(150,145)	7.75	6.80	7.13	5.16	7.70	8.09	8.36	14.34
(150,148)	5.92	7.62	7.09	6.60	7.28	9.34	9.39	9.58
(150,149)	5.76	6.10	6.60	6.34	7.88	8.09	10.63	10.10
(150,149.5)	6.43	7.58	7.24	7.55	8.44	8.32	10.94	11.79
(150,149.8)	5.61	6.82	6.55	8.08	7.08	8.63	11.09	12.73
(175,170)	7.97	6.78	6.73	8.56	6.51	9.63	10.05	11.53
(175,173)	6.97	7.65	6.95	7.36	8.31	8.70	9.67	11.78
(175,174)	7.94	6.60	7.29	7.79	8.32	10.12	8.24	11.82
(175,174.5)	8.26	6.99	7.55	6.89	7.60	6.72	11.83	11.48
(175,174.8)	7.11	7.12	6.66	9.18	8.72	7.74	8.87	12.75
(75,70)	6.92	7.63	6.31	6.51	7.97	9.03	6.90	11.64
(75,73)	5.28	5.87	6.01	6.57	7.26	6.39	11.73	18.00
(75,74)	4.70	6.26	5.73	7.35	6.07	8.81	8.81	12.80
(75,74.5)	6.98	5.82	6.38	8.53	6.09	8.30	7.96	10.88
(75,74.8)	5.83	4.50	6.88	6.46	6.09	10.05	10.08	12.08
(90,85)	5.59	6.25	6.35	6.52	8.42	9.36	8.38	11.45
(90,88)	4.38	5.41	5.13	6.41	7.31	7.62	8.70	11.24
(90,89)	6.30	7.08	6.99	5.90	7.96	6.37	8.08	13.55
(90,89.5)	5.66	7.02	6.94	7.14	8.08	6.58	7.30	11.09
(90,89.8)	8.16	4.94	6.91	7.65	6.44	7.48	7.39	11.81

Table 8.6.: Symmetric PDF uncertainty for the 2 jet SR. All results are reported as percentages.

BDT bin	bin1	bin2	bin3	bin4	bin5	bin6	bin7	bin8
$m(\tilde{\chi}_2^0/\tilde{\chi}_1^\pm,\tilde{\chi}_1^0)$	Symmetric uncertainty [%]							
(100,95)	5.04	8.26	6.61	6.93	8.02	14.56	11.56	8.00
(100,98)	5.21	5.96	5.44	6.83	7.66	8.55	9.01	14.43
(100,99)	4.97	6.41	7.35	6.08	7.21	7.18	6.64	13.09
(100,99.5)	5.31	5.20	5.29	6.19	6.53	6.59	9.09	14.61
(100,99.8)	5.78	5.11	4.64	7.25	7.01	7.80	10.75	11.09
(130,125)	5.97	6.22	6.26	7.55	7.69	6.99	13.54	10.20
(130,128)	6.25	6.50	6.56	7.59	6.77	8.55	10.47	9.92
(130,129)	5.41	5.97	7.45	7.45	10.33	8.12	8.65	11.24
(130,129.5)	6.52	6.35	6.41	6.56	7.07	8.71	10.75	12.43
(130,129.8)	7.32	7.85	6.72	6.55	6.98	6.78	11.65	11.75
(150,145)	5.78	7.02	5.60	8.10	7.66	7.64	10.14	12.23
(150,148)	5.10	5.31	6.61	6.78	6.10	9.18	9.03	9.85
(150,149)	5.78	5.30	6.97	6.85	7.21	9.09	7.93	13.77
(150,149.5)	6.81	6.69	8.10	7.29	7.01	9.26	7.12	12.84
(150,149.8)	6.52	6.93	5.18	6.63	7.17	7.12	8.85	12.62
(175,170)	8.08	6.66	49.74	6.95	10.26	7.05	9.53	14.06
(175,173)	6.24	6.80	8.54	8.13	6.62	7.46	11.11	12.03
(175,174)	6.46	8.40	6.21	6.57	7.56	8.64	7.94	15.92
(175,174.5)	7.02	6.56	7.75	6.69	8.86	9.08	8.60	11.29
(175,174.8)	5.15	6.06	7.10	7.03	7.91	7.84	8.73	11.43
(75,70)	5.60	5.70	4.61	4.74	4.75	8.79	6.61	17.10
(75,73)	5.51	5.48	5.18	4.71	6.66	7.89	6.61	18.63
(75,74)	5.95	6.33	4.39	6.17	7.77	8.45	8.68	16.07
(75,74.5)	4.79	3.81	4.61	6.16	6.02	9.04	8.53	9.39
(75,74.8)	4.15	6.41	4.97	5.41	7.10	6.37	7.08	11.65
(90,85)	5.19	5.33	4.44	5.08	5.12	9.01	8.55	11.14
(90,88)	4.93	6.65	5.72	5.83	7.97	8.13	8.00	10.72
(90,89)	6.22	4.53	6.03	5.22	7.52	8.14	8.40	7.59
(90,89.5)	4.88	5.78	5.58	6.03	5.35	9.64	6.92	12.55
(90,89.8)	5.39	6.29	5.33	5.15	4.91	7.47	13.87	13.64

Table 8.7.: Symmetric PDF uncertainty for the 3+ jet SR. All results are reported as percentages.

BDT Score	[0.6,0.64]	[0.64,0.68]	[0.68,0.72]	[0.72,0.76]	[0.76,0.8]	[0.8,0.92[
$m(\tilde{\chi}_2^0/\tilde{\chi}_1^\pm,\tilde{\chi}_1^0)$	Symmetric uncertainty [%]					
(100,95)	16.72	13.67	14.61	16.42	15.83	13.80
(100,98)	9.44	12.43	15.54	12.64	14.40	14.37
(100,99)	12.36	13.69	13.50	12.37	12.34	11.99
(100,99.5)	15.23	13.10	12.80	19.01	15.41	14.49
(100,99.8)	9.37	18.98	22.49	19.30	16.30	17.87
(130,125)	11.71	11.54	13.29	12.94	9.75	13.80
(130,128)	12.90	7.38	11.35	14.04	15.34	15.67
(130,129)	13.26	16.00	11.17	14.01	12.08	12.43
(130,129.5)	12.07	12.30	13.55	13.43	10.29	11.18
(130,129.8)	11.47	15.50	13.36	17.55	19.45	12.57
(150,145)	13.01	12.86	13.38	10.66	13.76	12.68
(150,148)	8.80	11.62	12.43	14.99	14.44	15.46
(150,149)	12.63	12.56	10.41	14.60	10.22	10.37
(150,149.5)	9.41	16.65	10.74	10.43	12.80	12.55
(150,149.8)	11.02	14.08	10.38	14.34	18.53	15.26
(175,170)	11.48	12.24	14.85	8.92	13.48	10.83
(175,173)	10.79	10.44	14.17	10.57	13.87	12.33
(175,174)	11.82	10.81	7.89	13.38	12.23	9.24
(175,174.5)	10.80	9.07	10.88	10.34	10.95	11.98
(175,174.8)	11.04	11.53	10.80	12.97	15.10	8.79
(75,70)	9.41	10.48	10.84	9.40	7.27	10.81
(75,73)	9.10	10.27	6.84	10.18	13.66	10.53
(75,74)	10.05	8.02	11.24	12.69	11.70	11.25
(75,74.5)	13.83	12.16	7.19	11.70	9.27	9.48
(75,74.8)	13.61	11.32	13.54	10.48	11.02	11.71
(90,85)	10.54	9.81	8.75	7.08	7.79	8.28
(90,88)	7.71	11.57	9.26	9.81	11.36	9.10
(90,89)	9.56	9.99	9.17	12.44	10.74	10.60
(90,89.5)	9.69	12.93	11.79	10.91	10.01	10.11
(90,89.8)	7.60	9.11	14.04	7.31	10.87	12.22

Table 8.8.: Symmetric radiation uncertainty for the 2 jet SR. All results are reported as percentages. Because the statistics of the last three bins are small and the statistical uncertainty is large, the last three bins are merged when evaluating the uncertainty for the corresponding SR bins.

BDT Score	[0.6,0.64]	[0.64,0.68]	[0.68,0.72]	[0.72,0.76]	[0.76,0.8]	[0.8,0.92[
$m(\tilde{\chi}_2^0/\tilde{\chi}_1^\pm,\tilde{\chi}_1^0)$	Symmetric uncertainty [%]					
(100,95)	5.40	7.03	6.26	7.85	8.38	9.69
(100,98)	7.91	7.22	10.46	7.55	7.35	11.30
(100,99)	8.74	9.56	8.44	7.65	12.75	10.79
(100,99.5)	8.02	8.25	11.66	11.73	10.26	10.21
(100,99.8)	9.26	13.20	14.14	10.68	16.52	14.72
(130,125)	6.69	5.51	10.66	12.28	8.39	7.32
(130,128)	6.27	6.65	11.15	10.12	7.28	10.58
(130,129)	4.35	8.86	8.20	9.67	9.91	7.08
(130,129.5)	7.33	9.65	10.64	6.83	9.38	8.35
(130,129.8)	6.75	7.81	5.75	10.26	16.65	9.95
(150,145)	7.94	6.73	8.75	5.20	7.98	7.05
(150,148)	6.66	8.65	6.30	8.65	9.79	8.89
(150,149)	6.60	6.70	9.10	11.08	6.37	8.92
(150,149.5)	9.25	8.09	7.16	7.91	9.17	9.18
(150,149.8)	6.25	9.83	8.67	13.45	11.90	15.35
(175,170)	7.35	7.74	7.29	9.09	6.89	6.58
(175,173)	4.19	10.27	5.83	6.52	7.14	8.53
(175,174)	6.43	5.54	8.34	7.64	7.91	6.59
(175,174.5)	7.65	9.07	7.28	6.51	11.63	9.21
(175,174.8)	5.34	8.84	6.42	11.36	8.34	10.27
(75,70)	6.15	6.34	8.98	9.36	5.41	5.91
(75,73)	5.49	5.31	7.90	7.76	7.46	8.79
(75,74)	7.18	5.71	4.27	7.86	8.58	4.21
(75,74.5)	6.11	5.68	7.25	3.98	5.88	8.68
(75,74.8)	5.91	4.17	7.46	7.56	7.55	6.86
(90,85)	6.30	7.33	4.51	7.19	6.54	4.54
(90,88)	5.26	7.44	6.17	6.31	6.34	6.76
(90,89)	7.17	8.63	5.04	6.12	7.02	5.37
(90,89.5)	6.58	6.26	6.94	5.05	6.42	4.50
(90,89.8)	8.26	6.20	5.71	6.84	6.16	9.23

Table 8.9.: Symmetric radiation uncertainty for the 3+ jet SR. All results are reported as percentages. Because the statistics of the last three bins are small and the statistical uncertainty is large, the last three bins are merged when evaluating the uncertainty for the corresponding SR bins.

8.3. Uncertainty on the QCD background estimate

8.3.1. Uncertainty on the QCD background estimate for SR

The systematic uncertainties for the QCD background estimate includes statistical uncertainties, uncertainties from the ABCD transfer factor, experimental uncertainties in the Monte Carlo subtraction in CRA, uncertainties from the BDT score fit in CRA and uncertainties from the $E_{\mathrm{T}}^{\mathrm{miss}}$ trigger inefficiency when a looser $E_{\mathrm{T}}^{\mathrm{miss}}$ cut is used. A summary of the systematic uncertainties for the QCD estimation that are applied in the signal regions is presented in Table 8.10.

Name	Systematic uncertainty
Statistical uncertainty	± 9.4%
Uncertainties from ABCD structure	± 9.5%
Experimental uncertainties in MC subtraction in CRA	± 34%
Theoretical uncertainties in MC subtraction in CRA	± 97.5%
Uncertainties from BDT fit in CRA	± 12.7%
Uncertainties from MET trigger inefficiency	± 5%

Table 8.10.: Summary of systematic uncertainties for the QCD estimation in the signal regions.

The statistical uncertainty has been calculated in Table 7.3. The statistics for QCD in the SR suggests that the statistical uncertainty is 9.4%.

The uncertainty from ABCD structure is calculated by comparing between the transfer factor calculated by CRC/CRB and the one calculated by VRF/VRE.

(8.3.1)

$$TF_{CRC/CRB} = (data - otherMC)_{CRC}/(data - otherMC)_{CRB} = 3371/5072 = 0.665$$

(8.3.2)

$$TF_{VRF/VRE} = (data - otherMC)_{VRF}/(data - otherMC)_{VRE} = 3143/4319 = 0.728$$

(8.3.3)

$$Uncertainty = (TF_{VRF/VRE} - TF_{CRC/CRB})/TF_{CRC/CRB} = (0.728 - 0.665)/0.665 = 9.5\%$$

The remaining uncertainties considered are related to the experimental and theoretical uncertainties on the MC subtraction in CRA. The relative uncertainty on $N_{\text{QCD}}^{\text{CRA}}$ is given by

(8.3.4)

$$\begin{aligned}\frac{\Delta N_{\text{QCD}}^{\text{CRA}}}{N_{\text{QCD}}^{\text{CRA}}} = \frac{\Delta N_{\text{nonQCD,MC}}^{\text{CRA}}}{N_{\text{QCD}}^{\text{CRA}}} &= \frac{N_{\text{nonQCD,MC}}^{\text{CRA}}}{N_{\text{QCD}}^{\text{CRA}}} \frac{\Delta N_{\text{nonQCD,MC}}^{\text{CRA}}}{N_{\text{nonQCD,MC}}^{\text{CRA}}} \\ &= \frac{8611}{2197} \frac{\Delta N_{\text{nonQCD,MC}}^{\text{CRA}}}{N_{\text{nonQCD,MC}}^{\text{CRA}}} \\ &\simeq 3.9 \frac{\Delta N_{\text{nonQCD,MC}}^{\text{CRA}}}{N_{\text{nonQCD,MC}}^{\text{CRA}}} .\end{aligned}$$

The experimental uncertainties in CRA are listed in Table 8.11 and in total are found to be 8.75%. This results in an experimental uncertainty on the QCD estimate in the SR of around 34%. The non-QCD background in CRA is dominated by V + jets events, hence a 25% theoretical uncertainty is assumed based on taking the magnitude of the theory uncertainties observed in the SR as a reference. This results in a 97.5% uncertainty due to the theory uncertainties. Although there is the presence of such large uncertainties on the QCD estimate in the signal regions, the impact of these uncertainties on the final results of the search are minimal since the QCD background constitutes a very small portion of the total background in the signal regions.

Uncertainty of channel	CRA
Total background expectation	9724.60
Total statistical ($\sqrt{N_{\text{exp}}}$)	±98.61
Total background systematic	±850.84 [8.75%]
alpha_JES_Flavor_Composition	±478.82
alpha_JES_Flavor_Response	±377.37
alpha_JES_EtaIntercalibration_Modelling	±280.32
alpha_btag_CT	±266.25
alpha_btag_ExtraFromCharm	±226.75
alpha_JES_EffectiveNP_Modelling1	±175.71
alpha_JES_Pileup_RhoTopology	±164.97
alpha_btag_LightT	±145.58
alpha_JES_EffectiveNP_Mixed1	±121.39
alpha_JES_Pileup_OffsetMu	±86.55
alpha_JES_EtaIntercalibration_NonClosure_2018data	±86.05
alpha_JER_EffectiveNP_1	±85.89
alpha_JES_Pileup_OffsetNPV	±84.98
alpha_JER_EffectiveNP_2	±71.15
alpha_JES_Pileup_PtTerm	±65.24
gamma_stat_CRA_cuts_bin_0	±62.87
alpha_JES_EffectiveNP_Mixed2	±54.90
alpha_Pileup	±38.46
alpha_JES_EffectiveNP_Modelling2	±38.41
alpha_JER_EffectiveNP_6	±32.23
alpha_MET_SoftTrk_Scale	±31.63
alpha_JES_EffectiveNP_Statistical1	±29.44
alpha_btag_BT	±26.29
alpha_MET_SoftTrk_ResoPara	±24.73
alpha_JES_EtaIntercalibration_TotalStat	±24.49
alpha_JER_EffectiveNP_4	±24.31
alpha_JER_DataVsMC_MC16	±21.67
alpha_JER_EffectiveNP_12restTerm	±21.18
alpha_btag_Extra	±18.89
alpha_JES_EffectiveNP_Statistical3	±18.73
alpha_JER_EffectiveNP_3	±13.78
alpha_JER_EffectiveNP_5	±13.39
alpha_MET_SoftTrk_ResoPerp	±13.21
alpha_JES_EffectiveNP_Modelling3	±12.89
alpha_JES_EffectiveNP_Detector1	±12.54
alpha_JES_EffectiveNP_Modelling4	±11.92
alpha_JvtEfficiency	±10.17
alpha_JES_EffectiveNP_Mixed3	±9.63
alpha_JES_EffectiveNP_Statistical6	±8.26
alpha_EG_SCALE_ALL	±7.60
alpha_JER_EffectiveNP_8	±6.82
alpha_JES_EffectiveNP_Statistical2	±5.97
alpha_JES_EtaIntercalibration_NonClosure_negEta	±5.86
alpha_JER_EffectiveNP_11	±5.28
alpha_JES_EffectiveNP_Statistical4	±5.22
alpha_JER_EffectiveNP_9	±4.92
alpha_JES_EtaIntercalibration_NonClosure_posEta	±4.66
alpha_JES_PunchThrough_MC16	±4.55
alpha_JES_EffectiveNP_Detector2	±3.16
alpha_JER_EffectiveNP_10	±2.82
alpha_JES_EtaIntercalibration_NonClosure_highE	±1.94
alpha_JES_EffectiveNP_Statistical5	±1.74
alpha_MUON_SCALE	±1.52
alpha_JER_EffectiveNP_7	±1.29
alpha_EG_RESOLUTION_ALL	±0.80
alpha_MUON_MS	±0.52
alpha_MUON_ID	±0.41
alpha_MUON_SAGITTA_RESBIAS	±0.11
alpha_MUON_SAGITTA_DATASTAT	±0.08

Table 8.11.: Breakdown of the dominant systematic uncertainties on background estimates in the various signal regions. Note that the individual uncertainties can be correlated, and do not necessarily add up quadratically to the total background uncertainty. The percentages show the size of the uncertainty relative to the total expected background.

The BDT score fit is performed in CRA and the function with fit parameters used are shown as below:

$$QCD = p1 * e^{-(BDTscore-0.250)^2/p2} - p3 + p4 * BDTscore\,. \tag{8.3.5}$$

Based on the fit parameters and their errors as shown in Tables 8.12 and 8.13, one can tune up and down each fit parameter by 1σ to derive the impact on the QCD yields as demonstrated in Tables 8.14 and 8.15. The largest impact on the QCD estimation from this method comes from the parameter p2, leading to a fit uncertainty of 12.7%.

	Value	Error
p1	2393.34	92.98
p2	0.150863	0.005824
p3	1544.56	22.62
p4	-1532.12	22.39

Table 8.12.: QCD fit parameters and their errors associated with the fit function in inclusive BDT CRA.

	Value	Error
p1	2251.14	111.12
p2	0.129987	0.005467
p3	1151.14	19.90
p4	-1120.78	19.50

Table 8.13.: QCD fit parameters and their errors associated with the fit function in BDT CRA (>=3J).

8.3.2. Uncertainty on the QCD background estimate for 0L VR

In the 0L VR, similar uncertainties are considered. The statistical uncertainty is the same as the one for the SR. The uncertainties from the ABCD structure are also the same as the one in the SR but with the opposite sign. The experimental uncertainties

	$+1\sigma$	-1σ
Nominal value	2202	
Change p1	2451	1953
Change p2	2475	1923
Change p3	2365	2039
Change p4	2426	1978

Table 8.14.: Fitted QCD for nominal fit parameters and tuned up and down for each fit parameter by 1σ in inclusive BDT CRA.

	$+1\sigma$	-1σ
Nominal value	2133	
Change p1	2382	1884
Change p2	2394	1867
Change p3	2276	1990
Change p4	2328	1938

Table 8.15.: Fitted QCD for nominal fit parameters and tuned up and down for each fit parameter by 1σ in BDT CRA (>=3J).

in the MC subtraction in VRE are approximated by those derived for CRA. The same impact of the theoretical uncertainties on the non-QCD MC predictions as in the SR are assumed in this VR. The summary of the systematic uncertainties for the 0L VR is shown in Table 8.16.

Name	Systematic uncertainty
Statistical uncertainty	± 9.4%
Uncertainties from ABCD structure	± 9.5%
Experimental uncertainties in MC subtraction in VRE	± 34%
Theoretical uncertainties in MC subtraction in VRE	± 97.5%
Theoretical uncertainties in MC subtraction in CRA	± 30%
Uncertainties from MET trigger inefficiency	± 5%

Table 8.16.: Summary of systematic uncertainties for the QCD estimation in the 0L VR.

8.4. Normalized Systematics in the Transfer Factor Approach

This analysis makes use of the transfer factor approach in which control regions are used to constrain the normalizations for the corresponding backgrounds that get propagated to the signal regions in the simultaneous fit. A key concept in this approach is that the background estimated in the signal region can be thought of as being the result of multiplying the fitted yield for that background in the corresponding control region by a transfer factor. This transfer factor would be the ratio of the predicted background yields in the signal region to those of the control region. Since the transfer factor is the ratio of Monte Carlo predictions, systematic uncertainties on the background predictions can be partially cancelled in this approach such that what remains are residual uncertainties on the extrapolation. The degree to which the systematic uncertainties can be cancelled in this procedure depends on how similar the systematic variations are between the signal and control regions.

This approach is built in the HistFitter [40] framework that is used for constructing the fit workspace through the use of "Norm" type systematics. By declaring a set of analysis regions as normalization regions, HistFitter normalizes the systematic uncertainties based on a normalization computed from the normalization regions. These "Norm" type systematics are to be specified only for samples with normalization factors that are to be normalized via dedicated control regions. In this analysis the V+jets backgrounds are to be normalized based on the W and Z control regions thus all systematic uncertainties for these samples are chosen to be normalized. The normalization regions are set to include both the W and Z control regions but are defined separately for the 2 and 3+ jet regions.

8.5. Smoothing of systematic templates

The up and down variations for certain systematics were smoothed across bins so as to avoid large fluctuations in the variations between adjacent bins. This was done to make the variations more well-behaved and stable such that the corresponding nuisance parameters would avoid being significantly pulled and constrained. The smoothing is done using a package called the CommonSystSmoothingTool. The algorithm used for performing the smoothing is based on one utilized by the TRExFitter [55] package with the following steps:

1. The systematic histograms are rebinned until the relative uncertainty is below a tolerance.

2. If the number of slopes in the plot of the ratio to the nominal are below a user-specified threshold, then the tolerance is halved and the first step is repeated.

3. Finally the native smoothing algorithm based on running medians from ROOT [44] is run to avoid artificially flat uncertainties from the rebinning procedure.

The following is a list of systematics for which smoothing is applied that includes those related to jet energy scale and resolution, $E_{\mathrm{T}}^{\mathrm{miss}}$, and strong W+jets scale uncertainties:

- JES_Flavor_Composition
- JES_Flavor_Response
- JES_Pileup_OffsetMu

- JES_Pileup_OffsetNPV
- JES_Pileup_RhoTopology
- JET_JER_DataVsMC_MC16
- JET_JER_EffectiveNP_1
- JET_JER_EffectiveNP_10
- JET_JER_EffectiveNP_11
- JET_JER_EffectiveNP_12restTerm
- JET_JER_EffectiveNP_2
- JET_JER_EffectiveNP_3
- JET_JER_EffectiveNP_4
- JET_JER_EffectiveNP_5
- JET_JER_EffectiveNP_6
- JET_JER_EffectiveNP_7
- JET_JER_EffectiveNP_8
- JET_JER_EffectiveNP_9
- MET_SoftTrk_ResoPerp
- MET_SoftTrk_Scale
- Strong_Wjets_scale

The reasoning behind why these particular systematics have been chosen to be smoothed is because these were the ones that had shown significant pulls or constraints when a partial unblinding was done for the first two bins of the signal regions (which have since been converted to validation regions). The smoothing is only performed for the multi-bin regions in this search as the single-bin regions hold no shape information.

Chapter 9

Results

9.1. Statistical Model

The statistical analysis of this search aims to determine the compatibility of the observed data to the prediction of the statistical model. This is done based on performing a simultaneous fit of the analysis regions and using the profile likelihood method. The statistical model is constructed based on the HistFactory [59] probability model using template histograms. The model consists of channels (regions) with one or more bins that have disjoint event selections. The bins are populated by events from the various signal and background processes (samples) that determine the expected number of events. The event rates of the samples may be modified by nuisance parameters that parametrize the impact of statistical and systematic uncertainties. The likelihood function L can be written as

$$L(\mathbf{n}, \boldsymbol{\theta}^{'} \mid \mu_{\text{sig}}, \mathbf{b}, \boldsymbol{\theta}) = \prod_{c \in \text{channels}} \prod_{i \in \text{bins}} \text{Pois}(n_{ci} \mid \lambda_{ci}(\mu_{\text{sig}}, \mathbf{b}, \boldsymbol{\theta})) \times C(\boldsymbol{\theta}^{'} \mid \boldsymbol{\theta}) \,. \tag{9.1.1}$$

The first term in the likelihood represents the product of the Poisson probabilities for each bin across all channels based on the number of expected (λ_{ci}) and observed (n_{ci}) events. The expected number of events λ_{ci} depends on the signal strength parameter

μ_{sig} (which is the parameter of interest in this search), the background prediction $\mathbf{b}$, and the nuisance parameters $\boldsymbol{\theta}$. The second term in the likelihood denoted as C is the constraint term for the nuisance parameters $\boldsymbol{\theta}$ based on auxiliary measurements $\boldsymbol{\theta}'$. From this definition for the likelihood, the profile likelihood ratio is defined as

$$\lambda(\mu_{\text{sig}}) = \frac{L(\mu_{\text{sig}}, \hat{\hat{\boldsymbol{\theta}}})}{L(\hat{\mu}_{\text{sig}}, \hat{\boldsymbol{\theta}})} \tag{9.1.2}$$

where $\hat{\mu}_{\text{sig}}$ and $\hat{\boldsymbol{\theta}}$ are the values for the signal strength and nuisance parameters that maximize the likelihood function. $\hat{\hat{\boldsymbol{\theta}}}$ are the values of the nuisance parameters that maximizes L for a particular choice of μ_{sig}. Since the likelihood is non-negative and the denominator of the profile likelihood ratio is the maximal value of L, the range of possible values is $0 \leq \lambda(\mu_{\text{sig}}) \leq 1$ with values closer to 1 signifying better agreement with the observed data for a particular value of μ_{sig}. A test statistic is constructed as

$$t_\mu = -2 \ln \lambda(\mu) \tag{9.1.3}$$

that can be used for hypothesis testing. There are modified definitions of the test statistic that are used depending on the bounds for the signal strength and whether the test is being performed for discovery or exclusion as described in [58]. The p-value can be computed for an observed value of the test statistic $t_{\mu,\text{obs}}$ as

$$p_\mu = \int_{t_{\mu,\text{obs}}}^{\infty} f(t_\mu|\mu)\, dt_\mu \tag{9.1.4}$$

where $f(t_\mu|\mu)$ is the distribution of the test statistic t_μ for a given μ. In this search the p-values are evaluated using approximations for the distributions of the test statistic based on asymptotic formulae that are valid in the limit of a large data sample [58]. When performing the exclusion hypothesis tests, limits are set using the CL_s [103]

method with the CL_s defined as

$$\mathrm{CL}_s = \frac{p_{s+b}}{1 - p_b} \tag{9.1.5}$$

in which p_{s+b} is the p-value for the nominal signal-plus-background hypothesis with $\mu_{\mathrm{sig}} = 1$ and p_b is the p-value for the background-only hypothesis. The upper limit on the signal strength is determined based on the value for which the corresponding CL_s falls below the alpha level which is set to $\alpha = 0.05$. Thus the results for this search are reported at 95% confidence level (CL).

Following the transfer factor method, the normalization factors for the W+jets and Z+jets backgrounds enter into the fit as floating parameters such that these backgrounds are constrained in the signal/validation regions through the corresponding control regions during the simultaneous fit. Separate normalization factors are defined based on the jet multiplicity in the same manner that the control regions are defined. This leads to the four background normalization factors that are denoted as mu_Wjets_njets2 for W+jets in the 2 jet regions, mu_Wjets_njets3p for W+jets in the 3+ jet regions, mu_Zjets_njets2 for Z+jets in the 2 jet regions, and mu_Zjets_njets3p for Z+jets in the 3+ jet regions. The same normalization factor is applied to both the strong and electroweak V+jets in each case. Regarding the implementation of the various systematic uncertainties, each is incorporated in the fit as a floating nuisance parameter that may adjust the normalization and/or shape of the associated sample across the analysis regions. These fit parameters are initialized with a value of zero and specified with up/down variations corresponding to the $\pm 1\sigma$ deviations for a Gaussian constraint. The experimental uncertainties are treated as correlated between all samples and across all regions. Theory uncertainties associated with scale variations of the V+jets backgrounds are treated as independent parameters between both the process (W and Z) and the component (strong and electroweak).

They are correlated across all analysis regions which means that there are ultimately four different nuisance parameters that are included in the fit for these uncertainties. This scheme is also applied in the same manner for the PDF and α_s uncertainties. Minor backgrounds are grouped together with "top" denoting the backgrounds from $t\bar{t}$ and single-top production while "other" contains multiboson backgrounds from VV and VVV. The ABCD regions used for the data-driven estimation of the multijet background are not included as part of the simultaneous fit described here. Instead, the data-driven multijet yields and uncertainties have been manually input into the statistical model based on the ABCD estimation that was performed separately.

The construction of the workspace and running of the fit is conducted using the HistFitter [40] package. Some figures with fit results are also produced after converting the HistFactory workspace produced with HistFitter to the pyhf [79, 80] JSON format and running the fit using pyhf while producing figures using the cabinetry [45] package.

9.2. Background-only Fit in Control Regions

The following results are from a fit that only includes the control regions. The control regions include the W control regions (CR_1L_njets2 and CR_1L_njets3p) and the Z control regions (CR_2L_njets2 and CR_2L_njets3p). Each of these regions consist of a single bin ranging from a BDT score of 0.5 to 0.84 . Only the background samples are included in this fit. The four floating background normalization factors are included in the fit to properly normalize the W + jets and Z + jets backgrounds according the the jet multiplicity requirement.

Table 9.1 shows the pre-fit and post-fit yields in the control regions. The pre-fit and post-fit distributions are shown in Figures 9.1 and 9.2. Table 9.2 shows a breakdown

channel	CR_1L_njets2	CR_1L_njets3p	CR_2L_njets2	CR_2L_njets3p
Observed events	21216	41814	2426	4633
Fitted bkg events	21215.37 ± 145.66	41813.42 ± 204.51	2425.70 ± 49.25	4632.92 ± 68.07
Fitted Strong Z + jets events	378.36 ± 11.43	843.61 ± 22.95	1944.68 ± 41.07	4009.59 ± 67.25
Fitted Strong W+ jets events	16221.77 ± 123.08	32914.91 ± 390.05	$0.27^{+0.34}_{-0.27}$	0.63 ± 0.62
Fitted EW Z + jets events	56.46 ± 1.44	56.54 ± 1.74	397.67 ± 8.50	320.59 ± 5.49
Fitted EW W+ jets events	3882.15 ± 29.49	3081.20 ± 36.57	0.00 ± 0.00	0.00 ± 0.00
Fitted top events	323.91 ± 31.48	3189.20 ± 259.92	20.36 ± 1.85	85.40 ± 8.31
Fitted other events	352.72 ± 13.06	1727.96 ± 134.58	62.71 ± 3.07	216.71 ± 19.10
MC exp. SM events	26323.50 ± 135.25	42276.80 ± 428.96	2908.96 ± 17.26	4442.56 ± 37.27
MC exp. Strong Z + jets events	456.37 ± 9.00	806.52 ± 15.40	2345.86 ± 14.76	3833.35 ± 25.98
MC exp. Strong W+ jets events	20271.23 ± 98.66	33375.26 ± 163.30	$0.34^{+0.42}_{-0.34}$	0.64 ± 0.63
MC exp. EW Z + jets events	68.10 ± 1.04	54.05 ± 1.33	479.70 ± 2.67	306.49 ± 2.18
MC exp. EW W+ jets events	4851.25 ± 22.48	3124.29 ± 14.61	0.00 ± 0.00	0.00 ± 0.00
MC exp. top events	323.86 ± 31.69	3188.91 ± 261.51	20.36 ± 1.86	85.39 ± 8.36
MC exp. other events	352.70 ± 13.13	1727.76 ± 135.41	62.70 ± 3.09	216.68 ± 19.22

Table 9.1.: Yields table for background-only fit of control regions.

of the contribution each systematic has in the control regions. Figures 9.3, 9.4, and 9.5 show respectively the fitted normalization factors, pulls and constraints on the fit parameters, and correlation matrix. The differences observed between the normalization factors that are measured in the regions requiring exactly two jets and at least three jets further motivates the need for these separate control regions. The fitted values are mu_Wjets_njets2 = 0.8002 ± 0.0072, mu_Zjets_njets2 = 0.8289 ± 0.0181, mu_Wjets_njets3p = 0.9862 ± 0.0129, and mu_Zjets_njets3p = 1.0459 ± 0.0188. As expected, there is no indication of any pulling or constraining of the nuisance parameters given the single-bin control regions and dedicated floating normalization factors.

Uncertainty of channel	CR_1L_njets2	CR_2L_njets2	CR_1L_njets3p	CR_2L_njets3p
Total background expectation	21215.37	2425.70	41813.42	4632.92
Total statistical ($\sqrt{N_{exp}}$)	±145.65	±49.25	±204.48	±68.07
Total background systematic	±145.66 [0.69%]	±49.25 [2.03%]	±204.51 [0.49%]	±68.07 [1.47%]
mu_Wjets_njets2	±183.12 [0.86%]	±0.00 [0.00%]	±0.00 [0.00%]	±0.00 [0.00%]
alpha_MUON_EFF_TrigSystUncertainty	±81.12 [0.38%]	±9.02 [0.37%]	±157.50 [0.38%]	±16.81 [0.36%]
gamma_stat_CR_1L_njets2_BDTscore_LepInvis_bin_0	±52.47 [0.25%]	±0.00 [0.00%]	±0.00 [0.00%]	±0.00 [0.00%]
alpha_EG_EFF_Trigger	±27.15 [0.13%]	±0.18 [0.01%]	±55.26 [0.13%]	±0.33 [0.01%]
alpha_JES_Pileup_RhoTopology	±25.30 [0.12%]	±0.23 [0.01%]	±20.44 [0.05%]	±5.46 [0.12%]
alpha_JES_Flavor_Composition	±22.05 [0.10%]	±0.66 [0.03%]	±188.07 [0.45%]	±15.30 [0.33%]
alpha_MUON_EFF_TrigStatUncertainty	±19.29 [0.09%]	±1.31 [0.05%]	±35.95 [0.09%]	±2.45 [0.05%]
Lumi	±11.45 [0.05%]	±1.41 [0.06%]	±83.20 [0.20%]	±5.11 [0.11%]
alpha_JET_JER_EffectiveNP_2	±10.08 [0.05%]	±1.96 [0.08%]	±53.69 [0.13%]	±5.64 [0.12%]
alpha_JES_Pileup_OffsetNPV	±9.56 [0.05%]	±0.48 [0.02%]	±10.72 [0.03%]	±4.07 [0.09%]
mu_Zjets_njets2	±9.53 [0.04%]	±51.33 [2.1%]	±0.00 [0.00%]	±0.00 [0.00%]
alpha_btag_BT	±8.33 [0.04%]	±0.48 [0.02%]	±164.51 [0.39%]	±5.27 [0.11%]
alpha_JET_JER_EffectiveNP_6	±7.28 [0.03%]	±0.83 [0.03%]	±18.03 [0.04%]	±0.68 [0.01%]
alpha_JES_EffectiveNP_Mixed1	±6.03 [0.03%]	±0.64 [0.03%]	±37.18 [0.09%]	±0.69 [0.01%]
alpha_JET_JER_EffectiveNP_7	±5.09 [0.02%]	±0.70 [0.03%]	±12.24 [0.03%]	±0.62 [0.01%]
alpha_JET_JER_EffectiveNP_9	±5.06 [0.02%]	±0.98 [0.04%]	±10.34 [0.02%]	±0.54 [0.01%]
alpha_JES_Pileup_OffsetMu	±4.86 [0.02%]	±0.98 [0.04%]	±24.28 [0.06%]	±5.22 [0.11%]
alpha_JES_EffectiveNP_Modelling1	±4.23 [0.02%]	±0.28 [0.01%]	±70.17 [0.17%]	±4.58 [0.10%]
alpha_btag_LightT	±4.17 [0.02%]	±0.54 [0.02%]	±58.10 [0.14%]	±3.73 [0.08%]
alpha_JES_Pileup_PtTerm	±3.83 [0.02%]	±0.87 [0.04%]	±38.53 [0.09%]	±0.19 [0.00%]
alpha_JET_JER_EffectiveNP_12restTerm	±3.78 [0.02%]	±0.58 [0.02%]	±4.19 [0.01%]	±3.56 [0.08%]
alpha_Pileup	±3.73 [0.02%]	±2.06 [0.09%]	±11.73 [0.03%]	±0.00 [0.00%]
alpha_MET_SoftTrk_Scale	±3.72 [0.02%]	±1.81 [0.07%]	±15.66 [0.04%]	±2.62 [0.06%]
alpha_btag_CT	±3.51 [0.02%]	±0.27 [0.01%]	±51.71 [0.12%]	±1.67 [0.04%]
alpha_JET_JER_DataVsMC_MC16	±3.48 [0.02%]	±0.26 [0.01%]	±32.92 [0.08%]	±5.13 [0.11%]
alpha_JET_JER_EffectiveNP_4	±3.17 [0.01%]	±0.10 [0.00%]	±15.82 [0.04%]	±3.02 [0.07%]
alpha_JES_EffectiveNP_Mixed2	±3.05 [0.01%]	±0.50 [0.02%]	±23.76 [0.06%]	±1.22 [0.03%]
alpha_JET_JER_EffectiveNP_1	±2.94 [0.01%]	±2.73 [0.11%]	±33.16 [0.08%]	±1.62 [0.04%]
alpha_JES_EtaIntercalibration_NonClosure_2018data	±2.92 [0.01%]	±0.11 [0.00%]	±35.40 [0.08%]	±0.80 [0.02%]
alpha_JvtEfficiency	±2.81 [0.01%]	±0.53 [0.02%]	±0.72 [0.00%]	±1.29 [0.03%]
alpha_JET_JER_EffectiveNP_5	±2.74 [0.01%]	±0.40 [0.02%]	±4.98 [0.01%]	±3.64 [0.08%]
alpha_JES_EtaIntercalibration_TotalStat	±2.48 [0.01%]	±0.83 [0.03%]	±8.02 [0.02%]	±1.35 [0.03%]
alpha_JES_EtaIntercalibration_Modelling	±2.44 [0.01%]	±1.41 [0.06%]	±104.26 [0.25%]	±6.19 [0.13%]
alpha_EG_EFF_TriggerEff	±2.35 [0.01%]	±0.00 [0.00%]	±9.81 [0.02%]	±0.00 [0.00%]
alpha_JES_EffectiveNP_Modelling3	±2.30 [0.01%]	±0.31 [0.01%]	±16.03 [0.04%]	±0.68 [0.01%]
alpha_JET_JER_EffectiveNP_10	±2.23 [0.01%]	±1.07 [0.04%]	±6.01 [0.01%]	±0.45 [0.01%]
alpha_JES_EffectiveNP_Modelling2	±2.00 [0.01%]	±0.17 [0.01%]	±12.14 [0.03%]	±0.04 [0.00%]
alpha_MET_SoftTrk_ResoPerp	±1.85 [0.01%]	±0.23 [0.01%]	±19.46 [0.05%]	±1.88 [0.04%]
alpha_JET_JER_EffectiveNP_3	±1.68 [0.01%]	±0.12 [0.00%]	±1.77 [0.00%]	±0.88 [0.02%]
alpha_JET_JER_EffectiveNP_11	±1.63 [0.01%]	±0.97 [0.04%]	±12.09 [0.03%]	±2.90 [0.06%]
alpha_Strong_Zjets_scale	±1.62 [0.01%]	±1.62 [0.07%]	±1.94 [0.00%]	±1.94 [0.04%]
alpha_btag_ExtraFromCharm	±1.48 [0.01%]	±0.39 [0.02%]	±17.10 [0.04%]	±3.35 [0.07%]
alpha_btag_Extra	±1.43 [0.01%]	±0.08 [0.00%]	±8.73 [0.02%]	±0.28 [0.01%]
alpha_JES_EffectiveNP_Statistical4	±1.36 [0.01%]	±0.28 [0.01%]	±9.10 [0.02%]	±0.13 [0.00%]
alpha_JES_Flavor_Response	±1.21 [0.01%]	±0.71 [0.03%]	±185.21 [0.44%]	±9.51 [0.21%]
alpha_JES_EffectiveNP_Statistical3	±1.14 [0.01%]	±0.01 [0.00%]	±5.96 [0.01%]	±0.04 [0.00%]
alpha_JES_EffectiveNP_Statistical2	±1.14 [0.01%]	±0.13 [0.01%]	±1.21 [0.00%]	±0.22 [0.00%]
alpha_Strong_Zjets_assew	±1.02 [0.00%]	±1.02 [0.04%]	±3.24 [0.01%]	±3.24 [0.07%]
alpha_MUON_EFF_RECO_SYS	±0.99 [0.00%]	±0.75 [0.03%]	±10.29 [0.02%]	±2.48 [0.05%]
alpha_MET_SoftTrk_ResoPara	±0.83 [0.00%]	±1.10 [0.05%]	±11.21 [0.03%]	±0.14 [0.00%]
alpha_EG_EFF_Iso	±0.81 [0.00%]	±1.48 [0.06%]	±1.00 [0.00%]	±3.98 [0.09%]
alpha_Strong_Zjets_PDF	±0.81 [0.00%]	±0.81 [0.03%]	±0.56 [0.00%]	±0.56 [0.01%]
alpha_JES_EffectiveNP_Detector1	±0.81 [0.00%]	±0.06 [0.00%]	±8.12 [0.02%]	±0.39 [0.01%]
alpha_JET_JER_EffectiveNP_8	±0.67 [0.00%]	±1.91 [0.08%]	±10.49 [0.03%]	±5.91 [0.13%]
alpha_JES_EffectiveNP_Statistical1	±0.65 [0.00%]	±0.00 [0.00%]	±3.99 [0.01%]	±0.10 [0.00%]
alpha_JES_EffectiveNP_Modelling4	±0.61 [0.00%]	±0.03 [0.00%]	±4.82 [0.01%]	±0.23 [0.00%]
alpha_JES_EffectiveNP_Statistical6	±0.58 [0.00%]	±0.09 [0.00%]	±4.31 [0.01%]	±0.07 [0.00%]
alpha_Strong_Zjets_alphaS	±0.47 [0.00%]	±0.47 [0.02%]	±0.04 [0.00%]	±0.04 [0.00%]
alpha_EG_SCALE_ALL	±0.46 [0.00%]	±0.27 [0.01%]	±7.84 [0.02%]	±0.05 [0.00%]
alpha_JES_EtaIntercalibration_NonClosure_posEta	±0.44 [0.00%]	±0.08 [0.00%]	±1.01 [0.00%]	±0.13 [0.00%]
alpha_EG_EFF_Reco	±0.37 [0.00%]	±0.60 [0.02%]	±4.53 [0.01%]	±1.36 [0.03%]
alpha_MUON_SCALE	±0.32 [0.00%]	±0.86 [0.04%]	±0.63 [0.00%]	±0.08 [0.00%]
alpha_JES_EtaIntercalibration_NonClosure_negEta	±0.27 [0.00%]	±0.27 [0.01%]	±2.40 [0.01%]	±0.11 [0.00%]
alpha_JES_EffectiveNP_Mixed3	±0.25 [0.00%]	±0.21 [0.01%]	±1.93 [0.00%]	±0.06 [0.00%]
alpha_MUON_EFF_ISO_SYS	±0.21 [0.00%]	±0.52 [0.02%]	±3.27 [0.01%]	±1.31 [0.03%]
alpha_MUON_ID	±0.19 [0.00%]	±0.10 [0.00%]	±0.25 [0.00%]	±0.29 [0.01%]
alpha_EG_RESOLUTION_ALL	±0.18 [0.00%]	±0.03 [0.00%]	±1.40 [0.00%]	±0.30 [0.01%]
alpha_MUON_TTVA_SYS	±0.13 [0.00%]	±0.14 [0.01%]	±1.54 [0.00%]	±0.39 [0.01%]
alpha_JES_EffectiveNP_Detector2	±0.13 [0.00%]	±0.01 [0.00%]	±0.83 [0.00%]	±0.11 [0.00%]
alpha_MUON_EFF_RECO_STAT	±0.11 [0.00%]	±0.14 [0.01%]	±1.20 [0.00%]	±0.36 [0.01%]
alpha_MUON_EFF_ISO_STAT	±0.08 [0.00%]	±0.16 [0.01%]	±1.30 [0.00%]	±0.40 [0.01%]
alpha_MUON_MS	±0.08 [0.00%]	±0.87 [0.04%]	±0.75 [0.00%]	±0.34 [0.01%]
alpha_MUON_TTVA_STAT	±0.08 [0.00%]	±0.14 [0.01%]	±1.11 [0.00%]	±0.40 [0.01%]
alpha_EW_Zjets_PDF	±0.06 [0.00%]	±0.06 [0.00%]	±0.25 [0.00%]	±0.25 [0.01%]
alpha_JES_SingleParticle_HighPt	±0.06 [0.00%]	±0.06 [0.00%]	±0.00 [0.00%]	±0.08 [0.00%]
alpha_JES_BJES_Response	±0.04 [0.00%]	±0.04 [0.00%]	±0.03 [0.00%]	±0.00 [0.00%]
alpha_MUON_SAGITTA_DATASTAT	±0.04 [0.00%]	±0.03 [0.00%]	±0.14 [0.00%]	±0.15 [0.00%]
alpha_Strong_Wjets_scale	±0.03 [0.00%]	±0.03 [0.00%]	±0.15 [0.00%]	±0.14 [0.00%]
alpha_EW_Zjets_alphaS	±0.02 [0.00%]	±0.02 [0.00%]	±0.04 [0.00%]	±0.04 [0.00%]
alpha_MUON_SAGITTA_RESBIAS	±0.02 [0.00%]	±0.11 [0.00%]	±0.34 [0.00%]	±0.07 [0.00%]
alpha_EW_Zjets_scale	±0.02 [0.00%]	±0.02 [0.00%]	±0.07 [0.00%]	±0.07 [0.00%]
alpha_EG_EFF_ID	±0.02 [0.00%]	±1.82 [0.07%]	±7.57 [0.02%]	±4.78 [0.10%]
alpha_JES_PunchThrough_MC16	±0.02 [0.00%]	±0.05 [0.00%]	±0.56 [0.00%]	±0.08 [0.00%]
alpha_Strong_Wjets_PDF	±0.01 [0.00%]	±0.02 [0.00%]	±0.08 [0.00%]	±0.08 [0.00%]
alpha_JES_EtaIntercalibration_NonClosure_highE	±0.01 [0.00%]	±0.01 [0.00%]	±0.44 [0.00%]	±0.04 [0.00%]
alpha_MUON_EFF_RECO_SYS_LOWPT	±0.00 [0.00%]	±0.04 [0.00%]	±0.14 [0.00%]	±0.14 [0.00%]
alpha_JES_EffectiveNP_Statistical5	±0.00 [0.00%]	±0.05 [0.00%]	±2.46 [0.01%]	±0.40 [0.01%]
alpha_MUON_EFF_RECO_STAT_LOWPT	±0.00 [0.00%]	±0.01 [0.00%]	±0.03 [0.00%]	±0.06 [0.00%]
alpha_Strong_Wjets_alphaS	±0.00 [0.00%]	±0.00 [0.00%]	±0.00 [0.00%]	±0.00 [0.00%]
gamma_stat_CR_2L_njets2_BDTscore_LepInvis_bin_0	±0.00 [0.00%]	±8.55 [0.35%]	±0.00 [0.00%]	±0.00 [0.00%]
gamma_stat_CR_1L_njets3p_BDTscore_LepInvis_bin_0	±0.00 [0.00%]	±0.00 [0.00%]	±109.11 [0.26%]	±0.00 [0.00%]
alpha_EW_Wjets_alphaS	±0.00 [0.00%]	±0.00 [0.00%]	±0.00 [0.00%]	±0.00 [0.00%]
alpha_QCD_estimation_transfer_factor	±0.00 [0.00%]	±0.00 [0.00%]	±0.00 [0.00%]	±0.00 [0.00%]
gamma_stat_VR_0L_lowBDT_njets2_BDTscore_bin_4	±0.00 [0.00%]	±0.00 [0.00%]	±0.00 [0.00%]	±0.00 [0.00%]
gamma_stat_VR_1L_njets3p_BDTscore_LepInvis_bin_0	±0.00 [0.00%]	±0.00 [0.00%]	±0.00 [0.00%]	±0.00 [0.00%]
gamma_stat_VR_1L_njets3p_BDTscore_LepInvis_bin_1	±0.00 [0.00%]	±0.00 [0.00%]	±0.00 [0.00%]	±0.00 [0.00%]
gamma_stat_VR_0L_lowBDT_njets2_BDTscore_bin_0	±0.00 [0.00%]	±0.00 [0.00%]	±0.00 [0.00%]	±0.00 [0.00%]
alpha_QCD_estimation_subtraction_theory	±0.00 [0.00%]	±0.00 [0.00%]	±0.00 [0.00%]	±0.00 [0.00%]
mu_Zjets_njets3p	±0.00 [0.00%]	±0.00 [0.00%]	±16.23 [0.04%]	±78.06 [1.7%]
gamma_stat_VR_0L_lowBDT_njets2_BDTscore_bin_1	±0.00 [0.00%]	±0.00 [0.00%]	±0.00 [0.00%]	±0.00 [0.00%]
gamma_stat_VR_0L_lowBDT_njets2_BDTscore_bin_3	±0.00 [0.00%]	±0.00 [0.00%]	±0.00 [0.00%]	±0.00 [0.00%]
gamma_stat_VR_0L_lowBDT_njets2_BDTscore_bin_2	±0.00 [0.00%]	±0.00 [0.00%]	±0.00 [0.00%]	±0.00 [0.00%]
alpha_EW_Wjets_PDF	±0.00 [0.00%]	±0.00 [0.00%]	±0.00 [0.00%]	±0.00 [0.00%]
alpha_QCD_estimation_MET_trig_eff	±0.00 [0.00%]	±0.00 [0.00%]	±0.00 [0.00%]	±0.00 [0.00%]
gamma_stat_VR_1L_njets2_BDTscore_LepInvis_bin_0	±0.00 [0.00%]	±0.00 [0.00%]	±0.00 [0.00%]	±0.00 [0.00%]
alpha_flatSys_other	±0.00 [0.00%]	±0.00 [0.00%]	±0.00 [0.00%]	±0.00 [0.00%]
gamma_stat_VR_0L_lowBDT_njets3p_BDTscore_bin_3	±0.00 [0.00%]	±0.00 [0.00%]	±0.00 [0.00%]	±0.00 [0.00%]
gamma_stat_VR_0L_lowBDT_njets3p_BDTscore_bin_2	±0.00 [0.00%]	±0.00 [0.00%]	±0.00 [0.00%]	±0.00 [0.00%]
gamma_stat_VR_0L_lowBDT_njets3p_BDTscore_bin_1	±0.00 [0.00%]	±0.00 [0.00%]	±0.00 [0.00%]	±0.00 [0.00%]
gamma_stat_VR_0L_lowBDT_njets3p_BDTscore_bin_0	±0.00 [0.00%]	±0.00 [0.00%]	±0.00 [0.00%]	±0.00 [0.00%]
gamma_stat_VR_0L_lowBDT_njets3p_BDTscore_bin_4	±0.00 [0.00%]	±0.00 [0.00%]	±0.00 [0.00%]	±0.00 [0.00%]
alpha_Strong_Wjets_assew	±0.00 [0.00%]	±0.01 [0.00%]	±0.00 [0.00%]	±0.03 [0.00%]
gamma_stat_VR_2L_njets3p_BDTscore_LepInvis_bin_1	±0.00 [0.00%]	±0.00 [0.00%]	±0.00 [0.00%]	±0.00 [0.00%]
gamma_stat_VR_1L_njets2_BDTscore_LepInvis_bin_1	±0.00 [0.00%]	±0.00 [0.00%]	±0.00 [0.00%]	±0.00 [0.00%]
alpha_QCD_estimation_subtraction_exp	±0.00 [0.00%]	±0.00 [0.00%]	±0.00 [0.00%]	±0.00 [0.00%]
gamma_stat_VR_2L_njets3p_BDTscore_LepInvis_bin_0	±0.00 [0.00%]	±0.00 [0.00%]	±0.00 [0.00%]	±0.00 [0.00%]
alpha_flatSys_top	±0.00 [0.00%]	±0.00 [0.00%]	±0.00 [0.00%]	±0.00 [0.00%]
gamma_stat_VR_2L_njets2_BDTscore_LepInvis_bin_0	±0.00 [0.00%]	±0.00 [0.00%]	±0.00 [0.00%]	±0.00 [0.00%]
alpha_QCD_estimation_statistical	±0.00 [0.00%]	±0.00 [0.00%]	±0.00 [0.00%]	±0.00 [0.00%]
gamma_stat_CR_2L_njets3p_BDTscore_LepInvis_bin_0	±0.00 [0.00%]	±0.00 [0.00%]	±0.00 [0.00%]	±19.78 [0.43%]
mu_Wjets_njets3p	±0.00 [0.00%]	±0.00 [0.00%]	±470.89 [1.1%]	±0.01 [0.00%]
gamma_stat_VR_2L_njets2_BDTscore_LepInvis_bin_1	±0.00 [0.00%]	±0.00 [0.00%]	±0.00 [0.00%]	±0.00 [0.00%]
alpha_EW_Wjets_scale	±0.00 [0.00%]	±0.00 [0.00%]	±0.00 [0.00%]	±0.00 [0.00%]

Table 9.2.: Breakdown of the systematic uncertainties in the control regions after the background-only fit.

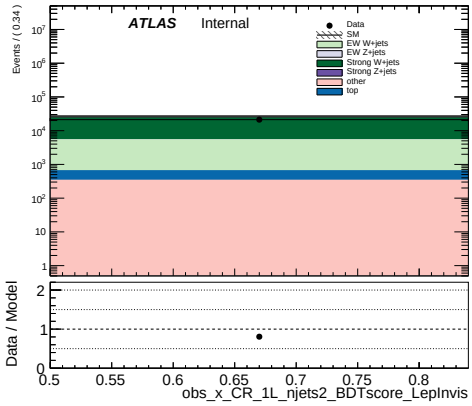

(a) CR_1L_njets2

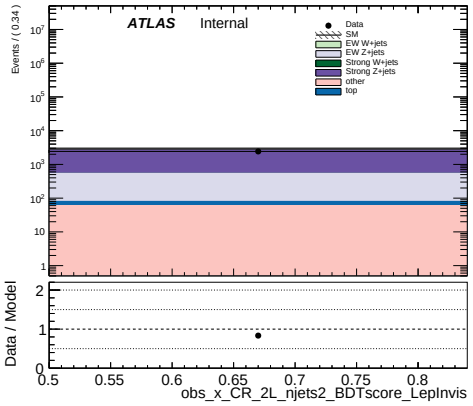

(b) CR_2L_njets2

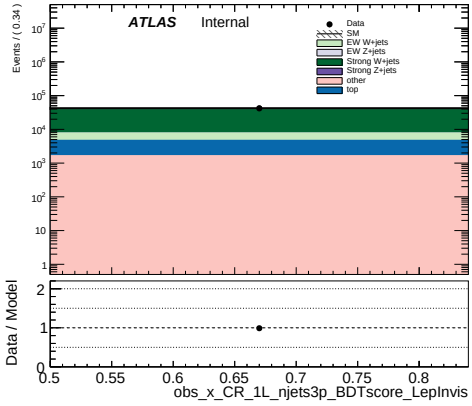

(c) CR_1L_njets3p

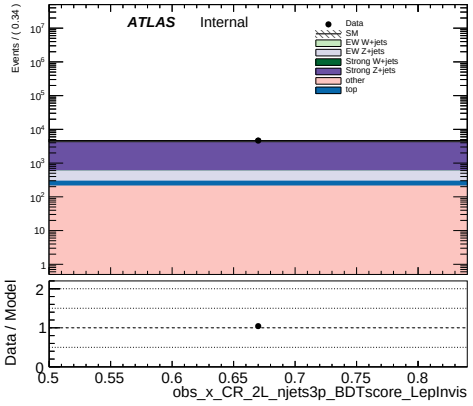

(d) CR_2L_njets3p

Figure 9.1: Pre-fit distributions in the single-bin control regions.

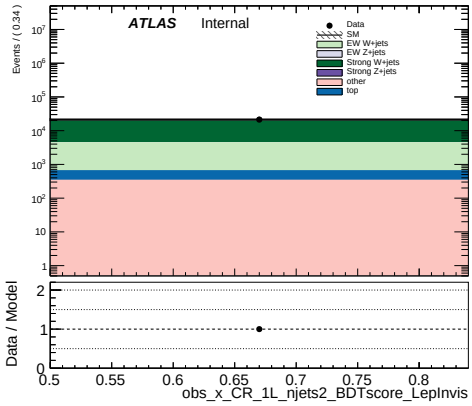

(a) CR_1L_njets2

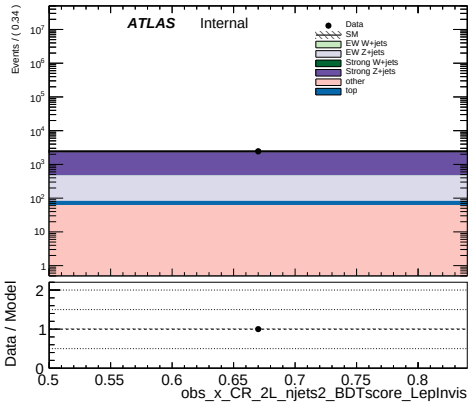

(b) CR_2L_njets2

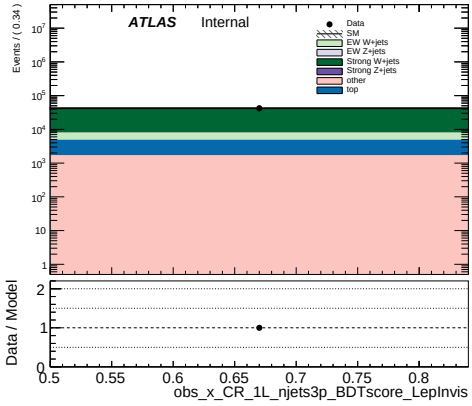

(c) CR_1L_njets3p

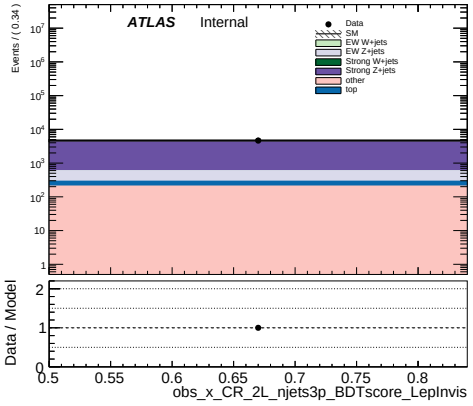

(d) CR_2L_njets3p

Figure 9.2: Post-fit distributions in the single-bin control regions.

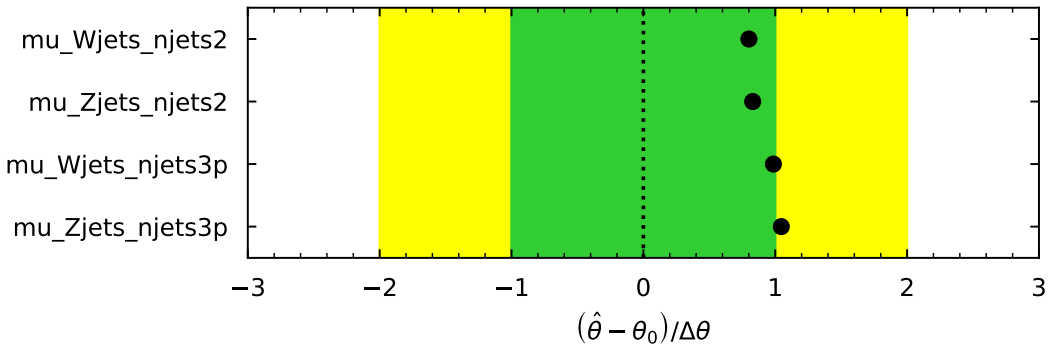

Figure 9.3: Normalization factors for the V + jets backgrounds after the background-only fit in control regions, with the expected value being 1. The fitted values are mu_Wjets_njets2 = 0.8002 ± 0.0072, mu_Zjets_njets2 = 0.8289 ± 0.0181, mu_Wjets_njets3p = 0.9862 ± 0.0129, and mu_Zjets_njets3p = 1.0459 ± 0.0188 .

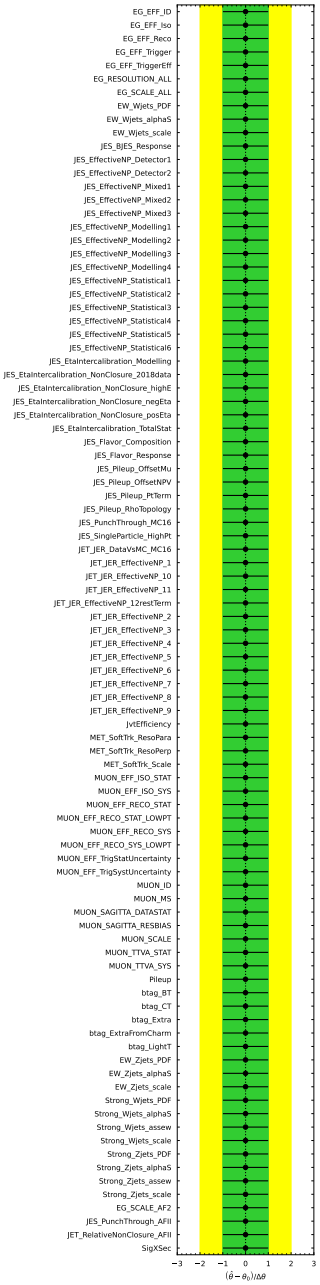

Figure 9.4: Pulls and constraints of fit parameters after the background-only fit in control regions, with the nominal value of the nuisance parameters being 0.

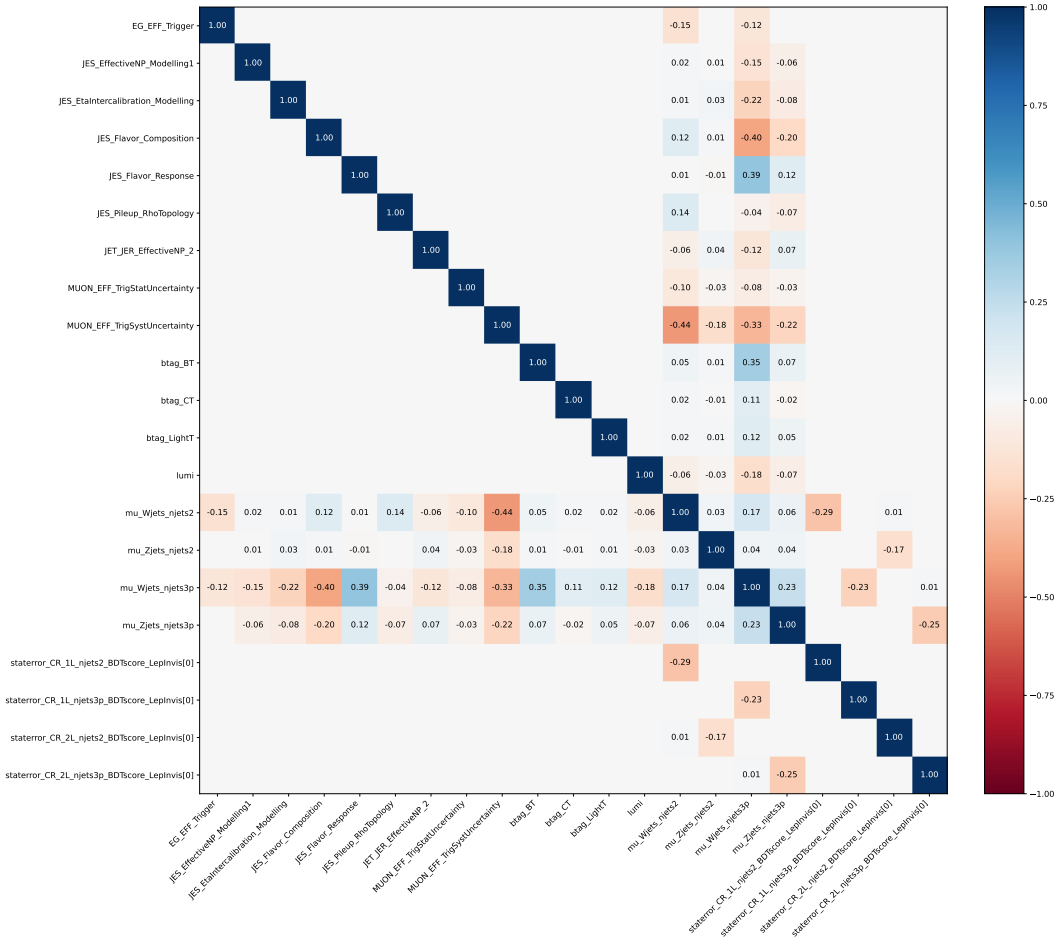

Figure 9.5: Correlation matrix (reduced) after the background-only fit in control regions.

9.3. Extrapolation to Validation Regions

To validate that the background extrapolation from the control regions is reasonable, the background-only fit results are propagated to validation regions and the agreement with the data is checked. Validation regions are defined for the W and Z control regions by requiring a BDT score greater than 0.84 while keeping all other selections the same. Additionally, these W and Z validation regions have 2 bins in the BDT score distribution to match the last two bins of the signal regions with the first bin going from 0.84 to 0.88 and the second from 0.88 to 0.92 (with overflow). The validation regions are defined separately based on the jet multiplicity in the same manner as the control regions leading to the four validation regions denoted as VR_1L_njets2, VR_1L_njets3p, VR_2L_njets2, VR_2L_njets3p. Tables 9.3–9.6 show the yields in the 1L and 2L VRs, while Figures 9.6–9.9 show the pre-fit and post-fit distributions of the BDT score as well as the significance for each VR bin. The significance reported in the significance plots is calculated using the following formula [28]

$$Z = \begin{cases} +\sqrt{2\left[n\ln\left(\frac{n(b+\sigma^2)}{b^2+n\sigma^2}\right) - \frac{b^2}{\sigma^2}\ln\left(1+\frac{\sigma^2(n-b)}{b(b+\sigma^2)}\right)\right]} & \text{if } n \geq b \\ -\sqrt{2\left[n\ln\left(\frac{n(b+\sigma^2)}{b^2+n\sigma^2}\right) - \frac{b^2}{\sigma^2}\ln\left(1+\frac{\sigma^2(n-b)}{b(b+\sigma^2)}\right)\right]} & \text{if } n < b \end{cases} \tag{9.3.1}$$

where n is the observed number of events, b is the predicted number of events, and σ is the uncertainty on b. In general, good agreement is found between the data and fitted background in these regions.

channel	VR_1L_njets2	bin0	bin1
Observed events	697	572	125
Fitted bkg events	679.89 ± 26.69	577.6 ± 21.6	102.3 ± 6.6
Fitted Strong Z + jets events	5.34 ± 0.63	4.8 ± 0.6	0.6 ± 0.1
Fitted Strong W+ jets events	308.14 ± 18.54	274.0 ± 15.8	34.1 ± 3.3
Fitted EW Z + jets events	4.44 ± 0.32	3.7 ± 0.3	0.8 ± 0.1
Fitted EW W+ jets events	337.62 ± 17.82	274.4 ± 13.4	63.2 ± 5.3
Fitted top events	8.45 ± 1.65	7.2 ± 1.9	1.2 ± 0.6
Fitted other events	15.90 ± 1.88	13.5 ± 1.8	2.4 ± 0.5
MC exp. SM events	842.99 ± 33.04	716.15 ± 26.74	126.84 ± 8.22
MC exp. Strong Z + jets events	6.44 ± 0.75	5.74 ± 0.74	0.70 ± 0.15
MC exp. Strong W+ jets events	385.01 ± 23.26	342.40 ± 19.85	42.61 ± 4.15
MC exp. EW Z + jets events	5.35 ± 0.37	4.42 ± 0.37	0.93 ± 0.15
MC exp. EW W+ jets events	421.85 ± 22.20	342.85 ± 16.74	79.00 ± 6.57
MC exp. top events	8.45 ± 1.66	7.21 ± 1.90	1.24 ± 0.59
MC exp. other events	15.90 ± 1.89	13.54 ± 1.84	2.36 ± 0.47

Table 9.3.: Yields table for VR_1L_njets2.

channel	VR_1L_njets3p	bin0	bin1
Observed events	652	582	70
Fitted bkg events	604.84 ± 33.19	543.4 ± 30.2	61.5 ± 5.8
Fitted Strong Z + jets events	8.04 ± 1.30	7.2 ± 1.1	0.8 ± 0.4
Fitted Strong W+ jets events	373.75 ± 32.66	339.0 ± 29.4	34.8 ± 5.0
Fitted EW Z + jets events	2.04 ± 0.22	1.8 ± 0.2	0.2 ± 0.2
Fitted EW W+ jets events	160.56 ± 7.43	142.1 ± 6.5	18.5 ± 1.9
Fitted top events	29.47 ± 3.15	25.7 ± 3.2	3.8 ± 1.1
Fitted other events	30.97 ± 4.93	27.6 ± 3.5	3.3 ± 1.9
MC exp. SM events	611.78 ± 32.43	549.63 ± 29.46	62.15 ± 5.89
MC exp. Strong Z + jets events	7.69 ± 1.23	6.91 ± 1.05	0.78 ± 0.38
MC exp. Strong W+ jets events	378.94 ± 31.71	343.70 ± 28.57	35.24 ± 4.99
MC exp. EW Z + jets events	1.95 ± 0.21	1.73 ± 0.20	0.22 ± 0.16
MC exp. EW W+ jets events	162.79 ± 7.76	144.02 ± 6.74	18.76 ± 1.98
MC exp. top events	29.46 ± 3.16	25.65 ± 3.19	3.81 ± 1.09
MC exp. other events	30.96 ± 4.96	27.62 ± 3.55	3.34 ± 1.91

Table 9.4.: Yields table for VR_1L_njets3p.

channel	VR_2L_njets2	bin0	bin1
Observed events	63	55	8
Fitted bkg events	70.01 ± 4.48	60.3 ± 4.0	9.7 ± 0.9
Fitted Strong Z + jets events	33.70 ± 2.48	30.0 ± 2.1	3.7 ± 0.6
Fitted Strong W+ jets events	0.00 ± 0.00	0.0 ± 0.0	0.0 ± 0.0
Fitted EW Z + jets events	30.59 ± 2.35	25.3 ± 1.9	5.3 ± 0.6
Fitted EW W+ jets events	0.00 ± 0.00	0.0 ± 0.0	0.0 ± 0.0
Fitted top events	0.21 ± 0.18	0.2 ± 0.2	0.0 ± 0.0
Fitted other events	5.51 ± 0.77	4.9 ± 0.8	0.6 ± 0.1
MC exp. SM events	83.26 ± 5.06	71.72 ± 4.46	11.54 ± 1.09
MC exp. Strong Z + jets events	40.64 ± 2.88	36.13 ± 2.45	4.52 ± 0.71
MC exp. Strong W+ jets events	0.00 ± 0.00	0.00 ± 0.00	0.00 ± 0.00
MC exp. EW Z + jets events	36.89 ± 2.73	30.50 ± 2.23	6.39 ± 0.71
MC exp. EW W+ jets events	0.00 ± 0.00	0.00 ± 0.00	0.00 ± 0.00
MC exp. top events	0.21 ± 0.18	0.21 ± 0.18	0.00 ± 0.00
MC exp. other events	5.50 ± 0.78	4.88 ± 0.81	0.63 ± 0.10

Table 9.5.: Yields table for VR_2L_njets2.

channel	VR_2L_njets3p	bin0	bin1
Observed events	67	62	5
Fitted bkg events	61.21 ± 4.43	54.9 ± 4.2	6.3 ± 0.7
Fitted Strong Z + jets events	41.08 ± 3.64	37.0 ± 3.4	4.1 ± 0.7
Fitted Strong W+ jets events	0.01 ± 0.00	0.0 ± 0.0	0.0 ± 0.0
Fitted EW Z + jets events	14.62 ± 1.05	13.0 ± 1.1	1.6 ± 0.3
Fitted EW W+ jets events	0.00 ± 0.00	0.0 ± 0.0	0.0 ± 0.0
Fitted top events	0.82 ± 0.42	0.8 ± 0.4	0.0 ± 0.0
Fitted other events	4.68 ± 0.46	4.0 ± 0.4	0.7 ± 0.2
MC exp. SM events	58.75 ± 4.08	52.71 ± 3.92	6.05 ± 0.71
MC exp. Strong Z + jets events	39.27 ± 3.37	35.40 ± 3.12	3.87 ± 0.62
MC exp. Strong W+ jets events	0.01 ± 0.00	0.01 ± 0.00	0.00 ± 0.00
MC exp. EW Z + jets events	13.97 ± 0.96	12.47 ± 0.98	1.50 ± 0.24
MC exp. EW W+ jets events	0.00 ± 0.00	0.00 ± 0.00	0.00 ± 0.00
MC exp. top events	0.82 ± 0.42	0.82 ± 0.42	0.00 ± 0.00
MC exp. other events	4.68 ± 0.46	4.01 ± 0.45	0.67 ± 0.16

Table 9.6.: Yields table for VR_2L_njets3p.

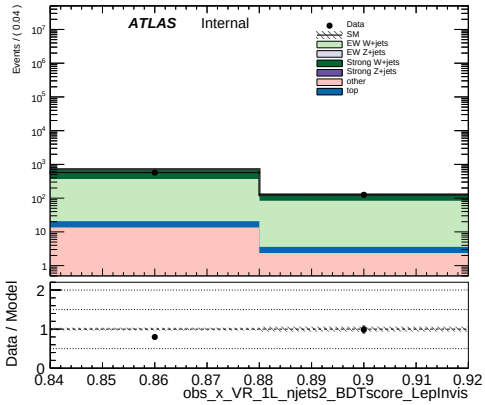

(a) VR_1L_njets2

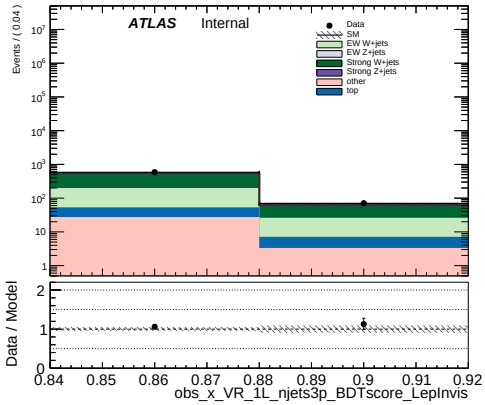

(b) VR_1L_njets3p

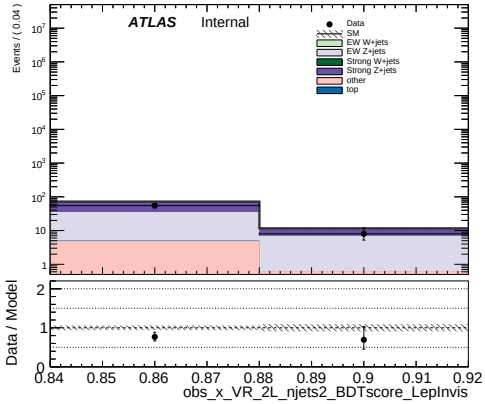

(c) VR_2L_njets2

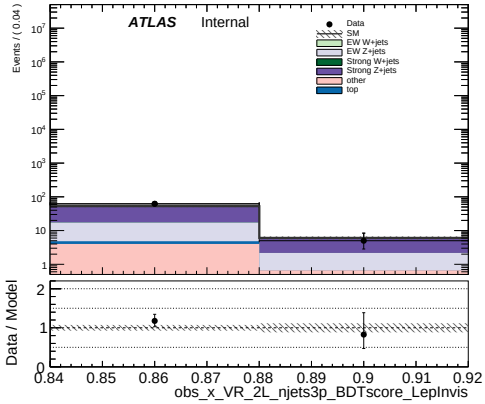

(d) VR_2L_njets3p

Figure 9.6: Pre-fit distributions in the W/Z validation regions.

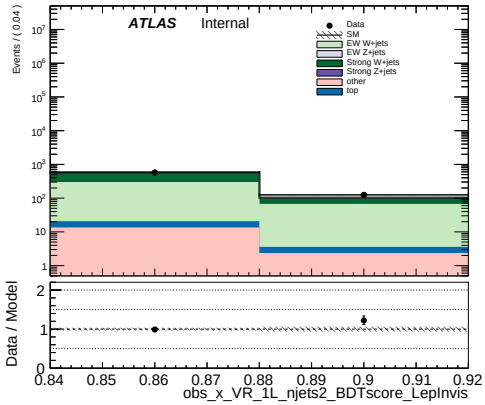

(a) VR_1L_njets2

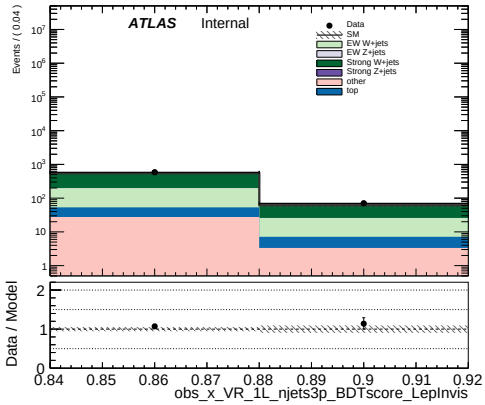

(b) VR_1L_njets3p

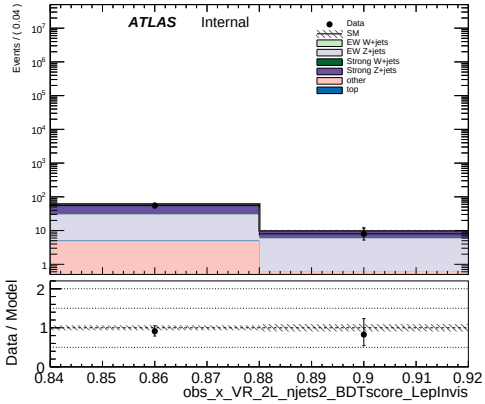

(c) VR_2L_njets2

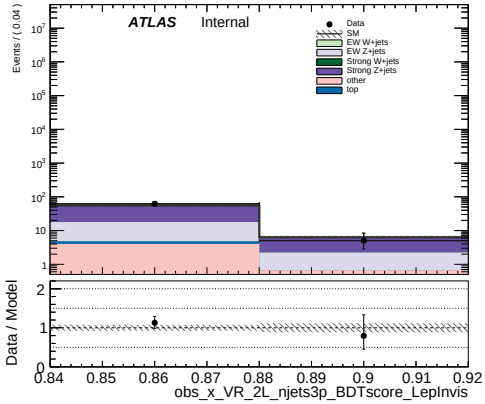

(d) VR_2L_njets3p

Figure 9.7: Post-fit distributions in the W/Z validation regions.

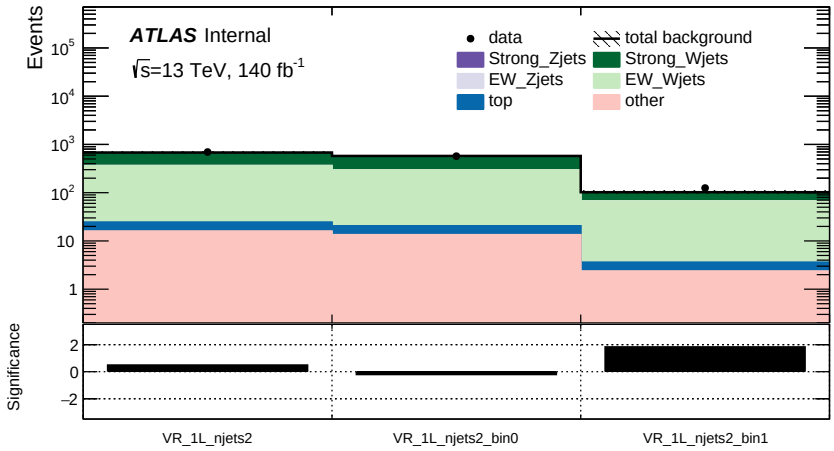

(a) VR_1L_njets2

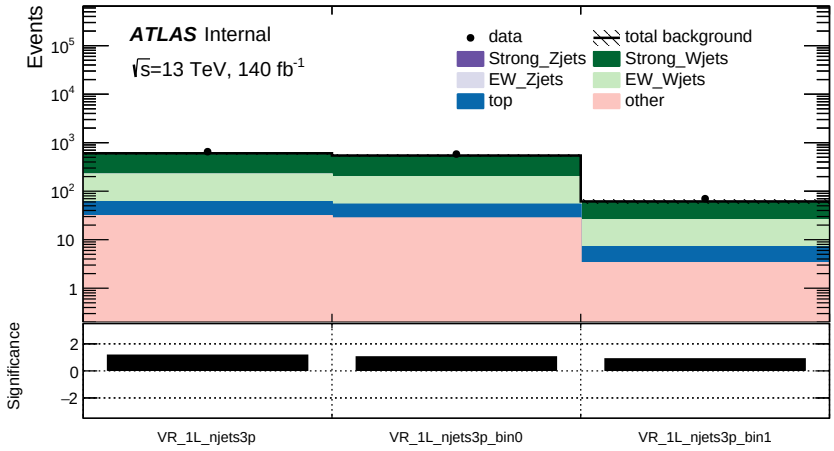

(b) VR_1L_njets3p

Figure 9.8: Significance plots in the W validation regions. The first bin shows the region inclusively while the other bins show each of the individual bins for the region.

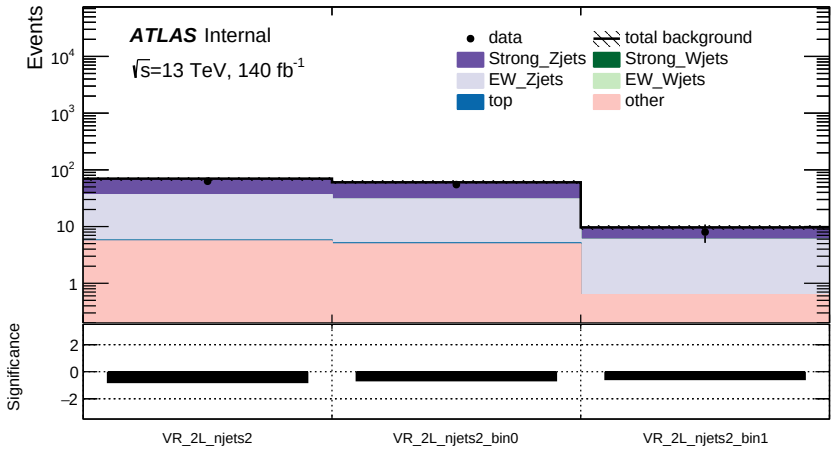

(a) VR_2L_njets2

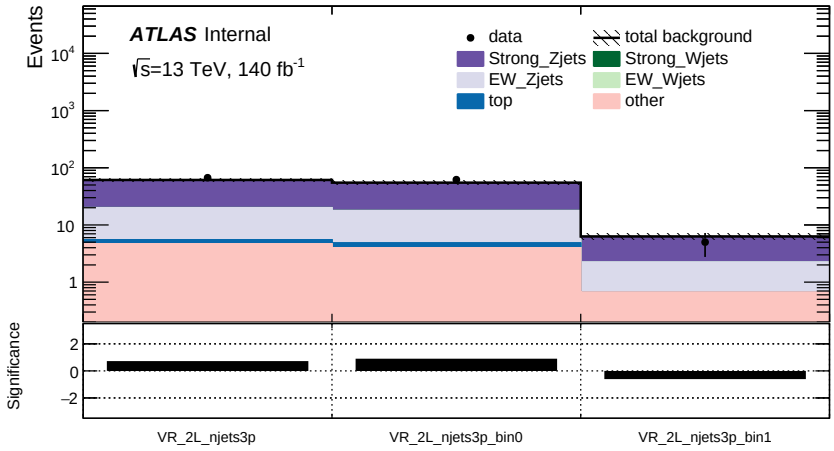

(b) VR_2L_njets3p

Figure 9.9: Significance plots in the Z validation regions. The first bin shows the region inclusively while the other bins show each of the individual bins for the region.

As the normalization of the W+ jets and Z + jets backgrounds is performed in 1L and 2L selections respectively, the extrapolation to the SR, which has a lepton veto, needs to be validated. For this purpose, two validation regions are constructed for the events with 2 jets (VR_0L_lowBDT_njets2) and 3+ jets (VR_0L_lowBDT_njets3p) at low BDT score ranging from 0.4 to 0.6 with 5 bins of equal widths. Aside from the BDT score, these regions include all the other same requirements as in the signal regions. The data-driven estimate of the multijet background based on the ABCD method is included in these validation regions. Tables 9.7 and 9.8 show the yields for the 0L VRs while Figures 9.10–9.12 show the pre-fit and post-fit BDT score distributions and the corresponding significance. The agreement with the data in these validation regions is reasonable in general with no deviations exceeding 2σ. In VR_0L_lowBDT_njets3p there is a trend of deficits, all around the 1σ level, that suggests a slight over-estimation of the backgrounds in that portion of the phase space. This discrepancy seems to be addressed once the signal regions are included as part of the simultaneous fit since the QCD contribution has very large pre-fit uncertainties and becomes heavily suppressed post-fit, as will be seen in the results of the next section.

channel	VR_0L_lowBDT_njets2	bin0	bin1	bin2	bin3	bin4
Observed events	11712	1546	1797	2225	2728	3416
Fitted bkg events	11219.44 ± 397.37	1441.0 ± 104.6	1718.1 ± 105.6	2188.2 ± 121.4	2627.8 ± 78.9	3244.3 ± 83.6
Fitted Strong Z + jets events	6750.33 ± 293.56	818.1 ± 64.5	1031.4 ± 73.0	1290.3 ± 79.0	1617.6 ± 61.7	1992.9 ± 67.0
Fitted Strong W+ jets events	3306.58 ± 123.11	478.5 ± 34.4	533.7 ± 39.1	662.1 ± 41.8	747.7 ± 40.4	884.6 ± 48.6
Fitted EW Z + jets events	619.21 ± 19.02	50.3 ± 2.5	71.7 ± 2.9	109.9 ± 4.0	156.9 ± 5.5	230.5 ± 8.5
Fitted EW W+ jets events	312.03 ± 8.47	29.5 ± 2.1	42.3 ± 1.9	58.6 ± 2.9	77.2 ± 3.3	104.3 ± 4.5
Fitted top events	39.95 ± 12.92	8.0 ± 2.6	8.1 ± 2.7	8.0 ± 2.7	9.0 ± 3.1	6.8 ± 2.3
Fitted other events	83.34 ± 26.19	8.6 ± 3.2	14.9 ± 5.1	17.3 ± 5.8	19.3 ± 6.3	23.2 ± 7.5
Fitted QCD multijet events	$108.01^{+112.59}_{-108.01}$	$48.0^{+50.0}_{-48.0}$	$16.0^{+16.7}_{-16.0}$	$42.0^{+43.8}_{-42.0}$	$0.0^{+0.0}_{-0.0}$	$2.0^{+2.1}_{-2.0}$
MC exp. SM events	13642.78 ± 416.99	1746.85 ± 119.08	2089.13 ± 122.79	2656.61 ± 137.03	3199.92 ± 80.84	3950.27 ± 81.45
MC exp. Strong Z + jets events	8142.42 ± 295.75	986.82 ± 73.79	1243.90 ± 82.13	1556.28 ± 86.98	1951.28 ± 59.59	2404.14 ± 61.35
MC exp. Strong W+ jets events	4132.19 ± 150.51	597.89 ± 42.49	666.79 ± 48.40	827.19 ± 51.51	934.52 ± 51.00	1105.81 ± 61.34
MC exp. EW Z + jets events	747.01 ± 15.71	60.64 ± 2.73	86.54 ± 2.84	132.53 ± 3.76	189.28 ± 5.23	278.02 ± 8.32
MC exp. EW W+ jets events	389.90 ± 10.20	36.93 ± 2.59	52.89 ± 2.36	73.26 ± 3.55	96.51 ± 4.01	130.32 ± 5.61
MC exp. top events	39.93 ± 12.93	7.96 ± 2.60	8.13 ± 2.72	8.04 ± 2.75	8.99 ± 3.05	6.81 ± 2.30
MC exp. other events	83.32 ± 26.20	8.61 ± 3.23	14.89 ± 5.12	17.32 ± 5.78	19.34 ± 6.28	23.17 ± 7.47
MC exp. QCD multijet events	$108.01^{+112.59}_{-108.01}$	$48.00^{+50.04}_{-48.00}$	$16.00^{+16.68}_{-16.00}$	$42.00^{+43.78}_{-42.00}$	$0.01^{+0.01}_{-0.01}$	$2.00^{+2.08}_{-2.00}$

Table 9.7.: Yields per bin in VR_0L_lowBDT_njets2 before and after background-only fit in control regions.

channel	VR_0L_lowBDT_njets3p	bin0	bin1	bin2	bin3	bin4
Observed events	35949	6680	7375	7782	7425	6687
Fitted bkg events	39753.33 ± 2940.24	7578.1 ± 784.7	8454.1 ± 750.5	8495.7 ± 569.7	8105.8 ± 522.2	7119.6 ± 389.8
Fitted Strong Z + jets events	22335.94 ± 860.26	4042.2 ± 245.2	4651.1 ± 280.8	4772.1 ± 169.2	4697.9 ± 146.3	4172.6 ± 130.3
Fitted Strong W+jets events	11785.44 ± 414.08	2372.3 ± 133.3	2605.3 ± 144.1	2584.3 ± 93.8	2272.1 ± 78.4	1951.4 ± 68.3
Fitted EW Z + jets events	934.05 ± 25.70	111.3 ± 5.7	151.8 ± 5.7	195.5 ± 7.3	228.6 ± 6.3	246.9 ± 7.2
Fitted EW W+jets events	599.12 ± 24.91	84.2 ± 5.0	107.2 ± 5.2	130.1 ± 5.8	137.1 ± 7.0	140.5 ± 5.9
Fitted top events	538.76 ± 174.71	117.2 ± 39.0	127.9 ± 41.8	117.8 ± 38.3	95.4 ± 30.7	80.5 ± 26.0
Fitted other events	1035.03 ± 325.78	198.0 ± 64.6	219.8 ± 69.4	206.9 ± 64.9	213.7 ± 66.7	196.7 ± 61.5
Fitted QCD multijet events	$2525.00^{+2632.06}_{-2525.00}$	$653.0^{+680.7}_{-653.0}$	$591.0^{+616.1}_{-591.0}$	$489.0^{+509.7}_{-489.0}$	$461.0^{+480.6}_{-461.0}$	$331.0^{+345.0}_{-331.0}$
MC exp. SM events	38902.18 ± 2956.57	7429.77 ± 790.58	8279.70 ± 758.48	8315.29 ± 568.53	7922.78 ± 519.88	6954.63 ± 386.62
MC exp. Strong Z + jets events	21352.92 ± 804.21	3864.28 ± 237.93	4445.77 ± 272.33	4562.27 ± 149.31	4491.24 ± 128.40	3989.36 ± 114.39
MC exp. Strong W+jets events	11950.14 ± 464.73	2405.59 ± 146.15	2641.51 ± 160.83	2620.50 ± 102.58	2303.84 ± 79.42	1978.71 ± 67.60
MC exp. EW Z + jets events	893.02 ± 19.72	106.38 ± 5.16	145.12 ± 4.85	186.94 ± 6.19	218.53 ± 5.14	236.05 ± 5.84
MC exp. EW W+jets events	607.45 ± 24.54	85.40 ± 4.95	108.65 ± 5.22	131.95 ± 5.88	139.05 ± 6.88	142.40 ± 5.91
MC exp. top events	538.67 ± 174.85	117.18 ± 39.02	127.83 ± 41.80	117.77 ± 38.30	95.43 ± 30.71	80.46 ± 26.02
MC exp. other events	1034.99 ± 325.94	197.95 ± 64.60	219.81 ± 69.45	206.86 ± 64.91	213.71 ± 66.74	196.65 ± 61.55
MC exp. QCD multijet events	$2525.00^{+2632.06}_{-2525.00}$	$653.00^{+680.71}_{-653.00}$	$591.00^{+616.08}_{-591.00}$	$489.00^{+509.75}_{-489.00}$	$461.00^{+480.56}_{-461.00}$	$331.00^{+345.04}_{-331.00}$

Table 9.8.: Yields per bin in VR_0L_lowBDT_njets3p before and after background-only fit in control regions.

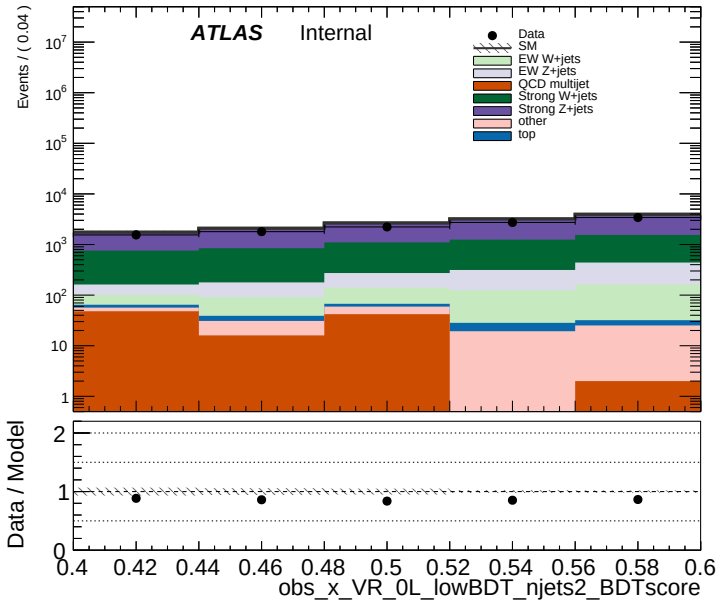

(a) VR_0L_lowBDT_njets2

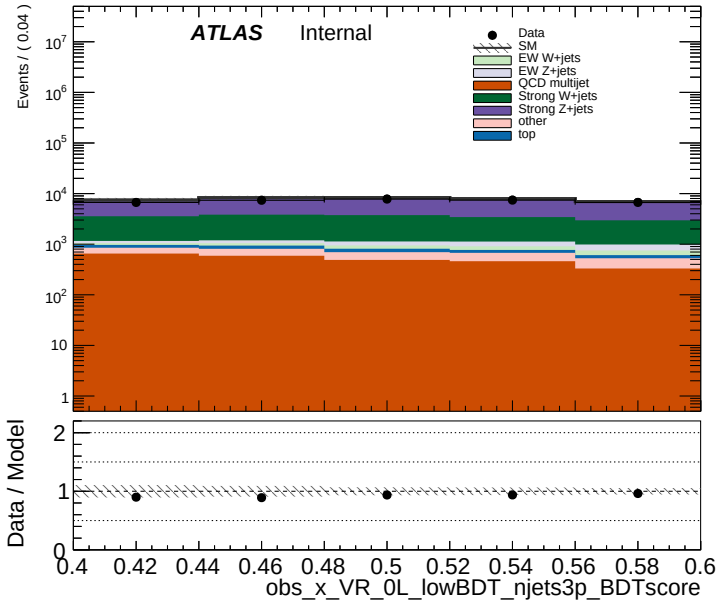

(b) VR_0L_lowBDT_njets3p

Figure 9.10: Pre-fit distributions in the 0L validation regions.

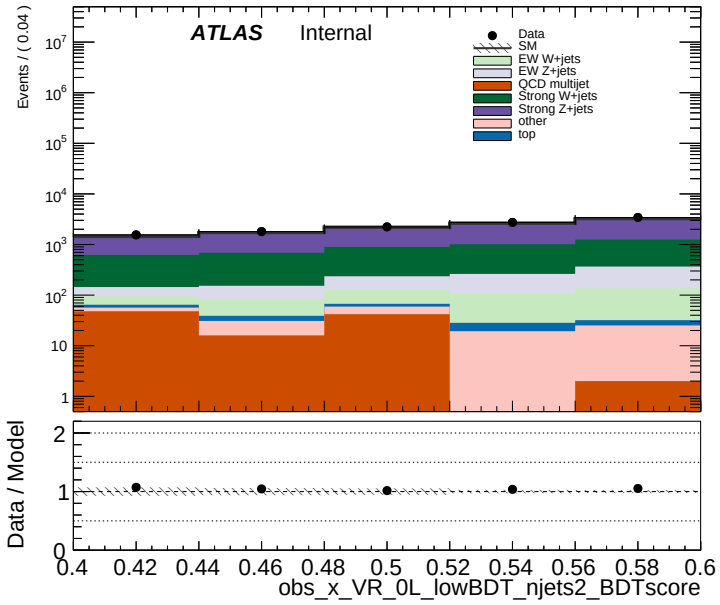

(a) VR_0L_lowBDT_njets2

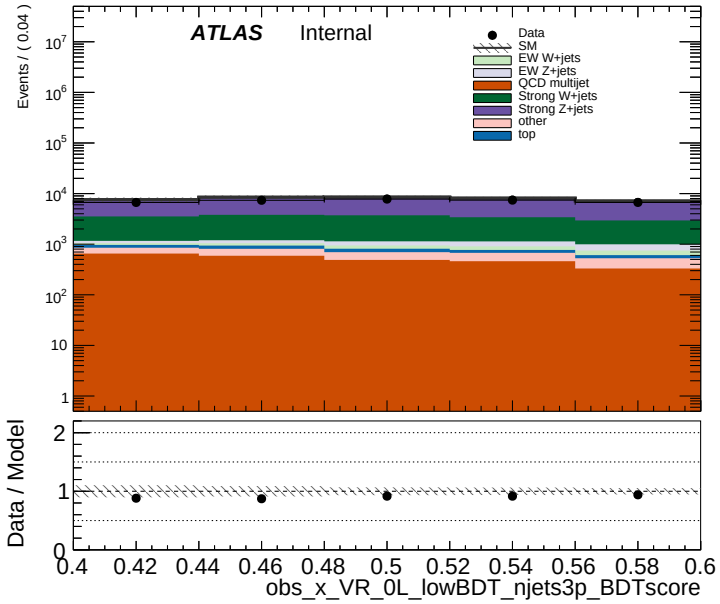

(b) VR_0L_lowBDT_njets3p

Figure 9.11: Post-fit distributions in the 0L validation regions.

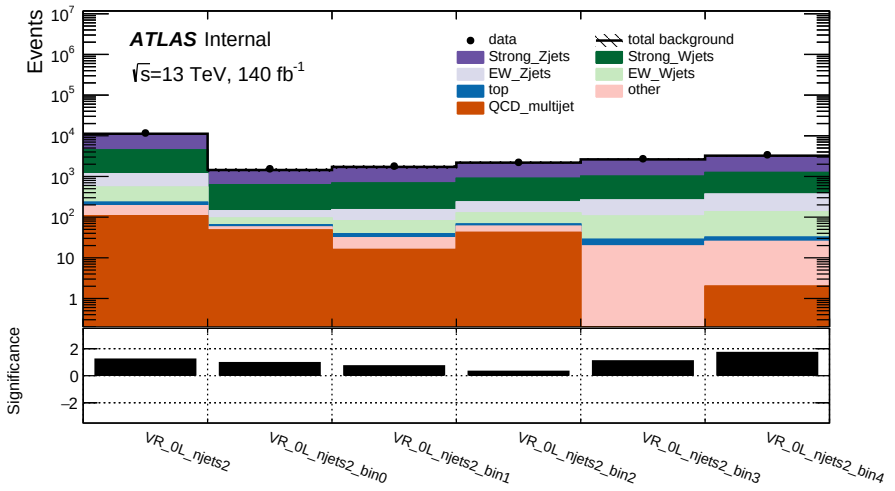

(a) VR_0L_lowBDT_njets2

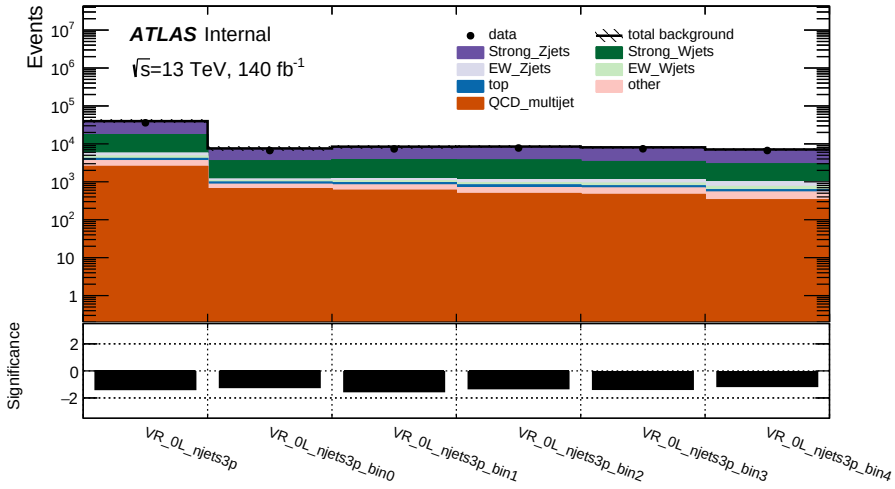

(b) VR_0L_lowBDT_njets3p

Figure 9.12: Significance plots in the 0L validation regions. The first bin shows the region inclusively while the other bins show each of the individual bins for the region.

9.4. Discovery Fit for Model-Independent Limits

Constraints on the number of events from generic physics processes beyond the Standard Model are set through a so-called "discovery" fit. In this configuration a discovery signal region is defined consisting of a single bin only. A dummy signal with a nominal yield of one is then added to the discovery SR. This signal can be scaled up with a floating signal strength parameter. The control regions are included along with the discovery region when running the fit. A scan of the signal strength parameter is performed and used to place a generic upper limit on the number of BSM signal events.

The very last BDT score bin ([0.88, 1.0]) of each of the exclusion signal regions is used for defining the discovery regions, keeping the split into 2 jet and 3+ jet events as in the rest of the analysis. Thus the definitions for the discovery regions are equivalent to imposing the exclusion SR requirements and additionally requiring BDT score > 0.88. This definition was chosen because the high BDT score regime is what drives most of the sensitivity to the signal model considered in the search and lower BDT scores are not expected to be particularly sensitive to other scenarios of BSM physics. The discovery signal regions are denoted as SR_disc_njets2 for the 2 jet selection and SR_disc_njets3p for the 3+ jet selection. When running the statistical fit, only one of the discovery signal regions and all control regions are included. The results from performing an upper limit scan on the signal strength for the dummy signal is shown in Figure 9.13 and 9.14. Yields tables for the discovery regions are shown in Tables 9.9 and 9.10. Upper limits on the visible cross section and number of signal events, along with the background-only confidence level and discovery p-value, are shown for each discovery region in Table 9.11. The minor excess in SR_disc_njets3p leads to a discovery p-value of 0.19 which corresponds to

a discovery significance below 1σ.

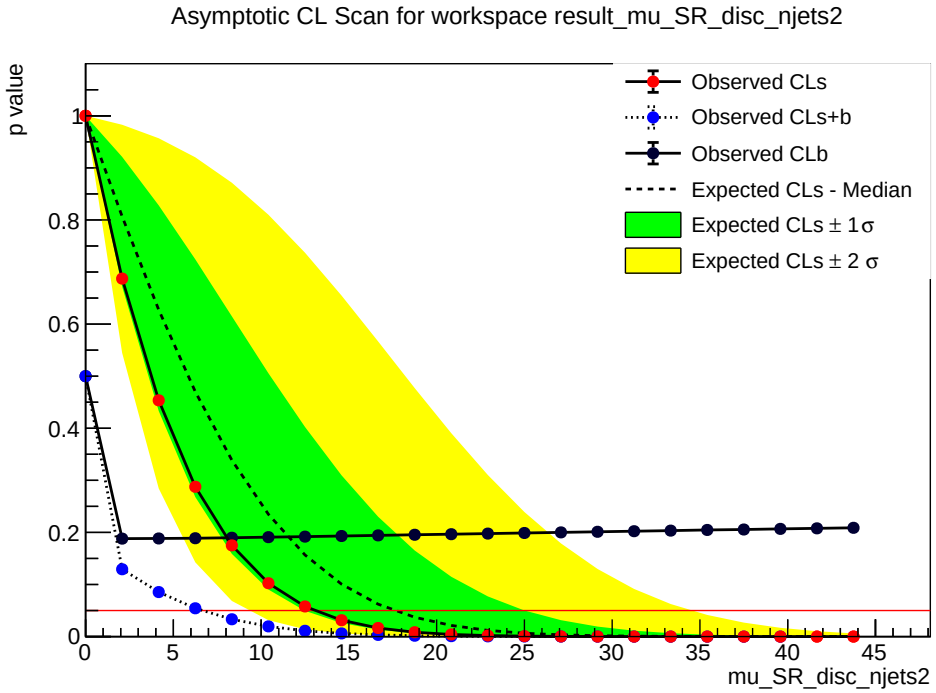

Figure 9.13: Upper limit scan at 95% CL on the signal strength for the dummy signal in SR_disc_njets2.

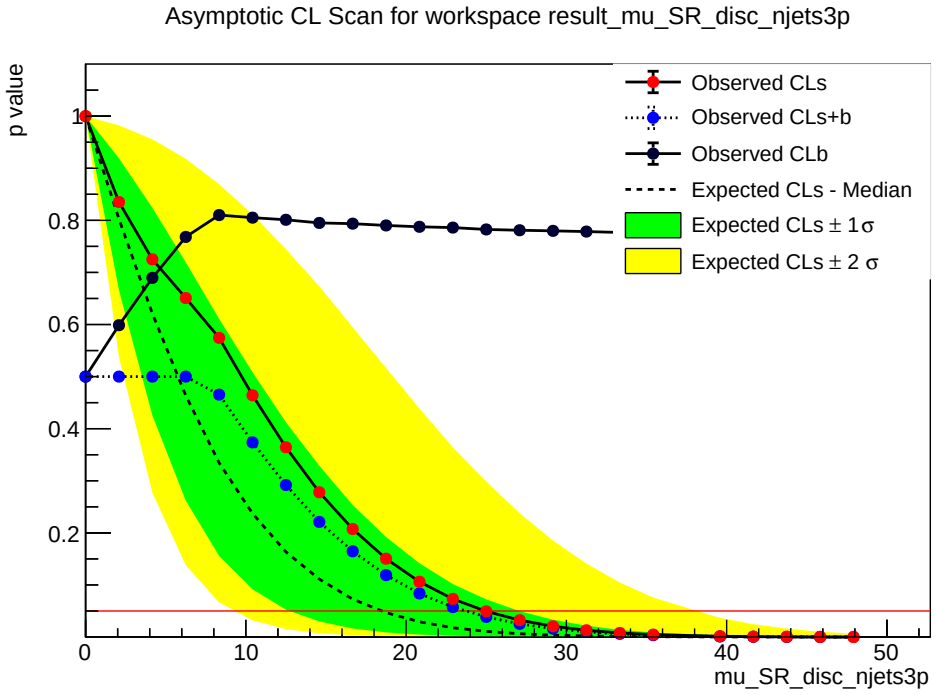

Figure 9.14: Upper limit scan at 95% CL on the signal strength for the dummy signal in SR_disc_njets3p.

channel	SR_disc_njets2
Observed events	50
Fitted bkg events	55.88 ± 3.70
Fitted Strong Z + jets events	16.64 ± 1.70
Fitted Strong W + jets events	3.72 ± 0.93
Fitted EW Z + jets events	26.43 ± 2.33
Fitted EW W + jets events	8.19 ± 0.83
Fitted top events	0.00 ± 0.00
Fitted other events	0.31 ± 0.13
Fitted QCD multijet events	$0.60^{+0.67}_{-0.60}$
MC exp. SM events	71.07 ± 5.49
MC exp. Strong Z + jets events	20.73 ± 2.27
MC exp. Strong W + jets events	4.83 ± 1.27
MC exp. EW Z + jets events	33.04 ± 3.25
MC exp. EW W + jets events	10.47 ± 1.13
MC exp. top events	0.00 ± 0.00
MC exp. other events	0.32 ± 0.13
MC exp. QCD multijet events	$0.69^{+0.72}_{-0.69}$

Table 9.9.: Yields table for discovery fit with SR_disc_njets2 including only the backgrounds.

channel	SR_disc_njets3p
Observed events	44
Fitted bkg events	39.78 ± 4.26
Fitted Strong Z + jets events	21.40 ± 3.82
Fitted Strong W+ jets events	3.98 ± 1.14
Fitted EW Z + jets events	7.07 ± 1.57
Fitted EW W+ jets events	2.84 ± 0.62
Fitted top events	0.33 ± 0.16
Fitted other events	1.57 ± 0.54
Fitted QCD multijet events	2.59 ± 2.26
MC exp. SM events	36.43 ± 5.35
MC exp. Strong Z + jets events	18.33 ± 4.19
MC exp. Strong W+ jets events	4.03 ± 1.23
MC exp. EW Z + jets events	6.42 ± 1.67
MC exp. EW W+ jets events	2.80 ± 0.66
MC exp. top events	0.29 ± 0.16
MC exp. other events	1.57 ± 0.55
MC exp. QCD multijet events	$1.99^{+2.09}_{-1.99}$

Table 9.10.: Yields table for discovery fit with SR_disc_njets3p including only the backgrounds.

Signal channel	$\langle \epsilon\sigma \rangle^{95}_{\text{obs}}$[fb]	S^{95}_{obs}	S^{95}_{exp}	CL_B	$p(s=0)$ (Z)
SR_disc_njets2	0.09	13.1	$17.7^{+7.3}_{-5.2}$	0.19	0.50 (0.00)
SR_disc_njets3p	0.18	24.9	$18.5^{+8.6}_{-5.8}$	0.78	0.19 (0.89)

Table 9.11.: Left to right: 95% CL upper limits on the visible cross section ($\langle \epsilon\sigma \rangle^{95}_{\text{obs}}$) and on the number of signal events (S^{95}_{obs}). The third column (S^{95}_{exp}) shows the 95% CL upper limit on the number of signal events, given the expected number (and possible $\pm 1\sigma$ excursions on the expectation) of background events. The last two columns indicate the CL_B value, i.e., the confidence level observed for the background-only hypothesis, and the discovery p-value ($p(s=0)$).

9.5. Exclusion Fit with Signal Regions

For the results in this section a simultaneous fit to the data is done with both the control regions and the signal regions SR_VBF_njets2 and SR_VBF_njets3p. The signal regions each have 8 bins ranging from 0.6 to 0.92 in the BDT score with identical bin widths of 0.04 (the last bin includes overflow). The exclusion fit has been performed for three different cases of the signal strength parameter: floating, fixed to zero, and fixed to one. The results shown in this section will be for the case of a floating signal strength, while the results for the cases where the signal strength is fixed are included in Appendix B. The fit is performed using the benchmark signal point of $m(\tilde{\chi}_2^0,\tilde{\chi}_1^\pm)$ = 100 GeV with $\Delta m(\tilde{\chi}_2^0,\tilde{\chi}_1^0)$ = 1 GeV which is denoted as "VBFWBall_100_99p0_MET125".

Tables 9.12, 9.13, and 9.14 show the yields in each region before and after running the exclusion fit with the signal strength as a floating parameter. Figures 9.15–9.18 shows the pre-fit and post-fit distributions in the signal regions and the significance in the signal regions. No significant deviations are found with respect to the data beyond the 2σ level. Table 9.15 gives a breakdown of the impact of each systematic in the analysis regions and the relative impact of different sources of uncertainty in the signal regions are shown in Figure 9.19. Figures 9.20, 9.21, and 9.22 show respectively the fitted normalization factors, pulls and constraints on the fit parameters, and correlation matrix. The fitted background normalizations are found to be consistent within their uncertainties of their values from the CR-only fit. The fitted signal strength is consistent with zero, indicating that the background-only model is favored when fitting to the observed data. In general the pulls and constraints seen for most the nuisance parameters in the fit appear well-behaved. There appear to be over-constraints and noticeable pulls for some of the jet-related nuisance parameters.

channel	CR_1L_njets2	CR_1L_njets3p	CR_2L_njets2	CR_2L_njets3p	SR_VBF_njets2	SR_VBF_njets3p
Observed events	21216	41814	2426	4633	12032	18214
Fitted bkg events	21200.88 ± 144.83	41820.24 ± 204.17	2358.27 ± 35.12	4672.70 ± 61.17	12112.93 ± 111.72	18169.06 ± 153.34
Fitted Strong Z + jets events	367.12 ± 6.95	859.11 ± 20.35	1884.75 ± 29.27	4066.44 ± 56.77	6820.11 ± 92.96	11488.75 ± 204.21
Fitted Strong W+ jets events	16198.92 ± 122.25	33149.09 ± 360.42	$0.06^{+0.24}_{-0.06}$	1.04 ± 0.81	2736.91 ± 67.32	4151.88 ± 132.53
Fitted EW Z + jets events	55.16 ± 1.14	57.77 ± 1.57	385.07 ± 5.80	324.97 ± 4.62	1709.04 ± 27.69	1205.60 ± 21.22
Fitted EW W+ jets events	3876.47 ± 29.30	3103.03 ± 33.79	0.00 ± 0.00	0.00 ± 0.00	725.47 ± 14.22	530.41 ± 12.47
Fitted top events	354.03 ± 31.66	3035.86 ± 238.83	23.50 ± 2.61	81.67 ± 7.21	25.02 ± 8.04	155.83 ± 48.74
Fitted other events	349.19 ± 12.40	1615.38 ± 113.42	64.89 ± 2.86	198.59 ± 16.10	93.75 ± 24.84	601.29 ± 167.27
Fitted QCD multijet events	0.00 ± 0.00	0.00 ± 0.00	0.00 ± 0.00	0.00 ± 0.00	$2.63^{+8.31}_{-2.63}$	$35.30^{+111.76}_{-35.30}$
Fitted VBFWBall_100_99p0_MET125 events	0.00 ± 0.02	0.00 ± 0.05	0.00 ± 0.00	0.00 ± 0.00	$0.00^{+51.47}_{-0.00}$	$0.00^{+67.03}_{-0.00}$
MC exp. SM events	26323.68 ± 135.25	42277.25 ± 428.98	2908.96 ± 17.26	4442.56 ± 37.27	15430.38 ± 243.24	18622.08 ± 764.33
MC exp. Strong Z + jets events	456.37 ± 9.00	806.52 ± 15.40	2345.86 ± 14.76	3833.35 ± 25.98	8446.46 ± 119.18	10684.88 ± 213.32
MC exp. Strong W+ jets events	20271.23 ± 98.66	33375.26 ± 163.30	$0.34^{+0.42}_{-0.34}$	0.64 ± 0.63	3345.34 ± 108.09	4319.03 ± 160.20
MC exp. EW Z + jets events	68.10 ± 1.04	54.05 ± 1.33	479.70 ± 2.67	306.49 ± 2.18	2152.12 ± 30.75	1139.69 ± 16.53
MC exp. EW W+ jets events	4851.25 ± 22.48	3124.29 ± 14.61	0.00 ± 0.00	0.00 ± 0.00	915.26 ± 19.98	532.07 ± 12.52
MC exp. top events	323.86 ± 31.69	3188.91 ± 261.51	20.36 ± 1.86	85.39 ± 8.36	25.28 ± 8.16	164.26 ± 51.76
MC exp. other events	352.70 ± 13.13	1727.76 ± 135.41	62.70 ± 3.09	216.68 ± 19.22	83.32 ± 25.85	575.33 ± 176.18
MC exp. QCD multijet events	0.00 ± 0.00	0.00 ± 0.00	0.00 ± 0.00	0.00 ± 0.00	$46.11^{+48.42}_{-46.11}$	$620.49^{+651.59}_{-620.49}$
MC exp. VBFWBall_100_99p0_MET125 events	0.18 ± 0.05	0.45 ± 0.11	0.00 ± 0.00	0.00 ± 0.00	416.47 ± 115.81	586.33 ± 185.53

Table 9.12.: Yields table for exclusion fit with a floating signal strength parameter.

This is anticipated to some extent due to irregularities in the template variations that were found for these parameters. Their impact has been somewhat mitigated by the smoothing procedure described in Section 8.5. The multijet background, which has a very large pre-fit uncertainty coming largely from the theory uncertainties in the MC subtraction of the ABCD estimation, is significantly suppressed after allowing the associated nuisance parameters to be pulled and constrained by the signal regions in the fit. An upper limit scan on the signal strength is performed for the benchmark signal point in Figure 9.23.

channel	SR_VBF_njets2_bin0	SR_VBF_njets2_bin1	SR_VBF_njets2_bin2	SR_VBF_njets2_bin3
Observed events	3712	2774	1946	1441
Fitted bkg events	3588.8 ± 42.4	2805.9 ± 33.1	1953.0 ± 25.1	1490.4 ± 21.5
Fitted Strong Z + jets events	2103.6 ± 33.6	1647.9 ± 27.5	1117.4 ± 22.1	826.2 ± 15.4
Fitted Strong W+ jets events	993.2 ± 29.5	691.4 ± 23.1	422.0 ± 18.0	292.1 ± 11.0
Fitted EW Z + jets events	322.2 ± 8.1	306.6 ± 5.9	272.7 ± 5.4	249.0 ± 5.1
Fitted EW W+ jets events	139.0 ± 3.4	131.0 ± 2.8	117.0 ± 2.8	108.6 ± 2.8
Fitted top events	7.5 ± 2.5	5.3 ± 1.7	5.3 ± 1.8	3.0 ± 1.0
Fitted other events	22.8 ± 6.6	23.1 ± 6.5	18.0 ± 4.9	11.0 ± 3.0
Fitted QCD multijet events	$0.5^{+1.6}_{-0.5}$	$0.6^{+1.9}_{-0.6}$	$0.6^{+1.8}_{-0.6}$	$0.5^{+1.4}_{-0.5}$
Fitted VBFWBall_100_99p0_MET125 events	$0.0^{+10.0}_{-0.0}$	$0.0^{+8.9}_{-0.0}$	$0.0^{+7.6}_{-0.0}$	$0.0^{+7.5}_{-0.0}$
MC exp. SM events	4426.30 ± 81.96	3536.14 ± 61.84	2501.10 ± 44.73	1935.61 ± 40.50
MC exp. Strong Z + jets events	2576.06 ± 46.47	2056.08 ± 36.60	1379.51 ± 25.02	1028.71 ± 21.71
MC exp. Strong W+ jets events	1168.42 ± 44.70	826.01 ± 34.17	538.24 ± 23.20	371.87 ± 17.18
MC exp. EW Z + jets events	392.07 ± 10.25	384.55 ± 6.21	342.08 ± 6.43	313.68 ± 5.65
MC exp. EW W+ jets events	172.38 ± 4.55	164.10 ± 3.85	146.28 ± 3.80	138.47 ± 4.12
MC exp. top events	7.95 ± 2.59	5.07 ± 1.69	5.63 ± 1.94	2.80 ± 0.94
MC exp. other events	19.83 ± 6.54	20.99 ± 6.74	16.27 ± 5.18	10.51 ± 3.29
MC exp. QCD multijet events	$8.58^{+9.01}_{-8.58}$	$10.51^{+11.04}_{-10.51}$	$10.11^{+10.62}_{-10.11}$	$8.04^{+8.44}_{-8.04}$
MC exp. VBFWBall_100_99p0_MET125 events	81.01 ± 23.13	68.83 ± 19.47	62.97 ± 17.19	61.52 ± 17.65

channel	SR_VBF_njets2_bin4	SR_VBF_njets2_bin5	SR_VBF_njets2_bin6	SR_VBF_njets2_bin7
Observed events	1054	729	326	50
Fitted bkg events	1100.1 ± 18.2	773.6 ± 14.0	346.7 ± 9.9	54.4 ± 2.7
Fitted Strong Z + jets events	576.0 ± 12.1	387.2 ± 9.9	145.1 ± 6.2	16.8 ± 1.1
Fitted Strong W+ jets events	189.8 ± 10.2	108.0 ± 6.7	36.6 ± 3.4	3.7 ± 0.7
Fitted EW Z + jets events	223.6 ± 5.5	192.4 ± 5.8	117.2 ± 5.0	25.4 ± 1.9
Fitted EW W+ jets events	98.1 ± 2.9	78.7 ± 2.9	44.9 ± 2.2	8.1 ± 0.6
Fitted top events	1.5 ± 0.5	2.0 ± 0.7	0.3 ± 0.2	0.0 ± 0.0
Fitted other events	10.8 ± 3.0	5.2 ± 1.4	2.5 ± 0.7	0.4 ± 0.1
Fitted QCD multijet events	$0.3^{+1.0}_{-0.3}$	$0.2^{+0.5}_{-0.2}$	$0.0^{+0.0}_{-0.0}$	$0.0^{+0.1}_{-0.0}$
Fitted VBFWBall_100_99p0_MET125 events	$0.0^{+6.6}_{-0.0}$	$0.0^{+6.3}_{-0.0}$	$0.0^{+3.6}_{-0.0}$	0.0 ± 1.0
MC exp. SM events	1448.79 ± 33.24	1029.67 ± 28.91	474.33 ± 19.25	78.44 ± 5.24
MC exp. Strong Z + jets events	721.47 ± 17.95	481.44 ± 16.07	182.47 ± 10.40	20.73 ± 1.85
MC exp. Strong W+ jets events	246.80 ± 15.57	140.58 ± 10.03	48.60 ± 4.35	4.83 ± 0.92
MC exp. EW Z + jets events	286.52 ± 7.57	247.42 ± 8.18	152.75 ± 6.96	33.04 ± 2.80
MC exp. EW W+ jets events	124.62 ± 3.91	101.24 ± 3.84	57.69 ± 3.18	10.47 ± 0.81
MC exp. top events	1.51 ± 0.53	1.89 ± 0.68	0.43 ± 0.23	0.00 ± 0.00
MC exp. other events	8.73 ± 2.80	4.45 ± 1.42	2.22 ± 0.71	0.32 ± 0.10
MC exp. QCD multijet events	$5.34^{+5.61}_{-5.34}$	$2.80^{+2.94}_{-2.80}$	$0.04^{+0.04}_{-0.04}$	$0.69^{+0.72}_{-0.69}$
MC exp. VBFWBall_100_99p0_MET125 events	53.80 ± 14.62	49.85 ± 14.13	30.12 ± 8.70	8.37 ± 2.55

Table 9.13.: Yields per bin in SR_VBF_njets2 for exclusion fit with a floating signal strength parameter.

channel	SR_VBF_njets3p_bin0	SR_VBF_njets3p_bin1	SR_VBF_njets3p_bin2	SR_VBF_njets3p_bin3
Observed events	5504	4295	3068	2358
Fitted bkg events	5531.4 ± 64.1	4306.6 ± 52.2	3117.6 ± 43.5	2344.1 ± 34.9
Fitted Strong Z + jets events	3533.2 ± 77.9	2737.2 ± 55.8	1976.4 ± 41.5	1480.8 ± 32.9
Fitted Strong W+ jets events	1385.5 ± 57.1	1048.8 ± 38.7	708.0 ± 28.6	502.9 ± 20.7
Fitted EW Z + jets events	249.2 ± 5.1	225.5 ± 4.5	203.9 ± 4.9	177.3 ± 4.0
Fitted EW W+ jets events	129.4 ± 5.1	111.4 ± 4.1	92.6 ± 2.8	77.4 ± 2.2
Fitted top events	55.5 ± 17.3	40.2 ± 12.9	25.9 ± 8.2	17.9 ± 5.7
Fitted other events	164.3 ± 46.1	133.8 ± 37.1	104.7 ± 29.3	84.7 ± 23.8
Fitted QCD multijet events	$14.3^{+45.4}_{-14.3}$	$9.8^{+30.9}_{-9.8}$	$6.0^{+19.1}_{-6.0}$	$3.3^{+10.5}_{-3.3}$
Fitted VBFWBall_100_99p0_MET125 events	$0.0^{+13.7}_{-0.0}$	$0.0^{+12.8}_{-0.0}$	$0.0^{+11.2}_{-0.0}$	$0.0^{+9.9}_{-0.0}$
MC exp. SM events	5775.31 ± 292.56	4405.00 ± 207.41	3182.04 ± 139.93	2378.09 ± 93.09
MC exp. Strong Z + jets events	3307.34 ± 71.08	2527.74 ± 57.93	1847.03 ± 48.52	1388.75 ± 43.20
MC exp. Strong W+ jets events	1505.87 ± 65.40	1102.34 ± 46.16	718.50 ± 34.45	499.68 ± 25.39
MC exp. EW Z + jets events	236.96 ± 4.00	213.52 ± 3.85	192.06 ± 3.93	168.10 ± 3.41
MC exp. EW W+ jets events	128.41 ± 5.39	108.20 ± 3.93	93.76 ± 2.83	77.86 ± 2.33
MC exp. top events	57.12 ± 17.99	43.92 ± 14.11	26.32 ± 8.41	19.62 ± 6.24
MC exp. other events	164.59 ± 50.77	129.08 ± 39.50	100.90 ± 30.92	78.37 ± 24.17
MC exp. QCD multijet events	$252.10^{+264.74}_{-252.10}$	$171.37^{+179.96}_{-171.37}$	$106.47^{+111.81}_{-106.47}$	$57.87^{+60.77}_{-57.87}$
MC exp. VBFWBall_100_99p0_MET125 events	122.92 ± 39.04	108.84 ± 34.73	97.01 ± 31.72	87.85 ± 28.34

channel	SR_VBF_njets3p_bin4	SR_VBF_njets3p_bin5	SR_VBF_njets3p_bin6	SR_VBF_njets3p_bin7
Observed events	1611	936	398	44
Fitted bkg events	1570.1 ± 26.6	904.4 ± 19.2	358.2 ± 10.9	36.6 ± 2.7
Fitted Strong Z + jets events	973.9 ± 24.0	564.0 ± 18.1	202.1 ± 9.7	21.3 ± 2.1
Fitted Strong W+ jets events	310.3 ± 16.6	137.6 ± 8.1	55.1 ± 4.9	3.6 ± 0.7
Fitted EW Z + jets events	153.9 ± 4.3	121.0 ± 3.7	68.2 ± 2.8	6.7 ± 0.8
Fitted EW W+ jets events	56.3 ± 1.9	41.6 ± 1.8	18.8 ± 0.9	2.9 ± 0.4
Fitted top events	9.5 ± 3.1	5.5 ± 1.8	1.1 ± 0.4	0.3 ± 0.1
Fitted other events	64.8 ± 18.2	34.4 ± 9.6	12.9 ± 3.8	1.7 ± 0.5
Fitted QCD multijet events	$1.4^{+4.5}_{-1.4}$	$0.3^{+1.1}_{-0.3}$	0.0 ± 0.0	$0.1^{+0.4}_{-0.1}$
Fitted VBFWBall_100_99p0_MET125 events	$0.0^{+9.2}_{-0.0}$	$0.0^{+6.4}_{-0.0}$	$0.0^{+3.5}_{-0.0}$	0.0 ± 0.5
MC exp. SM events	1576.62 ± 60.08	900.78 ± 34.95	364.86 ± 19.91	39.37 ± 4.07
MC exp. Strong Z + jets events	895.76 ± 32.90	514.41 ± 23.35	185.51 ± 13.74	18.33 ± 2.23
MC exp. Strong W+ jets events	305.68 ± 19.54	131.45 ± 10.47	51.48 ± 5.23	4.03 ± 0.60
MC exp. EW Z + jets events	143.37 ± 3.66	114.34 ± 3.62	64.93 ± 2.80	6.42 ± 0.84
MC exp. EW W+ jets events	58.73 ± 2.09	42.82 ± 2.00	19.49 ± 1.09	2.80 ± 0.42
MC exp. top events	9.80 ± 3.21	6.05 ± 1.99	1.15 ± 0.43	0.29 ± 0.09
MC exp. other events	57.66 ± 17.74	31.05 ± 9.56	12.11 ± 3.83	1.57 ± 0.49
MC exp. QCD multijet events	$24.84^{+26.09}_{-24.84}$	$5.85^{+6.14}_{-5.85}$	0.00 ± 0.00	$1.99^{+2.09}_{-1.99}$
MC exp. VBFWBall_100_99p0_MET125 events	80.78 ± 25.12	54.81 ± 17.44	30.19 ± 9.67	3.94 ± 1.39

Table 9.14.: Yields per bin in SR_VBF_njets3p for exclusion fit with a floating signal strength parameter.

Uncertainty of channel	SR_VBF_njets2	CR_1L_njets2	CR_2L_njets2	SR_VBF_njets3p	CR_1L_njets3p	CR_2L_njets3p
Total background expectation	12112.93	21200.88	2358.27	18169.06	41820.24	4672.70
Total statistical ($\sqrt{N_{exp}}$)	±110.06	±145.61	±48.56	±134.79	±204.50	±68.36
Total background systematic	±111.72 [0.92%]	±144.83 [0.68%]	±35.12 [1.49%]	±153.34 [0.84%]	±204.17 [0.49%]	±61.17 [1.31%]
mu_Zjets_njets2	±127.45 [1.1%]	±6.31 [0.03%]	±33.92 [1.4%]	±0.00 [0.00%]	±0.00 [0.00%]	±0.00 [0.00%]
alpha_MUON_EFF_RECO_SYS	±51.59 [0.43%]	±1.02 [0.00%]	±0.74 [0.03%]	±80.62 [0.44%]	±9.35 [0.02%]	±2.32 [0.05%]
mu_SIG	±51.47 [0.42%]	±0.02 [0.00%]	±0.00 [0.00%]	±67.03 [0.37%]	±0.05 [0.00%]	±0.00 [0.00%]
alpha_EG_EFF_ID	±44.28 [0.37%]	±0.08 [0.00%]	±1.74 [0.07%]	±70.68 [0.39%]	±6.73 [0.02%]	±4.59 [0.10%]
alpha_Strong_Wjets_assew	±35.94 [0.30%]	±0.00 [0.00%]	±0.00 [0.00%]	±96.96 [0.53%]	±0.00 [0.00%]	±0.05 [0.00%]
alpha_JET_JER_EffectiveNP_1	±33.16 [0.27%]	±2.20 [0.01%]	±1.82 [0.08%]	±45.81 [0.25%]	±19.41 [0.05%]	±0.75 [0.02%]
alpha_JET_JER_EffectiveNP_10	±33.00 [0.27%]	±1.89 [0.01%]	±1.08 [0.05%]	±16.41 [0.09%]	±8.43 [0.02%]	±0.41 [0.01%]
alpha_MET_SoftTrk_ResoPerp	±31.45 [0.26%]	±1.93 [0.01%]	±0.19 [0.01%]	±14.60 [0.08%]	±18.41 [0.04%]	±1.96 [0.04%]
mu_Wjets_njets2	±31.34 [0.26%]	±181.74 [0.86%]	±0.00 [0.00%]	±0.00 [0.00%]	±0.00 [0.00%]	±0.00 [0.00%]
alpha_JES_Pileup_RhoTopology	±30.95 [0.26%]	±25.20 [0.12%]	±0.41 [0.02%]	±102.21 [0.56%]	±18.13 [0.04%]	±4.66 [0.10%]
alpha_EG_EFF_Iso	±30.25 [0.25%]	±0.75 [0.00%]	±1.42 [0.06%]	±54.50 [0.30%]	±0.70 [0.00%]	±3.89 [0.08%]
alpha_JET_JER_EffectiveNP_6	±30.08 [0.25%]	±5.62 [0.03%]	±0.56 [0.02%]	±12.14 [0.07%]	±13.56 [0.03%]	±0.95 [0.02%]
alpha_JET_JER_EffectiveNP_2	±29.90 [0.25%]	±5.21 [0.02%]	±0.60 [0.03%]	±76.63 [0.42%]	±37.66 [0.09%]	±5.40 [0.12%]
alpha_JES_EffectiveNP_Mixed1	±29.68 [0.25%]	±8.72 [0.04%]	±0.84 [0.04%]	±66.28 [0.36%]	±49.18 [0.12%]	±0.64 [0.01%]
alpha_Strong_Wjets_PDF	±29.31 [0.24%]	±0.01 [0.00%]	±0.02 [0.00%]	±45.77 [0.25%]	±0.08 [0.00%]	±0.10 [0.00%]
alpha_JvtEfficiency	±26.66 [0.22%]	±2.99 [0.01%]	±0.50 [0.02%]	±32.90 [0.18%]	±1.12 [0.00%]	±1.31 [0.03%]
gamma_stat_SR_VBF_njets2_BDTscore_bin_0	±25.60 [0.21%]	±0.00 [0.00%]	±0.00 [0.00%]	±0.00 [0.00%]	±0.00 [0.00%]	±0.00 [0.00%]
alpha_JET_JER_EffectiveNP_5	±25.51 [0.21%]	±3.62 [0.02%]	±0.15 [0.01%]	±27.21 [0.15%]	±3.53 [0.01%]	±2.37 [0.05%]
alpha_flatSys_other	±24.92 [0.21%]	±0.00 [0.00%]	±0.00 [0.00%]	±159.86 [0.88%]	±0.00 [0.00%]	±0.00 [0.00%]
alpha_JES_Flavor_Response	±23.68 [0.20%]	±0.33 [0.00%]	±0.77 [0.03%]	±22.33 [0.12%]	±170.10 [0.41%]	±7.93 [0.17%]
alpha_Strong_Zjets_PDF	±22.49 [0.19%]	±0.73 [0.00%]	±0.73 [0.03%]	±56.24 [0.31%]	±0.53 [0.00%]	±0.53 [0.01%]
gamma_stat_SR_VBF_njets2_BDTscore_bin_1	±20.37 [0.17%]	±0.00 [0.00%]	±0.00 [0.00%]	±0.00 [0.00%]	±0.00 [0.00%]	±0.00 [0.00%]
alpha_JES_Pileup_OffsetMu	±18.27 [0.15%]	±5.12 [0.02%]	±1.15 [0.05%]	±17.43 [0.10%]	±22.39 [0.05%]	±5.74 [0.12%]
alpha_EG_EFF_Reco	±18.00 [0.15%]	±0.41 [0.00%]	±0.59 [0.03%]	±26.04 [0.14%]	±4.20 [0.01%]	±1.33 [0.03%]
alpha_MUON_EFF_ISO_SYS	±17.64 [0.15%]	±0.25 [0.00%]	±0.52 [0.02%]	±23.97 [0.13%]	±3.04 [0.01%]	±1.28 [0.03%]
alpha_JES_EffectiveNP_Modelling1	±17.01 [0.14%]	±4.97 [0.02%]	±0.23 [0.01%]	±12.41 [0.07%]	±71.05 [0.17%]	±4.57 [0.10%]
gamma_stat_SR_VBF_njets2_BDTscore_bin_2	±16.42 [0.14%]	±0.00 [0.00%]	±0.00 [0.00%]	±0.00 [0.00%]	±0.00 [0.00%]	±0.00 [0.00%]
alpha_JET_JER_EffectiveNP_11	±15.52 [0.13%]	±2.02 [0.01%]	±0.47 [0.02%]	±2.33 [0.01%]	±10.53 [0.03%]	±1.95 [0.04%]
alpha_Strong_Zjets_assew	±15.16 [0.13%]	±0.81 [0.00%]	±0.81 [0.03%]	±65.03 [0.36%]	±2.71 [0.01%]	±2.70 [0.06%]
alpha_JES_Flavor_Composition	±15.10 [0.12%]	±22.85 [0.11%]	±1.59 [0.07%]	±45.21 [0.25%]	±177.61 [0.42%]	±12.37 [0.26%]
alpha_JET_JER_EffectiveNP_12restTerm	±14.76 [0.12%]	±4.75 [0.02%]	±0.56 [0.02%]	±15.14 [0.08%]	±5.47 [0.01%]	±4.85 [0.10%]
alpha_JES_EtaIntercalibration_Modelling	±14.21 [0.12%]	±2.43 [0.01%]	±1.17 [0.05%]	±35.14 [0.19%]	±81.88 [0.20%]	±4.22 [0.09%]
alpha_JES_Pileup_OffsetNPV	±12.99 [0.11%]	±10.04 [0.05%]	±0.58 [0.02%]	±25.99 [0.14%]	±10.37 [0.02%]	±4.06 [0.09%]
alpha_JET_JER_EffectiveNP_8	±12.97 [0.11%]	±0.37 [0.00%]	±1.03 [0.04%]	±12.56 [0.07%]	±5.69 [0.01%]	±3.26 [0.07%]
alpha_MET_SoftTrk_ResoPara	±12.78 [0.11%]	±0.65 [0.00%]	±0.97 [0.04%]	±13.91 [0.08%]	±9.96 [0.02%]	±0.14 [0.00%]
alpha_JES_EffectiveNP_Modelling3	±12.35 [0.10%]	±3.26 [0.02%]	±0.34 [0.01%]	±22.32 [0.12%]	±21.35 [0.05%]	±0.68 [0.01%]
gamma_stat_SR_VBF_njets2_BDTscore_bin_3	±12.21 [0.10%]	±0.00 [0.00%]	±0.00 [0.00%]	±0.00 [0.00%]	±0.00 [0.00%]	±0.00 [0.00%]
alpha_JES_EffectiveNP_Mixed2	±11.84 [0.10%]	±3.19 [0.02%]	±0.11 [0.00%]	±10.60 [0.06%]	±24.50 [0.06%]	±1.03 [0.02%]
alpha_JET_JER_EffectiveNP_9	±11.48 [0.09%]	±3.52 [0.02%]	±0.57 [0.02%]	±6.87 [0.04%]	±6.92 [0.02%]	±0.05 [0.00%]
alpha_MET_SoftTrk_Scale	±11.14 [0.09%]	±4.05 [0.02%]	±2.00 [0.08%]	±6.12 [0.03%]	±17.08 [0.04%]	±3.03 [0.06%]
alpha_JES_EtaIntercalibration_NonClosure_2018data	±10.36 [0.09%]	±2.93 [0.01%]	±0.08 [0.00%]	±18.39 [0.10%]	±33.17 [0.08%]	±0.85 [0.02%]
gamma_stat_SR_VBF_njets2_BDTscore_bin_4	±10.28 [0.08%]	±0.00 [0.00%]	±0.00 [0.00%]	±0.00 [0.00%]	±0.00 [0.00%]	±0.00 [0.00%]
alpha_JET_JER_EffectiveNP_3	±9.68 [0.08%]	±1.02 [0.00%]	±0.05 [0.00%]	±28.89 [0.16%]	±0.92 [0.00%]	±0.48 [0.01%]
alpha_JES_EffectiveNP_Modelling2	±9.68 [0.08%]	±2.30 [0.01%]	±0.21 [0.01%]	±19.54 [0.11%]	±12.87 [0.03%]	±0.18 [0.00%]
alpha_JES_Pileup_PtTerm	±9.01 [0.07%]	±3.63 [0.02%]	±0.82 [0.03%]	±17.70 [0.10%]	±31.02 [0.07%]	±0.09 [0.00%]
alpha_QCD_estimation_subtraction_theory	±8.40 [0.07%]	±0.00 [0.00%]	±0.00 [0.00%]	±112.94 [0.62%]	±0.00 [0.00%]	±0.00 [0.00%]
alpha_Strong_Zjets_alphaS	±8.21 [0.07%]	±0.45 [0.00%]	±0.45 [0.02%]	±3.46 [0.02%]	±0.05 [0.00%]	±0.05 [0.00%]
alpha_EW_Zjets_scale	±7.67 [0.06%]	±0.07 [0.00%]	±0.07 [0.00%]	±5.03 [0.03%]	±0.04 [0.00%]	±0.04 [0.00%]
alpha_Strong_Wjets_alphaS	±7.62 [0.06%]	±0.00 [0.00%]	±0.00 [0.00%]	±18.01 [0.10%]	±0.00 [0.00%]	±0.00 [0.00%]
alpha_flatSys_top	±7.52 [0.06%]	±0.00 [0.00%]	±0.00 [0.00%]	±46.83 [0.26%]	±0.00 [0.00%]	±0.00 [0.00%]
alpha_MUON_TTVA_SYS	±7.29 [0.06%]	±0.14 [0.00%]	±0.14 [0.01%]	±10.64 [0.06%]	±1.45 [0.00%]	±0.38 [0.01%]
alpha_JES_EffectiveNP_Detector1	±7.28 [0.06%]	±1.03 [0.00%]	±0.03 [0.00%]	±1.89 [0.01%]	±8.87 [0.02%]	±0.36 [0.01%]
gamma_stat_SR_VBF_njets2_BDTscore_bin_5	±7.16 [0.06%]	±0.00 [0.00%]	±0.00 [0.00%]	±0.00 [0.00%]	±0.00 [0.00%]	±0.00 [0.00%]
alpha_MUON_EFF_ISO_STAT	±6.28 [0.05%]	±0.09 [0.00%]	±0.16 [0.01%]	±8.44 [0.05%]	±1.22 [0.00%]	±0.39 [0.01%]
alpha_MUON_TTVA_STAT	±6.12 [0.05%]	±0.09 [0.00%]	±0.15 [0.01%]	±8.85 [0.05%]	±1.04 [0.00%]	±0.39 [0.01%]
alpha_MUON_EFF_RECO_STAT	±5.86 [0.05%]	±0.12 [0.00%]	±0.14 [0.01%]	±8.44 [0.05%]	±1.12 [0.00%]	±0.35 [0.01%]
alpha_Strong_Zjets_scale	±5.40 [0.04%]	±0.52 [0.00%]	±0.52 [0.02%]	±17.52 [0.10%]	±0.80 [0.00%]	±0.80 [0.02%]
alpha_JET_JER_DataVsMC_MC16	±5.34 [0.04%]	±2.65 [0.01%]	±0.10 [0.00%]	±45.80 [0.25%]	±20.82 [0.05%]	±3.27 [0.07%]
alpha_EW_Wjets_scale	±5.16 [0.04%]	±0.00 [0.00%]	±0.00 [0.00%]	±0.11 [0.00%]	±0.00 [0.00%]	±0.00 [0.00%]
alpha_EW_Zjets_PDF	±5.12 [0.04%]	±0.06 [0.00%]	±0.06 [0.00%]	±5.23 [0.03%]	±0.25 [0.00%]	±0.25 [0.01%]
alpha_JES_EtaIntercalibration_NonClosure_negEta	±4.42 [0.04%]	±0.32 [0.00%]	±0.33 [0.01%]	±3.57 [0.02%]	±2.63 [0.01%]	±0.12 [0.00%]
gamma_stat_SR_VBF_njets2_BDTscore_bin_6	±4.21 [0.03%]	±0.00 [0.00%]	±0.00 [0.00%]	±0.00 [0.00%]	±0.00 [0.00%]	±0.00 [0.00%]
alpha_JES_EffectiveNP_Statistical3	±4.17 [0.03%]	±1.43 [0.01%]	±0.00 [0.00%]	±12.97 [0.07%]	±6.71 [0.02%]	±0.06 [0.00%]
alpha_JES_EtaIntercalibration_TotalStat	±4.16 [0.03%]	±2.29 [0.01%]	±0.82 [0.03%]	±7.72 [0.04%]	±6.36 [0.02%]	±1.14 [0.02%]
alpha_EW_Wjets_PDF	±4.06 [0.03%]	±0.00 [0.00%]	±0.00 [0.00%]	±3.19 [0.02%]	±0.00 [0.00%]	±0.00 [0.00%]
alpha_JES_EffectiveNP_Statistical6	±4.02 [0.03%]	±0.59 [0.00%]	±0.08 [0.00%]	±2.80 [0.02%]	±3.87 [0.01%]	±0.02 [0.00%]
alpha_btag_ExtraFromCharm	±3.81 [0.03%]	±1.50 [0.01%]	±0.37 [0.02%]	±26.76 [0.15%]	±16.36 [0.04%]	±3.42 [0.07%]
alpha_JES_EffectiveNP_Statistical1	±3.76 [0.03%]	±0.62 [0.00%]	±0.01 [0.00%]	±10.42 [0.06%]	±3.54 [0.01%]	±0.13 [0.00%]
alpha_JES_EffectiveNP_Modelling4	±3.62 [0.03%]	±0.50 [0.00%]	±0.03 [0.00%]	±7.78 [0.04%]	±3.86 [0.01%]	±0.16 [0.00%]
alpha_EG_SCALE_ALL	±2.98 [0.02%]	±0.47 [0.00%]	±0.27 [0.01%]	±2.12 [0.01%]	±7.47 [0.02%]	±0.01 [0.00%]
alpha_JET_JER_EffectiveNP_4	±2.25 [0.02%]	±3.90 [0.02%]	±0.55 [0.02%]	±63.76 [0.35%]	±11.97 [0.03%]	±5.33 [0.11%]
alpha_Strong_Wjets_scale	±2.24 [0.02%]	±0.02 [0.00%]	±0.03 [0.00%]	±8.80 [0.05%]	±0.10 [0.00%]	±0.12 [0.00%]
alpha_JES_EffectiveNP_Mixed3	±2.16 [0.02%]	±0.26 [0.00%]	±0.22 [0.01%]	±0.73 [0.00%]	±1.89 [0.00%]	±0.05 [0.00%]
alpha_JES_EffectiveNP_Statistical2	±2.10 [0.02%]	±1.26 [0.01%]	±0.12 [0.01%]	±6.32 [0.03%]	±1.26 [0.00%]	±0.21 [0.00%]
alpha_JES_BJES_Response	±2.10 [0.02%]	±0.04 [0.00%]	±0.04 [0.00%]	±4.11 [0.02%]	±0.03 [0.00%]	±0.00 [0.00%]
Lumi	±2.01 [0.02%]	±11.89 [0.06%]	±1.49 [0.06%]	±12.80 [0.07%]	±78.65 [0.19%]	±4.74 [0.10%]
alpha_EW_Wjets_alphaS	±1.97 [0.02%]	±0.00 [0.00%]	±0.00 [0.00%]	±1.12 [0.01%]	±0.00 [0.00%]	±0.00 [0.00%]
alpha_MUON_SCALE	±1.71 [0.01%]	±0.33 [0.00%]	±0.83 [0.04%]	±3.51 [0.02%]	±0.59 [0.00%]	±0.04 [0.00%]
alpha_btag_CT	±1.69 [0.01%]	±3.60 [0.02%]	±0.25 [0.01%]	±28.98 [0.16%]	±49.00 [0.12%]	±1.89 [0.04%]
alpha_JES_EtaIntercalibration_NonClosure_posEta	±1.66 [0.01%]	±0.37 [0.00%]	±0.07 [0.00%]	±1.19 [0.01%]	±0.96 [0.00%]	±0.02 [0.00%]
alpha_JES_EffectiveNP_Statistical5	±1.56 [0.01%]	±0.01 [0.00%]	±0.05 [0.00%]	±3.60 [0.02%]	±2.24 [0.01%]	±0.38 [0.01%]
gamma_stat_SR_VBF_njets2_BDTscore_bin_7	±1.47 [0.01%]	±0.00 [0.00%]	±0.00 [0.00%]	±0.00 [0.00%]	±0.00 [0.00%]	±0.00 [0.00%]
alpha_EW_Zjets_alphaS	±1.42 [0.01%]	±0.02 [0.00%]	±0.02 [0.00%]	±0.46 [0.00%]	±0.04 [0.00%]	±0.04 [0.00%]
alpha_MUON_EFF_RECO_SYS_LOWPT	±1.42 [0.01%]	±0.00 [0.00%]	±0.04 [0.00%]	±2.11 [0.01%]	±0.13 [0.00%]	±0.14 [0.00%]
alpha_JET_JER_EffectiveNP_7	±1.25 [0.01%]	±2.65 [0.01%]	±0.41 [0.02%]	±48.05 [0.26%]	±5.72 [0.01%]	±0.36 [0.01%]
alpha_JES_EffectiveNP_Statistical4	±1.11 [0.01%]	±1.33 [0.01%]	±0.20 [0.01%]	±5.36 [0.03%]	±8.21 [0.02%]	±0.07 [0.00%]
alpha_QCD_estimation_subtraction_exp	±0.91 [0.01%]	±0.00 [0.00%]	±0.00 [0.00%]	±12.19 [0.07%]	±0.00 [0.00%]	±0.00 [0.00%]
alpha_EG_RESOLUTION_ALL	±0.85 [0.01%]	±0.23 [0.00%]	±0.01 [0.00%]	±4.31 [0.02%]	±1.31 [0.00%]	±0.27 [0.01%]
alpha_JES_EffectiveNP_Detector2	±0.79 [0.01%]	±0.10 [0.00%]	±0.01 [0.00%]	±3.75 [0.02%]	±0.68 [0.00%]	±0.09 [0.00%]
alpha_MUON_EFF_RECO_STAT_LOWPT	±0.77 [0.01%]	±0.00 [0.00%]	±0.01 [0.00%]	±1.05 [0.01%]	±0.03 [0.00%]	±0.06 [0.00%]
alpha_btag_LightT	±0.70 [0.01%]	±4.30 [0.02%]	±0.57 [0.02%]	±13.89 [0.08%]	±54.79 [0.13%]	±3.45 [0.07%]
alpha_MUON_SAGITTA_RESBIAS	±0.68 [0.01%]	±0.02 [0.00%]	±0.13 [0.01%]	±1.12 [0.01%]	±0.32 [0.00%]	±0.08 [0.00%]
alpha_MUON_MS	±0.48 [0.00%]	±0.07 [0.00%]	±0.97 [0.04%]	±0.79 [0.00%]	±0.71 [0.00%]	±0.37 [0.01%]
alpha_btag_Extra	±0.45 [0.00%]	±1.52 [0.01%]	±0.08 [0.00%]	±3.02 [0.02%]	±8.27 [0.02%]	±0.26 [0.01%]
alpha_JES_PunchThrough_MC16	±0.39 [0.00%]	±0.02 [0.00%]	±0.05 [0.00%]	±1.23 [0.01%]	±0.51 [0.00%]	±0.08 [0.00%]
alpha_QCD_estimation_fit	±0.33 [0.00%]	±0.00 [0.00%]	±0.00 [0.00%]	±4.47 [0.02%]	±0.00 [0.00%]	±0.00 [0.00%]
alpha_MUON_ID	±0.32 [0.00%]	±0.20 [0.00%]	±0.13 [0.01%]	±1.07 [0.01%]	±0.24 [0.00%]	±0.28 [0.01%]
alpha_QCD_estimation_transfer_factor	±0.25 [0.00%]	±0.00 [0.00%]	±0.00 [0.00%]	±3.34 [0.02%]	±0.00 [0.00%]	±0.00 [0.00%]
alpha_QCD_estimation_statistical	±0.25 [0.00%]	±0.00 [0.00%]	±0.00 [0.00%]	±3.30 [0.02%]	±0.00 [0.00%]	±0.00 [0.00%]
alpha_Pileup	±0.20 [0.00%]	±3.62 [0.02%]	±1.80 [0.08%]	±14.25 [0.08%]	±9.37 [0.02%]	±0.12 [0.00%]
alpha_JES_EtaIntercalibration_NonClosure_highE	±0.14 [0.00%]	±0.01 [0.00%]	±0.01 [0.00%]	±0.30 [0.00%]	±0.40 [0.00%]	±0.04 [0.00%]
alpha_QCD_estimation_MET_trig_eff	±0.13 [0.00%]	±0.00 [0.00%]	±0.00 [0.00%]	±1.75 [0.01%]	±0.00 [0.00%]	±0.00 [0.00%]
alpha_btag_BT	±0.09 [0.00%]	±9.08 [0.04%]	±0.55 [0.02%]	±7.78 [0.04%]	±156.41 [0.37%]	±5.03 [0.11%]
alpha_MUON_SAGITTA_DATASTAT	±0.06 [0.00%]	±0.03 [0.00%]	±0.03 [0.00%]	±0.54 [0.00%]	±0.14 [0.00%]	±0.16 [0.00%]
alpha_JES_SingleParticle_HighPt	±0.00 [0.00%]	±0.05 [0.00%]	±0.05 [0.00%]	±0.00 [0.00%]	±0.00 [0.00%]	±0.08 [0.00%]
alpha_SigXSec	±0.00 [0.00%]	±0.00 [0.00%]	±0.00 [0.00%]	±0.00 [0.00%]	±0.00 [0.00%]	±0.00 [0.00%]
alpha_signal_scale	±0.00 [0.00%]	±0.00 [0.00%]	±0.00 [0.00%]	±0.00 [0.00%]	±0.00 [0.00%]	±0.00 [0.00%]
alpha_signal_radiation	±0.00 [0.00%]	±0.00 [0.00%]	±0.00 [0.00%]	±0.00 [0.00%]	±0.00 [0.00%]	±0.00 [0.00%]
alpha_signal_pdf	±0.00 [0.00%]	±0.00 [0.00%]	±0.00 [0.00%]	±0.00 [0.00%]	±0.00 [0.00%]	±0.00 [0.00%]
alpha_JET_RelativeNonClosure_AFII	±0.00 [0.00%]	±0.00 [0.00%]	±0.00 [0.00%]	±0.00 [0.00%]	±0.00 [0.00%]	±0.00 [0.00%]
alpha_JET_JER_DataVsMC_AFII	±0.00 [0.00%]	±0.00 [0.00%]	±0.00 [0.00%]	±0.00 [0.00%]	±0.00 [0.00%]	±0.00 [0.00%]
alpha_EG_SCALE_AF2	±0.00 [0.00%]	±0.00 [0.00%]	±0.00 [0.00%]	±0.00 [0.00%]	±0.00 [0.00%]	±0.00 [0.00%]
gamma_stat_SR_VBF_njets3p_BDTscore_bin_3	±0.00 [0.00%]	±0.00 [0.00%]	±0.00 [0.00%]	±25.32 [0.14%]	±0.00 [0.00%]	±0.00 [0.00%]
gamma_stat_SR_VBF_njets3p_BDTscore_bin_2	±0.00 [0.00%]	±0.00 [0.00%]	±0.00 [0.00%]	±29.91 [0.16%]	±0.00 [0.00%]	±0.00 [0.00%]
gamma_stat_SR_VBF_njets3p_BDTscore_bin_1	±0.00 [0.00%]	±0.00 [0.00%]	±0.00 [0.00%]	±37.47 [0.21%]	±0.00 [0.00%]	±0.00 [0.00%]
gamma_stat_CR_2L_njets2_BDTscore_LepInvis_bin_0	±0.00 [0.00%]	±0.00 [0.00%]	±8.24 [0.35%]	±0.00 [0.00%]	±0.00 [0.00%]	±0.00 [0.00%]
gamma_stat_CR_1L_njets3p_BDTscore_LepInvis_bin_0	±0.00 [0.00%]	±0.00 [0.00%]	±0.00 [0.00%]	±0.00 [0.00%]	±109.08 [0.26%]	±0.00 [0.00%]
gamma_stat_SR_VBF_njets3p_BDTscore_bin_0	±0.00 [0.00%]	±0.00 [0.00%]	±0.00 [0.00%]	±46.42 [0.26%]	±0.00 [0.00%]	±0.00 [0.00%]
gamma_stat_SR_VBF_njets3p_BDTscore_bin_7	±0.00 [0.00%]	±0.00 [0.00%]	±0.00 [0.00%]	±1.96 [0.01%]	±0.00 [0.00%]	±0.00 [0.00%]
gamma_stat_SR_VBF_njets3p_BDTscore_bin_6	±0.00 [0.00%]	±0.00 [0.00%]	±0.00 [0.00%]	±7.03 [0.04%]	±0.00 [0.00%]	±0.00 [0.00%]
gamma_stat_SR_VBF_njets3p_BDTscore_bin_5	±0.00 [0.00%]	±0.00 [0.00%]	±0.00 [0.00%]	±13.30 [0.07%]	±0.00 [0.00%]	±0.00 [0.00%]
gamma_stat_SR_VBF_njets3p_BDTscore_bin_4	±0.00 [0.00%]	±0.00 [0.00%]	±0.00 [0.00%]	±18.77 [0.10%]	±0.00 [0.00%]	±0.00 [0.00%]
gamma_stat_CR_1L_njets2_BDTscore_LepInvis_bin_0	±0.00 [0.00%]	±52.39 [0.25%]	±0.00 [0.00%]	±0.00 [0.00%]	±0.00 [0.00%]	±0.00 [0.00%]
alpha_MUON_EFF_TrigStatUncertainty	±0.00 [0.00%]	±19.26 [0.09%]	±1.28 [0.05%]	±0.00 [0.00%]	±35.89 [0.09%]	±2.47 [0.05%]
mu_Zjets_njets3p	±0.00 [0.00%]	±0.00 [0.00%]	±0.00 [0.00%]	±185.73 [1.0%]	±13.41 [0.03%]	±64.25 [1.4%]
alpha_JES_PunchThrough_AFII	±0.00 [0.00%]	±0.00 [0.00%]	±0.00 [0.00%]	±0.00 [0.00%]	±0.00 [0.00%]	±0.00 [0.00%]
alpha_EG_EFF_Trigger	±0.00 [0.00%]	±27.13 [0.13%]	±0.17 [0.01%]	±0.00 [0.00%]	±55.20 [0.13%]	±0.33 [0.01%]
alpha_MUON_EFF_TrigSystUncertainty	±0.00 [0.00%]	±79.40 [0.37%]	±8.59 [0.36%]	±0.00 [0.00%]	±154.39 [0.37%]	±16.61 [0.36%]
alpha_EG_EFF_TriggerEff	±0.00 [0.00%]	±2.41 [0.01%]	±0.00 [0.00%]	±0.00 [0.00%]	±9.45 [0.02%]	±0.00 [0.00%]
gamma_stat_CR_2L_njets3p_BDTscore_LepInvis_bin_0	±0.00 [0.00%]	±0.00 [0.00%]	±0.00 [0.00%]	±0.00 [0.00%]	±0.00 [0.00%]	±19.79 [0.42%]
mu_Wjets_njets3p	±0.00 [0.00%]	±0.00 [0.00%]	±0.00 [0.00%]	±56.83 [0.31%]	±440.02 [1.1%]	±0.01 [0.00%]

Table 9.15.: Breakdown of the systematic uncertainties in the signal and control regions after the exclusion fit with a floating signal strength parameter.

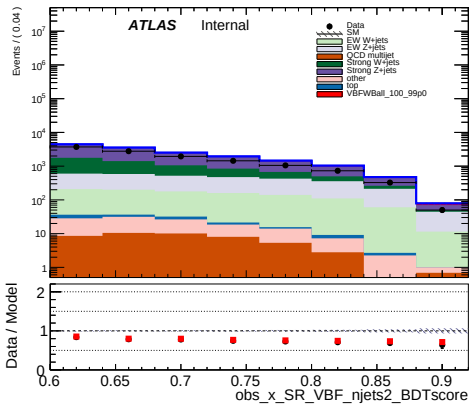

(a) pre-fit SR_VBF_njets2

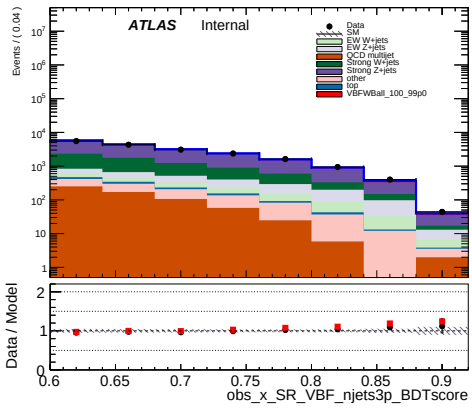

(b) pre-fit SR_VBF_njets3p

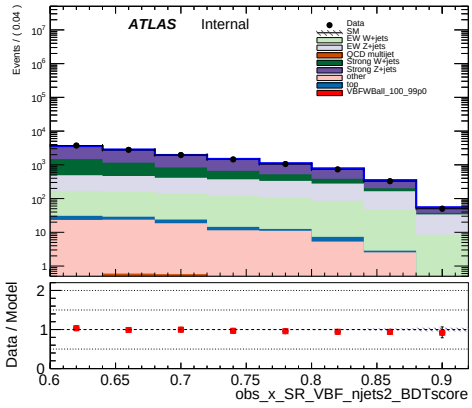

(c) post-fit SR_VBF_njets2

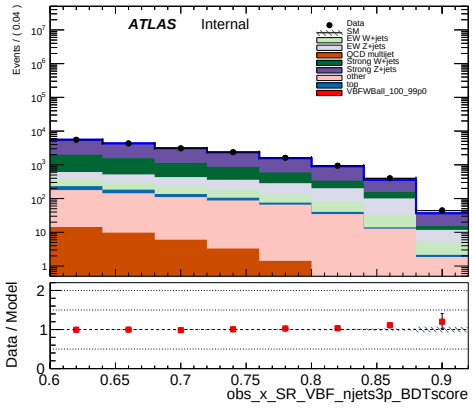

(d) post-fit SR_VBF_njets3p

Figure 9.15: Pre/post-fit distributions in the signal regions for the exclusion fit with a floating signal strength parameter.

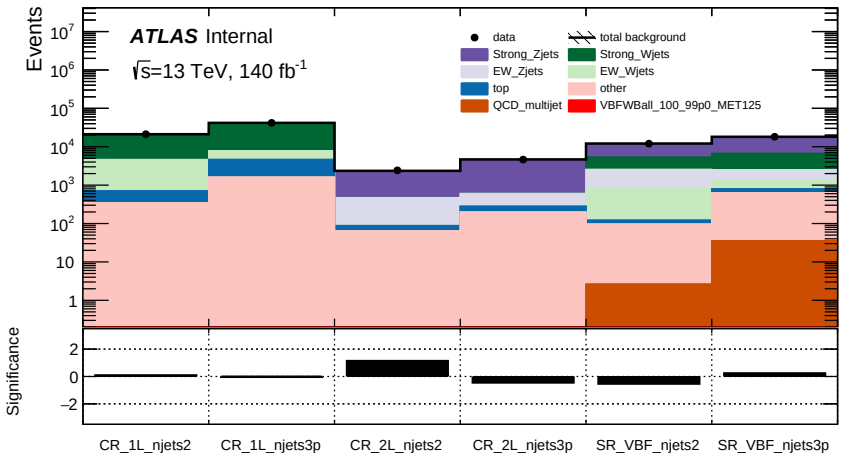

Figure 9.16: Significance plots in the control and signal regions for exclusion fit with floating signal strength.

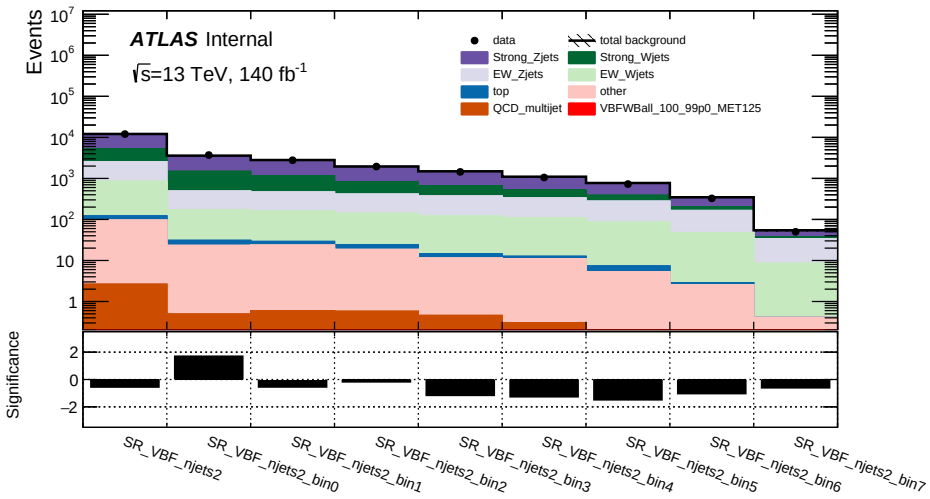

Figure 9.17: Significance plots in SR_VBF_njets2 for exclusion fit with floating signal strength. The first bin shows the region inclusively while the other bins show each of the individual bins for the region.

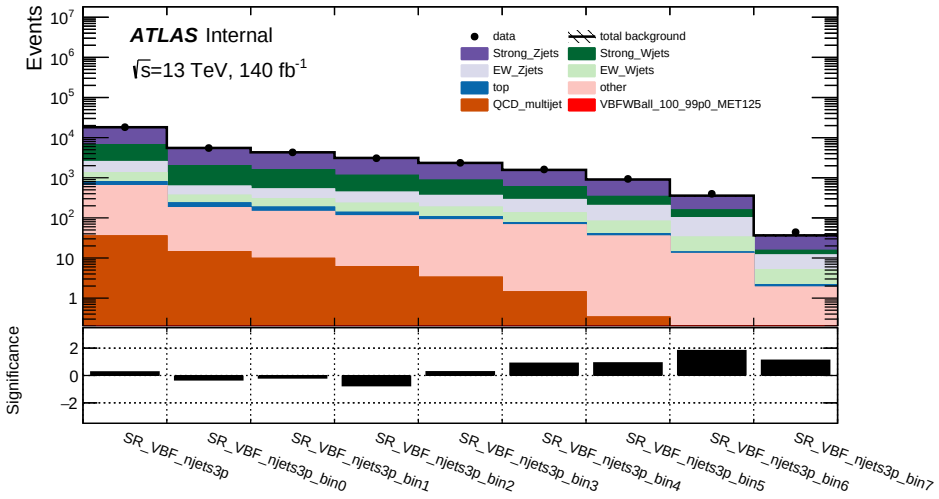

Figure 9.18: Significance plots in SR_VBF_njets3p for exclusion fit with floating signal strength. The first bin shows the region inclusively while the other bins show each of the individual bins for the region.

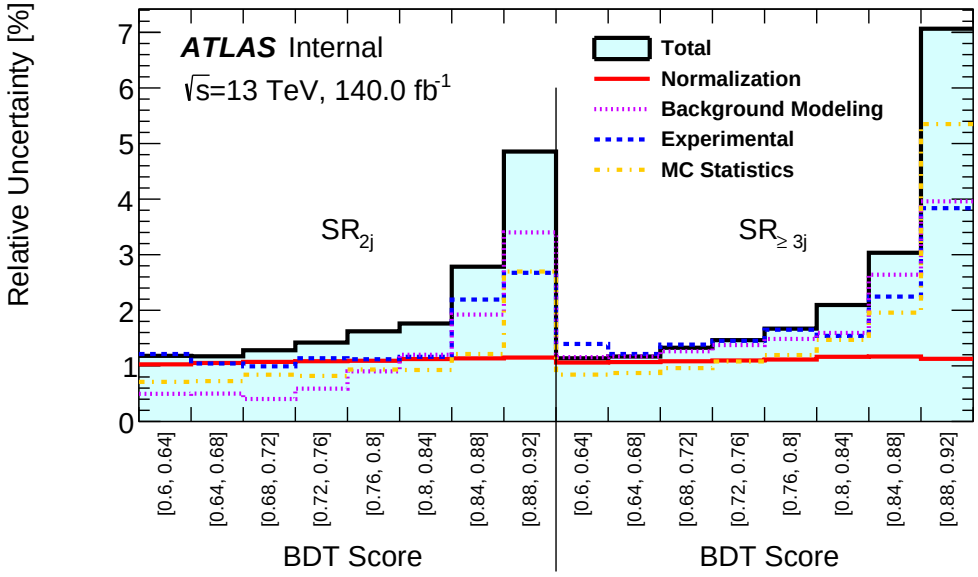

Figure 9.19: Relative size of different sources of uncertainty after a background-only exclusion fit. The Normalization uncertainty arises from the use of CRs to normalize W+jets and Z+jets, while Background Modeling includes the different sources of theoretical modeling uncertainties in the distribution of BDT scores, as well as the uncertainties on the data-driven multijet background estimation. The uncertainties arising from the reconstruction and selection of signal leptons, jets and $E_{\mathrm{T}}^{\mathrm{miss}}$ are included under the Experimental category. The MC Statistics uncertainty originates from the limited size of the MC samples used to model the irreducible background contributions. The individual uncertainties can be correlated and do not necessarily add up in quadrature to the total uncertainty.

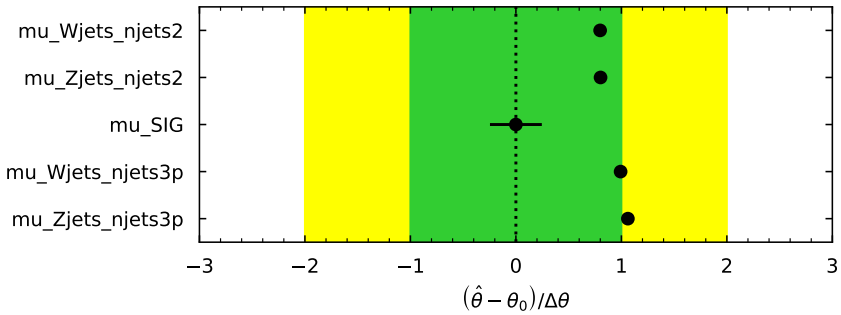

Figure 9.20: Normalization factors after the exclusion fit with a floating signal strength parameter, with the expected value being 1. The fitted values are mu_Wjets_njets2 = 0.7985 ± 0.0072, mu_Zjets_njets2 = 0.8025 ± 0.0119, mu_Wjets_njets3p = 0.9926 ± 0.0120, and mu_Zjets_njets3p = 1.0616 ± 0.0155 .

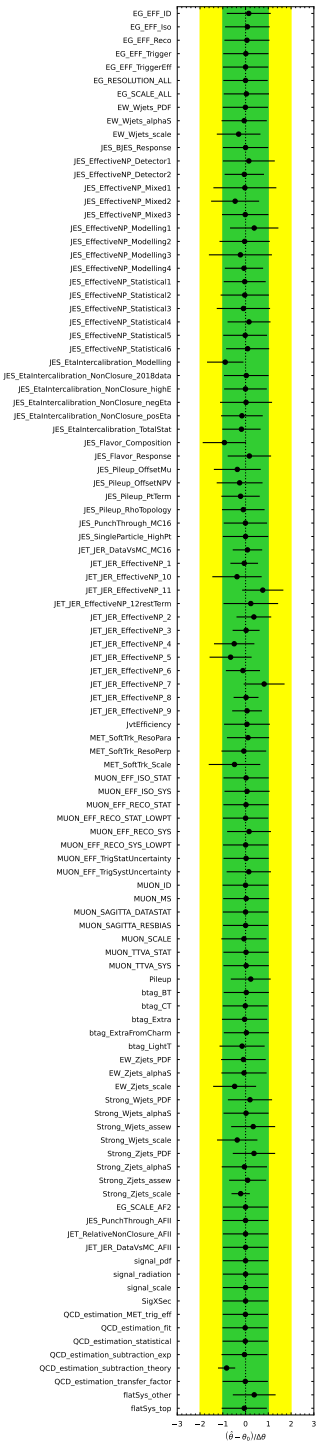

Figure 9.21: Pulls and constraints of fit parameters after the exclusion fit with a floating signal strength parameter, with the nominal value of the nuisance parameters being 0.

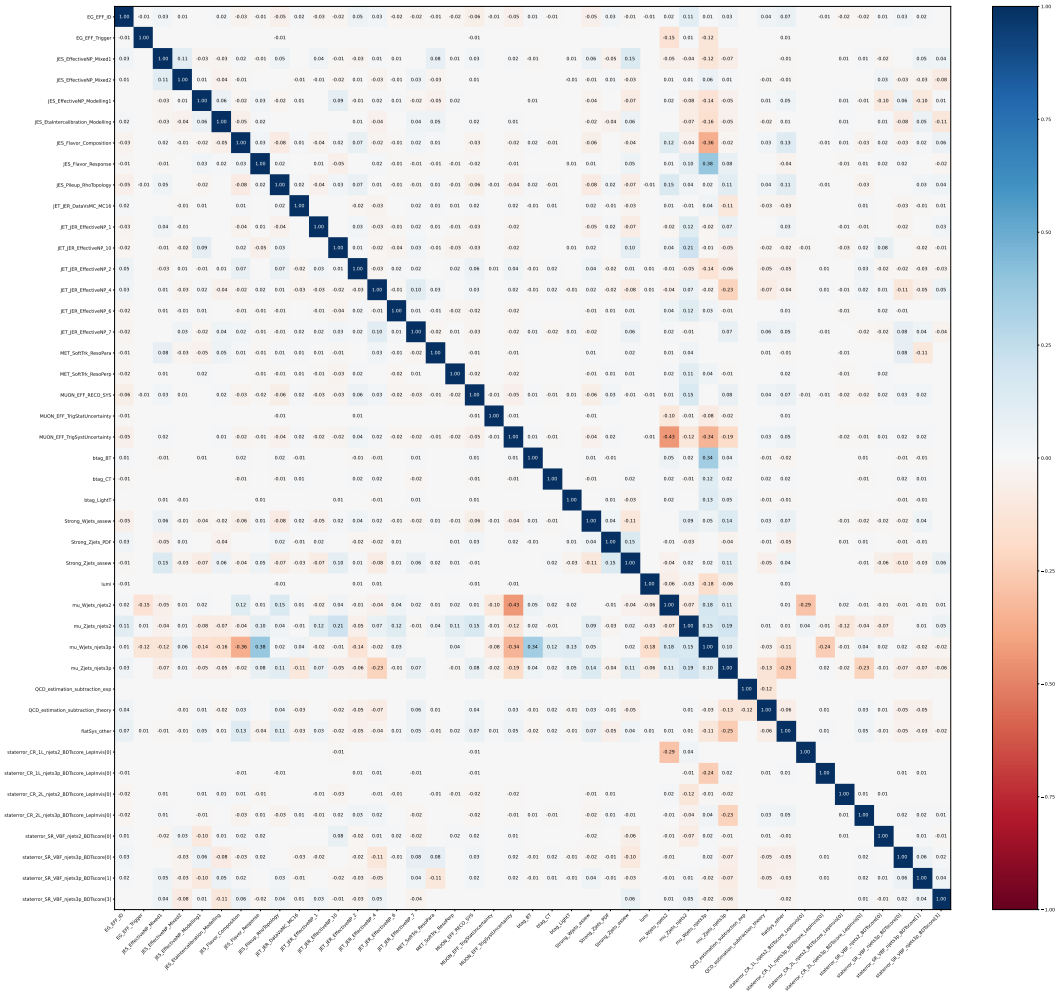

Figure 9.22: Correlation matrix (reduced) after the exclusion fit with a floating signal strength parameter.

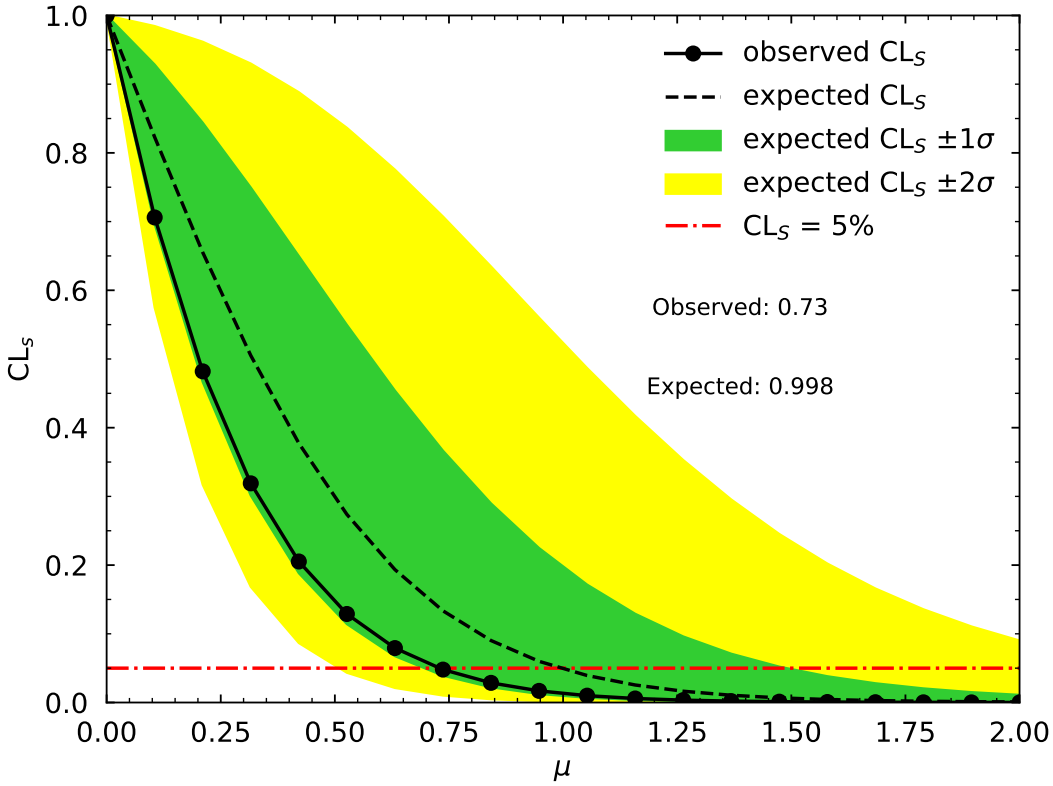

Figure 9.23: Upper limit scan on the signal strength at 95% CL for the $m(\tilde{\chi}_2^0,\tilde{\chi}_1^{\pm})$ = 100 GeV with $\Delta m(\tilde{\chi}_2^0,\tilde{\chi}_1^0)$ = 1 GeV signal point using the exclusion fit with a floating signal strength parameter.

As no significant excesses had been observed in the discovery regions, model-dependent limits are derived based on the exclusion fit configuration. The CL_s values are computed by running the exclusion fit for all signal grid points. A contour corresponding to $CL_s = 0.05$ is generated by interpolating between the results for each grid point. The exclusion as a function of $m(\tilde{\chi}_2^0,\tilde{\chi}_1^\pm)$ and $\Delta m(\tilde{\chi}_2^0,\tilde{\chi}_1^0)$ is shown in Figure 9.24. The observed limit extends up to $m(\tilde{\chi}_2^0,\tilde{\chi}_1^\pm) = 120$ GeV for mass splittings below 1 GeV and surpasses previous limits placed by LEP [1]. The expected limit lies around $m(\tilde{\chi}_2^0,\tilde{\chi}_1^\pm) = 100$ GeV with the difference with respect to the observed limit being largely driven by the mild deficit of events present in the high BDT score portion of SR_VBF_njets2.

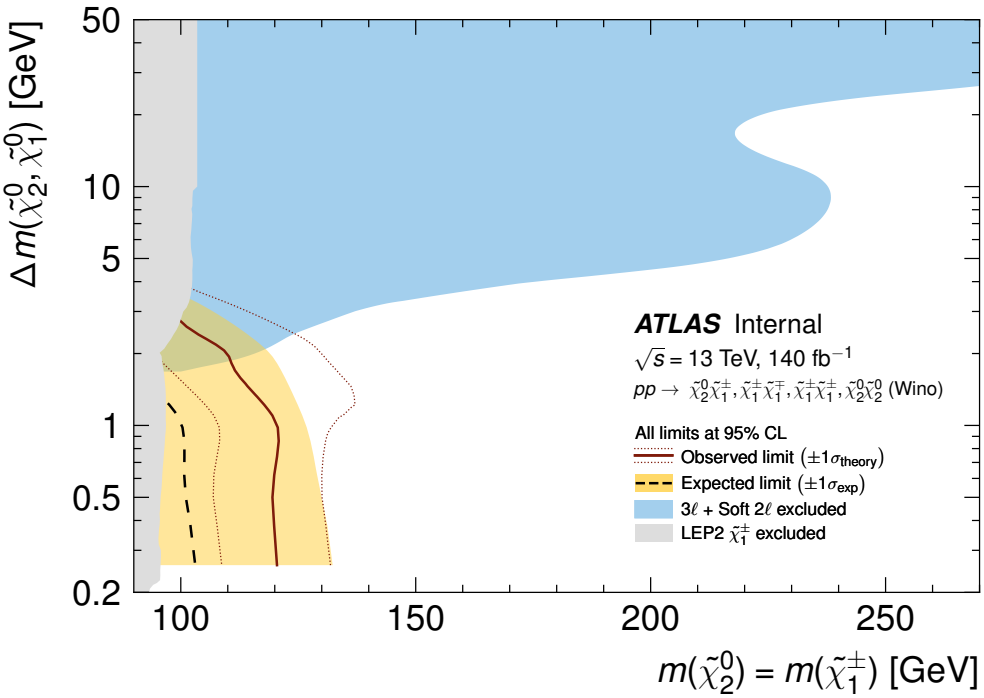

Figure 9.24: Expected (dashed black line) and observed (solid red line) 95% CL exclusion limits on the compressed SUSY simplified model with a bino-like LSP and wino-like NLSPs being considered. These are shown with $\pm 1\sigma_{\text{exp}}$ (yellow band) from experimental systematic and statistical uncertainties, and with $\pm 1\sigma^{\text{SUSY}}_{\text{theory}}$ (red dotted lines) from signal cross-section uncertainties, respectively. The limits set by the ATLAS searches using the soft lepton [30, 33] signature is illustrated by the blue region while the limit imposed by the LEP experiments [1] is shown in gray.

Chapter 10

Conclusion

This dissertation reports the results of a search for the production of electroweakinos with compressed mass spectra using data from $\sqrt{s} = 13$ TeV pp collisions at the LHC corresponding to an integrated luminosity of 140 fb^{-1} recorded by the ATLAS detector. A simplified SUSY model is utilized featuring a pair of mass-degenerate, wino-like $\tilde{\chi}_1^{\pm}$ and $\tilde{\chi}_2^0$ and a bino-like $\tilde{\chi}_1^0$ LSP with $\Delta m(\tilde{\chi}_2^0, \tilde{\chi}_1^0) \lesssim 1$ GeV. The search was optimized to target this SUSY model by selecting events consistent with a VBF topology containing at least two jets with a large separation in pseudorapidity and dijet invariant mass, large missing transverse momentum, and zero leptons. Events are further classified into two categories based on the jet multiplicity with those requiring exactly two or at least three reconstructed jets. The separation between the SUSY signal and Standard Model backgrounds is enhanced by the use of a BDT classifier with a shape fit of the BDT score distribution performed to obtain the final results of the search. The dominant backgrounds from V + jets are modeled based on dedicated control regions while the QCD multijet background has been estimated using a data-driven technique. Both experimental and theoretical sources of uncertainty have been evaluated and taken into account in the statistical model as nuisance parameters. The data are found to be consistent with the SM

predictions across all analysis regions and indicate no evidence for supersymmetry. Exclusion limits are set at 95% CL on the chargino and neutralino masses based on the simplified SUSY model, and model-independent limits are set on the visible cross-section for generic BSM processes in the targeted phase space. A lower limit around 120 GeV is set on m($\tilde{\chi}_2^0$,$\tilde{\chi}_1^{\pm}$) for Δm($\tilde{\chi}_2^0$,$\tilde{\chi}_1^0$) below 1 GeV. This result extends past previous constraints from the LEP experiment. In addition, this result provides unique sensitivity to compressed SUSY scenarios compared to existing searches that relied on soft lepton signatures and required assumptions regarding the branching ratios to leptons of the produced SUSY states.

Nevertheless, the sensitivity reach of this search is relatively limited compared to initial expectations and a large portion of the target parameter space remains unexcluded. The inclusion of more data with the Run 3 dataset would help to extend the limits to some degree but significant improvements to the sensitivity will need to rely on major changes to the analysis strategy. Possible ideas for improvements include using a more sophisticated machine learning setup with multiclass classification that could provide better handles for background rejection, and performing a combined fit that includes additional event topologies besides VBF such as monojet. Despite the lack of evidence for supersymmetry thus far, a large portion of viable parameter space has yet to be explored. In the author's view, both this fact and the compelling theoretical motivations provide sufficient justification for the continued search for supersymmetry.

Appendix

A. List of background MC samples

Table 1.: List of background MC samples. The columns show the dataset identifier, the physics short tag, the cross section times branching ratio and the filter efficiency at generator level of the sample, respectively.

Dataset ID	Process	$\sigma\times$ BR [pb]	$\epsilon_{\text{Gen}}^{\text{Filter}}$
	Strong Z+jets Samples		
700320	Sh_2211_Zee_maxHTpTV2_BFilter	2221.200	0.025
700321	Sh_2211_Zee_maxHTpTV2_CFilterBVeto	2221.200	0.130
700322	Sh_2211_Zee_maxHTpTV2_CVetoBVeto	2221.200	0.846
700323	Sh_2211_Zmumu_maxHTpTV2_BFilter	2221.300	0.024
700324	Sh_2211_Zmumu_maxHTpTV2_CFilterBVeto	2221.300	0.130
700325	Sh_2211_Zmumu_maxHTpTV2_CVetoBVeto	2221.300	0.846
700326	Sh_2211_Ztautau_LL_maxHTpTV2_BFilter	275.330	0.025
700327	Sh_2211_Ztautau_LL_maxHTpTV2_CFilterBVeto	275.330	0.125
700328	Sh_2211_Ztautau_LL_maxHTpTV2_CVetoBVeto	275.330	0.850
700329	Sh_2211_Ztautau_LH_maxHTpTV2_BFilter	1013.200	0.024
700330	Sh_2211_Ztautau_LH_maxHTpTV2_CFilterBVeto	1013.200	0.125
700331	Sh_2211_Ztautau_LH_maxHTpTV2_CVetoBVeto	1013.200	0.850
700332	Sh_2211_Ztautau_HH_maxHTpTV2_BFilter	932.530	0.025
700333	Sh_2211_Ztautau_HH_maxHTpTV2_CFilterBVeto	932.530	0.125
700334	Sh_2211_Ztautau_HH_maxHTpTV2_CVetoBVeto	932.530	0.850
700335	Sh_2211_Znunu_pTV2_BFilter	447.130	0.084
700336	Sh_2211_Znunu_pTV2_CFilterBVeto	447.130	0.202
700337	Sh_2211_Znunu_pTV2_CVetoBVeto	447.130	0.713
	Electroweak Z+jets Samples		
700358	Sh_2211_Zee2jets_Min_N_TChannel	0.779	1.000
700359	Sh_2211_Zmm2jets_Min_N_TChannel	0.779	1.000
700360	Sh_2211_Ztt2jets_Min_N_TChannel	0.779	1.000
700361	Sh_2211_Znunu2jets_Min_N_TChannel	3.657	1.000
	Strong W+jets Samples		
700338	Sh_2211_Wenu_maxHTpTV2_BFilter	21742.000	0.009
700339	Sh_2211_Wenu_maxHTpTV2_CFilterBVeto	21742.000	0.149
700340	Sh_2211_Wenu_maxHTpTV2_CVetoBVeto	21742.000	0.844
700341	Sh_2211_Wmunu_maxHTpTV2_BFilter	21806.000	0.010

700342	Sh_2211_Wmunu_maxHTpTV2_CFilterBVeto	21806.000	0.146
700343	Sh_2211_Wmunu_maxHTpTV2_CVetoBVeto	21806.000	0.844
700344	Sh_2211_Wtaunu_L_maxHTpTV2_BFilter	7680.000	0.009
700345	Sh_2211_Wtaunu_L_maxHTpTV2_CFilterBVeto	7680.000	0.146
700346	Sh_2211_Wtaunu_L_maxHTpTV2_CVetoBVeto	7680.000	0.847
700347	Sh_2211_Wtaunu_H_maxHTpTV2_BFilter	14126.000	0.009
700348	Sh_2211_Wtaunu_H_maxHTpTV2_CFilterBVeto	14126.000	0.143
700349	Sh_2211_Wtaunu_H_maxHTpTV2_CVetoBVeto	14126.000	0.847
	Electroweak W+jets Samples		
700362	Sh_2211_Wenu2jets_Min_N_TChannel	8.502	1.000
700363	Sh_2211_Wmunu2jets_Min_N_TChannel	8.503	1.000
700364	Sh_2211_Wtaunu2jets_Min_N_TChannel	8.501	1.000
	Diboson Samples		
363355	Sherpa_221_NNPDF30NNLO_ZqqZvv	15.561	0.280
363356	Sherpa_221_NNPDF30NNLO_ZqqZll	15.564	0.141
363357	Sherpa_221_NNPDF30NNLO_WqqZvv	6.798	1.000
363358	Sherpa_221_NNPDF30NNLO_WqqZll	3.433	1.000
363359	Sherpa_221_NNPDF30NNLO_WpqqWmlv	24.708	1.000
363360	Sherpa_221_NNPDF30NNLO_WplvWmqq	24.724	1.000
363489	Sherpa_221_NNPDF30NNLO_WlvZqq	11.420	1.000
363494	Sherpa_221_NNPDF30NNLO_vvvv	0.603	1.000
364250	Sherpa_222_NNPDF30NNLO_llll	1.252	1.000
364253	Sherpa_222_NNPDF30NNLO_lllv	4.573	1.000
364254	Sherpa_222_NNPDF30NNLO_llvv	12.500	1.000
364255	Sherpa_222_NNPDF30NNLO_lvvv	3.234	1.000
	Electroweak Diboson Samples		
700587	Sh_2212_lllljj	0.012	1.000
700588	Sh_2212_lllvjj	0.048	1.000
700589	Sh_2212_llvvjj_os	0.193	1.000
700590	Sh_2212_llvvjj_ss	0.046	1.000
700591	Sh_2212_lllljj_Int	0.002	1.000
700592	Sh_2212_lllvjj_Int	0.008	1.000
700593	Sh_2212_llvvjj_os_Int	0.006	1.000
700594	Sh_2212_llvvjj_ss_Int	0.003	1.000
	Top Samples		
410470	PhPy8EG_A14_ttbar_hdamp258p75_nonallhad	729.770	0.544

410471	PhPy8EG_A14_ttbar_hdamp258p75_allhad	729.770	0.456
410644	PowhegPythia8EvtGen_A14_singletop_schan_lept_top	2.027	1.000
410645	PowhegPythia8EvtGen_A14_singletop_schan_lept_antitop	1.267	1.000
410646	PowhegPythia8EvtGen_A14_Wt_DR_inclusive_top	37.935	1.000
410647	PowhegPythia8EvtGen_A14_Wt_DR_inclusive_antitop	37.905	1.000
410658	PhPy8EG_A14_tchan_BW50_lept_top	36.996	1.000
410659	PhPy8EG_A14_tchan_BW50_lept_antitop	22.173	1.000
	Triboson Samples		
364242	Sherpa_222_NNPDF30NNLO_WWW_3l3v_EW6	0.007	1.000
364243	Sherpa_222_NNPDF30NNLO_WWZ_4l2v_EW6	0.002	1.000
364244	Sherpa_222_NNPDF30NNLO_WWZ_2l4v_EW6	0.004	1.000
364245	Sherpa_222_NNPDF30NNLO_WZZ_5l1v_EW6	0.000	1.000
364246	Sherpa_222_NNPDF30NNLO_WZZ_3l3v_EW6	0.002	0.446
364247	Sherpa_222_NNPDF30NNLO_ZZZ_6l0v_EW6	0.000	1.000
364248	Sherpa_222_NNPDF30NNLO_ZZZ_4l2v_EW6	0.000	0.224
364249	Sherpa_222_NNPDF30NNLO_ZZZ_2l4v_EW6	0.000	0.445
	Multijet Samples		
364700	Pythia8EvtGen_A14NNPDF23LO_jetjet_JZ0WithSW	78420000000.000	0.976
364702	Pythia8EvtGen_A14NNPDF23LO_jetjet_JZ2WithSW	2432800000.000	0.010
364703	Pythia8EvtGen_A14NNPDF23LO_jetjet_JZ3WithSW	26452000.000	0.012
364704	Pythia8EvtGen_A14NNPDF23LO_jetjet_JZ4WithSW	254610.000	0.013
364705	Pythia8EvtGen_A14NNPDF23LO_jetjet_JZ5WithSW	4553.500	0.015
364706	Pythia8EvtGen_A14NNPDF23LO_jetjet_JZ6WithSW	257.560	0.009
364707	Pythia8EvtGen_A14NNPDF23LO_jetjet_JZ7WithSW	16.214	0.011
364708	Pythia8EvtGen_A14NNPDF23LO_jetjet_JZ8WithSW	0.625	0.010
364709	Pythia8EvtGen_A14NNPDF23LO_jetjet_JZ9WithSW	0.020	0.012
364710	Pythia8EvtGen_A14NNPDF23LO_jetjet_JZ10WithSW	0.001	0.006
364711	Pythia8EvtGen_A14NNPDF23LO_jetjet_JZ11WithSW	0.000	0.003
364712	Pythia8EvtGen_A14NNPDF23LO_jetjet_JZ12WithSW	0.000	0.000
800036	Py8EG_A14N23LO_jetjet_JZ1WwithSW	78050000000.000	0.001

B. Exclusion Fit with Signal Regions using a fixed signal strength

B.1. Signal strength fixed to 0

Tables 2, 3, and 4 show the yields in each region before and after running the exclusion fit with the signal strength fixed to zero. Figures 4, 5, and 6 show respectively the fitted normalization factors, pulls and constraints on the fit parameters, and correlation matrix.

channel	CR_1L_njets2	CR_1L_njets3p	CR_2L_njets2	CR_2L_njets3p	SR_VBF_njets2	SR_VBF_njets3p
Observed events	21216	41814	2426	4633	12032	18214
Fitted bkg events	21200.87 ± 144.83	41820.26 ± 204.17	2358.27 ± 35.12	4672.70 ± 61.17	12112.86 ± 100.26	18168.91 ± 139.50
Fitted Strong_Zjets events	367.12 ± 6.95	859.10 ± 20.35	1884.74 ± 29.27	4066.44 ± 56.77	6820.08 ± 92.96	11488.66 ± 204.22
Fitted Strong_Wjets events	16198.92 ± 122.25	33149.14 ± 360.42	$0.06^{+0.24}_{-0.06}$	1.04 ± 0.81	2736.89 ± 67.32	4151.87 ± 132.54
Fitted EW_Zjets events	55.16 ± 1.14	57.77 ± 1.57	385.07 ± 5.80	324.97 ± 4.62	1709.03 ± 27.69	1205.60 ± 21.22
Fitted EW_Wjets events	3876.47 ± 29.30	3103.03 ± 33.79	0.00 ± 0.00	0.00 ± 0.00	725.47 ± 14.22	530.41 ± 12.47
Fitted top events	354.02 ± 31.66	3035.84 ± 238.83	23.50 ± 2.61	81.67 ± 7.21	25.02 ± 8.04	155.83 ± 48.74
Fitted other events	349.18 ± 12.40	1615.38 ± 113.43	64.89 ± 2.86	198.59 ± 16.10	93.74 ± 24.84	601.27 ± 167.27
Fitted QCD_multijet events	0.00 ± 0.00	0.00 ± 0.00	0.00 ± 0.00	0.00 ± 0.00	$2.62^{+8.32}_{-2.62}$	$35.28^{+111.85}_{-35.28}$
Fitted VBFWBall_100_99p0_MET125 events	0.00 ± 0.00	0.00 ± 0.00	0.00 ± 0.00	0.00 ± 0.00	0.00 ± 0.00	0.00 ± 0.00
MC exp. SM events	26323.68 ± 135.25	42277.25 ± 428.98	2908.96 ± 17.26	4442.56 ± 37.27	15430.38 ± 243.24	18622.08 ± 764.33
MC exp. Strong_Zjets events	456.37 ± 9.00	806.52 ± 15.40	2345.86 ± 14.76	3833.35 ± 25.98	8446.46 ± 119.18	10684.88 ± 213.32
MC exp. Strong_Wjets events	20271.23 ± 98.66	33375.26 ± 163.30	$0.34^{+0.42}_{-0.34}$	0.64 ± 0.63	3345.34 ± 108.09	4319.03 ± 160.20
MC exp. EW_Zjets events	68.10 ± 1.04	54.05 ± 1.33	479.70 ± 2.67	306.49 ± 2.18	2152.12 ± 30.75	1139.69 ± 16.53
MC exp. EW_Wjets events	4851.25 ± 22.48	3124.29 ± 14.61	0.00 ± 0.00	0.00 ± 0.00	915.26 ± 19.98	532.07 ± 12.52
MC exp. top events	323.86 ± 31.69	3188.91 ± 261.51	20.36 ± 1.86	85.39 ± 8.36	25.28 ± 8.16	164.26 ± 51.76
MC exp. other events	352.70 ± 13.13	1727.76 ± 135.41	62.70 ± 3.09	216.68 ± 19.22	83.32 ± 25.85	575.33 ± 176.18
MC exp. QCD_multijet events	0.00 ± 0.00	0.00 ± 0.00	0.00 ± 0.00	0.00 ± 0.00	$46.11^{+48.42}_{-46.11}$	$620.49^{+651.59}_{-620.49}$
MC exp. VBFWBall_100_99p0_MET125 events	0.18 ± 0.05	0.45 ± 0.11	0.00 ± 0.00	0.00 ± 0.00	416.47 ± 115.81	586.33 ± 185.53

Table 2.: Yields table for exclusion fit with the signal strength fixed to 0.

channel	SR_VBF_njets2_bin0	SR_VBF_njets2_bin1	SR_VBF_njets2_bin2	SR_VBF_njets2_bin3
Observed events	3712	2774	1946	1441
Fitted bkg events	3588.8 ± 41.3	2805.9 ± 32.0	1953.0 ± 24.1	1490.4 ± 20.3
Fitted Strong_Zjets events	2103.6 ± 33.6	1647.9 ± 27.5	1117.4 ± 22.1	826.2 ± 15.4
Fitted Strong_Wjets events	993.2 ± 29.5	691.4 ± 23.1	422.0 ± 18.0	292.1 ± 11.0
Fitted EW_Zjets events	322.2 ± 8.1	306.6 ± 5.9	272.7 ± 5.4	249.0 ± 5.1
Fitted EW_Wjets events	139.0 ± 3.4	131.0 ± 2.8	117.0 ± 2.8	108.6 ± 2.8
Fitted top events	7.5 ± 2.5	5.3 ± 1.7	5.3 ± 1.8	3.0 ± 1.0
Fitted other events	22.8 ± 6.6	23.1 ± 6.5	18.0 ± 4.9	11.0 ± 3.0
Fitted QCD_multijet events	$0.5^{+1.6}_{-0.5}$	$0.6^{+1.9}_{-0.6}$	$0.6^{+1.8}_{-0.6}$	$0.5^{+1.4}_{-0.5}$
Fitted VBFWBall_100_99p0_MET125 events	0.0 ± 0.0	0.0 ± 0.0	0.0 ± 0.0	0.0 ± 0.0
MC exp. SM events	4426.30 ± 81.96	3536.14 ± 61.84	2501.10 ± 44.73	1935.61 ± 40.50
MC exp. Strong_Zjets events	2576.06 ± 46.47	2056.08 ± 36.60	1379.51 ± 25.02	1028.71 ± 21.71
MC exp. Strong_Wjets events	1168.42 ± 44.70	826.01 ± 34.17	538.24 ± 23.20	371.87 ± 17.18
MC exp. EW_Zjets events	392.07 ± 10.25	384.55 ± 6.21	342.08 ± 6.43	313.68 ± 5.65
MC exp. EW_Wjets events	172.38 ± 4.55	164.10 ± 3.85	146.28 ± 3.80	138.47 ± 4.12
MC exp. top events	7.95 ± 2.59	5.07 ± 1.69	5.63 ± 1.94	2.80 ± 0.94
MC exp. other events	19.83 ± 6.54	20.99 ± 6.74	16.27 ± 5.18	10.51 ± 3.29
MC exp. QCD_multijet events	$8.58^{+9.01}_{-8.58}$	$10.51^{+11.04}_{-10.51}$	$10.11^{+10.62}_{-10.11}$	$8.04^{+8.44}_{-8.04}$
MC exp. VBFWBall_100_99p0_MET125 events	81.01 ± 23.13	68.83 ± 19.47	62.97 ± 17.19	61.52 ± 17.65

channel	SR_VBF_njets2_bin4	SR_VBF_njets2_bin5	SR_VBF_njets2_bin6	SR_VBF_njets2_bin7
Observed events	1054	729	326	50
Fitted bkg events	1100.1 ± 17.0	773.6 ± 12.6	346.7 ± 9.2	54.4 ± 2.5
Fitted Strong_Zjets events	576.0 ± 12.1	387.2 ± 9.9	145.1 ± 6.2	16.8 ± 1.1
Fitted Strong_Wjets events	189.8 ± 10.2	108.0 ± 6.7	36.6 ± 3.4	3.7 ± 0.7
Fitted EW_Zjets events	223.6 ± 5.5	192.4 ± 5.8	117.2 ± 5.0	25.4 ± 1.9
Fitted EW_Wjets events	98.1 ± 2.9	78.7 ± 2.9	44.9 ± 2.2	8.1 ± 0.6
Fitted top events	1.5 ± 0.5	2.0 ± 0.7	0.3 ± 0.2	0.0 ± 0.0
Fitted other events	10.8 ± 3.0	5.2 ± 1.4	2.5 ± 0.7	0.4 ± 0.1
Fitted QCD_multijet events	$0.3^{+1.0}_{-0.3}$	$0.2^{+0.5}_{-0.2}$	$0.0^{+0.0}_{-0.0}$	$0.0^{+0.1}_{-0.0}$
Fitted VBFWBall_100_99p0_MET125 events	0.0 ± 0.0	0.0 ± 0.0	0.0 ± 0.0	0.0 ± 0.0
MC exp. SM events	1448.79 ± 33.24	1029.67 ± 28.91	474.33 ± 19.25	78.44 ± 5.24
MC exp. Strong_Zjets events	721.47 ± 17.95	481.44 ± 16.07	182.47 ± 10.40	20.73 ± 1.85
MC exp. Strong_Wjets events	246.80 ± 15.57	140.58 ± 10.03	48.60 ± 4.35	4.83 ± 0.92
MC exp. EW_Zjets events	286.52 ± 7.57	247.42 ± 8.18	152.75 ± 6.96	33.04 ± 2.80
MC exp. EW_Wjets events	124.62 ± 3.91	101.24 ± 3.84	57.69 ± 3.18	10.47 ± 0.81
MC exp. top events	1.51 ± 0.53	1.89 ± 0.68	0.43 ± 0.23	0.00 ± 0.00
MC exp. other events	8.73 ± 2.80	4.45 ± 1.42	2.22 ± 0.71	0.32 ± 0.10
MC exp. QCD_multijet events	$5.34^{+5.61}_{-5.34}$	$2.80^{+2.94}_{-2.80}$	$0.04^{+0.04}_{-0.04}$	$0.69^{+0.72}_{-0.69}$
MC exp. VBFWBall_100_99p0_MET125 events	53.80 ± 14.62	49.85 ± 14.13	30.12 ± 8.70	8.37 ± 2.55

Table 3.: Yields per bin in SR_VBF_njets2 for exclusion fit with the signal strength fixed to 0.

channel	SR_VBF_njets3p_bin0	SR_VBF_njets3p_bin1	SR_VBF_njets3p_bin2	SR_VBF_njets3p_bin3
Observed events	5504	4295	3068	2358
Fitted bkg events	5531.4 ± 62.8	4306.6 ± 50.8	3117.5 ± 42.2	2344.1 ± 33.7
Fitted Strong_Zjets events	3533.2 ± 77.9	2737.1 ± 55.8	1976.4 ± 41.5	1480.7 ± 32.9
Fitted Strong_Wjets events	1385.5 ± 57.1	1048.8 ± 38.7	708.0 ± 28.6	502.9 ± 20.7
Fitted EW_Zjets events	249.2 ± 5.1	225.5 ± 4.5	203.9 ± 4.9	177.3 ± 4.0
Fitted EW_Wjets events	129.4 ± 5.1	111.4 ± 4.1	92.6 ± 2.8	77.4 ± 2.2
Fitted top events	55.5 ± 17.3	40.2 ± 12.9	25.9 ± 8.2	17.9 ± 5.7
Fitted other events	164.3 ± 46.1	133.8 ± 37.1	104.7 ± 29.3	84.7 ± 23.8
Fitted QCD_multijet events	$14.3^{+45.4}_{-14.3}$	$9.7^{+30.9}_{-9.7}$	$6.0^{+19.1}_{-6.0}$	$3.3^{+10.5}_{-3.3}$
Fitted VBFWBall_100_99p0_MET125 events	0.0 ± 0.0	0.0 ± 0.0	0.0 ± 0.0	0.0 ± 0.0
MC exp. SM events	5775.31 ± 292.56	4405.00 ± 207.41	3182.04 ± 139.93	2378.09 ± 93.09
MC exp. Strong_Zjets events	3307.34 ± 71.08	2527.74 ± 57.93	1847.03 ± 48.52	1388.75 ± 43.20
MC exp. Strong_Wjets events	1505.87 ± 65.40	1102.34 ± 46.16	718.50 ± 34.45	499.68 ± 25.39
MC exp. EW_Zjets events	236.96 ± 4.00	213.52 ± 3.85	192.06 ± 3.93	168.10 ± 3.41
MC exp. EW_Wjets events	128.41 ± 5.39	108.20 ± 3.93	93.76 ± 2.83	77.86 ± 2.33
MC exp. top events	57.12 ± 17.99	43.92 ± 14.11	26.32 ± 8.41	19.62 ± 6.24
MC exp. other events	164.59 ± 50.77	129.08 ± 39.50	100.90 ± 30.92	78.37 ± 24.17
MC exp. QCD_multijet events	$252.10^{+264.74}_{-252.10}$	$171.37^{+179.96}_{-171.37}$	$106.47^{+111.81}_{-106.47}$	$57.87^{+60.77}_{-57.87}$
MC exp. VBFWBall_100_99p0_MET125 events	122.92 ± 39.04	108.84 ± 34.73	97.01 ± 31.72	87.85 ± 28.34

channel	SR_VBF_njets3p_bin4	SR_VBF_njets3p_bin5	SR_VBF_njets3p_bin6	SR_VBF_njets3p_bin7
channel	SR_VBF_njets3p_bin4	SR_VBF_njets3p_bin5	SR_VBF_njets3p_bin6	SR_VBF_njets3p_bin7
Observed events	1611	936	398	44
Fitted bkg events	1570.0 ± 25.2	904.4 ± 18.1	358.2 ± 10.4	36.6 ± 2.6
Fitted Strong_Zjets events	973.9 ± 24.0	564.0 ± 18.1	202.1 ± 9.7	21.3 ± 2.1
Fitted Strong_Wjets events	310.3 ± 16.6	137.6 ± 8.1	55.1 ± 4.9	3.6 ± 0.7
Fitted EW_Zjets events	153.9 ± 4.3	121.0 ± 3.7	68.2 ± 2.8	6.7 ± 0.8
Fitted EW_Wjets events	56.3 ± 1.9	41.6 ± 1.8	18.8 ± 0.9	2.9 ± 0.4
Fitted top events	9.5 ± 3.1	5.5 ± 1.8	1.1 ± 0.4	0.3 ± 0.1
Fitted other events	64.8 ± 18.2	34.4 ± 9.6	12.9 ± 3.8	1.7 ± 0.5
Fitted QCD_multijet events	$1.4^{+4.5}_{-1.4}$	$0.3^{+1.1}_{-0.3}$	0.0 ± 0.0	$0.1^{+0.4}_{-0.1}$
Fitted VBFWBall_100_99p0_MET125 events	0.0 ± 0.0	0.0 ± 0.0	0.0 ± 0.0	0.0 ± 0.0
MC exp. SM events	1576.62 ± 60.08	900.78 ± 34.95	364.86 ± 19.91	39.37 ± 4.07
MC exp. Strong_Zjets events	895.76 ± 32.90	514.41 ± 23.35	185.51 ± 13.74	18.33 ± 2.23
MC exp. Strong_Wjets events	305.68 ± 19.54	131.45 ± 10.47	51.48 ± 5.23	4.03 ± 0.60
MC exp. EW_Zjets events	143.37 ± 3.66	114.34 ± 3.62	64.93 ± 2.80	6.42 ± 0.84
MC exp. EW_Wjets events	58.73 ± 2.09	42.82 ± 2.00	19.49 ± 1.09	2.80 ± 0.42
MC exp. top events	9.80 ± 3.21	6.05 ± 1.99	1.15 ± 0.43	0.29 ± 0.09
MC exp. other events	57.66 ± 17.74	31.05 ± 9.56	12.11 ± 3.83	1.57 ± 0.49
MC exp. QCD_multijet events	$24.84^{+26.09}_{-24.84}$	$5.85^{+6.14}_{-5.85}$	0.00 ± 0.00	$1.99^{+2.09}_{-1.99}$
MC exp. VBFWBall_100_99p0_MET125 events	80.78 ± 25.12	54.81 ± 17.44	30.19 ± 9.67	3.94 ± 1.39

Table 4.: Yields per bin in SR_VBF_njets3p for exclusion fit with the signal strength fixed to 0.

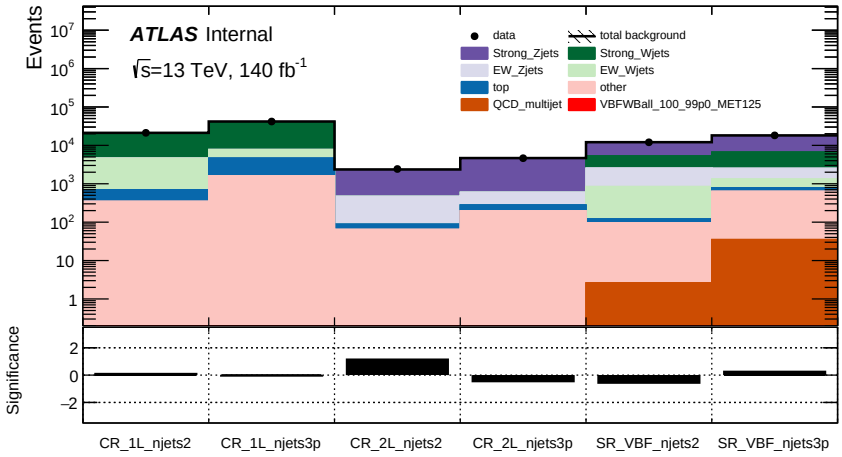

Figure 1: Significance plots in the control and signal regions for exclusion fit with signal strength fixed to 0.

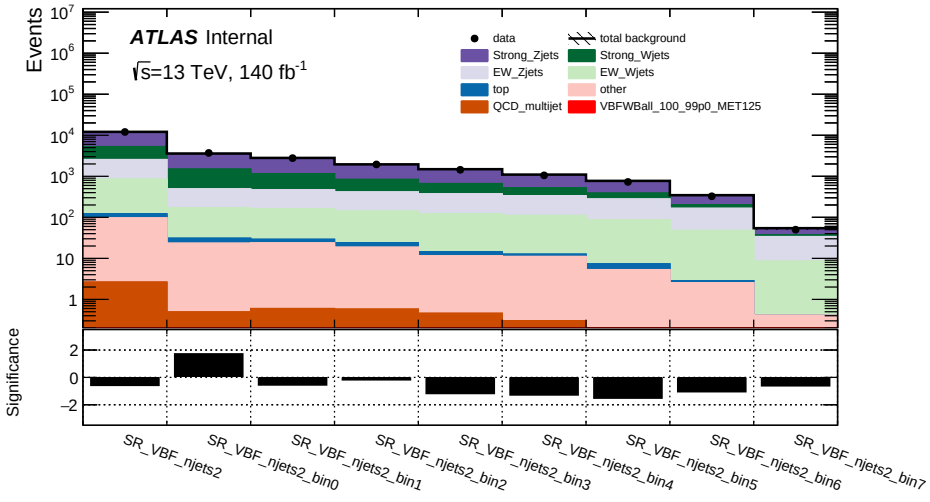

Figure 2: Significance plots in SR_VBF_njets2 for exclusion fit with signal strength fixed to 0.

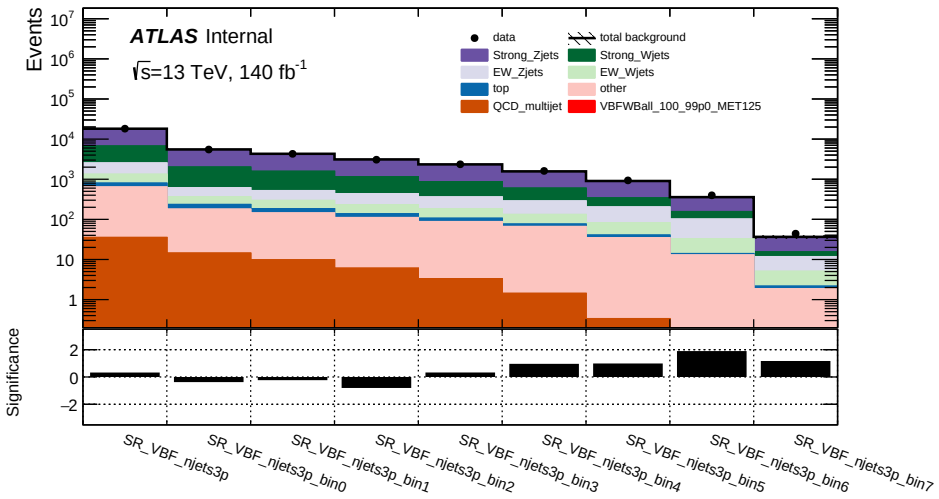

Figure 3: Significance plots in SR_VBF_njets3p for exclusion fit with signal strength fixed to 0.

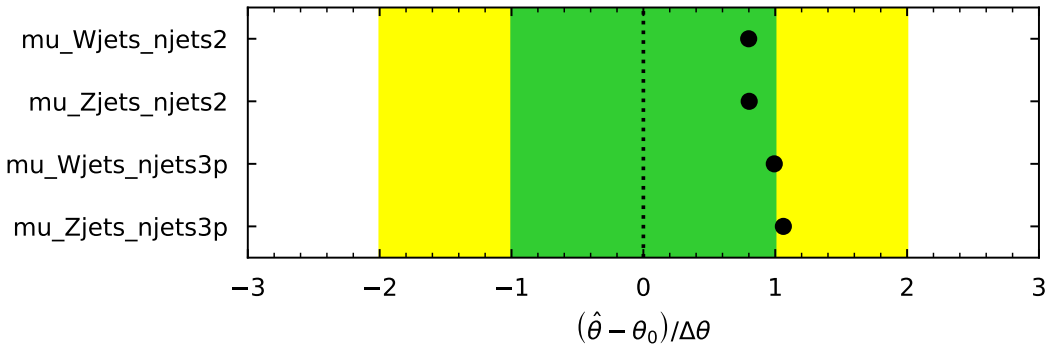

Figure 4: Normalization factors after the exclusion fit with the signal strength fixed to 0. The fitted values are mu_Wjets_njets2 = 0.7985 ± 0.0072, mu_Zjets_njets2 = 0.8025 ± 0.0119, mu_Wjets_njets3p = 0.9926 ± 0.0120, and mu_Zjets_njets3p = 1.0616 ± 0.0155 .

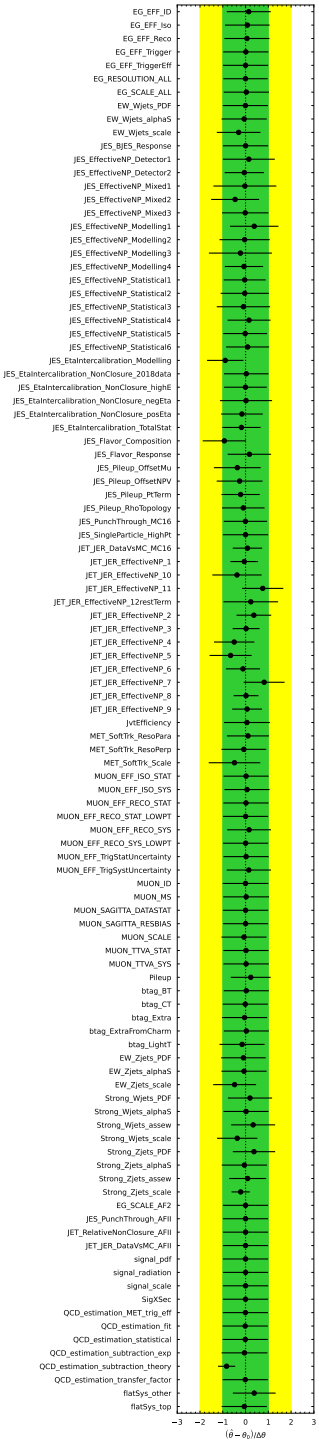

Figure 5: Pulls and constraints of fit parameters after the exclusion fit with the signal strength fixed to 0.

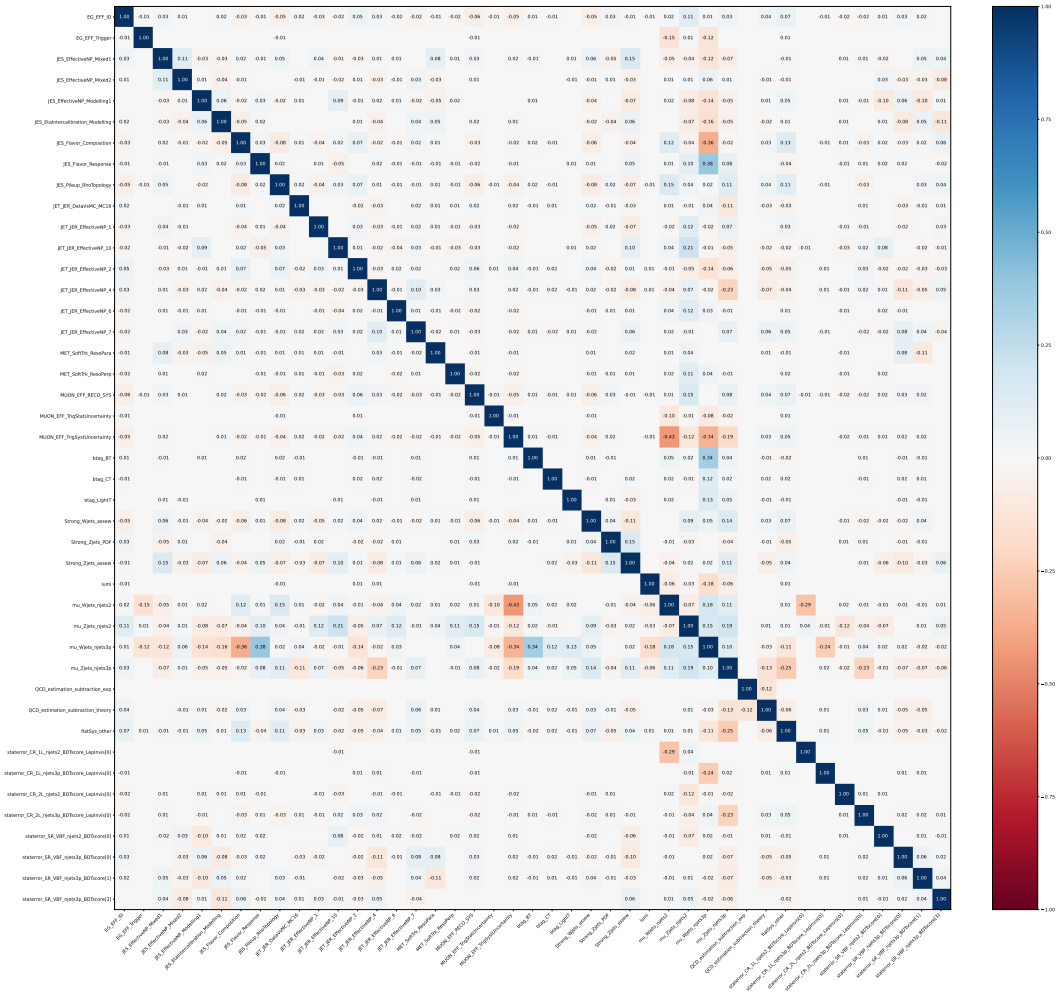

Figure 6: Correlation matrix (reduced) after the exclusion fit with the signal strength fixed to 0.

B.2. Signal strength fixed to 1

Tables 5, 6, and 7 show the yields in each region before and after running the exclusion fit with the signal strength fixed to one. Figures 10, 11, and 12 show respectively the fitted normalization factors, pulls and constraints on the fit parameters, and correlation matrix.

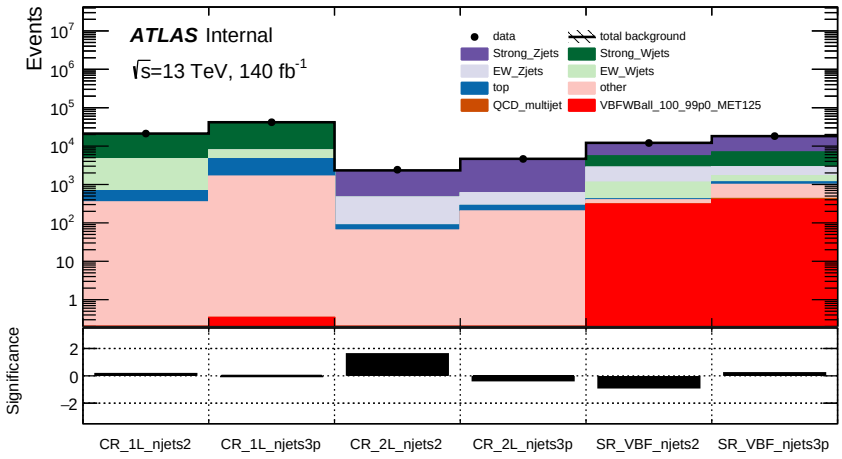

Figure 7: Significance plots in the control and signal regions for exclusion fit with signal strength fixed to 1.

channel	CR_1L_njets2	CR_1L_njets3p	CR_2L_njets2	CR_2L_njets3p	SR_VBF_njets2	SR_VBF_njets3p
Observed events	21216	41814	2426	4633	12032	18214
Fitted bkg events	21190.74 ± 144.78	41817.26 ± 204.28	2331.20 ± 35.38	4661.67 ± 60.76	12156.40 ± 100.72	18178.99 ± 136.86
Fitted Strong_Zjets events	361.12 ± 6.92	854.07 ± 20.36	1863.55 ± 29.44	4053.76 ± 56.79	6672.69 ± 99.34	11247.27 ± 216.48
Fitted Strong_Wjets events	16209.84 ± 122.23	33157.70 ± 360.72	$0.06^{+0.23}_{-0.06}$	1.04 ± 0.88	2673.97 ± 68.39	4065.41 ± 133.17
Fitted EW_Zjets events	54.17 ± 1.14	57.35 ± 1.61	380.74 ± 5.86	324.02 ± 4.63	1676.81 ± 28.65	1192.41 ± 21.18
Fitted EW_Wjets events	3878.87 ± 29.29	3103.67 ± 33.82	0.00 ± 0.00	0.00 ± 0.00	717.29 ± 14.89	525.36 ± 12.57
Fitted top events	340.94 ± 31.23	3017.86 ± 236.40	22.91 ± 2.43	82.29 ± 7.32	23.65 ± 7.71	151.08 ± 47.69
Fitted other events	345.66 ± 12.51	1626.26 ± 115.22	63.95 ± 2.83	200.55 ± 16.41	86.25 ± 23.06	567.61 ± 158.30
Fitted QCD_multijet events	0.00 ± 0.00	0.00 ± 0.00	0.00 ± 0.00	0.00 ± 0.00	$2.42^{+7.68}_{-2.42}$	$32.52^{+103.29}_{-32.52}$
Fitted VBFWBall_100_99p0_MET125 events	0.14 ± 0.04	0.34 ± 0.08	0.00 ± 0.00	0.00 ± 0.00	303.33 ± 75.00	397.33 ± 116.10
MC exp. SM events	26323.68 ± 135.25	42277.25 ± 428.98	2908.96 ± 17.26	4442.56 ± 37.27	15430.38 ± 243.24	18622.08 ± 764.33
MC exp. Strong_Zjets events	456.37 ± 9.00	806.52 ± 15.40	2345.86 ± 14.76	3833.35 ± 25.98	8446.46 ± 119.18	10684.88 ± 213.32
MC exp. Strong_Wjets events	20271.23 ± 98.66	33375.26 ± 163.30	$0.34^{+0.42}_{-0.34}$	0.64 ± 0.63	3345.34 ± 108.09	4319.03 ± 160.20
MC exp. EW_Zjets events	68.10 ± 1.04	54.05 ± 1.33	479.70 ± 2.67	306.49 ± 2.18	2152.12 ± 30.75	1139.69 ± 16.53
MC exp. EW_Wjets events	4851.25 ± 22.48	3124.29 ± 14.61	0.00 ± 0.00	0.00 ± 0.00	915.26 ± 19.98	532.07 ± 12.52
MC exp. top events	323.86 ± 31.69	3188.91 ± 261.51	20.36 ± 1.86	85.39 ± 8.36	25.28 ± 8.16	164.26 ± 51.76
MC exp. other events	352.70 ± 13.13	1727.76 ± 135.41	62.70 ± 3.09	216.68 ± 19.22	83.32 ± 25.85	575.33 ± 176.18
MC exp. QCD_multijet events	0.00 ± 0.00	0.00 ± 0.00	0.00 ± 0.00	0.00 ± 0.00	$46.11^{+48.42}_{-46.11}$	$620.49^{+651.59}_{-620.49}$
MC exp. VBFWBall_100_99p0_MET125 events	0.18 ± 0.05	0.45 ± 0.11	0.00 ± 0.00	0.00 ± 0.00	416.47 ± 115.81	586.33 ± 185.53

Table 5.: Yields table for exclusion fit with the signal strength fixed to 1.

channel	SR_VBF_njets2_bin0	SR_VBF_njets2_bin1	SR_VBF_njets2_bin2	SR_VBF_njets2_bin3
Observed events	3712	2774	1946	1441
Fitted bkg events	3587.9 ± 41.1	2805.8 ± 31.4	1959.9 ± 24.4	1497.7 ± 20.2
Fitted Strong_Zjets events	2071.4 ± 34.5	1615.5 ± 28.5	1098.0 ± 22.6	804.1 ± 15.9
Fitted Strong_Wjets events	972.9 ± 29.4	678.3 ± 23.6	411.2 ± 18.7	284.9 ± 11.0
Fitted EW_Zjets events	318.3 ± 8.1	302.5 ± 5.9	266.8 ± 5.4	244.8 ± 5.1
Fitted EW_Wjets events	137.4 ± 3.5	130.0 ± 2.8	116.2 ± 2.9	107.0 ± 2.8
Fitted top events	7.1 ± 2.4	5.0 ± 1.7	5.1 ± 1.8	2.8 ± 0.9
Fitted other events	20.7 ± 6.0	21.5 ± 6.0	16.6 ± 4.5	10.0 ± 2.8
Fitted QCD_multijet events	$0.5^{+1.4}_{-0.5}$	$0.6^{+1.7}_{-0.6}$	$0.5^{+1.7}_{-0.5}$	$0.4^{+1.3}_{-0.4}$
Fitted VBFWBall_100_99p0_MET125 events	59.6 ± 15.2	52.4 ± 13.0	45.4 ± 11.1	43.8 ± 11.4
MC exp. SM events	4426.30 ± 81.96	3536.14 ± 61.84	2501.10 ± 44.73	1935.61 ± 40.50
MC exp. Strong_Zjets events	2576.06 ± 46.47	2056.08 ± 36.60	1379.51 ± 25.02	1028.71 ± 21.71
MC exp. Strong_Wjets events	1168.42 ± 44.70	826.01 ± 34.17	538.24 ± 23.20	371.87 ± 17.18
MC exp. EW_Zjets events	392.07 ± 10.25	384.55 ± 6.21	342.08 ± 6.43	313.68 ± 5.65
MC exp. EW_Wjets events	172.38 ± 4.55	164.10 ± 3.85	146.28 ± 3.80	138.47 ± 4.12
MC exp. top events	7.95 ± 2.59	5.07 ± 1.69	5.63 ± 1.94	2.80 ± 0.94
MC exp. other events	19.83 ± 6.54	20.99 ± 6.74	16.27 ± 5.18	10.51 ± 3.29
MC exp. QCD_multijet events	$8.58^{+9.01}_{-8.58}$	$10.51^{+11.04}_{-10.51}$	$10.11^{+10.62}_{-10.11}$	$8.04^{+8.44}_{-8.04}$
MC exp. VBFWBall_100_99p0_MET125 events	81.01 ± 23.13	68.83 ± 19.47	62.97 ± 17.19	61.52 ± 17.65

channel	SR_VBF_njets2_bin4	SR_VBF_njets2_bin5	SR_VBF_njets2_bin6	SR_VBF_njets2_bin7
Observed events	1054	729	326	50
Fitted bkg events	1110.8 ± 16.9	785.1 ± 12.7	352.0 ± 9.9	57.2 ± 2.7
Fitted Strong_Zjets events	558.9 ± 12.6	372.6 ± 10.5	136.6 ± 6.5	15.6 ± 1.1
Fitted Strong_Wjets events	184.9 ± 10.1	103.7 ± 6.6	34.7 ± 3.4	3.4 ± 0.6
Fitted EW_Zjets events	218.8 ± 5.5	187.6 ± 5.9	113.7 ± 5.2	24.3 ± 1.9
Fitted EW_Wjets events	97.1 ± 3.0	77.7 ± 2.9	43.9 ± 2.2	8.0 ± 0.6
Fitted top events	1.4 ± 0.5	1.9 ± 0.7	0.3 ± 0.2	0.0 ± 0.0
Fitted other events	10.1 ± 2.8	4.7 ± 1.3	2.3 ± 0.6	0.3 ± 0.1
Fitted QCD_multijet events	$0.3^{+0.9}_{-0.3}$	$0.1^{+0.5}_{-0.1}$	$0.0^{+0.0}_{-0.0}$	$0.0^{+0.1}_{-0.0}$
Fitted VBFWBall_100_99p0_MET125 events	39.5 ± 9.5	36.8 ± 9.2	20.4 ± 5.4	5.5 ± 1.6
MC exp. SM events	1448.79 ± 33.24	1029.67 ± 28.91	474.33 ± 19.25	78.44 ± 5.24
MC exp. Strong_Zjets events	721.47 ± 17.95	481.44 ± 16.07	182.47 ± 10.40	20.73 ± 1.85
MC exp. Strong_Wjets events	246.80 ± 15.57	140.58 ± 10.03	48.60 ± 4.35	4.83 ± 0.92
MC exp. EW_Zjets events	286.52 ± 7.57	247.42 ± 8.18	152.75 ± 6.96	33.04 ± 2.80
MC exp. EW_Wjets events	124.62 ± 3.91	101.24 ± 3.84	57.69 ± 3.18	10.47 ± 0.81
MC exp. top events	1.51 ± 0.53	1.89 ± 0.68	0.43 ± 0.23	0.00 ± 0.00
MC exp. other events	8.73 ± 2.80	4.45 ± 1.42	2.22 ± 0.71	0.32 ± 0.10
MC exp. QCD_multijet events	$5.34^{+5.61}_{-5.34}$	$2.80^{+2.94}_{-2.80}$	$0.04^{+0.04}_{-0.04}$	$0.69^{+0.72}_{-0.69}$
MC exp. VBFWBall_100_99p0_MET125 events	53.80 ± 14.62	49.85 ± 14.13	30.12 ± 8.70	8.37 ± 2.55

Table 6.: Yields per bin in SR_VBF_njets2 for exclusion fit with the signal strength fixed to 1.

channel	SR_VBF_njets3p_bin0	SR_VBF_njets3p_bin1	SR_VBF_njets3p_bin2	SR_VBF_njets3p_bin3
Observed events	5504	4295	3068	2358
Fitted bkg events	5536.7 ± 62.8	4307.4 ± 51.0	3110.3 ± 42.0	2338.6 ± 33.6
Fitted Strong_Zjets events	3485.0 ± 77.7	2689.6 ± 57.4	1933.0 ± 43.7	1440.3 ± 34.9
Fitted Strong_Wjets events	1371.9 ± 56.1	1031.8 ± 38.0	688.0 ± 28.1	488.9 ± 20.8
Fitted EW_Zjets events	247.1 ± 5.2	223.0 ± 4.5	203.0 ± 4.8	175.1 ± 4.1
Fitted EW_Wjets events	127.5 ± 5.1	110.8 ± 4.2	92.0 ± 2.7	77.0 ± 2.2
Fitted top events	54.3 ± 17.1	38.7 ± 12.6	25.3 ± 8.1	17.0 ± 5.5
Fitted other events	155.6 ± 43.7	127.6 ± 35.5	98.4 ± 27.6	79.2 ± 22.3
Fitted QCD_multijet events	$13.2^{+41.9}_{-13.2}$	$9.0^{+28.5}_{-9.0}$	$5.6^{+17.7}_{-5.6}$	$3.0^{+9.7}_{-3.0}$
Fitted VBFWBall_100_99p0_MET125 events	82.0 ± 24.6	76.8 ± 22.5	65.1 ± 19.8	58.0 ± 17.6
MC exp. SM events	5775.31 ± 292.56	4405.00 ± 207.41	3182.04 ± 139.93	2378.09 ± 93.09
MC exp. Strong_Zjets events	3307.34 ± 71.08	2527.74 ± 57.93	1847.03 ± 48.52	1388.75 ± 43.20
MC exp. Strong_Wjets events	1505.87 ± 65.40	1102.34 ± 46.16	718.50 ± 34.45	499.68 ± 25.39
MC exp. EW_Zjets events	236.96 ± 4.00	213.52 ± 3.85	192.06 ± 3.93	168.10 ± 3.41
MC exp. EW_Wjets events	128.41 ± 5.39	108.20 ± 3.93	93.76 ± 2.83	77.86 ± 2.33
MC exp. top events	57.12 ± 17.99	43.92 ± 14.11	26.32 ± 8.41	19.62 ± 6.24
MC exp. other events	164.59 ± 50.77	129.08 ± 39.50	100.90 ± 30.92	78.37 ± 24.17
MC exp. QCD_multijet events	$252.10^{+264.74}_{-252.10}$	$171.37^{+179.96}_{-171.37}$	$106.47^{+111.81}_{-106.47}$	$57.87^{+60.77}_{-57.87}$
MC exp. VBFWBall_100_99p0_MET125 events	122.92 ± 39.04	108.84 ± 34.73	97.01 ± 31.72	87.85 ± 28.34

channel	SR_VBF_njets3p_bin4	SR_VBF_njets3p_bin5	SR_VBF_njets3p_bin6	SR_VBF_njets3p_bin7
Observed events	1611	936	398	44
Fitted bkg events	1573.7 ± 24.8	913.3 ± 18.5	361.4 ± 10.4	37.6 ± 2.7
Fitted Strong_Zjets events	941.9 ± 25.0	546.6 ± 18.7	190.8 ± 10.0	20.1 ± 2.1
Fitted Strong_Wjets events	298.0 ± 16.7	131.4 ± 8.0	52.0 ± 4.9	3.4 ± 0.7
Fitted EW_Zjets events	152.3 ± 4.3	118.7 ± 3.7	66.9 ± 2.8	6.4 ± 0.7
Fitted EW_Wjets events	55.6 ± 1.9	40.9 ± 1.7	18.5 ± 0.9	2.9 ± 0.4
Fitted top events	9.2 ± 3.0	5.2 ± 1.7	1.1 ± 0.4	0.3 ± 0.1
Fitted other events	60.8 ± 17.1	32.4 ± 9.1	11.9 ± 3.5	1.6 ± 0.5
Fitted QCD_multijet events	$1.3^{+4.2}_{-1.3}$	$0.3^{+1.0}_{-0.3}$	0.0 ± 0.0	$0.1^{+0.3}_{-0.1}$
Fitted VBFWBall_100_99p0_MET125 events	54.6 ± 15.7	37.8 ± 11.1	20.3 ± 6.0	2.7 ± 0.9
MC exp. SM events	1576.62 ± 60.08	900.78 ± 34.95	364.86 ± 19.91	39.37 ± 4.07
MC exp. Strong_Zjets events	895.76 ± 32.90	514.41 ± 23.35	185.51 ± 13.74	18.33 ± 2.23
MC exp. Strong_Wjets events	305.68 ± 19.54	131.45 ± 10.47	51.48 ± 5.23	4.03 ± 0.60
MC exp. EW_Zjets events	143.37 ± 3.66	114.34 ± 3.62	64.93 ± 2.80	6.42 ± 0.84
MC exp. EW_Wjets events	58.73 ± 2.09	42.82 ± 2.00	19.49 ± 1.09	2.80 ± 0.42
MC exp. top events	9.80 ± 3.21	6.05 ± 1.99	1.15 ± 0.43	0.29 ± 0.09
MC exp. other events	57.66 ± 17.74	31.05 ± 9.56	12.11 ± 3.83	1.57 ± 0.49
MC exp. QCD_multijet events	$24.84^{+26.09}_{-24.84}$	$5.85^{+6.14}_{-5.85}$	0.00 ± 0.00	$1.99^{+2.09}_{-1.99}$
MC exp. VBFWBall_100_99p0_MET125 events	80.78 ± 25.12	54.81 ± 17.44	30.19 ± 9.67	3.94 ± 1.39

Table 7.: Yields per bin in SR_VBF_njets3p for exclusion fit with the signal strength fixed to 1.

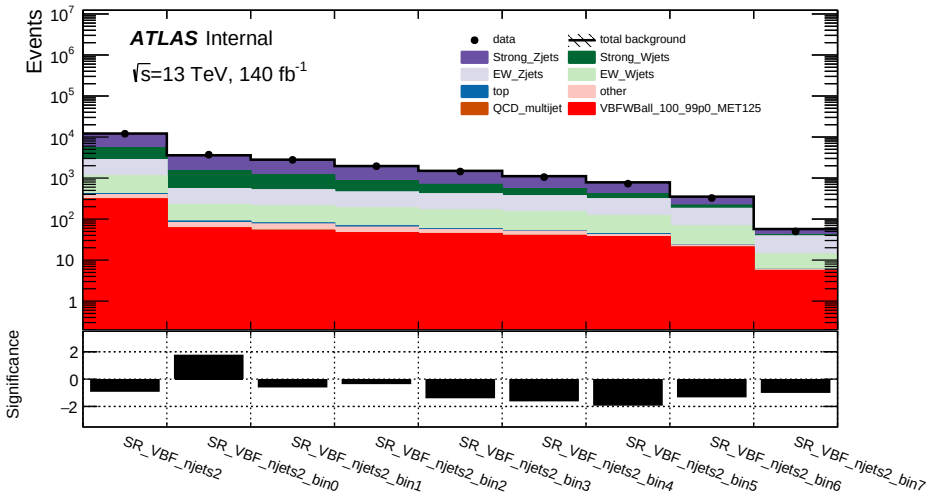

Figure 8: Significance plots in SR_VBF_njets2 for exclusion fit with signal strength fixed to 1.

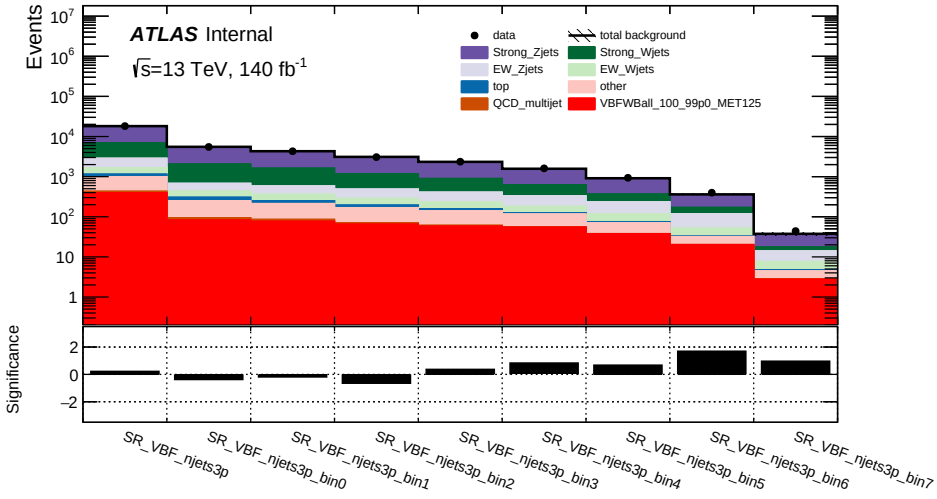

Figure 9: Significance plots in SR_VBF_njets3p for exclusion fit with signal strength fixed to 1.

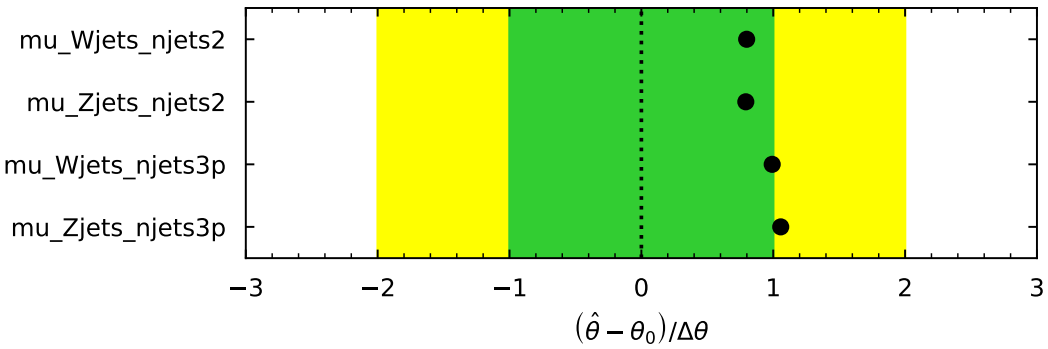

Figure 10: Normalization factors after the exclusion fit with the signal strength fixed to 1. The fitted values are mu_Wjets_njets2 = 0.7984 ± 0.0072, mu_Zjets_njets2 = 0.7919 ± 0.0121, mu_Wjets_njets3p = 0.9921 ± 0.0120, and mu_Zjets_njets3p = 1.0567 ± 0.0155 .

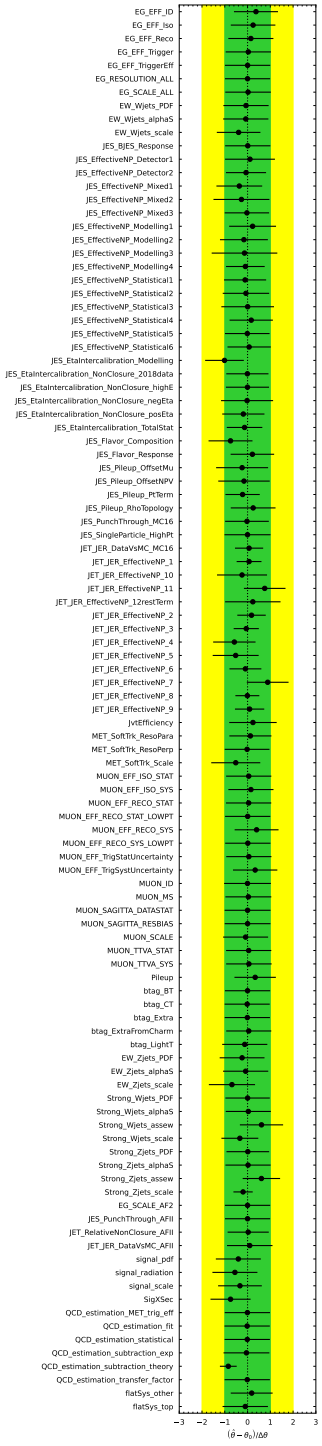

Figure 11: Pulls and constraints of fit parameters after the exclusion fit with the signal strength fixed to 1.

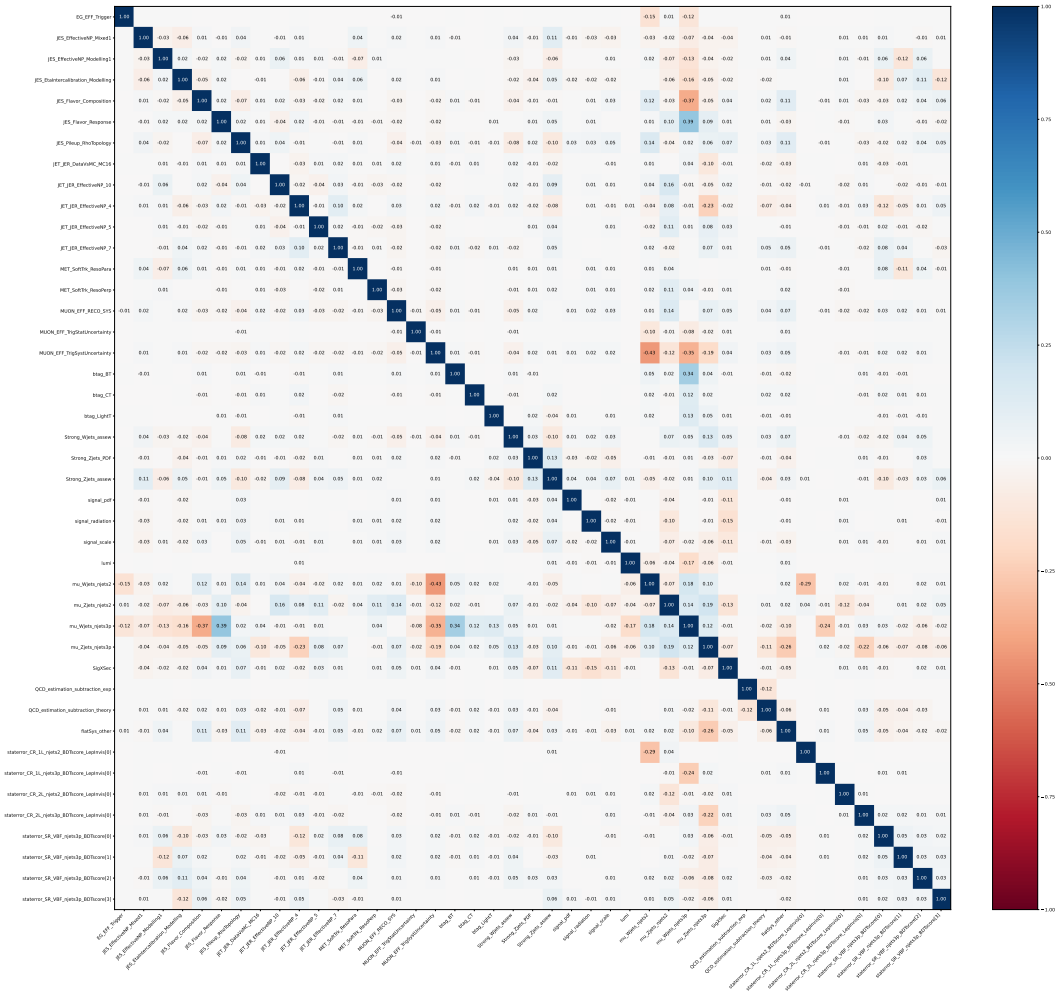

Figure 12: Correlation matrix (reduced) after the exclusion fit with the signal strength fixed to 1.

Bibliography

[1] ALEPH, DELPHI, L3, OPAL Experiments. *Combined LEP Chargino Results, up to 208 GeV for low DM*. LEPSUSYWG/02-04.1. 2002. URL: http://lepsusy.web.cern.ch/lepsusy/www/inoslowdmsummer02/charginolowdm_pub.html.

[2] ALICE Collaboration. "The ALICE experiment at the CERN LHC". In: *Journal of Instrumentation* 3 (2008), S08002–S08002. DOI: 10.1088/1748-0221/3/08/S08002. URL: https://doi.org/10.1088/1748-0221/3/08/S08002.

[3] S. Alioli et al. "A general framework for implementing NLO calculations in shower Monte Carlo programs: the POWHEG BOX". In: *JHEP* 06 (2010), p. 043. DOI: 10.1007/JHEP06(2010)043. arXiv: 1002.2581 [hep-ph].

[4] B. Allanach et al. "SUSY Les Houches Accord 2". In: *Computer Physics Communications* 180.1 (Jan. 2009), pp. 8–25. ISSN: 0010-4655. DOI: 10.1016/j.cpc.2008.08.004. URL: http://dx.doi.org/10.1016/j.cpc.2008.08.004.

[5] D. Alves et al. "Simplified models for LHC new physics searches". In: *J. Phys. G* 39 (2012), p. 105005. DOI: 10.1088/0954-3899/39/10/105005. arXiv: 1105.2838 [hep-ph].

[6] J. Alwall et al. "The automated computation of tree-level and next-to-leading order differential cross sections, and their matching to parton shower simulations". In: *JHEP* 07 (2014), p. 079. DOI: 10.1007/JHEP07(2014)079. arXiv: 1405.0301 [hep-ph].

[7] J. Alwall, P. Schuster, and N. Toro. "Simplified models for a first characterization of new physics at the LHC". In: *Phys. Rev. D* 79 (2009), p. 075020. DOI: 10.1103/PhysRevD.79.075020. arXiv: 0810.3921 [hep-ph].

[8] J. Alwall et al. "Searching for directly decaying gluinos at the Tevatron". In: *Phys. Lett. B* 666 (2008), p. 34. DOI: 10.1016/j.physletb.2008.06.065. arXiv: 0803.0019 [hep-ph].

[9] P. Artoisenet et al. "Automatic spin-entangled decays of heavy resonances in Monte Carlo simulations". In: *JHEP* 03 (2013), p. 015. DOI: 10.1007/JHEP03(2013)015. arXiv: 1212.3460 [hep-ph].

[10] ATLAS Collaboration. *ATLAS Liquid Argon Calorimeter: Technical Design Report*. ATLAS-TDR-2; CERN-LHCC-96-041. 1996. URL: https://cds.cern.ch/record/331061.

[11] ATLAS Collaboration. *ATLAS Tile Calorimeter: Technical Design Report*. ATLAS-TDR-3; CERN-LHCC-96-042. 1996. URL: https://cds.cern.ch/record/331062.

[12] ATLAS Collaboration. *ATLAS Muon Spectrometer: Technical Design Report*. ATLAS-TDR-10; CERN-LHCC-97-022. CERN, 1997. URL: https://cds.cern.ch/record/331068.

[13] ATLAS Collaboration. "The ATLAS Experiment at the CERN Large Hadron Collider". In: *JINST* 3 (2008), S08003. DOI: 10.1088/1748-0221/3/08/S08003.

[14] ATLAS Collaboration. *ATLAS Insertable B-Layer Technical Design Report*. ATLAS-TDR-19; CERN-LHCC-2010-013. 2010. URL: https://cds.cern.ch/record/1291633. Addendum: ATLAS-TDR-19-ADD-1; CERN-LHCC-2012-009. 2012. URL: https://cds.cern.ch/record/1451888.

[15] ATLAS Collaboration. *Particle Identification Performance of the ATLAS Transition Radiation Tracker*. ATLAS-CONF-2011-128. 2011. URL: https://cds.cern.ch/record/1383793.

[16] ATLAS Collaboration. "Observation of a new particle in the search for the Standard Model Higgs boson with the ATLAS detector at the LHC". In: *Phys. Lett. B* 716 (2012), p. 1. DOI: 10.1016/j.physletb.2012.08.020. arXiv: 1207.7214 [hep-ex].

[17] ATLAS Collaboration. *ATLAS Pythia 8 tunes to 7 TeV data*. ATL-PHYS-PUB-2014-021. 2014. URL: https://cds.cern.ch/record/1966419.

[18] ATLAS Collaboration. *Selection of jets produced in 13 TeV proton–proton collisions with the ATLAS detector*. ATLAS-CONF-2015-029. 2015. URL: https://cds.cern.ch/record/2037702.

[19] ATLAS Collaboration. "Measurement of the photon identification efficiencies with the ATLAS detector using LHC Run-1 data". In: *Eur. Phys. J. C* 76 (2016), p. 666. DOI: 10.1140/epjc/s10052-016-4507-9. arXiv: 1606.01813 [hep-ex].

[20] ATLAS Collaboration. "Performance of pile-up mitigation techniques for jets in pp collisions at $\sqrt{s} = 8$ TeV using the ATLAS detector". In: *Eur. Phys. J. C* 76 (2016), p. 581. DOI: 10.1140/epjc/s10052-016-4395-z. arXiv: 1510.03823 [hep-ex].

[21] ATLAS Collaboration. *Studies on top-quark Monte Carlo modelling for Top2016*. ATL-PHYS-PUB-2016-020. 2016. URL: https://cds.cern.ch/record/2216168.

[22] ATLAS Collaboration. "Identification and rejection of pile-up jets at high pseudorapidity with the ATLAS detector". In: *Eur. Phys. J. C* 77 (2017), p. 580. DOI: 10.1140/epjc/s10052-017-5081-5. arXiv: 1705.02211 [hep-ex]. Erratum: in: *Eur. Phys. J. C* 77 (2017), p. 712. DOI: 10.1140/epjc/s10052-017-5245-3.

[23] ATLAS Collaboration. "Jet reconstruction and performance using particle flow with the ATLAS Detector". In: *Eur. Phys. J. C* 77 (2017), p. 466. DOI: 10.1140/epjc/s10052-017-5031-2. arXiv: 1703.10485 [hep-ex].

[24] ATLAS Collaboration. "Performance of the ATLAS trigger system in 2015". In: *Eur. Phys. J. C* 77 (2017), p. 317. DOI: 10.1140/epjc/s10052-017-4852-3. arXiv: 1611.09661 [hep-ex].

[25] ATLAS Collaboration. *Object-based missing transverse momentum significance in the ATLAS Detector*. ATLAS-CONF-2018-038. 2018. URL: https://cds.cern.ch/record/2630948.

[26] ATLAS Collaboration. "Electron and photon performance measurements with the ATLAS detector using the 2015–2017 LHC proton–proton collision data". In: *JINST* 14 (2019), P12006. DOI: 10.1088/1748-0221/14/12/P12006. arXiv: 1908.00005 [hep-ex].

[27] ATLAS Collaboration. "Electron reconstruction and identification in the ATLAS experiment using the 2015 and 2016 LHC proton–proton collision data at $\sqrt{s}$ = 13 TeV". In: *Eur. Phys. J. C* 79 (2019), p. 639. DOI: 10.1140/epjc/s10052-019-7140-6. arXiv: 1902.04655 [physics.ins-det].

[28] ATLAS Collaboration. *Formulae for Estimating Significance*. ATL-PHYS-PUB-2020-025. 2020. URL: https://cds.cern.ch/record/2736148.

[29] ATLAS Collaboration. "Performance of the missing transverse momentum triggers for the ATLAS detector during Run-2 data taking". In: *JHEP* 08 (2020), p. 080. DOI: 10.1007/JHEP08(2020)080. arXiv: 2005.09554 [hep-ex].

[30] ATLAS Collaboration. "Searches for electroweak production of supersymmetric particles with compressed mass spectra in $\sqrt{s}$ = 13 TeV pp collisions with the ATLAS detector". In: *Phys. Rev. D* 101 (2020), p. 052005. DOI: 10.1103/PhysRevD.101.052005. arXiv: 1911.12606 [hep-ex].

[31] ATLAS Collaboration. "Jet energy scale and resolution measured in proton–proton collisions at $\sqrt{s}$ = 13 TeV with the ATLAS detector". In: *Eur. Phys. J. C* 81 (2021), p. 689. DOI: 10.1140/epjc/s10052-021-09402-3. arXiv: 2007.02645 [hep-ex].

[32] ATLAS Collaboration. "Muon reconstruction and identification efficiency in ATLAS using the full Run 2 pp collision data set at $\sqrt{s}$ = 13 TeV". In: *Eur. Phys. J. C* 81 (2021), p. 578. DOI: 10.1140/epjc/s10052-021-09233-2. arXiv: 2012.00578 [hep-ex].

[33] ATLAS Collaboration. "Search for chargino–neutralino pair production in final states with three leptons and missing transverse momentum in $\sqrt{s}$ = 13 TeV pp collisions with the ATLAS detector". In: *Eur. Phys. J. C* 81 (2021), p. 1118. DOI: 10.1140/epjc/s10052-021-09749-7. arXiv: 2106.01676 [hep-ex].

[34] ATLAS Collaboration. "Modelling and computational improvements to the simulation of single vector-boson plus jet processes for the ATLAS experiment". In: *JHEP* 08 (2022), p. 089. DOI: 10.1007/JHEP08(2022)089. arXiv: 2112.09588 [hep-ex].

[35] ATLAS Collaboration. "Operation and performance of the ATLAS semiconductor tracker in LHC Run 2". In: *JINST* 17 (2022), P01013. DOI: 10.1088/1748-0221/17/01/P01013. arXiv: 2109.02591 [physics.ins-det].

[36] ATLAS Collaboration. "Search for long-lived charginos based on a disappearing-track signature using 136 fb^{-1} of pp collisions at $\sqrt{s}$ = 13 TeV with the ATLAS detector". In: *Eur. Phys. J. C* 82 (2022), p. 606. DOI: 10.1140/epjc/s10052-022-10489-5. arXiv: 2201.02472 [hep-ex].

[37] ATLAS Collaboration. "ATLAS flavour-tagging algorithms for the LHC Run 2 pp collision dataset". In: *Eur. Phys. J. C* 83 (2023), p. 681. DOI: 10.1140/epjc/s10052-023-11699-1. arXiv: 2211.16345 [physics.data-an].

[38] ATLAS Collaboration. "Luminosity determination in pp collisions at $\sqrt{s}$ = 13 TeV using the ATLAS detector at the LHC". In: *Eur. Phys. J. C* 83 (2023), p. 982. DOI: 10.1140/epjc/s10052-023-11747-w. arXiv: 2212.09379 [hep-ex].

[39] ATLAS Collaboration. *Luminosity Public Results Run2*. URL: https://twiki.cern.ch/twiki/bin/view/AtlasPublic/LuminosityPublicResultsRun2.

[40] M. Baak et al. "HistFitter software framework for statistical data analysis". In: *Eur. Phys. J. C* 75 (2015), p. 153. DOI: 10.1140/epjc/s10052-015-3327-7. arXiv: 1410.1280 [hep-ex].

[41] M. Baugh. "Characterization of the Background due to Lepton Scattering to the $\chi^{\pm} \to \chi^0 \pi^{\pm}$ Disappearing Track Signature with the ATLAS Detector". UC Santa Cruz, 2019. URL: https://escholarship.org/uc/item/4p46z1r2.

[42] E. Bothmann et al. “Event generation with Sherpa 2.2”. In: *SciPost Phys.* 7.3 (2019), p. 034. DOI: 10.21468/SciPostPhys.7.3.034. arXiv: 1905.09127 [hep-ph].

[43] L. Boyle. *Standard Model Of Particle Physics–Most Complete Diagram*. Licensed under CC BY-SA 4.0. 2014. URL: https://commons.wikimedia.org/wiki/File:Standard_Model_Of_Particle_Physics--Most_Complete_Diagram.png.

[44] R. Brun and F. Rademakers. “ROOT – An object oriented data analysis framework”. In: *Nucl. Instrum. Meth. A* 389.1 (1997), pp. 81–86. ISSN: 0168-9002. DOI: 10.1016/S0168-9002(97)00048-X.

[45] *Building and steering template fits with cabinetry*. Zenodo, Mar. 2021. DOI: 10.5281/zenodo.4627038. URL: https://doi.org/10.5281/zenodo.4627038.

[46] M. Cacciari, G. P. Salam, and G. Soyez. “The anti-k_t jet clustering algorithm”. In: *JHEP* 04 (2008), p. 063. DOI: 10.1088/1126-6708/2008/04/063. arXiv: 0802.1189 [hep-ph].

[47] M. Cacciari, G. P. Salam, and G. Soyez. “The catchment area of jets”. In: *Journal of High Energy Physics* 2008.04 (Apr. 2008), p. 005. DOI: 10.1088/1126-6708/2008/04/005. URL: https://dx.doi.org/10.1088/1126-6708/2008/04/005.

[48] S. Catani et al. “QCD Matrix Elements + Parton Showers”. In: *JHEP* 11 (2001), p. 063. DOI: 10.1088/1126-6708/2001/11/063. arXiv: hep-ph/0109231.

[49] D. Clowe et al. “A Direct Empirical Proof of the Existence of Dark Matter*”. In: *The Astrophysical Journal* 648.2 (Aug. 2006), p. L109. DOI: 10.1086/508162. URL: https://dx.doi.org/10.1086/508162.

[50] CMS Collaboration. “The CMS experiment at the CERN LHC”. In: *Journal of Instrumentation* 3 (2008), S08004–S08004. DOI: 10.1088/1748-0221/3/08/S08004. URL: https://doi.org/10.1088/1748-0221/3/08/S08004.

[51] CMS Collaboration. “Observation of a new boson at a mass of 125 GeV with the CMS experiment at the LHC”. In: *Phys. Lett. B* 716 (2012), p. 30. DOI: 10.1016/j.physletb.2012.08.021. arXiv: 1207.7235 [hep-ex].

[52] CMS Collaboration. “Search for supersymmetry with a compressed mass spectrum in the vector boson fusion topology with 1-lepton and 0-lepton final states in proton–proton collisions at $\sqrt{s} = 13$ TeV”. In: *JHEP* 08 (2019), p. 150. DOI: 10.1007/JHEP08(2019)150. arXiv: 1905.13059 [hep-ex].

[53] A. Collaboration. “ATLAS pixel detector electronics and sensors”. In: *Journal of Instrumentation* 3.07 (July 2008), P07007. DOI: 10.1088/1748-0221/3/07/P07007. URL: https://dx.doi.org/10.1088/1748-0221/3/07/P07007.

[54] A. Collaboration. “Experiment Briefing: Keeping the ATLAS Inner Detector in perfect alignment”. General Photo. 2020. URL: https://cds.cern.ch/record/2723878.

[55] A. Collaboration. *TRExFitter Documentation*. Accessed: 2024-08-01. 2024. URL: https://trexfitter-docs.web.cern.ch/trexfitter-docs/.

[56] P. Collaboration. “Planck 2015 results - XIII. Cosmological parameters”. In: *A&A* 594 (2016), A13. DOI: 10.1051/0004-6361/201525830. URL: https://doi.org/10.1051/0004-6361/201525830.

[57] S.-K. Collaboration. “Search for proton decay via $p \to e^+\pi^0$ and $p \to \mu^+\pi^0$ with an enlarged fiducial volume in Super-Kamiokande I-IV”. In: *Phys. Rev. D* 102 (2020), p. 112011. DOI: 10.1103/PhysRevD.102.112011.

[58] G. Cowan et al. “Asymptotic formulae for likelihood-based tests of new physics”. In: *Eur. Phys. J. C* 71 (2011), p. 1554. DOI: 10.1140/epjc/s10052-011-1554-0. arXiv: 1007.1727 [physics.data-an]. Erratum: in: *Eur. Phys. J. C* 73 (2013), p. 2501. DOI: 10.1140/epjc/s10052-013-2501-z.

[59] K. Cranmer et al. *HistFactory: A tool for creating statistical models for use with RooFit and RooStats*. Tech. rep. New York: New York U., 2012. DOI: 10.17181/CERN-OPEN-2012-016. URL: https://cds.cern.ch/record/1456844.

[60] M. D’Onofrio and K. Rummukainen. “Standard model cross-over on the lattice”. In: *Physical Review D* 93.2 (Jan. 2016). ISSN: 2470-0029. DOI: 10.1103/physrevd.93.025003. URL: http://dx.doi.org/10.1103/PhysRevD.93.025003.

[61] S. Dimopoulos, S. Raby, and F. Wilczek. “Supersymmetry and the scale of unification”. In: *Phys. Rev. D* 24 (1981), p. 1681. DOI: 10.1103/PhysRevD.24.1681.

[62] A. Djouadi et al. *The Minimal Supersymmetric Standard Model: Group Summary Report*. 1999. arXiv: hep-ph/9901246 [hep-ph]. URL: https://arxiv.org/abs/hep-ph/9901246.

[63] B. Dolgoshein. “Transition radiation detectors”. In: *Nuclear Instruments and Methods in Physics Research Section A: Accelerators, Spectrometers, Detectors and Associated Equipment* 326.3 (1993), pp. 434–469. ISSN: 0168-9002. DOI: https://doi.org/10.1016/0168-9002(93)90846-A. URL: https://www.sciencedirect.com/science/article/pii/016890029390846A.

[64] J. Edsjö and P. Gondolo. “Neutralino relic density including coannihilations”. In: *Physical Review D* 56.4 (Aug. 1997), pp. 1879–1894. ISSN: 1089-4918. DOI: 10.1103/physrevd.56.1879. URL: http://dx.doi.org/10.1103/PhysRevD.56.1879.

[65] F. Englert and R. Brout. “Broken Symmetry and the Mass of Gauge Vector Mesons”. In: *Phys. Rev. Lett.* 13 (1964). Ed. by J. C. Taylor, pp. 321–323. DOI: 10.1103/PhysRevLett.13.321.

[66] L. Evans and P. Bryant. “LHC Machine”. In: *JINST* 3 (2008), S08001. DOI: 10.1088/1748-0221/3/08/S08001. URL: https://doi.org/10.1088/1748-0221/3/08/S08001.

[67] G. R. Farrar and P. Fayet. “Phenomenology of the production, decay, and detection of new hadronic states associated with supersymmetry”. In: *Phys. Lett. B* 76 (1978), p. 575. DOI: 10.1016/0370-2693(78)90858-4.

[68] R. Frederix, E. Re, and P. Torrielli. “Single-top t-channel hadroproduction in the four-flavour scheme with POWHEG and aMC@NLO”. In: *JHEP* 09 (2012), p. 130. DOI: 10.1007/JHEP09(2012)130. arXiv: 1207.5391 [hep-ph].

[69] S. Frixione, P. Nason, and C. Oleari. “Matching NLO QCD computations with parton shower simulations: the POWHEG method”. In: *JHEP* 11 (2007), p. 070. DOI: 10.1088/1126-6708/2007/11/070. arXiv: 0709.2092 [hep-ph].

[70] S. Frixione, G. Ridolfi, and P. Nason. “A positive-weight next-to-leading-order Monte Carlo for heavy flavour hadroproduction”. In: *JHEP* 09 (2007), p. 126. DOI: 10.1088/1126-6708/2007/09/126. arXiv: 0707.3088 [hep-ph].

[71] S. Frixione et al. “Single-top hadroproduction in association with a W boson”. In: *JHEP* 07 (2008), p. 029. DOI: 10.1088/1126-6708/2008/07/029. arXiv: 0805.3067 [hep-ph].

[72] L. Girardello and M. T. Grisaru. “Soft Breaking of Supersymmetry”. In: *Nucl. Phys. B* 194 (1982), p. 65. DOI: 10.1016/0550-3213(82)90512-0.

[73] S. L. Glashow. “Partial Symmetries of Weak Interactions”. In: *Nucl. Phys.* 22 (1961), pp. 579–588. DOI: 10.1016/0029-5582(61)90469-2.

[74] T. Gleisberg and S. Höche. "Comix, a new matrix element generator". In: *JHEP* 12 (2008), p. 039. DOI: 10.1088/1126-6708/2008/12/039. arXiv: 0808.3674 [hep-ph].

[75] Y. Golfand and E. Likhtman. "Extension of the Algebra of Poincare Group Generators and Violation of P Invariance". In: *JETP Lett.* 13 (1971). [Pisma Zh. Eksp. Teor. Fiz. **13** (1971) 452], p. 323.

[76] K. Griest and D. Seckel. "Three exceptions in the calculation of relic abundances". In: *Phys. Rev. D* 43 (10 May 1991), pp. 3191–3203. DOI: 10.1103/PhysRevD.43.3191. URL: https://link.aps.org/doi/10.1103/PhysRevD.43.3191.

[77] D. J. Gross and F. Wilczek. "Ultraviolet Behavior of Nonabelian Gauge Theories". In: *Phys. Rev. Lett.* 30 (1973). Ed. by J. C. Taylor, pp. 1343–1346. DOI: 10.1103/PhysRevLett.30.1343.

[78] G. S. Guralnik, C. R. Hagen, and T. W. B. Kibble. "Global Conservation Laws and Massless Particles". In: *Phys. Rev. Lett.* 13 (1964). Ed. by J. C. Taylor, pp. 585–587. DOI: 10.1103/PhysRevLett.13.585.

[79] L. Heinrich, M. Feickert, and G. Stark. *pyhf: v0.7.6*. Version 0.7.6. https://github.com/scikit-hep/pyhf/releases/tag/v0.7.6. DOI: 10.5281/zenodo.1169739. URL: https://doi.org/10.5281/zenodo.1169739.

[80] L. Heinrich et al. "pyhf: pure-Python implementation of HistFactory statistical models". In: *Journal of Open Source Software* 6.58 (2021), p. 2823. DOI: 10.21105/joss.02823. URL: https://doi.org/10.21105/joss.02823.

[81] P. W. Higgs. "Broken Symmetries and the Masses of Gauge Bosons". In: *Phys. Rev. Lett.* 13 (1964). Ed. by J. C. Taylor, pp. 508–509. DOI: 10.1103/PhysRevLett.13.508.

[82] S. Höche et al. "QCD matrix elements and truncated showers". In: *JHEP* 05 (2009), p. 053. DOI: 10.1088/1126-6708/2009/05/053. arXiv: 0903.1219 [hep-ph].

[83] S. Höche et al. "A critical appraisal of NLO+PS matching methods". In: *JHEP* 09 (2012), p. 049. DOI: 10.1007/JHEP09(2012)049. arXiv: 1111.1220 [hep-ph].

[84] S. Höche et al. "QCD matrix elements + parton showers. The NLO case". In: *JHEP* 04 (2013), p. 027. DOI: 10.1007/JHEP04(2013)027. arXiv: 1207.5030 [hep-ph].

[85] G. Ke et al. "LightGBM: A Highly Efficient Gradient Boosting Decision Tree". In: *Advances in Neural Information Processing Systems*. Ed. by I. Guyon et al. Vol. 30. Curran Associates, Inc., 2017. URL: https://proceedings.neurips.cc/paper_files/paper/2017/file/6449f44a102fde848669bdd9eb6b76fa-Paper.pdf.

[86] P. Langacker. “Grand unification”. In: *Scholarpedia* 7.10 (2012), p. 11419. URL: http://www.scholarpedia.org/article/Grand_unification.

[87] D. J. Lange. “The EvtGen particle decay simulation package”. In: *Nucl. Instrum. Meth. A* 462 (2001), p. 152. DOI: 10.1016/S0168-9002(01)00089-4.

[88] LHCb Collaboration. “The LHCb Detector at the LHC”. In: *Journal of Instrumentation* 3 (2008), S08005–S08005. DOI: 10.1088/1748-0221/3/08/S08005. URL: https://doi.org/10.1088/1748-0221/3/08/S08005.

[89] W. Lukas. *Fast Simulation for ATLAS: Atlfast-II and ISF*. Tech. rep. Geneva: CERN, 2012. DOI: 10.1088/1742-6596/396/2/022031. URL: https://cds.cern.ch/record/1458503.

[90] S. M. Lundberg and S.-I. Lee. “A Unified Approach to Interpreting Model Predictions”. In: *Advances in Neural Information Processing Systems 30*. Ed. by I. Guyon et al. Curran Associates, Inc., 2017, pp. 4765–4774. URL: http://papers.nips.cc/paper/7062-a-unified-approach-to-interpreting-model-predictions.pdf.

[91] S. P. Martin. “A Supersymmetry Primer”. In: *Adv. Ser. Direct. High Energy Phys.* 18 (1998), p. 1. DOI: 10.1142/9789812839657_0001. arXiv: hep-ph/9709356.

[92] E. Mobs. *The CERN accelerator complex. Complexe des accOlOrateurs du CERN*. General Photo. URL: https://cds.cern.ch/record/2197559.

[93] P. Nason. “A new method for combining NLO QCD with shower Monte Carlo algorithms”. In: *JHEP* 11 (2004), p. 040. DOI: 10.1088/1126-6708/2004/11/040. arXiv: hep-ph/0409146.

[94] NNPDF Collaboration, R. D. Ball, et al. “Parton distributions with LHC data”. In: *Nucl. Phys. B* 867 (2013), p. 244. DOI: 10.1016/j.nuclphysb.2012.10.003. arXiv: 1207.1303 [hep-ph].

[95] NNPDF Collaboration, R. D. Ball, et al. “Parton distributions for the LHC run II”. In: *JHEP* 04 (2015), p. 040. DOI: 10.1007/JHEP04(2015)040. arXiv: 1410.8849 [hep-ph].

[96] J. Pequenao. “Computer Generated image of the ATLAS calorimeter”. 2008. URL: https://cds.cern.ch/record/1095927.

[97] J. Pequenao. “Computer generated image of the ATLAS inner detector”. 2008. URL: https://cds.cern.ch/record/1095926.

[98] J. Pequenao. “Computer generated image of the ATLAS Muons subsystem”. 2008. URL: https://cds.cern.ch/record/1095929.

[99] J. Pequenao. "Computer generated image of the whole ATLAS detector". 2008. URL: https://cds.cern.ch/record/1095924.

[100] J. Pequenao and P. Schaffner. "How ATLAS detects particles: diagram of particle paths in the detector". 2013. URL: https://cds.cern.ch/record/1505342.

[101] M. E. Peskin and D. V. Schroeder. *An Introduction to quantum field theory*. Reading, USA: Addison-Wesley, 1995. ISBN: 978-0-201-50397-5, 978-0-429-50355-9, 978-0-429-49417-8. DOI: 10.1201/9780429503559.

[102] E. Re. "Single-top Wt-channel production matched with parton showers using the POWHEG method". In: *Eur. Phys. J. C* 71 (2011), p. 1547. DOI: 10.1140/epjc/s10052-011-1547-z. arXiv: 1009.2450 [hep-ph].

[103] A. L. Read. "Presentation of search results: the CL_S technique". In: *J. Phys. G* 28 (2002), p. 2693. DOI: 10.1088/0954-3899/28/10/313.

[104] V. C. Rubin, J. Ford W. K., and N. Thonnard. "Extended rotation curves of high-luminosity spiral galaxies. IV. Systematic dynamical properties, Sa -> Sc." In: *Astrophysical Journal* 225 (1978), pp. L107–L111. DOI: 10.1086/182804.

[105] A. Salam. "Weak and Electromagnetic Interactions". In: *Conf. Proc. C* 680519 (1968), pp. 367–377. DOI: 10.1142/9789812795915_0034.

[106] S. Schumann and F. Krauss. "A parton shower algorithm based on Catani–Seymour dipole factorisation". In: *JHEP* 03 (2008), p. 038. DOI: 10.1088/1126-6708/2008/03/038. arXiv: 0709.1027 [hep-ph].

[107] M. D. Schwartz. *Quantum Field Theory and the Standard Model*. Cambridge University Press, Mar. 2014. ISBN: 978-1-107-03473-0, 978-1-107-03473-0.

[108] A. Seiden. *Particle physics: A comprehensive introduction*. 2004. ISBN: 978-0-8053-8736-0.

[109] J. Shahinian. "Soft Leptons, Hard Problems: Searches for the Electroweak Production of Supersymmetric Particles in Compressed Mass Spectra with the ATLAS Detector". Presented 16 Mar 2020. UC, Santa Cruz, 2020. URL: https://cds.cern.ch/record/2719353.

[110] T. Sjöstrand et al. "An introduction to PYTHIA 8.2". In: *Comput. Phys. Commun.* 191 (2015), p. 159. DOI: 10.1016/j.cpc.2015.01.024. arXiv: 1410.3012 [hep-ph].

[111] S. Weinberg. "A Model of Leptons". In: *Phys. Rev. Lett.* 19 (1967), pp. 1264–1266. DOI: 10.1103/PhysRevLett.19.1264.

[112] J. Wess and B. Zumino. "Supergauge transformations in four dimensions". In: *Nucl. Phys. B* 70 (1974), p. 39. DOI: 10.1016/0550-3213(74)90355-1.

[113] R. L. Workman et al. “Review of Particle Physics”. In: *PTEP* 2022 (2022), p. 083C01. DOI: 10.1093/ptep/ptac097.